

# Cuttings transport and hydraulics optimisation for underbalanced drilling (UBD) operations in concentric and eccentric, directional and extended reach wells.

SALUBI, V.

2022

*The author of this thesis retains the right to be identified as such on any occasion in which content from this thesis is referenced or re-used. The licence under which this thesis is distributed applies to the text and any original images only – re-use of any third-party content must still be cleared with the original copyright holder.*

**Cuttings transport and hydraulics optimisation for underbalanced drilling UBD operations in concentric and eccentric, directional and extended reach wells.**

**Voke Salubi**

**A thesis submitted in partial fulfilment of the requirements of Robert Gordon University for the degree of Doctor of Philosophy**

**Sept 2022**

## **DECLARATION**

I declare that I am the sole author of this thesis and that all verbatim extracts contained in the thesis have been identified and the sources of information specifically acknowledged in the bibliography.

## **ABSTRACT**

Underbalanced drilling facilitates the effective control of wellbore pressures amongst several other important advantages when compared to conventional drilling technology. However, this involves the flow of multiphase fluids which introduces additional complexities due to highly transient flow patterns, unpredictable wellbore hydraulics and increased tendency for the settling of drilled cuttings in the wellbore. An accurate prediction of the fluid dynamics and cutting transport efficiency is required to achieve an effective pressure management hole cleaning operation

In this research, a theoretical, numerical and experimental study was performed to analyse and investigate the cutting transport dynamics and wellbore hydraulics. The analytical study involved the development of several mechanistic models that are valid for both single phase and two-phase flows in the concentric and eccentric annuli with and without inner pipe rotation. Reynolds number and effective viscosity equations valid for annuli flow of both Newtonian and non-Newtonian Power law, Bingham plastic and Yield power law fluids were derived and presented. New Laminar and turbulent friction geometry parameter and friction factor equations that take in account the combined effect of the fluid rheology, fluid circulation rate, pipe eccentricity and inner pipe rotation speed for the evaluation of the that flow dynamics and pressure losses in the annuli were formulated from the solution of the continuity equation of motion for axial steady-state flows. In addition, new flow gas-liquid pattern dependent multi-layered models valid for horizontal and inclined annuli flows were developed for the different cuttings transport mechanisms. Numerical computational fluid dynamics simulations were performed to discretise and solve the governing equations for fluid flow using a finite volume mathematical approach to obtain velocity, viscosity and pressure fields for different input conditions. Furthermore, an experimental study was carried out to evaluate the interplay between the two-phase gas-liquid flow patterns and the major drilling parameters and investigate its influence on the cuttings and fluid flow dynamics in a horizontal and inclined drilling wellbore.

Results showed that the effect of the drillpipe rotation on cuttings transport in the annuli is highly dependent on the fluid rheological properties, the drillpipe eccentricity, the wellbore inclination and fluid flow pattern. The annuli pressure

gradient was found to be dependent on the fluid flow pattern and the prevailing cutting transport mechanism. The minimum requirements to clean an eccentric annulus is higher than that required for the concentric annulus. Furthermore, the local mixture properties and gas-liquid flow pattern of the fluid is strongly influenced by the inclination angle of the wellbore which as of a result, influences the annuli pressure losses and cutting transport dynamics. Although drillpipe rotation can improve cuttings transport through the annuli, the influence of drillpipe rotation on the cutting's movement in the two-phase gas-liquid drilling fluid is much less than that of the single-phase drilling fluid.

Overall, a good match was found when the mathematical models were compared to the experimental data. The output of this research is very useful for implementing an efficient cutting transport operation, hydraulic program optimisation and effective wellbore control, particularly for managed pressure drilling operations.

## **ACKNOWLEDGEMENTS**

I would like to extend my sincere gratitude to my supervisory team Dr Gbenga Oluyemi, Professor Babs Oyeneyin and Dr Firdaus Muhammad-Sukki for their support, guidance and direction during my PhD programme. Thank you for your expressions of encouragement, insightful comments and suggestions.

I am grateful to the School of Engineering at Robert Gordon University–Professor Iain Steel, Professor James Njuguna, Dr Rosslyn Shanks and Kirsty Stevenson for helping to facilitate my research project.

My sincere appreciation goes to the technical support team–Alan McLean, Alexander Laing, Allan MacPherson, Patrick Kane, David Howie, Ross Henderson and Andy Ross for their support with my experimental rig setup.

I would like to thank my colleague and lab partner Ruissein Mahon.

Finally, I am deeply grateful to my family for their unconditional support and

## TABLE OF CONTENTS

<i>DECLARATION</i> .....	<i>ii</i>
<i>ABSTRACT</i> .....	<i>iii</i>
<i>ACKNOWLEDGEMENTS</i> .....	<i>v</i>
<i>TABLE OF CONTENTS</i> .....	<i>vi</i>
<i>LIST OF FIGURES</i> .....	<i>ix</i>
<i>LIST OF TABLES</i> .....	<i>xiv</i>
<i>NOMENCLATURES</i> .....	<i>xv</i>
<b>Chapter1</b> .....	<b>1</b>
<i>Introduction</i> .....	<i>1</i>
1.1 Background .....	<i>1</i>
1.2 Research objectives .....	<i>3</i>
1.3 Method and Approach .....	<i>4</i>
<b>Chapter2</b> .....	<b>6</b>
<i>Literature review</i> .....	<i>6</i>
2.1 Non-Newtonian fluid flow in annuli .....	<i>6</i>
2.2 Multiphase Gas – Liquid flow in pipes .....	<i>27</i>
2.3 Multiphase Gas – Liquid flow in annuli .....	<i>62</i>
2.4 Cuttings transport in drilling annuli .....	<i>75</i>
2.4.1 Multiphase cutting transport in annuli .....	<i>87</i>
2.5 Summary of research gaps .....	<i>88</i>
<b>Chapter3</b> .....	<b>90</b>
<i>Experimental study</i> .....	<i>90</i>
3.1 Experimental rig design and setup .....	<i>91</i>
3.1.1 Test sections.....	<i>96</i>
3.1.2 Pressure transmitters .....	<i>98</i>
3.1.3 Flow meter .....	<i>99</i>
3.1.4 DC motor.....	<i>99</i>
3.1.5 Photoelectric sensors.....	<i>100</i>
3.1.6 Data acquisition system.....	<i>101</i>
3.2 Calibration of experimental rig .....	<i>101</i>
3.2.1 Pressure transducers.....	<i>101</i>
3.2.2 Fluid flow meter .....	<i>102</i>
3.3 Data acquisition techniques .....	<i>103</i>
3.3.1 Pressure readings .....	<i>103</i>
3.3.2 Rotary speed of the inner pipe.....	<i>104</i>
3.4 Material analysis for experimental fluids <b>Error! Bookmark not defined.</b>	
3.4.1 Determination of rheological parameters.....	<i>92</i>
3.5 Granular materials used in experiments <b>Error! Bookmark not defined.</b>	
3.6 Experimental test procedures .....	<i>106</i>
3.6.1 Single-phase flow .....	<i>106</i>
3.6.2 Single-phase flow with solid particles.....	<i>107</i>
3.6.3 Two-phase flow .....	<i>107</i>

3.6.4 Two-phase flow with solid particles .....	108
<b>Chapter4.....</b>	<b>110</b>
<i>Mathematical modelling of multiphase flow in annuli .....</i>	<i>110</i>
4.1 Reynolds number for annuli flow of non-Newtonian fluids.....	110
4.2 Friction factor for laminar flow of non-Newtonian fluids.....	117
4.2.1 Generalised rheology model .....	119
4.2.2 Annuli shear stress and velocity profiles.....	120
4.3 Friction geometry parameter .....	134
4.4 Friction factor for turbulent flow of non-Newtonian fluids.....	141
4.5 Multiphase drilling hydraulics modelling .....	142
4.5.1 Pressure drop for dispersed bubble flow .....	144
4.5.2 Pressure drop for bubble flow .....	145
4.5.3 Pressure drop for stratified flow .....	146
4.5.4 Pressure drop for slug flow .....	147
4.6 Geometric and Closure relationships .....	158
<b>Chapter5.....</b>	<b>164</b>
<i>Cuttings transport modelling .....</i>	<i>164</i>
5.1 Concept of minimum transport velocity.....	165
5.1.1 Initiation of cutting movement.....	166
5.1.2 Factors affecting cutting transport.....	169
5.2 Multi-layered model development .....	171
5.2.1 Dispersed bubble flow .....	174
5.2.2 Stratified flow .....	177
5.2.3 Slug flow .....	182
<b>Chapter6.....</b>	<b>192</b>
<i>Numerical CFD methodology.....</i>	<i>192</i>
6.1 Discretisation of governing equations .....	194
6.1.1 Concentric annuli $E = 0$ .....	195
6.1.2 Eccentric annuli $E > 0$ .....	207
6.2 Geometry and mesh generation.....	211
6.3 Single-phase flow simulations .....	214
6.4 Two phase flow .....	222
6.4.1 Fluid density field.....	222
6.4.2 Interface tracking .....	223
6.4.3 Effect of rpm and eccentricity on flow pattern .....	228
6.5 Validation of mathematical modelling .....	230
<b>Chapter7 .....</b>	<b>234</b>
<i>Results and discussion .....</i>	<i>234</i>
7.1 Effect of inner pipe rotation on flow pattern transitions .....	234
7.2 Effect of inner pipe rotation on annuli pressure drop.....	237
7.2.1 Annuli pressure gradient .....	237
7.2.2 Liquid film length.....	243
7.3 Cuttings transport .....	245
7.3.1 Effect of Fluid Flowrate .....	245
7.3.2 Effect of wellbore inclination.....	252
7.3.3 Effect of fluid viscosity .....	256

7.3.4 Effect of inner pipe rotation .....	257
7.4 Pressure gradient due to particle transport.....	262
7.4.1 Cutting transport model validation .....	265
<b>Chapter8.....</b>	<b>269</b>
<i>Conclusions and recommendations .....</i>	<i>269</i>
8.1 Conclusions .....	269
8.2 Contribution to knowledge .....	274
8.3 Recommendations .....	277
<i>References.....</i>	<i>278</i>
<i>Appendix A: MATLAB code for the determination of the rheological parameters of fluids .....</i>	<i>283</i>

## LIST OF FIGURES

Figure 2.1: Shear stress to shear strain relationship for non-Newtonian fluids.....	7
Figure 2.2: Wellbore velocity profiles in eccentric annuli .....	9
Figure 2.3: Axial velocity and shear stress distribution for annuli flows (Fredrickson & Bird, 1958) .....	14
Figure 2.4: Eccentric annulus defined by bipolar coordinates (Haciislamoglu & Langlinais, 1990) .....	19
Figure 2.5: Eccentric annulus grid in bipolar coordinates (Haciislamoglu & Langlinais, 1990).....	21
Figure 2.6: Process of formation of the slug flow pattern (Duckler & Hubbard, 1975).....	54
Figure 2.7: Voltage-time trace illustrating the estimation of the PDF (Kelessidis & Dukler, 1988) .....	63
Figure 2.8: Example of PDF plots for the bubble (left) and slug flow pattern (right) (Kelessidis & Dukler, 1988). .....	64
Figure 2.9: Example of PDF plots for the churn (left) and annular flow pattern (right) (Kelessidis & Dukler, 1988).....	65
Figure 2.10: Friction geometry parameter for laminar flow in annuli and circular pipes.....	68
Figure 3.1: Shear stress versus shear rate data for the test fluids .....	91
Figure 3.2: Variation of correlation coefficient with assumed values of yield stress.....	93
Figure 3.3: (a) solids separation tank and (b) glass and plastic beads .....	95
Figure 3.4: Schematic diagram of the experimental unit.....	96
Figure 3.5: Acrylic glass tube and ABS pipe used to construct a concentric/eccentric annulus test section.....	97
Figure 3.6: Concentric and eccentric flanges.....	98
Figure 3.7: DC motor connected to inner pipe and the motor speed controller .....	100
Figure 3.8: Photoelectric sensor and reflector tape arrangement .....	100
Figure 3.9: Data acquisition devices.....	101
Figure 3.10: LabVIEW block diagram for pressure to flowrate data acquisition .....	104
Figure 3.11: LabVIEW block diagram for inner pipe rotary speed calculation .....	105
Figure 4.1: Annuli velocity profile of a non-Newtonian with a yield stress .....	123
Figure 4.2: Eccentric annulus with a variable outer radius .....	125
Figure 4.3: Axial velocity profiles for the Power law fluid flow in the concentric annulus with drillpipe rotation .....	130
Figure 4.4: Axial velocity profiles for the Power law fluid flow in the eccentric annulus with drillpipe rotation .....	131
Figure 4.5: Effect of drillpipe rotation on the axial velocity at the largest region of the eccentric annulus for the Power law fluid flow .....	132

Figure 4.6:Effect of drillpipe rotation on the axial velocity at the smallest region of the eccentric annulus for the Power law fluid flow .....	132
Figure 4.7:Axial velocity profiles for the Herschel-Bulkley fluid flow in the eccentric annulus with drillpipe rotation .....	133
Figure 4.8:Effect of drillpipe rotation on the axial velocity at the smallest region of the eccentric annulus for the Herschel-Bulkley fluid flow. ....	134
Figure 4.9: Friction geometry parameter plot ( $n = 0.75$ ) .....	136
Figure 4.10:Friction geometry parameter plot ( $n = 0.55$ ) .....	137
Figure 4.11:Pressure gradient versus eccentricity .....	139
Figure 4.12:Effect of drillpipe rotation on the friction geometry parameter( $e = 0.5,n = 0.75$ ) .....	140
Figure 4.13:Effect of drillpipe rotation on the friction geometry parameter( $e = 0.5,n=0.55$ ) .....	140
Figure 4.14:Configuration of a fully developed in an inclined wellbore annulus.....	148
Figure 4.15:Annulus geometry schematic for rate of change of liquid area with height.....	150
Figure 4.16:Change in the liquid film height with distance in the liquid film region.....	153
Figure 4.17:Schematic showing the annuli geometric parameters .....	159
Figure 5.1:Forces acting on cutting particles in an inclined wellbore annulus.....	167
Figure 5.2:Configuration of the three-layered cutting transport mechanism in wellbore annuli.....	172
Figure 5.3:Schematic diagram of the three-layer model for dispersed bubble flow .....	175
Figure 5.4:Schematic diagram of the four-layer model for stratified (gas, liquid and cuttings) flow .....	179
Figure 5.5:A fully developed slug flow with different cutting transport mechanisms in an inclined wellbore annulus.....	183
Figure 5.6:Schematic diagram of the mathematical model for liquid film/gas pocket region .....	185
Figure 6.1 Control volume in cylindrical coordinates.....	195
Figure 6.2:Control volume showing the location of the pressure and velocity fields in cylindrical coordinates.....	197
Figure 6.3: Control volume staggered by half a mesh in the axial direction .....	199
Figure 6.4:Control volume staggered by half a mesh in the angular direction .....	199
Figure 6.5:Control volume staggered by half a mesh in the radial direction .....	200
Figure 6.6:x-y plane of the control volumes for a structured mesh in the annuli .....	208
Figure 6.7: Concentric and eccentric annuli geometry and mesh for fluid flow simulations .....	212
Figure 6.8: Mesh independence test .....	213

Figure 6.9:Velocity fields in the concentric annulus ( $Q = 12\text{m}^3/\text{h}$ , $\epsilon = 0.0054$ , $n = 1$ , $\tau \epsilon = 0$ ) .....	215
Figure 6.10:Velocity fields in the concentric annulus ( $Q = 7\text{m}^3/\text{h}$ , $\epsilon = 0.094$ , $n = 0.62$ , $\tau \epsilon = 0$ ) .....	215
Figure 6.11:Velocity fields in the eccentric annulus, $e = 0.3$ ( $Q = 7\text{m}^3/\text{h}$ , $\epsilon = 0.094$ , $n = 0.62$ , $\tau \epsilon = 0$ ) .....	216
Figure 6.12:Velocity fields in the eccentric annulus, $e = 0.7$ ( $Q = 7\text{m}^3/\text{h}$ , $\epsilon = 0.094$ , $n = 0.62$ , $\tau \epsilon = 0$ ) .....	217
Figure 6.13:Velocity fields in the eccentric annulus, $e = 0.7$ ( $Q = 7\text{m}^3/\text{h}$ , $\epsilon = 0.643$ , $n = 0.44$ , $\tau \epsilon = 1.5$ ) .....	217
Figure 6.14:Improvement in fluid velocity in the bottom region of the eccentric annuli with inner pipe rotation .....	218
Figure 6.15:Tangential velocity field in the concentric annuli ( $e = 0$ , rpm = 150) .....	218
Figure 6.16:Tangential velocity field in the eccentric annuli ( $e = 0.7$ , rpm = 150) .....	219
Figure 6.17: Fluid viscosity field in the eccentric annuli ( $e = 0$ , rpm = 0) .....	219
Figure 6.18:Fluid viscosity in eccentric annuli ( $e = 0$ , rpm = 150) .....	220
Figure 6.19:Interpretation of the location of the centroid of a front element within a fixed grid.....	224
Figure 6.20:Air-water stratified flow density field using the interface tracking method.....	227
Figure 6.21:Air-water stratified flow velocity field using the interface tracking method.....	227
Figure 6.22:Velocity field for 2D single phase pipe flow simulation.....	227
Figure 6.23:Effect of drillpipe rotation on annular flow in the concentric annuli .....	228
Figure 6.24: Effect of drillpipe rotation on annular flow in the eccentric annuli .....	229
Figure 6.25: Effect of drillpipe rotation on slug flow in the eccentric annuli .....	229
Figure 6.26:Comparison of the numerical and theoretical pressure gradient data (Fluid type A).....	231
Figure 6.27:Comparison of the numerical and theoretical pressure gradient data (Fluid type B).....	232
Figure 7.1:Bubble flow pattern in horizontal concentric annulus (Fluid type 2).....	235
Figure 7.2:Stratified flow pattern in horizontal concentric annulus (Fluid type 2).....	235
Figure 7.3:Slug flow pattern in inclined eccentric annulus ( $E = 0.7$ , Fluid type 4).....	236
Figure 7.4:Effect of inner pipe rotation on the pressure drop in the horizontal concentric annulus (Water).....	238
Figure 7.5:Effect of inner pipe rotation on the pressure drop in the horizontal concentric annulus(Water and air, stratified flow pattern) .....	239

Figure 7.6:Effect of inner pipe rotation on the pressure drop in the 30° inclined concentric annulus (Water) .....	239
Figure 7.7:Effect of inner pipe rotation on the pressure drop in the 30° inclined concentric annulus (Polymer (0.1% XG) and air, slug flow pattern) .....	240
Figure 7.8:Model performance for annuli differential pressure (Water) ...	241
Figure 7.9:Model performance for annuli differential pressure (0.5% XG and air).....	241
Figure 7.10:Model performance for annuli differential pressure (0.1% XG and air).....	242
Figure 7.11:Liquid film length in the horizontal concentric annulus (air and water) .....	243
Figure 7.12:Liquid film length in the 30° inclined concentric annulus (air and water).....	244
Figure 7.13:Model performance for length of the liquid film in the annuli .....	244
Figure 7.14:Cutting transport mechanism in different fluid flow patterns and gas-liquid flowrates .....	246
Figure 7.15:Annuli differential pressure at different mixture velocities for two-phase air-liquid flows with and without particles .....	247
Figure 7.16:Effect of pipe eccentricity on the minimum transport velocity .....	248
Figure 7.17:Two-phase dispersed bubble flow pattern for the different fluid and particle mixtures at the same air-liquid flowrates. a) moving bed mechanism in air-water mixtures and (b) suspension mechanism in air-polymer mixtures .....	249
Figure 7.18:Minimum transport velocity versus the annuli inclination angle for different particle properties.....	251
Figure 7.19:Effect of the particle properties on particle transport mechanism. (a) Single-phase water with the red and blue particles, (b) two-phase water and air with the red particles (b) two-phase water and air with the blue particles .....	252
Figure 7.20:Comparison of the fluid distribution and mixture properties of slug flow in the horizontal and inclined annuli test sections.....	253
Figure 7.21:Comparison of particle transport in the horizontal and inclined annuli for (a) Moving bed with slug flow pattern in the horizontal annulus (Fluid type 2) and (b) Stationary bed for the slug flow pattern in 30° inclined annulus (Fluid type 2) .....	254
Figure 7.22: Change in cutting transport mechanism from suspension to a moving bed with increase in inclination angle from (a) 20° to (b) 30° .....	254
Figure 7.23:Effect of inclination angle on the MTV for rolling in the concentric annuli .....	255
Figure 7.24:Effect of inclination angle on the MTV for rolling in the eccentric annuli .....	256
Figure 7.25:Effect of single-phase fluid viscosity on stationary bed thickness.....	257

Figure 7.26:Effect of inner pipe rotation on bed thickness in horizontal concentric annuli .....	258
Figure 7.27:Effect of inner pipe rotation on bed thickness in 20° inclined concentric annuli .....	258
Figure 7.28: The effect of inner pipe rotation (150rpm) on a stationary bed formed in the 20° inclined concentric annulus (water and particles)	259
Figure 7.29:The effect of inner pipe rotation (150rpm) on a stationary bed formed in the inclined annulus (Fluid type 2 ) .....	260
Figure 7.30:Effect of inner pipe rotation on bed thickness in horizontal eccentric annuli .....	261
Figure 7.31:Effect of inner pipe rotation on bed thickness in inclined eccentric annuli .....	261
Figure 7.32:Real-time annuli differential pressure for (a) single-phase flow (water) and (b) two-phase slug flow (water and air) .....	262
Figure 7.33: Examples of different cutting transport mechanisms and fluid flow patterns .....	263
Figure 7.34: Particle transport dynamics with time in the slug flow pattern(Particle1: 3-4mm, 950Kg/m <sup>3</sup> ) .....	264
Figure 7.35:Stationary bed height model performance for the annuli flow of water and water and air .....	265
Figure 7.36:Stationary bed height model performance for the annuli flow of polymer(0.5% XG) and polymer and air .....	266
Figure 7.37:Model performance for the annuli differential pressure with the particles in the suspension mechanism (Particle1: 3-4mm, 950Kg/m <sup>3</sup> ) .....	266
Figure 7.38:Model performance for the annuli differential pressure with the particles in the suspension, moving bed and stationary bed mechanism(Particle3: 2.5-3.7mm, 2100Kg/m <sup>3</sup> ) .....	267
Figure 7.39:Model performance of the total pressure gradient with the particles in the suspension and moving bed mechanism(Particle3: 1.25-1.65mm, 2000Kg/m <sup>3</sup> ) .....	267

## LIST OF TABLES

Table 2.1: Chisholm 1967 correlation coefficients for the constant $C$ .....	39
Table 2.2: List of major two-phase flow models and their range of applicability.....	39
Table 2.3: Beggs and Brill flow pattern transition boundaries.....	41
Table 2.4: Beggs and Brill empirical coefficients for horizontal liquid holdup.....	42
Table 2.5: Beggs and Brill empirical coefficients for $\beta$ .....	43
Table 2.6: Closure relationships for mechanistic slug flow model for pipe flow ...	61
Table 2.7: Studies of the effect of the major drilling parameters on hole cleaning .....	83
Table 3.1: Rheological parameters for experimental test fluids.....	94
Table 3.2: Experimental test fluid types.....	94
Table 3.3: Types of the particles used in experimental study .....	95
Table 4.1: Constants for the generalised rheology model.....	120
Table 4.2: Input parameters for sample calculations .....	137

## NOMENCLATURES

$a_n$	=	Constant in the bipolar coordinate system
$A$	=	Cross-sectional area
$A_P$	=	Cross-sectional area of pipe
$C$	=	Cutting concentration
$C_D$	=	Co-efficient of drag
$C_L$	=	Co-efficient of lift
$C_p$	=	Input cuttings concentration
$\partial P/\partial L$	=	Pressure gradient
$d_p$	=	Cutting size
$d_2$	=	Inner diameter of casing or wellbore
$d_1$	=	Outer diameter of drillpipe
$d_x$	=	Distance between the drillpipe and the casing wall at the lowest side
$d_e$	=	Distance between the centroid of the outer pipe to that of the inner pipe
$D$	=	Pipe diameter
$D_h$	=	Annuli hydraulic diameter
$e$	=	Wellbore eccentricity
$F_B$	=	Buoyancy force
$F_D$	=	Drag force
$F_G$	=	Gravitational force
$F_L$	=	Lift force
$f_s$	=	Coefficient of friction
$f$	=	Friction factor
$F_\pi$	=	Friction geometry parameter
$F_t$	=	Frequency
$g, g_c$	=	Acceleration due to gravity
$g_r, g_\theta, g_z$	=	Acceleration due to gravity in the cylindrical coordinates system
$h$	=	Height
$h_b$	=	Stationary bed height
$h_{Lf}$	=	Liquid film height
$H$	=	Hold up
$K$	=	Consistency index of non-Newtonian fluid
$K_a$	=	Pipe diameter ratio
$L$	=	Length
$L_f$	=	Length of liquid film
$L_s$	=	Length of slug body
$L_u$	=	Length of slug unit
$n$	=	Flow behaviour index of non-Newtonian fluid
$N_{Fr}$	=	Froude number
$P$	=	Pressure
$Q$	=	Volumetric flowrate
$Re$	=	Reynolds number
$Re_{Gen}$	=	Generalised Reynolds number
$S$	=	Wetted perimeter
$V$	=	Average velocity
$V_m$	=	Gas-liquid mixture velocity
$V_{SG}$	=	Superficial gas velocity
$V_{SL}$	=	Superficial liquid velocity
$v_r, v_\theta, v_z$	=	Velocity in the cylindrical coordinates system
$V_T$	=	Translational velocity
$v_G$	=	Relative velocity of gas in the liquid-film/gas pocket region

$v_{Lf}$	=	Relative velocity of liquid in the liquid-film/gas pocket region
$W$	=	Mass flowrate
$z, r, \theta$	=	Cylindrical coordinates (axial, radial and angular)
$\rho$	=	Density
$\rho_c$	=	Cuttings density
$\rho_{ns}$	=	No-slip gas-liquid mixture density
$\tau$	=	Shear stress
$\tau_{df}$	=	Shear stress of the liquid film in contact with the drillpipe
$\tau_{gc}$	=	Shear stress on wall/casing in contact with gas
$\tau_{gp}$	=	Shear stress on drillpipe in contact with gas
$\tau_{Lc}$	=	Shear stress on wall/casing in contact with liquid
$\tau_{Lp}$	=	Shear stress on drillpipe in contact with liquid
$\tau_o$	=	Yield stress of Herschel-Bulkley fluids
$\tau_y$	=	Yield stress of Bingham plastic fluids
$\gamma$	=	Shear rate of fluids
$\mu$	=	Viscosity
$\mu_a$	=	Apparent viscosity
$\mu_{aB}$	=	Apparent viscosity of Bingham plastic fluids
$\mu_{aHB}$	=	Apparent viscosity of Herschel-Bulkley fluids
$\mu_{ap}$	=	Apparent viscosity of Power law fluids
$\mu_{Gen}$	=	Generalized fluid viscosity
$\mu_p$	=	Plastic viscosity of Bingham plastic fluids
$\lambda$	=	No-slip hold up
$\theta_p$	=	Angle of inclination between the horizontal and flow axis
$\epsilon$	=	Absolute roughness
$\beta$	=	Inclination angle between the vertical and flow axis
$\omega$	=	Angular velocity
<b>AM</b>	=	Analytical modelling
<b>EM</b>	=	Empirical modelling
<b>TLM</b>	=	Two-layer model
<b>THLM</b>	=	Three-layer model
<b>CFD</b>	=	Computational fluid dynamics
<b>DEM</b>	=	Discrete Element Method

### Subscripts

$a$	=	Annulus
$bed$	=	Stationary cuttings bed
$c$	=	Cutting
$dLf$	=	Liquid film in contact with the drillpipe
$dgf$	=	Gas in contact with the drillpipe (Liquid film region)
$1$	=	Layer 1
$2$	=	Layer 2
$3$	=	Layer 3
$f$	=	Fluid
$G$	=	Gas
$Gf$	=	Gas in the liquid-film/gas pocket region
$i$	=	Gas-liquid interface
$L$	=	Liquid
$Lf$	=	Liquid film/ Liquid film in contact with the wall/casing
$gf$	=	Gas in contact with the wall/casing (Liquid film region)
$Gs$	=	Gas in the slug body
$Ls$	=	Liquid in the slug body
$M$	=	Gas-liquid mixture

ns = No-slip  
p = Drillpipe wall  
pw = Pipe wall  
SG = Superficial gas  
SL = Superficial liquid  
w = Annuli wall  
wG = Pipe wall in contact with gas  
wL = Pipe wall in contact with liquid

## **Chapter 1**

### **Introduction**

#### **1.1 Background**

Drilling of complex wells in the oil and gas industry has been on the rise due to the increasing demand for crude oil. These complex wells such as horizontal wells, extended reach wells and multilateral wells are often drilled in order to maximise the hydrocarbon recovery from the reservoir and optimise productivity. In depleted or low-pressure reservoirs, if the hydrostatic pressure is higher than the formation pressure, wellbore instability issues emerge, leading to lost circulation, and formation damage. Multiphase (gas-liquid) drilling fluids or underbalanced drilling techniques are mostly used in these environments to control the wellbore pressures and improve the stability and productivity of the field by reducing formation damage (Baojiang, 2016). While operating in underbalanced drilling (UBD) conditions, the pressure in the wellbore is kept below the static pressure of the formation, allowing formation fluids to flow into wellbore and up to the surface. In some cases, an inert gas is pumped into the drilling fluid in order to reduce the equivalent density of the fluid and thereby reduce the hydrostatic pressure throughout the entire wellbore. Due to the complexity of multiphase flow, the prediction of the flow dynamics, wellbore hydraulics and the effective transport of the cuttings out of the wellbore is a lot more challenging when compared to conventional drilling operations. An improper hole cleaning job can lead to increased torque and drag, lost circulation, weight stacking, increased hydraulic requirements, stuck pipe and wellbore instability, all of which have a negative impact on the effectiveness or cost of the drilling project and may affect the productivity of the field (Hajipour, 2020).

Field and laboratory analysis over the years has shown that an effective cutting transport during drilling operation is dependent on a number of important parameters including the rheological properties of the drilling fluid, the drillpipe and wellbore/casing sizes, the wellbore inclination angle, the cutting sizes, rate of penetration (ROP), drillpipe rotary speeds, eccentricity and most importantly the fluid flowrates (Ford, et al., 1990). However, the influence of these drilling

parameters on the effectiveness of hole cleaning has not been adequately investigated for UBD conditions where a multiphase drilling fluid is flowing in the wellbore annuli. If the velocity of the drilling fluid in the wellbore annuli is not high enough to transport the cuttings, the cuttings would settle out of the flow and form a stationary bed at the low-side or bottom of the wellbore. The fluid velocity required to avoid the formation of this stationary bed is often referred to as the critical velocity or the minimum transport velocity. The magnitude of this velocity is dependent on the cutting transport mechanism, meaning that the cuttings would be transported as a moving bed if the fluid velocity is higher than the minimum transport velocity for the moving/sliding bed and in suspension if the fluid velocity is higher than the minimum transport velocity required to suspend the cuttings in the annuli. In general, for multiphase (gas-liquid-solid) flow in pipes or tiebacks, it has been reported that the fluid flow pattern has a major influence on solids transport and the ability of the fluid to transport the solids effectively is highly dependent on the prevailing flow pattern. Other than the influence of the flow pattern on solids transport, the flow pattern also has a direct impact on the pressure losses experienced by the two-phase flow through the pipe. It is fair to assume that if this phenomenon exists for multiphase flow in pipes it would also be an issue of concern in the for multiphase flow in the annuli. Due to the complexity and highly transient flow pattern of multiphase flow, at the present time, there is no rigorous method available for the prediction of the pressure gradient for multiphase flows through pipes or annuli. For this reason, the alternative has been to develop either empirical or mechanistic models that are flow pattern dependent for the determination of the pressure losses for two-phase flows. For underbalanced drilling operations, since the need for wellbore pressure management is critical, it is important that the methods employed for the prediction of the pressure profile through the length of the wellbore be dependent on the flow pattern existing in the entire wellbore. Two-layered or three-layered cutting transport models developed for the prediction of cutting transport efficiency and the pressure losses for the flow of single-phase drilling fluid in the wellbore annuli has been applied directly to that of the underbalanced drilling scenario by various researcher to develop a method for performing wellbore predictive calculations (Doan et al., 2000; Li and Kuru, 2005; Ozbayoglu and Miska, 2003). However, the direct application of these models for underbalanced drilling operations is questionable and may lead to highly inaccurate predictions,

the main reason being that the transient gas-liquid fluid flow pattern has been ignored. There are several cutting transport mechanisms that may exist either individually or simultaneously in the wellbore annuli and unlike the single-phase flow, is most likely to be highly influenced by the fluid flow pattern in the multiphase flow. Again, due to gas expansion with changes in pressure and temperature, the fluid properties change rapidly, thereby changing the speed of the phases, the in-situ hold up and hence the flow pattern. This phenomenon also has to be taken into account when performing predictive calculations as it has a huge influence on the wellbore pressure losses and cutting transport efficiency. It is important to understand the fundamental physics of the hydraulics of multiphase flow in the annuli and how to manipulate the key drilling parameters to optimise the wellbore pressure management and ensure an effective hole-cleaning process. In this research, a theoretical, numerical and experimental study is performed to investigate the effect of the major drilling parameters on wellbore hydraulics and cutting transport efficiency for both single-phase and two-phase Newtonian and non-Newtonian fluid flow.

## **1.2 Research objectives**

The aim of this study is to investigate the effect of the major drilling parameters on wellbore hydraulics and cutting transport efficiency and to develop reliable methods that can be used to perform the accurate design and predictive wellbore calculations required to optimise and maximise the benefits of underbalanced drilling operations. This research focused on the following objectives:

1. Conduct an intensive literature review of single-phase and two-phase Newtonian and non-Newtonian flow in both pipes and annuli, evaluating the current predictive methods of the flow dynamics and cuttings transport.
2. Design and construct an experimental rig and data acquisition system to imitate the wellbore drilling process using single-phase and two-phase drilling fluids.

3. Establish methods to determine the rheological parameters for non-Newtonian drilling fluids.
4. Experimentally investigate the flow dynamics and cutting transport phenomenon in single-phase and two-phase flow in the annuli for different flow patterns.
5. Develop new analytical and mechanistic equations for the determination of the friction factor for Newtonian and non-Newtonian fluid flow in an annulus with any level of eccentricity and with or without drillpipe rotation.
6. Develop using a computational fluid dynamics (CFD) approach a method to discretise fluid flow governing equations, create geometry and mesh a concentric and eccentric annulus to perform numerical simulations for the flow of Newtonian and non-Newtonian fluids in a wellbore with and without drillpipe rotation.
7. Develop new flow pattern dependent mechanistic models for the prediction of wellbore hydraulics for underbalanced drilling operations.
8. Develop new flow pattern dependent multi-layered cutting transport models for the evaluation of cuttings transport performance for underbalanced drilling operations
9. Validate and refine developed mathematical models using the data obtained from the numerical and experimental study.

### **1.3 Method and Approach**

A theoretical, numerical and experimental study was carried out to explore the effect of several input conditions on wellbore hydraulics and cuttings transport efficiency. Generally, the methodology was based on the exploration of fundamental studies previously performed for single-phase and two-phase flow in both pipes and annuli, identifying the gaps in regard to their direct application to a wellbore with underbalanced drilling conditions and developing new mathematical models from the fundamental physics of single-phase and two-phase Newtonian and non-Newtonian annuli flows. New mathematical flow pattern dependent models were developed to determine the pressure losses in the concentric and eccentric annuli with or without inner pipe rotation, by considering the fluid properties and momentum equations for each of the phases flowing in

the annuli. A novel idea is applied to develop new flow pattern dependent multi-layered cutting transport models from the consideration of the different cutting transport mechanisms that exists in the wellbore annuli. The numerical computational fluid dynamics (CFD) simulations were generated using a finite volume technique to mesh the annuli and discretise the governing equation for fluid flow to obtain optimum data required to test and validate the theories and mathematical modelling performed in the theoretical study. Furthermore, an experimental rig equipped with data acquisition tools is designed and constructed to emulate the conventional and underbalanced wellbore drilling process, perform flow pattern characterisation and investigate how the key drilling parameters influence the wellbore hydraulics and cuttings transport dynamics. Experimental data was obtained and compared with the results generated from the theoretical study in other to validate the new mathematical models.

## Chapter 2

### Literature review

#### 2.1 Non-Newtonian fluid flow in annuli

In oil well drilling, the drilling fluid, which generally has a non-Newtonian rheological behavior, flows into the wellbore through the drillpipe and out through the annular space between the drillpipe and the wellbore or casing to the surface. The main functions of the drilling fluid are to control or maintain wellbore pressure, lubricate the drilling bit and transport the drilled cuttings out of the wellbore. Unlike the Newtonian fluids, the drilling fluid is shear rate dependent and deforms under the action of a shear stress in a manner that is dependent on the rheological characteristics of the fluid. Although various rheological models have been proposed to describe the rheological behavior of non-Newtonian fluids, the most popular and widely accepted models are the power law, Bingham plastic and the Yield power law generally known as the Herschel-Bulkley model (Kelessidis, et al., 2006). The figure 2.1 shows the shear stress to strain relationship for models that describes the rheological behavior of the different fluid types. The flow curve of the Newtonian fluid shows a straight line through the origin of the coordinates which means that the shear stress is directly proportional to the shear rate. The slope of the curve is referred to as the viscosity of the fluid and for a Newtonian fluid, remains constant under the application of a shear stress at a given temperature and pressure. The power law model describes fluids which are shear dependent and are functions of the flow behaviour index and the consistency index of the fluid. The flow curves of this type of fluids pass through the origin but they are not linear. Thus, there exist a term referred to as the apparent viscosity which is not constant and highly dependent on the magnitude of the applied shear stress. The Bingham plastic and the Herschel-Bulkley fluids are non-Newtonian fluids that possess a yield stress. For these types of fluids, a finite shear stress is required to be overcome before flow commences and thus the flow curve does not pass through the origin but intercepts the shear stress coordinate at the yield stress point. After the yield stress has been overcome, the Bingham plastic fluids exhibit a trend that is similar to the Newtonian fluids while the Herschel-Bulkley fluids follows a non-linear trend that is similar to that of the power law fluids.

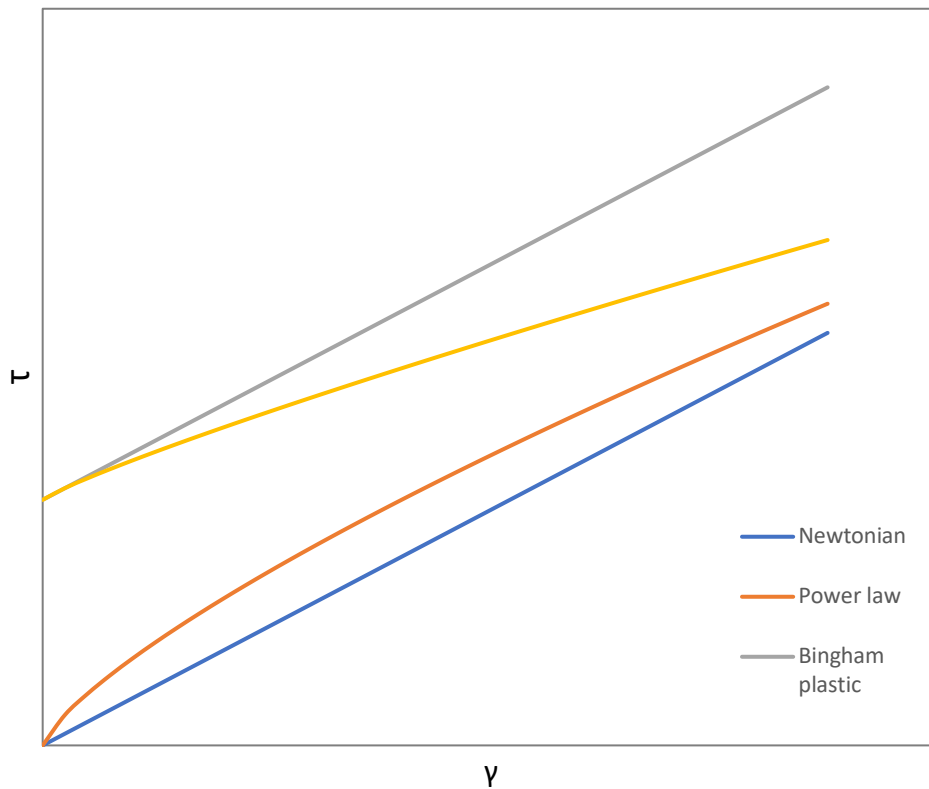


Figure 2.1: Shear stress to shear strain relationship for non-Newtonian fluids

The fundamental models that are used to describe the rheological behavior of bentonite mixtures particularly for drilling applications are the power law, Bingham plastic or the Herschel-Bulkley model. The shear stress to strain relationship and the apparent viscosity of the drilling fluids can be expressed as a function of the flow behaviour index,  $n$  and the consistency index,  $K$  of the fluid.

Power law model:

$$\tau = K \gamma^n \quad 2.1$$

$$\mu_{ap} = K \gamma^{n-1} \quad 2.2$$

Bingham plastic model:

$$\tau = \tau_y + \mu_p \gamma \quad 2.3$$

$$\mu_{aB} = \frac{\tau_y}{\gamma} + \mu_p \quad 2.4$$

Herschel-Bulkley model:

$$\tau = \tau_o + K \gamma^n \quad 2.5$$

$$\mu_{aHB} = \frac{\tau_o}{\gamma} + K \gamma^{n-1} \quad 2.6$$

During drilling operations, the drilling fluid flows through the annulus under the action of an axial pressure gradient and in order to control wellbore pressures, it is important to perform drilling hydraulic calculations that are dependent on the rheological characteristics of the drilling fluid that is being used. The drilling fluids being shear dependent are highly influenced by the flowrate and most importantly the geometry of the wellbore. In some cases, the drillpipe is rotated with the idea of improving the drilling process and improving the cutting transport efficiency (Xiaofeng, et al., 2014). The drillpipe rotation subjects the drilling fluid to an axial and tangential force that makes the fluid flow in a helical pattern due to the presence of an axial and tangential velocity component. The tangential velocities are highest at the drillpipe wall and zero at the borehole or casing wall, while the axial velocities are zero at the drillpipe wall and at the borehole or casing wall due to the no-slip effect that occurs at the boundaries. Unlike the Newtonian fluid flow, the axial and tangential velocity components are coupled and thus, needs to be solved simultaneously, adding more complexity to the solution procedure. The drillpipe may be positioned eccentrically in the wellbore, especially in a deviated wellbore where the drillpipe has a strong tendency to be offset towards the low side of the wellbore due of gravitational effects (Luo & Penden, 1987). This creates an uneven distribution of the velocity fields where a higher velocity exists in the larger space in contrast to a lower velocity in the smaller area of the wellbore annuli (Figure 2.2).

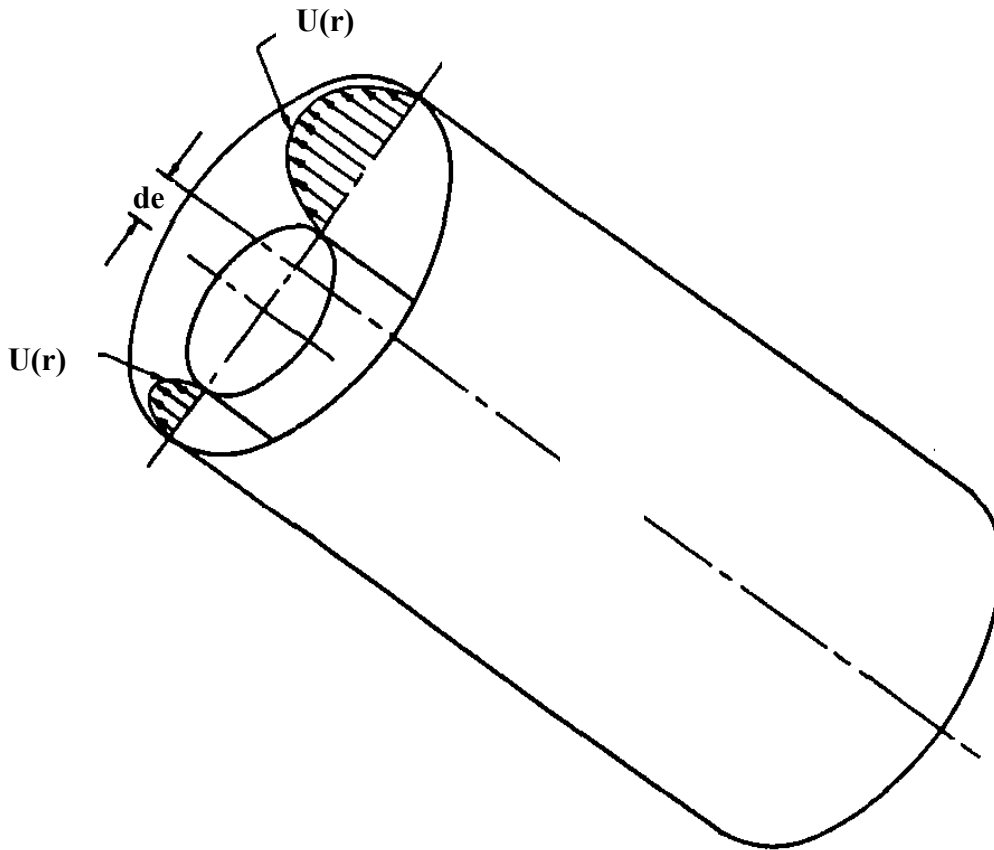


Figure 2.2: Wellbore velocity profiles in eccentric annuli

The pump rate, eccentricity, drillpipe rotary speed and the drilling fluid rheological properties has been the major parameters used to perform or model hydraulic calculations even though some of the reports of various researchers has been conflicting. For example, while the earlier researchers that investigated the effect of drillpipe rotation on wellbore hydraulics reported that the annuli pressure gradient decreases with an increase with drillpipe rotation due to the shear-thinning effect of the drilling fluid, later studies and field measurements have reported the reverse effect (Terry, 2015). Some other investigators have either reported an increase or a decrease in pressure gradient depending on the annuli geometry and the fluid rheology. (Luo & Penden, 1990) showed that the annular frictional pressure gradient reduces with an increase in drillpipe rotation due to the shear-thinning behavior of drilling fluids. They showed from theoretical analysis that the effect of drillpipe rotation on annular pressure losses depends on three dimensionless variables, which are the dimensionless drillpipe rotary speed, the flow behaviour index and the ratio of the annular diameters.

(Ooms, et al., 1999) carried out a numerical, analytical and experimental study to investigate the influence of drillpipe rotation on drilling hydraulics and concluded that for laminar flow through an eccentric annulus, the inertia effect induced by the pipe rotation increases the axial pressure drop. They inferred that the magnitude of this increase was dependent on the annular gap width, the eccentricity and the Taylor number of the flow. (Ahmed & Miska, 2008) carried out an experimental investigation of different power law and yield power law polymer-based fluid flow with inner pipe rotation in several annular geometries. They reported that inner pipe rotation creates an inertia effect and induces a shear thinning effect on the fluids and in a slightly eccentric annulus, shear-thinning effect dominates the inertial effect, whereas for the highly eccentric annulus, the inertial effect dominates. Their results indicated that the inner pipe rotation increases the frictional pressure loss and the magnitude of increase was dependent on the fluid flow regime. Under laminar flow conditions, the effect of the rotary speed on the friction factor and consequently the pressure loss is relatively large in comparison to higher Reynolds number flows, where the effect of the inner pipe rotary speed on the pressure loss is minimal. (Ozbayoglu & Sorgun, 2010) also reported from an experimental study that increase in pipe rotatory speed increases the friction factor for low Reynolds number flows and has a little or no effect for flows with high Reynolds number. They concluded that an increase in pipe rotation leads to a corresponding increase in drillpipe rotation and failure to consider rotation effects may lead to underestimating the pressure gradient.

(Podryabinkin, et al., 2013) carried out numerical studies in an attempt to investigate the hydrodynamic behavior of drilling fluid flow in an eccentric annulus. A finite volume method was used to obtain numerical solutions for the flow of Newtonian and non-Newtonian Herschel-Bulkley rheological fluids with the combined effect of inner pipe rotation and eccentricity. They pointed out the importance of the consideration of eccentricity and drillpipe rotation when performing drilling hydraulics modeling and concluded that eccentricity usually decreases the pressure drop as much as 50%. They showed that drillpipe rotation significantly alters the velocity distribution of the flow and when the axial flow dominates, rotation in the eccentric annulus increases the pressure drop when compared to the normal axial flow. Furthermore, it was suggested that performing systematic flow modelling and study can enable recommendations to modify

drilling parameters in order to optimize fluid flow for maximum rates of penetration and prevent wellbore instability issues.

(Viera, et al., 2014) presented results obtained from an experimental and numerical CFD simulation of the pressure drop of non-Newtonian fluid flow through a concentric and eccentric annulus ( $e=0.75$ ). The experiments involved the use of aqueous solutions of Xanthan gum, XG and Carboxymethylcellulose, CMC with a rheology best fitted to the power law model to simulate the drilling fluids and considered an inner cylinder rotation in the range of 0 - 300rpm. Their experimental and numerical simulation results showed that for a concentric annulus, the pressure drop was slightly reduced with an increase in pipe rotation speed. The reverse effect of inner pipe rotation was reported to take place in the eccentric annulus where an increase in pressure drop occurred with inner pipe rotation of up to 200rpm. They also presented CFD simulation results for the velocity profiles at different sections of the annuli that showed that inner cylinder rotation had little or no effect on the axial velocity fields for the concentric annulus but altered the distribution of the axial velocity fields for the eccentric annulus. (Bicalho, et al., 2016) experimentally and numerically studied the laminar and isothermal helical flow of non-Newtonian fluids through horizontal annular sections with partial obstruction and analysed the effect of the orbital motion of the inner pipe for fluid flow through the eccentric annulus. Xanthan gum, XG of different concentrations by mass (0.1, 0.3 and 0.5%) that were best fitted to the Herschel-Bulkley model were used in order to simulate the behavior of non-Newtonian drilling fluids. From the analyses of the results obtained, they reported that the effect of inner cylinder rotation on pressure drop was not well defined in their experiments using the 0.1 and 0.3% concentrations of XG. However, experiments using the 0.5% concentrations of XG resulted in a decrease in pressure drop with inner pipe rotation. It was pointed out that in the case of the obstructed eccentric annulus, preferential zones are found in the larger sector of the annulus and favours the accumulation of particles in the smaller sector of the annulus when there is no inner pipe rotation. They concluded that the inner pipe rotation results in a uniform distribution of the velocity axial velocity fields and improves the flow in the smaller sector of the annulus, thereby improving cuttings transport during drilling.

The published results of the effect of inner pipe rotation on the pressure gradient of single-phase non-Newtonian fluid flow through annuli has been conflicting. While some researchers have shown that the increase in inner pipe rotation increased the pressure gradient, others have shown analytically and experimentally that the increase in pipe rotation decreased the annuli pressure gradient. The effect of inner pipe rotation on the annuli velocity distribution has also been of concern especially during drilling operations as this effect might help to improve the cutting transport efficiency and the drilling process.

An accurate prediction of the velocity distribution in the annuli is required for a successful design of mud displacement in cementing operations and cutting transport modelling especially in highly deviated wellbores. To obtain the annuli velocity fields, analytical solutions of the equation of motion for the steady state axial flow of an incompressible non-Newtonian fluid flow between two coaxial cylinders has been developed and presented by several investigators. The governing equations that can be used to describe the isothermal flow of fluids through a concentric or eccentric annulus is the equations of continuity and the equations of motion.

The equation of continuity can be expressed in cylindrical coordinates as (Bird, et al., 2002)

$$\frac{1}{r} \frac{\partial(rv_r)}{\partial r} + \frac{1}{r} \frac{\partial(v_\theta)}{\partial \theta} + \frac{\partial(v_z)}{\partial z} = 0 \quad 2.7$$

and the equations of motion may be expressed as:

$$\begin{aligned} r: \rho \left( \frac{\partial v_r}{\partial t} + v_r \frac{\partial v_r}{\partial r} + \frac{v_\theta}{r} \frac{\partial v_r}{\partial \theta} - \frac{v_\theta^2}{r} + v_z \frac{\partial v_r}{\partial z} \right) \\ = \rho g_r - \frac{\partial P}{\partial r} - \left[ \frac{1}{r} \frac{\partial}{\partial r} (r\tau_{rr}) + \frac{1}{r} \frac{\partial(\tau_{r\theta})}{\partial \theta} + \frac{\partial(\tau_{rz})}{\partial z} - \frac{\tau_{\theta\theta}}{r} \right] \end{aligned} \quad 2.8$$

$$\begin{aligned}
\theta: \rho \left( \frac{\partial v_\theta}{\partial t} + v_r \frac{\partial v_\theta}{\partial r} + \frac{v_\theta}{r} \frac{\partial v_\theta}{\partial \theta} + \frac{v_r v_\theta}{r} + v_z \frac{\partial v_\theta}{\partial z} \right) \\
= \rho g_\theta - \frac{1}{r} \frac{\partial P}{\partial \theta} - \left[ \frac{1}{r^2} \frac{\partial}{\partial r} (r^2 \tau_{\theta r}) + \frac{1}{r} \frac{\partial (\tau_{\theta\theta})}{\partial \theta} + \frac{\partial (\tau_{\theta z})}{\partial z} \right]
\end{aligned}
\tag{2.9}$$

$$\begin{aligned}
z: \rho \left( \frac{\partial v_z}{\partial t} + v_r \frac{\partial v_z}{\partial r} + \frac{v_\theta}{r} \frac{\partial v_z}{\partial \theta} + v_z \frac{\partial v_z}{\partial z} \right) \\
= \rho g_z - \frac{\partial P}{\partial z} - \left[ \frac{1}{r} \frac{\partial}{\partial r} (r \tau_{zr}) + \frac{1}{r} \frac{\partial (\tau_{z\theta})}{\partial \theta} + \frac{\partial (\tau_{zz})}{\partial z} \right]
\end{aligned}
\tag{2.10}$$

(Fredrickson & Bird, 1958) simplified the governing equations of fluid motion (Equations 2.8-2.10) in order to analyze the flow of non-Newtonian Bingham plastic and Power law fluid flow in a concentric annulus. They published plots that showed the relationship between the flowrate and frictional pressure gradient for laminar non-Newtonian fluid flow through a concentric annulus. However, as the outcome of this study could not be applied when the annuli is eccentric, later studies were carried out to develop a relationship between the flowrate and pressure gradient for fluid flow through an eccentric annulus. The equation of fluid motion for an isothermal steady-state incompressible laminar flow of a specific system can be simplified and expressed in cylindrical coordinates as:

$$\frac{1}{r} \frac{d}{dr} (r \tau_{zr}) = \frac{dP}{dL} + \rho g_z
\tag{2.11}$$

This first-order differential equation is valid for any kind of fluid flow through an annulus and may be integrated to yield the axial shear stress across the entire region of the flow

$$\tau_{zr} = \frac{P}{2} \left( r - \frac{(\lambda R)^2}{r} \right)$$

2.12

P designates the sum of forces per unit volume of the fluid flow and  $\lambda$  is the constant of integration. The radial distance  $\lambda R = 0$  represents the radial position at which the magnitude of the local shear stress value is zero  $\tau_{zr} = 0$  for fluids without a yield stress and is the point at which maximum axial velocity exists. This equation was taken as the starting point for the derivations of the velocity profiles and the pressure gradient to volumetric flowrate relationship for the non-Newtonian fluids.

They showed that the shear stress distribution and velocity profiles for axial flow of non-Newtonian fluids through annuli are a function of the rheological characteristics of the fluid (Figure 2.3). Thus, it is strictly important that the annuli flow behavior and pressure gradient for non-Newtonian fluids is modeled in line with the rheological characteristics of the fluid.

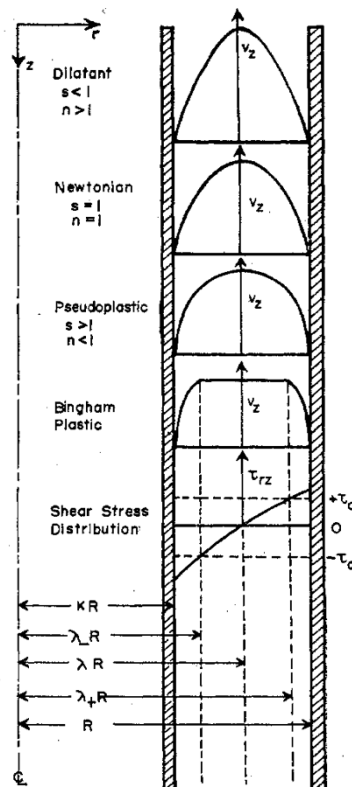


Figure 2.3: Axial velocity and shear stress distribution for annuli flows (Fredrickson & Bird, 1958)

(Uner, et al., 1988) presented an approximate solution to predict the relationship between the flowrate and the pressure gradient for a steady-state laminar flow of non-Newtonian fluids through an eccentric annulus. The solutions to the equations of motion for non-Newtonian fluid flow in annuli geometries are usually difficult to obtain due to the nonlinear nature of the shear stress-shear rate relationship. Eccentricity, however, adds more complexity to the problem because unlike the concentric annuli, the fluid forces acting in the flow vary across the angular direction of the eccentric annuli creating an additional difficulty to obtain analytical solutions. This makes the derivations of the analytical solutions for the equations of motion for non-Newtonian fluids unattainable at this present time.

In this study, the exact model for the slot height and the solutions of the velocity profiles for Power law fluids derived by (Iyoho & Azar, 1981) was extended to approximate the volumetric flowrate for eccentric annuli flows. The eccentric annulus was modelled as a slit of variable height (Figure 2.4) to develop an analytical relationship between the flowrate and pressure drop for the Power law, Bingham plastic models, by simplifying the equations of continuity and motion.

The slit height,  $h$  is expressed as a function of the angle,  $0 < \theta < 2\pi$  as:

$$h = r_o[(1 - k^2 \sin^2 \theta)^{1/2} + k \cos \theta - r^*] \quad 2.13$$

where

$$k = \epsilon(1 - r^*) \quad 2.14$$

The eccentric annulus is characterized by two parameters, namely, an eccentric ratio,  $\epsilon$  and a radius ratio,  $r^*$  defined by

$$\epsilon = \frac{d_e}{r_o - r_i} \quad 2.15$$

and

$$r^* = r_i/r_o \quad 2.16$$

where,  $r_i$  and  $r_o$  are the radii of the inner and outer pipe respectively

The velocity profiles and pressure drop to flowrate relationships were developed, taking into consideration the fundamental rheological behavior of the non-Newtonian Power law and Bingham plastic models and applying the no-slip boundary conditions that exist at the walls of the geometry. The equation for the axial velocity profile and pressure drop to flowrate relationship for the Power law fluids in an eccentric annulus were presented as:

$$v_z = \frac{1}{s+1} \left( \frac{P_0 - P_L}{KL} \right)^s \left( \frac{h}{2} \right)^{s+1} \left[ 1 - \left( \frac{2y}{h} \right)^{s+1} \right] \quad 2.17$$

where  $s = 1/n$

and

$$\bar{Q} = \frac{\pi}{s+1} \left( \frac{1}{2} \right)^{s+1} \left( \frac{1 - r^{*2}}{2E - \pi r^*} \right)^s \int_0^\pi [(1 - k^2 \sin^2 \theta)^{1/2} + k \cos \theta - r^*]^{s+2} d\theta \quad 2.18$$

where

$$\bar{Q} = \frac{Q}{r_o^{s+3} \left( \frac{P_0 - P_L}{KL} \right)^s} \quad 2.19$$

and

$$E = \int_0^{\pi/2} (1 - k^2 \sin^2 \theta)^{1/2} d\theta \quad 2.20$$

The term  $P_0 - P_L$  represents the modified axial pressure drop between  $z = 0$  and  $z = L$ .

The velocity profile equations and the pressure drop to flowrate relationship for the Bingham plastic fluid flow in an eccentric annulus were presented as follows

$$v_z = \frac{P_0 - P_L}{2\mu_p L} \left(\frac{h}{2}\right)^s \left[1 - \left(\frac{2y}{h}\right)^2\right] - \frac{\tau_y}{\mu_p} \left(\frac{h}{2}\right) \left[1 - \left(\frac{2y}{h}\right)\right] \quad y_0 \leq y \leq h/2 \quad 2.21$$

$$v_z = \frac{P_0 - P_L}{2\mu_p L} \left(\frac{h}{2}\right)^s \left[1 - \left(\frac{2y_0}{h}\right)^2\right] - \frac{\tau_y}{\mu_p} \left(\frac{h}{2}\right) \left[1 - \left(\frac{2y_0}{h}\right)\right] \quad 0 \leq y \leq y_0 \quad 2.22$$

$$\bar{Q} = \frac{\pi}{12} \left(\frac{1 - r^{*2}}{2E - \pi r^*}\right) \left[H + 4\pi \left(\frac{y_0}{r_0}\right)^3 - 3G \left(\frac{y_0}{r_0}\right)\right] \quad 2.23$$

$$\bar{Q} = \frac{Q}{r_0^4 \left(\frac{P_0 - P_L}{\mu_p L}\right)} \quad 2.24$$

$$G = \pi(1 + r^{*2}) - 4Er^* \quad 2.25$$

$$H = 2E \left(\frac{k^2 + 7}{3} + 3r^{*2}\right) - \frac{8}{3}M(1 - k^2) - \pi r^*(3 + r^{*2}) \quad 2.26$$

$$M = \int_0^{\pi/2} d\theta / (1 - k^2 \sin^2 \theta)^{1/2} \quad 2.27$$

These models were compared to previously published theoretical and experimental data and was reported to show a significant agreement. They pointed out that the application of these models for geometries with small radius ratios,  $r^*$  produces inaccurate results. However, satisfactory results can be obtained for geometries with radius ratios,  $r^* \geq 0.5$ .

There have been issues regarding the accuracy of the slot models in terms of the obtaining reliable solutions for the velocity and shear stress profiles (Luo & Penden, 1990). The reason for this is that the slot models are derived on the basis

of modifying the models for flow between parallel plates the only difference being that the distance between the plates varies across the domain. As a result, the shear stress profiles obtained from the slot models are linear and the velocity profiles are symmetric about the center line of the annulus. Unlike the case of pipe flow the shear stress profile for annuli flows are not linear and the velocity profiles are not symmetric about the center line of the annulus. This makes the application of the slot models for velocity profile predictions invalid as unrealistic solutions can be obtained.

(Haciislamoglu & Langlinais, 1990) presented numerical studies investigating the flow of non-Newtonian fluids through eccentric annuli. The equations of motion were discretized using a finite difference technique and solved on grids transformed to the bipolar coordinate system. The velocity profiles in the eccentric annuli were analyzed from data obtained from the numerical procedures. The numerical results showed that the velocity in the narrow part of the annulus was reduced due to the increased resistance of flow created by the reduction in the gap between the inner and outer pipes while the velocity in the larger region of the annuli was increased. This effect was seen to be increasingly emphatic as the eccentricity was increased showing a high velocity in the larger region of the annuli while a no flow or stagnant region was created in the narrow region of the annuli. The effect of eccentricity on the frictional pressure losses in the annuli were also analyzed and it was shown that for a constant flowrate, the frictional pressure gradient decreases with an increase in eccentricity. With fluids that are more shear thinning (decreasing  $n$ ), their velocity profiles in the large and narrow parts of the annuli become flatter; thus, increasing the overall viscosity of the flow. Consequently, these fluids are subject to less reduction in frictional pressure losses in eccentric annulus. A non-linear regression analysis was performed on the generated numerical data to develop an empirical correlation that serves as a correction factor for the prediction of pressure gradient in an eccentric annulus. The correction factor  $R$ , developed as a function of the pipe diameter ratios, the eccentricity  $e$ , and the flow behaviour index  $n$ , is given as

$$R = 1 - 0.072 \frac{e}{n} \left( \frac{d_i}{d_o} \right)^{0.8454} - 1.5 e^2 \sqrt{n} \left( \frac{d_i}{d_o} \right)^{0.1852} + 0.96 e^3 \sqrt{n} \left( \frac{d_i}{d_o} \right)^{0.2527} \quad 2.28$$

where  $d_i$  and  $d_o$  are the diameters of the inner and outer pipe respectively

The pressure gradient in the eccentric annuli  $(dP/dL)_e$  can thus be calculated from the knowledge of the pressure gradient in the concentric annuli  $(dP/dL)_c$  using the following relationship:

$$\left( \frac{dP}{dL} \right)_e = R \left( \frac{dP}{dL} \right)_c \quad 2.29$$

However, the correlation was reported to be accurate within  $\pm 5\%$  and valid for eccentricities from 0 to 0.95, pipe diameter ratios of 0.3 to 0.9 and flow behavior indexes of within 0.4 to 1.0.

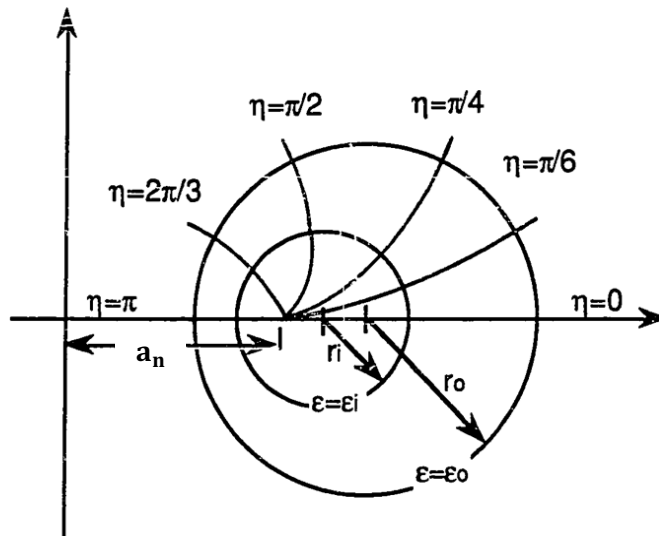


Figure 2.4: Eccentric annulus defined by bipolar coordinates (Haciislamoglu & Langlinais, 1990)

The numerical data was obtained using a method where the eccentric annular geometry was defined in a bipolar coordinate system, which consists of two orthogonal families of circles. The walls of the eccentric annulus are represented

by two constant values of  $\varepsilon$  while  $\eta$ , varied from 0 to  $2\pi$ , across the angular direction of the eccentric annulus (Figure 2.4). The relationship between the cartesian coordinates,  $x$  and  $y$ , and the bipolar coordinates,  $\varepsilon$  and  $\eta$ , can be obtained as follows:

$$x = \frac{a_n \sinh(\varepsilon)}{\cosh(\varepsilon) - \cos(\eta)} \quad 2.30$$

$$y = \frac{a_n \sin(\eta)}{\cosh(\varepsilon) - \cos(\eta)} \quad 2.31$$

where  $a_n = r_i \sinh(\varepsilon_i) = r_o \sinh(\varepsilon_o)$  and  $0 \leq \eta \leq 2\pi$

The circle  $\varepsilon = \varepsilon_i$  represents the inner tube and the circle  $\varepsilon = \varepsilon_o$  represents the outer tube. Thus, any point within the eccentric annulus can be described by  $\varepsilon$  from  $\varepsilon_i$  to  $\varepsilon_o$  and by  $\eta$  from 0 to  $2\pi$ . Based on these geometric considerations and the coordinate transformation, the following relationships to compute  $\varepsilon_i$  and  $\varepsilon_o$  may be expressed respectively as:

$$\varepsilon_i = \cosh^{-1} \left[ \frac{(1 + (r_i/r_o)) - e^2(1 + (r_i/r_o))}{a_n e (r_i/r_o)} \right] \quad 2.32$$

$$\varepsilon_o = \cosh^{-1} \left[ \frac{(1 + (r_i/r_o)) - e^2(1 + (r_i/r_o))}{a_n e} \right] \quad 2.33$$

where,  $e$  is the dimensionless eccentricity.

The unidirectional equation of motion expressed in the cartesian coordinate system (Equation 2.34) may be transformed to the bipolar coordinate system and expressed as (Equation 2.35) after a tedious process.

$$\frac{dP}{dL} + \frac{\partial}{\partial x} \left( \mu \frac{\partial v}{\partial x} \right) + \frac{\partial}{\partial y} \left( \mu \frac{\partial v}{\partial y} \right) = 0 \quad 2.34$$

$$\left( \frac{a}{\psi} \right)^2 \frac{dP}{dL} + \frac{\partial}{\partial \varepsilon} \left( \mu \frac{\partial v}{\partial \varepsilon} \right) + \frac{\partial}{\partial \eta} \left( \mu \frac{\partial v}{\partial \eta} \right) = 0 \quad 2.35$$

where  $\psi = \cosh(\varepsilon) - \cos(\eta)$   $\varepsilon_i \leq \varepsilon \leq \varepsilon_o$ ,  $0 \leq \eta \leq 2\pi$

The Herschel-Bulkley model (Equation 2.5) was used in this study to characterize the rheological property of the fluids as it combines both the Power law and Bingham plastic models. It reduces to the Power law model when yield stress is zero and the Bingham plastic model when flow behaviour index,  $n = 1$ . The viscosity of the fluid is transformed to the bipolar coordinate system with a similar technique to yield:

$$\mu = \frac{\tau_o}{\left| \frac{a_n}{\psi} \sqrt{\left( \frac{\partial v}{\partial \varepsilon} \right)^2 + \left( \frac{\partial v}{\partial \eta} \right)^2} \right|} + K \left| \frac{a_n}{\psi} \sqrt{\left( \frac{\partial v}{\partial \varepsilon} \right)^2 + \left( \frac{\partial v}{\partial \eta} \right)^2} \right|^{n-1} \quad 2.36$$

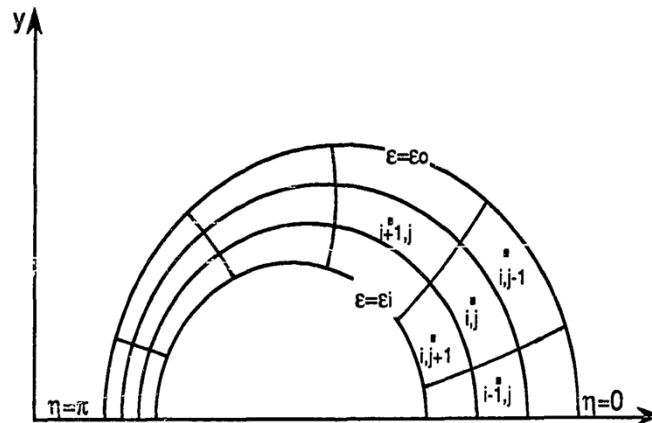


Figure 2.5: Eccentric annulus grid in bipolar coordinates (Haciislamoglu & Langlinais, 1990)

This equation for viscosity is substituted into the equation of motion expressed in bipolar coordinates (Equation 2.35) and solved with the application of a numerical and computational approach. The equation of fluid motion is discretized based on a finite difference technique where the eccentric annular geometry is subdivided into a network of grids. Since the axis that goes through the central points of the inner and outer pipes is the line-of-symmetry which divides the velocity fields into two identical parts, the governing equations are only solved in one half of the eccentric annulus to reduce computational cost. The Figure 2.5 shows the grid network in bipolar coordinates. They concluded that the previous studies performed for eccentric annuli flows have been shown to employ an inadequate approach to the solution of the equation of motion and this proposed bipolar coordinate method developed is a rigorous numerical solution of the equation of motion for non-Newtonian annuli flow that can be used to predict the velocity profiles, viscosity profiles, and frictional pressure gradients in the eccentric annuli. (Luo & Penden, 1990) analyzed the non-Newtonian laminar flow of fluids through an eccentric annulus in order to develop an analytical and rigorous solution for the prediction of the velocity profiles and pressure gradient to volumetric flowrate relationship. They claimed that the use of the slot approximation method was inaccurate, and the procedures involved with the bipolar coordinate method were extremely tedious and involved a lot of time-consuming computations. They proposed a method that was based on the representation of the annulus by an infinite number of concentric annuli with variable outer radii, with the idea of developing mathematical equations that were functions of the radius and angular positions in the eccentric annulus. Although the proposed models were developed for laminar flows of non-Newtonian fluids through the eccentric annuli, the application of the models for calculations involving the flow of non-Newtonian fluids through the concentric annuli is pretty much straight forward and follows the same computational procedures.

(Fredrickson & Bird, 1958) simplified the equations of motion for a steady-state isothermal flow of incompressible fluids (Equations 2.8-2.10) and integrated the product of the simplification to obtain an equation that represents the axial shear stress profile as a function of the radii and modified pressure gradient as

$$\frac{G_P}{2} r^2 - r\tau_{zr} = B \quad 2.37$$

The term B is the constant of integration and  $G_P$  represents the modified pressure gradient defined by:

$$G_P = \rho g_z - \frac{\partial P}{\partial z} \quad 2.38$$

Applying the appropriate boundary conditions to the Equation 2.37 yields the following expressions of the shear stress profiles for the Power law and Bingham plastic fluids respectively

$$\begin{aligned} \tau_{zr} &= 0 \text{ at } r = r_{me} \\ \tau_{zr} &= \frac{G_P}{2} r \left( 1 - \frac{r_{me}^2}{r} \right) \end{aligned} \quad 2.39$$

$$\begin{aligned} \tau_{zr} &= -\tau_y \text{ at } r = r_{ne} \\ \tau_{zr} &= -\frac{G_P}{2} \left( \frac{r_{ne}^2}{r} - r \right) - \left( \frac{r_{ne}}{r} \right) \tau_y, \quad r_1 \leq r \leq r_{ne} \\ \tau_{zr} &= \tau_y \text{ at } r = r_{pe} \end{aligned} \quad 2.40$$

$$\tau_{zr} = \frac{G_P}{2} \left( r - \frac{r_{pe}^2}{r} \right) + \left( \frac{r_{pe}}{r} \right) \tau_y, \quad r_{pe} \leq r \leq r_2$$

Combining the shear stress Equations (2.39-2.40) with the appropriate rheological models Equations (2.1-2.4) and integrating the results yields the following expressions for the velocity profiles for the Power law and Bingham plastic fluids.

Power law:

$$v^e = \left( \frac{G_P}{2K} \right)^s \int_{r_1}^r \left( \frac{r_{me}^2}{r} - r \right)^s dr, \quad r_1 \leq r \leq r_{me} \quad 2.41$$

$$v^e = \left(\frac{G_p}{2K}\right)^s \int_r^{r_{2e}} \left(r - \frac{r_{me}^2}{r}\right)^s dr, \quad r_{me} \leq r \leq r_{2e} \quad 2.42$$

where  $s = 1/n$

Bingham plastic:

$$v = \frac{G_p}{2\mu_p} \left( r_{ne}^2 \ln \frac{r}{r_1} - \frac{r^2 - r_1^2}{2} \right) + \frac{\sigma}{\mu_p} \left[ r_{ne} \ln \frac{r}{r_1} - (r - r_1) \right], \quad r_1 \leq r \leq r_{ne} \quad 2.43$$

$$v = \frac{G_p}{2\mu_p} \left( \frac{r_{2e}^2 - r^2}{2} - r_{pe}^2 \ln \frac{r_{2e}}{r} \right) + \frac{\sigma}{\mu_p} \left[ r_{pe} \ln \frac{r_{2e}}{r} - (r_{2e} - r) \right], \quad r_{pe} \leq r \leq r_{2e} \quad 2.44$$

The parameter  $r_{2e}$  represents the distance between the inner pipe and the outer pipe and is not constant across the angular direction of the eccentric annuli. However, if the annulus is concentric the value of  $r_{2e}$  becomes constant and is equal to the radius of the outer pipe. The value  $r_{2e}$  can be calculated from the Equation 2.45 where  $\theta$  represents the angular position in the annulus and  $e$  is the fractional eccentricity.

$$r_{2e} = (r_2 - r_1)e \cos \theta + \sqrt{r_2^2 - [(r_2 - r_1)e \sin \theta]^2} \quad 2.45$$

The radial position of the maximum velocity for the power law fluid,  $r_{me}$  may be obtained from the Equation 2.46 for cases where  $n > 0.5$  and  $r_1/r_{2e} > 0.3$  while the boundaries of the unsheared plug  $r_{pe}$  and  $r_{ne}$  can be obtained from the Equations (2.47-2.48) for cases where  $r_1/r_{2e} > 0.3$  and  $B_p/(r_{2e} - r_1) \leq 0.5$ .

$$r_{me} = \sqrt{((r_{2e}^2 - r_1^2)/2 \ln(r_{2e}/r_1))} \quad 2.46$$

$$B_p = 2\tau_y/G_p = r_{pe} - r_{ne} \quad 2.47$$

$$r_{pe} = \sqrt{((r_{2e}^2 - r_1^2)/2 \ln(r_{2e}/r_1)) + \tau_y/G_P} \quad 2.48$$

The results of the solution of these equations show that the velocity profiles and the magnitudes of shear stress/shear rate are not symmetric about the radial position at which the maximum velocity exists and where the magnitude of the shear stress is zero  $\tau_{zr} = 0$ . This occurrence shows why the assumption that the maximum velocity exists at the midpoint in the radial space of the annulus would lead to erroneous results.

The pressure gradient to volumetric flowrate relationship was derived for the Power law and Bingham plastic fluids as:

Power law:

$$Q = r_2^3 \left( \frac{G_P r_2}{K} \right)^s \bar{Q}_{pL} \quad 2.49$$

$$\bar{Q}_{pL} = \frac{n}{1 + 3n} \left( \frac{1}{2} \right)^s \int_0^\pi \left( \frac{r_{2e}}{r_2} \right)^{3+s} \left\{ \left[ 1 - \left( \frac{r_{me}}{r_{2e}} \right)^2 \right]^{s+1} - \left( \frac{r_1}{r_{2e}} \right)^{1-s} \left[ \left( \frac{r_{me}}{r_{2e}} \right)^2 - \left( \frac{r_1}{r_{2e}} \right)^2 \right]^{1+s} \right\} d\theta \quad 2.50$$

Bingham plastic:

$$Q = \left( \frac{G_P r_2^4}{\mu_p} \right) \bar{Q}_{Bp} \quad 2.51$$

$$\bar{Q}_{Bp} = \frac{1}{8} \int_0^\pi \left(\frac{r_{2e}}{r_2}\right)^4 \left\{ \left[ 1 - \left(\frac{r_1}{r_{2e}}\right)^4 \right] - 2 \frac{r_{pe}}{r_{2e}} \left(\frac{r_{pe} - B_p}{r_{pe}}\right) \left[ 1 - \left(\frac{r_1}{r_{2e}}\right)^2 \right] - \frac{4B_p}{3r_{2e}} \left[ 1 + \left(\frac{r_1}{r_{2e}}\right)^3 \right] + \frac{B_p}{3r_{2e}} \left(\frac{2r_{pe} - B_p}{r_{2e}}\right)^3 \right\} d\theta \quad 2.52$$

Although the method required for the solution of these equations are far less tedious than that required for the slot models or the bipolar coordinate transformation method, iterative and numerical integrations would be needed to solve these equations as the analytical solution does not exist at this present time. The results obtained from the solution of the volumetric flow rate for Power law fluids were numerically compared with those obtained from the slot models or the bipolar coordinate transformation method. They concluded that for low fractional eccentricity cases, their proposed method produced more accurate results while for middle and higher eccentricity cases the slot model produced better approximations.

Experimental, numerical and theoretical modelling studies has been performed over the years with the aim of investigating and predicting the behaviour of non-Newtonian fluids flow through the concentric/eccentric annuli with or without inner cylinder rotation. Most of these studies have pointed out that eccentricity alters the axial velocity distribution in the annuli where a higher magnitude of velocity exists in the larger region of the eccentric annuli while a significantly lower magnitude of velocity exists in the smaller region. Inner pipe rotation has been shown to influence the velocity fields in the eccentric annuli as it redistributes velocity fields and improves the flow of fluids in the stagnation zones or the smaller region of the eccentric annuli. Although literature has shown no disputing to the effect of the inner pipe rotation on the velocity fields in annuli flows, the results published on the effect of the inner pipe rotation on the annuli pressure gradient has been quite conflicting. While some researchers have concluded that inner pipe rotation can be used to decrease the pressure drop for non-Newtonian flows through an eccentric annulus, some have reported that the increase in the inner pipe rotation leads to a corresponding increase in the pressure drop. (Diaz, et al., 2004) in an attempt to develop a method to account for the effect of inner pipe rotation on the pressure drop for fluid flow in concentric annuli using an experimental and theoretical approach reported that for the shear-thinning fluid,

the pressure drop decreased with an increase in pipe rotary speed and started to increase again. Hence literature has shown that the effect of the inner pipe rotation on the axial pressure drop in a concentric or eccentric annulus is not quite certain. For drilling applications, it is important to be able to accurately predict the velocity fields and pressure gradient behavior in order to alleviate wellbore control and stability issues. In cases where a multiphase fluid (gas and non-Newtonian liquid) is used as the drilling fluid for oil well drilling operations, it is imperative that the hydraulic modeling and design of the drilling process takes into account the distinctive properties of two-phase flow, because unlike single-phase flow of general fluids through conduits, multiphase flow is highly transient in nature and adds more complexity to the system. While the velocity field prediction is required for the modeling of an effective cutting transport system during drilling, the accurate prediction of the annuli pressure gradient is necessary especially for wellbore bottom-hole pressure management.

## **2.2 Multiphase Gas – Liquid flow in pipes**

The hydrodynamics of single-phase flow in pipes and annuli is well understood at this present time. Pressure gradient vs flowrate behaviour and the heat transfer processes for single-phase fluid flow in pipes and annuli can be determined in a relatively straightforward manner although the solution of non-Newtonian flow in annuli requires a more compound approach. The simultaneous flow of two phases in a pipe presents more complexity due to its transient nature, flow pattern variation and a large number of flow variables associated with the flow. The mechanism of mass, momentum and energy transfer between phases vary depending on the prevailing flow pattern (Guo, et al., 2007). In order to investigate the multiphase flow of fluids through the annuli, it is necessary to explore the primary studies that have been done on the multiphase flow of fluids through pipes as the ideas and modelling techniques developed for two-phase flows in pipes have been the fundamental basis on which the methods for the prediction and modelling of the hydrodynamic behaviour of two phase flows in annuli are being developed. In fact, the early methods used for the prediction of two-phase flow behaviour in annuli have either applied correlations originally developed for flow in pipes by use of the hydraulic diameter concept or have

applied empirical correlations developed from data obtained from two-phase flow through annuli (Brill & Mukherjee, 1999).

Over the years extensive experimental and theoretical studies have been carried out to develop models that can be used to predict the dynamics of multiphase flow. Based on experimental data, correlations developed to describe the flow are only valid for a limited range of operating conditions. However, improvements in technology has provided the flexibility to construct and use large-scale computational models to simulate two-phase flows especially in complex geometries where experimental investigation is not feasible (Sandra, et al., 2008). Two-phase flow models were developed using an empirical and mechanistic approach, limiting their applicability to the number of flow parameters and conditions considered. For example, the early two-phase models developed neglected the flow patterns in predicting the flow behaviour and were found to be inaccurate under various flow conditions. This brought about a drive for several investigator to determine the important parameters that govern multiphase flow in an attempt to close the gap of the uncertainty posed by two-phase flow.

(Wallis, 1969) derived a simple yet versatile model well known as the Homogeneous No-slip Model. This model assumes that the flow is a pseudo single-phase fluid and that both fluids move at the same velocity. The physical properties of the system are determined from the single-phase liquid and gas properties using the input or No-slip liquid holdup. They assumed that the flow was a steady state compressible one-dimensional flow, all phases were mixed and exist at any point in the flow field, and no slippage occurs between the phases. These assumptions limited the accuracy and applicability of the Homogeneous No-slip Model.

The homogeneous No-slip model is based on the determination of the pressure gradient of a two-phase flow by the solution of the conservation of momentum and energy equations using average mixture properties of the fluid. The total pressure gradient of a multiphase flow can be obtained from the summation of the gravitational, frictional and acceleration components which makes up the momentum Equation 2.53.

The conservation of energy equation can be expressed as

$$\frac{dQ_E}{dL} = \rho_{ns} V_m A_P \frac{dh_M}{dL} + \rho_{ns} V_m A_P \frac{d}{dL} \left( \frac{V_M^2}{2} \right) + \rho_{ns} V_m A_P g \sin \theta_p + \frac{dw_s}{dL} \quad 2.53$$

$$-\frac{dP}{dL} = \frac{S_{PW}}{A_P} \tau_{pw} + \rho_{ns} g \sin \theta_p + \rho_{ns} V_m \frac{dV_M}{dL} \quad 2.54$$

$$-\left( \frac{dP}{dL} \right)_T = \left( \frac{dP}{dL} \right)_F + \left( \frac{dP}{dL} \right)_G + \left( \frac{dP}{dL} \right)_A \quad 2.55$$

Where  $dQ_E/dL$  represents the heat transfer per unit length of the pipe and  $h_M$  represents the mixture enthalpy of the system. The term  $dw_s/dL$  is the shaft work rate per unit length of the pipe and is usually assumed to be negligible for flow in pipes.

The first component of the Equation 2.54 represents the frictional pressure gradient which is derived by expressing the wall shear stress in terms of the friction factor. The wall shear stress and the resulting frictional pressure gradient expressed in terms of the friction factor can be written respectively as:

$$\tau_w = \frac{1}{2} f \rho_{ns} V_M^2 \quad 2.56$$

$$\left( \frac{dP}{dL} \right)_F = \frac{2}{D} f \rho_{ns} V_M^2 = \frac{2}{D} f \frac{G^2}{\rho_{ns}} \quad 2.57$$

$$G = \rho_{ns} V_M \quad 2.58$$

where  $f$ , is the fanning friction factor and  $G$  is the total mass flux of the mixture assuming that the conditions for no-slipage exists. The friction factor is

determined from standard methods using the mixture no-slip Reynolds number defined as:

$$Re_{ns} = \frac{\rho_{ns} V_M D}{\mu_{ns}} \quad 2.59$$

The mixture properties can be utilized to calculate the pressure distribution and the temperature distribution of the flow, by applying standard single-phase flow methods. The mixture average properties of the flow are determined from the input liquid hold (no-slip liquid hold up) or in terms of the mass fraction (quality) as follows:

The mixture velocity of the mixture can be calculated from the summation of the superficial velocity of the gas and the liquid phase obtained from dividing the liquid and gas flowrates by the total cross-sectional area of the pipe  $V_{SL} = Q_L/A_P$ ;  $V_{SG} = Q_G/A_P$ ;

$$V_M = V_{SL} + V_{SG} \quad 2.60$$

The no-slip mixture density and viscosity of the fluid is calculated using the input or no-slip liquid hold up as:

$$\rho_{ns} = \rho_L \lambda_L + \rho_G (1 - \lambda_L) \quad 2.61$$

$$\mu_{ns} = \mu_L \lambda_L + \mu_G (1 - \lambda_L) \quad 2.62$$

The no-slip mixture density can also be expressed in terms of the mass fraction (quality) as:

$$\frac{1}{\rho_{ns}} = \frac{x}{\rho_G} + \frac{1-x}{\rho_L} = xV_G + (1-x)V_L \quad 2.63$$

The mass fraction (quality) is the ratio of the mass flux of the gas phase to the total flux of the mixture and can be written in terms of the liquid hold up as:

$$x = \frac{\rho_G V_G A_P (1 - H_L)}{\rho_G V_G A_P (1 - H_L) + \rho_L V_L A_P H_L} \quad 2.64$$

For no-slip conditions,  $V_G = V_L$  and  $H_L = \lambda_L$  reducing equation 2.64 to

$$x = \frac{\rho_G (1 - \lambda_L)}{\rho_{ns}} \quad 2.65$$

The mixture enthalpy is averaged based on the mass fraction and is given by

$$h_M = x h_G + (1 - x) h_L \quad 2.66$$

The determination of two-phase mixture properties has not been a simple task. Various methods have been proposed by two-phase flow researchers to estimate the mixture parameters of two-phase flows. By all means, these are not rigorous methods, and are merely approximations.

The gravitational pressure gradient component can be determined directly from

$$\left(\frac{dP}{dL}\right)_G = \rho_{ns} g \sin \theta_p \quad 2.67$$

In general, the use of the density based on the in-situ liquid holdup in the determination of the gravitational pressure gradient component is rigorous. This is mainly because the gravitational head depends on the accumulative weight of the two phases, which are related to the in-situ volume fractions of the two phases. In the Homogeneous No-Slip Model, however, the no-slip liquid holdup is used to determine the mixture density, resulting in an inaccurate prediction of the gravitational pressure gradient. This represents the largest limitation of the homogeneous no-slip model. The prediction of the accelerational pressure gradient component in the no-slip homogeneous model is determined using a

systematic approach that is well attached to the physical phenomena of two-phase flow.

The mass flow rate of the two-phase mixture can be expressed in terms of the no-slip density and mixture velocity as:

$$\dot{M} = \rho_{ns} V_M A_P \quad 2.68$$

From Equation 2.54 the accelerational pressure gradient component can be written in terms of the mass flux of the two-phase mixture

$$\left(\frac{dP}{dL}\right)_A = \rho_{ns} V_M \frac{dV_M}{dL} = \frac{\dot{M}}{A_P} \frac{dV_M}{dL} = G \frac{d}{dL} \left( \frac{\dot{M}}{\rho_{ns} A_P} \right) \quad 2.69$$

Taking the partial derivative of the Equation 2.69 yields:

$$\left(\frac{dP}{dL}\right)_A = G^2 \frac{d}{dL} \left( \frac{1}{\rho_{ns}} \right) - \frac{G^2}{\rho_{ns}} \frac{1}{A_P} \frac{dA_P}{dL} \quad 2.70$$

Differentiating the Equation 2.70 in terms of the specific volumes of the phases, yields the following equations

$$\frac{d}{dL} \left( \frac{1}{\rho_{ns}} \right) = \frac{d}{dL} (xV_G + (1-x)V_L) \quad 2.71$$

$$\frac{d}{dL} \left( \frac{1}{\rho_{ns}} \right) = (V_G - V_L) \frac{dx}{dL} + x \frac{dV_G}{dL} + (1-x) \frac{dV_L}{dL} \quad 2.72$$

Assuming that the flow is compressible, the equation 2.72 can be expanded in terms of pressure as:

$$\frac{d}{dL} \left( \frac{1}{\rho_{ns}} \right) = (V_G - V_L) \frac{dx}{dL} + x \frac{dV_G}{dP} \frac{dP}{dL} + (1-x) \frac{dV_L}{dP} \frac{dP}{dL} \quad 2.73$$

Substituting the equation 2.73 into equation 2.70 yields the final form of the accelerational pressure gradient equation

$$\left( \frac{dP}{dL} \right)_A = G^2 \left( (V_G - V_L) \frac{dx}{dL} + x \frac{dV_G}{dP} \frac{dP}{dL} + (1-x) \frac{dV_L}{dP} \frac{dP}{dL} \right) - \frac{G^2}{\rho_{ns}} \frac{1}{A_P} \frac{dA_P}{dL} \quad 2.74$$

Combining the frictional, gravitational and accelerational pressure gradient components Equation 2.57, 2.67 and 2.74 yields the total pressure gradient for a two-phase gas-liquid flow:

$$\begin{aligned} - \left( \frac{dP}{dL} \right)_T &= \frac{2}{D} f \rho_{ns} V_M^2 + \rho_{ns} g \sin \theta_p \\ &+ G^2 \left( (V_G - V_L) \frac{dx}{dL} + x \frac{dV_G}{dP} \frac{dP}{dL} + (1-x) \frac{dV_L}{dP} \frac{dP}{dL} \right) - \frac{G^2}{\rho_{ns}} \frac{1}{A_P} \frac{dA_P}{dL} \end{aligned} \quad 2.75$$

Rearranging the equation 2.75 and solving for the pressure gradient term the yields

$$- \left( \frac{dP}{dL} \right)_T = \frac{\frac{2}{D} f \rho_{ns} V_M^2 + \rho_{ns} g \sin \theta + G^2 (V_G - V_L)^2 \frac{dx}{dL} - \frac{G^2}{\rho_{ns}} \frac{1}{A_P} \frac{dA_P}{dL}}{1 + G^2 \left( x \frac{dV_G}{dP} + (1-x) \frac{dV_L}{dP} \right)} \quad 2.76$$

The denominator of the total pressure gradient equation 2.76 can be related to the velocity of sound of the two-phase mixture as

$$M_a^2 = \left( \frac{V_M}{c_M} \right)^2 = - G^2 \left( x \frac{dV_G}{dP} + (1-x) \frac{dV_L}{dP} \right) \quad 2.77$$

Where  $c_M$  and  $M_a$  represents the mixture velocity of sound and the Mach number respectively. The velocity of sound of the gas and the liquid phases are defined as

$$\frac{1}{c_G^2} = \rho_G^2 \frac{d}{dP} \left( \frac{1}{\rho_G} \right) = -\rho_G^2 \frac{dV_G}{dP}, \quad \text{and} \quad \frac{1}{c_L^2} = \rho_L^2 \frac{d}{dP} \left( \frac{1}{\rho_L} \right) = -\rho_L^2 \frac{dV_L}{dP} \quad 2.78$$

Using equation 2.58 and solving equation 2.77 for the mixture velocity of sound yields the following equations

$$\frac{1}{c_M^2} = -\rho_{ns}^2 \left( x \frac{dV_G}{dP} + (1-x) \frac{dV_L}{dP} \right) \quad 2.79$$

$$\frac{1}{c_M^2} = -\left( \rho_L \lambda_L + \rho_G (1 - \lambda_L) \right) \left[ \rho_G (1 - \lambda_L) \left( -\frac{dV_G}{dP} \right) + \rho_L \lambda_L \left( -\frac{dV_L}{dP} \right) \right] \quad 2.80$$

Substituting the velocity of sound of the gas and the liquid phases Equation 2.78 into Equation 2.80 yields

$$\frac{1}{c_M^2} = \left( \rho_L \lambda_L + \rho_G (1 - \lambda_L) \right) \left( \frac{(1 - \lambda_L)}{\rho_G c_G^2} + \frac{\lambda_L}{\rho_L c_L^2} \right) \quad 2.81$$

Lockhart & Martinelli (1949) developed a separated flow model that assumes that the gas phase and liquid phase flows separately from each other and is limited to determination of frictional pressure drop for horizontal pipes. The solution of the frictional pressure gradient is performed via a method that is similar to that of the single-phase flow methods but applies the hydraulic diameter concept to account for flow of each of the phases. Although the model was derived theoretically using the concept of the single-phase flow, experimental data was required to complete the process, providing a solution for the separated flow model. The concept applied in the development of this model and the solution procedures are explained further.

The frictional pressure loss for the flow of two-phase gas-liquid fluids in pipes, obtained by applying the hydraulic diameter concept to each of the phases, may be written as

$$-\left(\frac{dP}{dL}\right)_L = \frac{2f_L\rho_L V_L^2}{D_L} \quad 2.82$$

$$-\left(\frac{dP}{dL}\right)_G = \frac{2f_G\rho_G V_G^2}{D_G} \quad 2.83$$

The liquid and gas phase velocities can be determined respectively from

$$v_L = \frac{Q_L}{A_L} = \frac{Q_L}{a\frac{\pi}{4}D_L^2} \quad \text{and} \quad v_G = \frac{Q_G}{A_G} = \frac{Q_G}{b\frac{\pi}{4}D_G^2} \quad 2.84$$

The parameters  $a$  and  $b$  represent the ratio of the cross-sectional area of the flow of each of the phases to the total area of the pipe based on the hydraulic diameter of the phase.  $D_L$  and  $D_G$  are the hydraulic diameters of the liquid and gas phase respectively.

The liquid holdup which represents the actual cross-sectional area of the flow of each of the phases to the total area of the pipe can be determined with the following expressions

$$\frac{A_L}{A_p} + \frac{A_G}{A_p} = H_L + H_G = 1 \quad 2.85$$

$$\frac{a\frac{\pi}{4}D_L^2 + b\frac{\pi}{4}D_G^2}{\frac{\pi}{4}D^2} = 1 \quad 2.86$$

$$H_L = a\left(\frac{D_L}{D}\right)^2 = 1 - b\left(\frac{D_G}{D}\right)^2 \quad 2.87$$

Using the general Blasius equation for friction,  $f = C_i Re^{-m_i}$  and the phase velocities, the pressure gradient equations 2.82 and 2.83 can be written as

$$-\left(\frac{dP}{dL}\right)_L = \left(\frac{2}{D} C_L \left[ \left(\frac{Q_L}{\frac{\pi}{4} D^2}\right) \frac{\rho_L D}{\mu_L} \right]^{-m_1} \rho_L \left(\frac{Q_L}{\frac{\pi}{4} D^2}\right)^2\right) a^{m_1-2} \left(\frac{D}{D_L}\right)^{5-m_1} \quad 2.88$$

$$-\left(\frac{dP}{dL}\right)_G = \left(\frac{2}{D} C_G \left[ \left(\frac{Q_G}{\frac{\pi}{4} D^2}\right) \frac{\rho_G D}{\mu_G} \right]^{-m_g} \rho_G \left(\frac{Q_G}{\frac{\pi}{4} D^2}\right)^2\right) b^{m_g-2} \left(\frac{D}{D_G}\right)^{5-m_g} \quad 2.89$$

where  $C_L$  and  $m_1$  and  $C_G$  and  $m_g$  are friction factor constants for the liquid and gas phase.

The pressure gradient that would occur assuming only the liquid or gas phase were flowing individually in the pipe is referred to as the superficial pressure gradient. Equation 2.90 and 2.91 expresses the superficial pressure gradient of the liquid and gas phase respectively.

$$-\left(\frac{dP}{dL}\right)_{SL} = C_L \left[ \frac{\rho_L V_{SL} D}{\mu_L} \right]^{-m_1} \frac{2 \rho_L V_{SL}^2}{D} = \left(\frac{2}{D} C_L \left[ \left(\frac{Q_L}{\frac{\pi}{4} D^2}\right) \frac{\rho_L D}{\mu_L} \right]^{-m_1} \rho_L \left(\frac{Q_L}{\frac{\pi}{4} D^2}\right)^2\right) \quad 2.90$$

$$-\left(\frac{dP}{dL}\right)_{SG} = C_G \left[ \frac{\rho_G V_{SG} D}{\mu_G} \right]^{-m_g} \frac{2 \rho_G V_{SG}^2}{D} = \left(\frac{2}{D} C_G \left[ \left(\frac{Q_G}{\frac{\pi}{4} D^2}\right) \frac{\rho_G D}{\mu_G} \right]^{-m_g} \rho_G \left(\frac{Q_G}{\frac{\pi}{4} D^2}\right)^2\right) \quad 2.91$$

From the Equations 2.90 and 2.91, it is clear that the terms in the bracket of Equations 2.88 and 2.89 are the same making it possible to express the liquid and gas pressure gradients in terms of their superficial pressure gradient.

$$-\left(\frac{dP}{dL}\right)_L = -\left(\frac{dP}{dL}\right)_{SL} a^{m_1-2} \left(\frac{D}{D_L}\right)^{5-m_1} \quad 2.92$$

$$-\left(\frac{dP}{dL}\right)_G = -\left(\frac{dP}{dL}\right)_{SG} b^{m_g-2} \left(\frac{D}{D_G}\right)^{5-m_g} \quad 2.93$$

Lockhart and Martinelli defined two dimensionless groups  $\phi_L$  and  $\phi_G$  as the square root of the ratio of the phase pressure gradient to its superficial pressure gradient. Taking a ratio of the gas to liquid dimensionless group and assuming that the pressure gradient in the liquid and the pressure gradient in the gas phase are equal for a steady-state flow, they obtained a dimensionless parameter  $X$  which they defined as the Lockhart and Martinelli parameter. From equation 2.98 it is clear that the parameter  $X$  is just the square root of the ratio of the liquid superficial pressure gradient to the gas superficial pressure gradient.

$$\phi_L = \sqrt{\frac{-\left(\frac{dP}{dL}\right)_L}{-\left(\frac{dP}{dL}\right)_{SL}}} = a^{\frac{m_1-2}{2}} \left(\frac{D}{D_L}\right)^{\frac{5-m_1}{2}} \quad 2.94$$

$$\phi_G = \sqrt{\frac{-\left(\frac{dP}{dL}\right)_G}{-\left(\frac{dP}{dL}\right)_{SG}}} = b^{\frac{m_g-2}{2}} \left(\frac{D}{D_G}\right)^{\frac{5-m_g}{2}} \quad 2.95$$

$$X = \frac{\phi_G}{\phi_L} = \sqrt{\frac{-\left(\frac{dP}{dL}\right)_G}{-\left(\frac{dP}{dL}\right)_{SG}} \times \frac{-\left(\frac{dP}{dL}\right)_{SL}}{-\left(\frac{dP}{dL}\right)_L}} \quad 2.96$$

$$-\left(\frac{dP}{dL}\right)_L = -\left(\frac{dP}{dL}\right)_G \quad 2.97$$

From equation 2.97 Equation 2.96 reduces to

$$X = \frac{\phi_G}{\phi_L} = \frac{\sqrt{-\left(\frac{dP}{dL}\right)_{SL}}}{\sqrt{-\left(\frac{dP}{dL}\right)_{SG}}}; \quad 2.98$$

The Lockhart and Martinelli model cannot be solved analytically to obtain the solution of the pressure gradient in the pipe due to the fact that the model contains various unknowns. However, they developed a method for the solution of the model using an experimental approach. Four scenarios depending on the flow regime that each of the phases were flowing in that is, whether the gas or the liquid phase exists in the laminar or turbulent flow domain. The experiments were carried out using the air and water or diesel, kerosene and several oils to simulate the flow of two-phases in small diameter pipes in the range of 0.15 to 2.54 (Shoham, 2005). Using the experimental data obtained from the study, they plotted the dimensionless groups  $\phi_L$  and  $\phi_G$  vs the parameter  $X$  and reported a significant correlation of the experimental data with the parameter  $X$ . In order to calculate the pressure gradient one has to first determine  $\phi_L$  or  $\phi_G$  from the plots.

The pressure gradient calculation using the separated model can be made more convenient by using the Equations 2.99 and 2.100 derived by (Chisholm 1967) using a curve fitting to the original plots for the parameter  $\phi_L$  and the liquid hold up  $H_L$ . However, the constant  $C$  in Equation 2.99 is dependent on the flow regime of each of the phases and can be determined as provided in the table 2.1

$$\phi_L^2 = 1 + \frac{C}{X} + \frac{1}{X^2} \quad 2.99$$

$$H_L = 1 - (1 + X^{0.8})^{-0.378}$$

2.100

Table 2.1: Chisholm 1967 correlation coefficients for the constant  $C$

Liquid phase	Gas phase	Constant $C$
Turbulent	Turbulent	20
Laminar	Turbulent	12
Turbulent	Laminar	10
Laminar	Laminar	5

The early investigators of multiphase flow as explained previously, treated the flow as a homogenous mixture of gas and liquid. This led to some drawbacks as these methods did not recognise that slippage occurs between the gas and the liquid phase and did not account for the effect of the prevailing flow pattern. For this reason, the no-slip approach underpredicted the pressure gradient.

Empirical correlations were developed to make improvements to the no-slip approach. This approach used empirical liquid holdup correlations to account for the slippage between the phases, and the liquid holdup and friction factor predictions were dependent on empirically developed flow pattern maps. Unfortunately, these methods also treated the flow as a homogenous mixture of gas and liquid resulting in an inaccurate prediction of the flow dynamics.

Table 2.2: List of major two-phase flow models and their range of applicability

Empirical Models	Flow pattern	Slippage	Angle
(Poettmann & Carpenter, 1952)	●	●	$\theta = 90$
(Baxendell & Thomas, 1961)	●	●	$\theta = 90$
(Fancher & Brown, 1963)	●	●	$\theta = 90$
(Hagedorn & Brown, 1965)	●	●	$\theta = 90$
(Asheim, 1986)	●	●	$\theta = 90$
(Duns & Ros, 1963)	●	●	$\theta = 90$
(Orkiszewski, 1967)	●	●	$\theta = 90$
(Aziz, et al., 1972)	●	●	$\theta = 90$
(Chierici, et al., 1974)	●	●	$\theta = 90$
(Beggs & Brill, 1973)	●	●	$-90 \leq \theta \leq 90$
(Mukherjee & Brill, 1985)	●	●	$-90 \leq \theta \leq 90$

● Considered      ● Not considered

The empirical correlations developed were separated into three major categories: The correlations placed in the first category were not flow pattern dependent and did not consider the slippage between the gas and the liquid phase. The mixture properties of the flow were calculated based on the no-slip or input liquid holdup as both phases were assumed to travel at the same velocity. The second category correlations considered the slippage between the phases but are independent on the flow pattern. Although a correlation is required for both liquid holdup and friction factor calculations, the same correlations are used for all the flow patterns. To account for the slippage effect of the liquid and gas flowing at different velocities, a method to predict the portion of the pipe occupied by the liquid phase at any local point is required. In the third category correlations, slippage between the phases and the flow pattern are considered. However, several correlations are required to predict the liquid holdup and friction factor along with methods to predict the prevailing flow pattern.

Table 2.2 gives a list of some of the major empirical models developed by various researchers and their ranges of applicability. It is clear that most of the early empirical models were built for vertical two-phase flow in pipes except for the Beggs and Brill and the Mukherjee and Brill multiphase correlations. This made the Beggs and Brill and the Mukherjee and Brill multiphase correlations more attractive to end users as the models were flow pattern dependent, accounted for slippage effects, and could be applied to a wide range of pipe inclination angles. The models were also reported to be applicable to injection wells and hilly terrain pipelines.

Beggs and Brill (1973) presented the first method to predict the two-phase flow behaviour and determine pressure gradient at all inclinations. They developed empirical correlations for predicting the flow pattern and the corresponding pressure drop using experimental data obtained from a 90ft long transparent acrylic pipe. The parameters considered in the study and the range in which they

varied were: gas-liquid flow patterns, maximum gas flowrate of 300 Mscf/D, liquid flowrate up to 30 gal/min, system average pressure within 35 to 95 psia, 1 to 1.5in pipe sizes, Liquid holdup varying from 0 to 0.870 and inclination angle of -90° to +90°.

For each of the selected pipe sizes, the liquid and gas rates (water and air) were varied while observing the resulting flow patterns when the pipe was horizontal. After this the pipe angle was varied through the range of angles considered so that the effect of the pipe inclination on hold up and pressure gradient could be studied. In this study they showed that the input liquid holdup and Froude number were very important parameters for two-phase flow in terms of flow pattern prediction. They concluded that the inclination angle significantly affected the liquid holdup and pressure gradient for most flow conditions, and the frictional pressure drop is highly affected by liquid holdup. A correlation was developed to determine the pressure gradient after determining the flow pattern and in-situ liquid hold up.

Beggs and Brill (1973) presented several correlations that predict the transition boundaries between several flow patterns as a function of the no-slip liquid holdup and the mixture Froude number. The Table 2.3 shows the inequality equations that were developed for the different gas-liquid flow patterns considered.

Table 2.3: Beggs and Brill flow pattern transition boundaries

Flow pattern	Existing range
Segregated	$\lambda_L < 0.01 \& N_{Fr} < L_1$ or $\lambda_L \geq 0.01 \& N_{Fr} < L_2$
Intermittent	$0.01 \leq \lambda_L < 0.4 \& L_3 < N_{Fr} \leq L_1$
	or $\lambda_L \geq 0.4 \& L_3 < N_{Fr} \leq L_4$
Distributed	$\lambda_L < 0.4 \& N_{Fr} \geq L_1$
	or $\lambda_L \geq 0.4 \& N_{Fr} > L_4$
Transition	$\lambda_L \geq 0.01 \& L_2 < N_{Fr} \leq L_3$

The equation for the flow pattern transition boundaries are given as:

$$L_1 = 316\lambda_L^{0.302} \quad 2.101$$

$$L_2 = 0.0009252\lambda_L^{-2.4684} \quad 2.102$$

$$L_3 = 0.10\lambda_L^{-1.4516} \quad 2.103$$

$$L_4 = 0.50\lambda_L^{-6.738} \quad 2.104$$

Since the pipe inclination angle has an impact on the liquid holdup, the horizontal liquid holdup is first calculated and then corrected to account for the pipe angle. The liquid holdup in the dispersed bubble flow pattern was reported to be independent of the pipe inclination angle and needs no correction. The horizontal liquid holdup is given as:

$$H_L^{(0)} = \frac{a\lambda_L^b}{N_{Fr}^c}; \quad H_L^{(0)} \geq \lambda_L \quad 2.105$$

$$N_{Fr} = \frac{V_m^2}{gD} \quad 2.106$$

Equation 2.105 is used to calculate the horizontal liquid holdup for all the flow patterns. However, the empirical coefficients used are different for each flow pattern as given in Table 2.4

Table 2.4: Beggs and Brill empirical coefficients for horizontal liquid holdup

Flow pattern	a	b	c
Segregated	0.980	0.4846	0.0868
Intermittent	0.845	0.5351	0.0173
Distributed	1.065	0.5824	0.0609

The correction factor  $\psi$  that is applied to account for the effect of pipe inclination on the liquid holdup is given by

$$\psi = 1.0 + \beta i [\sin(1.8\theta_p) - 0.333\sin^3(1.8\theta_p)] \quad 2.107$$

where  $\theta_p$ , is the pipe angle and  $\beta i$  is defined by Equation 2.108.

$$\beta i = (1.0 - \lambda_L) \ln(e\lambda_L^f N_{Fr}^g N_{LV}^h); \text{ where } \beta i \geq 0 \quad 2.108$$

The empirical coefficients  $f$ ,  $g$  and  $h$  for the different flow patterns are given in Table 2.5

Table 2.5: Beggs and Brill (1973) empirical coefficients for  $\beta$

Flow pattern	e	f	g	h
Segregated uphill	0.011	-3.7680	-1.6140	3.5390
Intermittent uphill	2.960	0.3050	0.0978	-0.4473
Distributed uphill		No correction $C = 0$ ;		
All downhill flows	4.70	-0.3692	-0.5056	0.1244

The expression for the inclination angle corrected liquid holdup is then given as

$$H_L^{(\theta)} = H_L^{(0)}\psi \quad 2.109$$

If the transition flow pattern exists, the liquid holdup is obtained by interpolating between the segregated and intermittent flow pattern to obtain the transition liquid holdup

$$(H_L^{(\theta)})_{\text{Transition}} = W(H_L^{(\theta)})_{\text{Segregated}} + (1 - W)(H_L^{(\theta)})_{\text{Intermittent}} \quad 2.110$$

Where the interpolation weight parameter  $W$  is given as:

$$W = \frac{L_3 - N_{Fr}}{L_3 - L_2}$$

The two-phase friction factor  $f_{tp}$  is calculated from the following equations

$$\frac{f_{tp}}{f_{ns}} = e^s \quad 2.111$$

$$y = \ln\left(\frac{\lambda_L}{(H_L^{(\theta)})^2}\right) \quad 2.112$$

There are discontinuities for  $y$  values of about  $2.63 \times 10^{-4}$  and 1.1016. It is unlikely that the discontinuity at the smaller value of  $y$  would be encountered. However, it is necessary that  $s$  is set to zero if equals one. This ensures that the correlation degenerates to the single-phase i.e.  $s(y = 1) = 0$ ;

$$s = \frac{y}{-0.0523 + 3.28y - 0.872y^2 + 0.01853y^4} \quad 2.113$$

$$s = \ln(2.2y - 1.2) ; \quad 1 < y < 1.2 \quad 2.114$$

Payne et al. (1979) carried out an experimental study on two-phase flow in an inclined pipe and found out that because the Beggs and Brill (1973) method was based on experimental data obtained for smooth pipes, it underpredicted the friction factors. They recommended that the no-slip friction factor should be obtained from the moody friction chart or from equation 2.115 for the actual value of the relative roughness, using an iterative procedure.

$$\frac{1}{f_{ns}} = 1.74 - 2 \log\left(\frac{2\varepsilon}{D} + \frac{18.7}{Re_{ns}\sqrt{f_{ns}}}\right) \quad 2.115$$

Where  $Re_{ns}$ , is the no slip Reynolds number defined by Equation 2.59

Payne et al discovered that the Beggs and Brill method also overpredicted the liquid holdup for both uphill and downhill flows. They recommended correction factors for the liquid holdup defined by:

$$H_L^{(\theta)} = 0.924H_L^{(\theta)}; \quad \theta_p > 0 \quad 2.116$$

$$H_L^{(\theta)} = 0.685H_L^{(\theta)}; \quad \theta_p < 0 \quad 2.117$$

The pressure gradient for all the flow patterns can then be calculated from

$$-\frac{dP}{dZ} = \frac{[\rho_L H_L^{(\theta)} + \rho_G(1 - H_L^{(\theta)})]g \sin \theta_p + \frac{f_{tp}[\rho_L \lambda_L + \rho_G(1 - \lambda_L)]V_m^2}{2D}}{1 - \frac{V_m V_{SG} [\rho_L \lambda_L + \rho_G(1 - \lambda_L)]}{P}} \quad 2.118$$

This correlation has been one of the most widely used method to predict two-phase flow patterns and calculate the pressure gradient in pipes due to its ease of application and the vast range of parameters considered. The pressure gradient Equation 2.118 was derived by considering the sum of the individual components that contribute to the pressure drop in a steady state fluid flow. These are made up of the potential energy change, kinetic energy change and the frictional loss component.

Mukherjee and Brill (1985) carried out an experimental study using air, kerosene and lube oil in an attempt to alleviate some of the limitations of the Beggs and Brill (1973) method. They carried out experiments using an inverted U-shaped, 1.5-in. nominal ID steel pipe which could be raised or lowered to allow the varying

of the pipe inclination angle within a range of  $0^\circ$  to  $\pm 90^\circ$  from the horizontal. Transparent test sections were used to allow for flow-pattern observations and permitted the use of capacitance sensors to measure liquid holdup. About 1000 pressure drop measurements were taken and more than 1500 liquid holdup measurements for a broad range of gas and liquid flowrates. Flow pattern and liquid prediction methods were developed using an empirical approach and the suggested pressure gradient calculation methods are very similar to that of the Beggs & Brill (1973) method. However, a steady state momentum balance on the gas and liquid phases was applied to generate a method to calculate the pressure gradient for stratified flow in a highly deviated or horizontal well.

The models generated using the empirical approach were found to be inaccurate under certain conditions and often proved inadequate in that they are limited by conditions and the range of experimental data on which they were developed. The empirical models cannot be used with confidence for all types of fluids and conditions encountered in the oil and gas industry. Furthermore, some of the empirical models produce large discontinuities at flow pattern transitions which may create convergence errors (Petalas and Aziz, 2000).

Further along the line, the mechanistic modelling approach was developed to improve the prediction of the flow dynamics and was a compromise between the empirical and the two-fluid approach. The mechanistic modelling approach tends to consider the important parameters that govern the flow dynamics by applying the fundamental laws of physics. However, a relatively much lower amount of empiricism is still required to determine closure relationships or predict certain flow mechanisms. Although most mechanistic models that predict two-phase flow behaviour in pipes are for an isolated mechanism, such as flow pattern, liquid film thickness, or bubble rise velocity in liquid columns, the mechanistic models being based on fundamental laws, offered more accurate modelling of the geometric and fluid property variations.

Taitel and Dukler (1976) developed a mechanistic model for the unambiguous analytical prediction of the transition between flow patterns. The model predicts the relationship between the following variables at which the flow pattern transitions occur; gas and liquid mass flowrates, fluid properties, pipe sizes and pipe inclination angle. The mechanisms for the flow pattern transitions are based on physical concepts and are fully predictive in the sense that no flow pattern data was used in the model development.

The study provided considerable insight to the mechanism for transition between five basic flow patterns which were dispersed bubble, stratified smooth, stratified wavy, intermittent (slug and plug), and annular with dispersed liquid. No distinction is made between slug, plug, or elongated bubble flows, which are considered as different conditions in the intermittent flow pattern.

The process of analysing the transitions between the different flow patterns starts from the condition of stratified flow. The approach is to visualize a stratified liquid and then do determine the mechanism by which a change from stratified flow can be expected to take place, as well as the flow pattern that can be expected to result from the change.

Assuming a stratified flow of gas and liquid in a pipe, if the liquid flowrate is increased, the liquid level in the pipe rises, and a wave is formed which grows rapidly tending to block the flow. At lower gas flowrates, the liquid bridges the pipe to produce the slug or plug flow pattern. At higher gas flowrates, there is insufficient liquid flowing to maintain or, in some cases, even to form the liquid bridge, so the liquid is swept up and around the pipe to form an annulus with some entrainment if the gas flowrate is high enough. A summary of the transition criteria of the different gas-liquid fluid flow patterns are presented in Table 2.6:

Table 2.6: Taitel and Dukler (1976) gas-liquid flow pattern transition criteria

---

**Stratified to non-stratified transition:**

---

$$F^2 \left[ \frac{1}{C_2^2} \frac{\widetilde{V}_G \frac{d\widetilde{A}_L}{d\widetilde{h}_L}}{\widetilde{A}_G} \right] \geq 1 \quad C_2 = 1 - \frac{h_L}{D} \quad F = \sqrt{\frac{\rho_G}{(\rho_L - \rho_G)}} \frac{V_{SG}}{\sqrt{Dg \cos \theta_p}}$$


---

**Intermittent to Annular Transition:**

---

$$h_L/D = 0.5$$

If the equilibrium liquid level in the pipe is above the pipe centre line, intermittent flow pattern would occur, and if  $h_L/D < 0.5$ , the annular flow pattern would occur. Barnea et al (1980) modified the criterion for the transition and suggested the following equation:

$$\widetilde{h}_L = \frac{h_L}{D} = 0.5 \times 0.7 = 0.35$$

Thus, for  $\widetilde{h}_L > 0.35$ , the slug flow pattern would occur whereas for  $\widetilde{h}_L \leq 0.35$ , the intermittent flow pattern would occur.

---

**Stratified smooth to stratified wavy transition:**

---

$$K \geq \frac{2}{\sqrt{\widetilde{V}_G \widetilde{V}_L \sqrt{s}}}$$

$$K^2 = \frac{\rho_G V_{SG}^2 \rho_L V_{SL}}{\mu_L (\rho_L - \rho_G) g \cos \theta_p} = \frac{\rho_G V_{SG}^2}{(\rho_L - \rho_G) g D \cos \theta_p} \left( \frac{\rho_L V_{SL} D}{\mu_L} \right)$$


---

**Intermittent to dispersed bubble transition:**

---

$$T^2 \geq \left[ \frac{8 \widetilde{A}_G}{\widetilde{S}_i \widetilde{V}_L^2 (\widetilde{V}_L \widetilde{D}_L)^{-ml}} \right]$$

$$T = \left[ \frac{C_L \left[ \frac{\rho_L V_{SL} D}{\mu_L} \right]^{-ml} 2 \frac{\rho_L V_{SL}^2}{D}}{(\rho_L - \rho_G) g \cos \theta_p} \right]^{1/2} = \left[ \frac{-\left(\frac{dP}{dL}\right)_{SL}}{(\rho_L - \rho_G) g \cos \theta_p} \right]^{1/2}$$


---

The flow pattern transition criteria are a unique function of the dimensionless liquid level in the pipe, which has to be obtained initially before the prevailing flow pattern can be predicted. The equilibrium liquid level in the pipe can be determined for a given set of input flow conditions by applying the momentum balance on the gas and liquid phases. Assuming a steady state flow and neglecting the rate of

change of momentum across the control volume, the momentum balances for the liquid and the gas phase can be expressed respectively as

$$-\frac{dP}{dL} - \frac{S_L}{A_L} \tau_{wL} + \frac{S_i}{A_L} \tau_i - \rho_L g \sin \theta_p = 0 \quad 2.119$$

$$-\frac{dP}{dL} - \frac{S_G}{A_G} \tau_{wG} + \frac{S_i}{A_G} \tau_i - \rho_G g \sin \theta_p = 0 \quad 2.120$$

The combination of Equations 2.119 and 2.120 eliminates the pressure gradient term and yields an equation that is implicit for the equilibrium liquid height  $h_L$ .

$$\frac{S_G}{A_G} \tau_{wG} - \frac{S_L}{A_L} \tau_{wL} + \tau_i S_i \left( \frac{1}{A_L} + \frac{1}{A_G} \right) - (\rho_L - \rho_G) g \sin \theta_p = 0 \quad 2.121$$

The liquid, gas and interfacial shear stresses can be calculated respectively from the following equations

$$\tau_{wL} = \frac{1}{2} f_L \rho_L V_L^2 \quad 2.122$$

$$\tau_{wG} = \frac{1}{2} f_G \rho_G V_G^2 \quad 2.123$$

$$\tau_i = \frac{1}{2} f_i \rho_G (V_G - V_L)^2 \quad 2.124$$

The calculation of the friction factors for the different shear stress equations are carried out using the standard single-phase flow method by applying the hydraulic diameter for each of the phases. The friction factor for smooth pipes equations can be expressed as

$$f_L = C_L Re_L^{-m_l} \quad \text{and} \quad f_G = C_G Re_G^{-m_g} \quad 2.125$$

The following coefficients are utilised for the friction factor equations:  $C_L = C_G = 16$  and  $m_l = m_g = 1$  for laminar flow, and  $C_L = C_G = 0.046$  and  $m_l = m_g = 0.2$  for turbulent flow.

The Reynold numbers and hydraulic diameters for each of the phases are given as

$$Re_L = \frac{\rho_L V_L D_L}{\mu_L} \quad 2.126$$

$$Re_G = \frac{\rho_G V_G D_G}{\mu_G} \quad 2.127$$

$$D_L = \frac{4 A_L}{S_L} \quad 2.128$$

$$D_G = \frac{4 A_G}{S_G + S_i} \quad 2.129$$

The interfacial shear stress can be approximated by

$$\tau_i = \frac{1}{2} f_i \rho_G (V_G - V_i)^2 \approx \frac{1}{2} f_i \rho_G (V_G - V_L)^2 \quad 2.130$$

For a stratified smooth flow, Taitel and Dukler (1976) suggested the friction factor of the gas phase should be used the interfacial friction factor  $f_i = f_G$ , while for a stratified wavy flow a value of  $f_i = 0.0142$  can be used (Shoham, 2005).

Using the dimensionless variables in Equation 2.127 it is useful to transform these equations to a dimensionless form making the variables a function of the dimensionless liquid height  $\widetilde{h}_L$ . The resulting dimensionless form of the equations can be expressed as:

$$\widetilde{V}_L = \frac{V_L}{V_{SL}}, \quad \widetilde{V}_G = \frac{V_G}{V_{SG}}, \quad \widetilde{S}_L = \frac{S_L}{D}, \quad \widetilde{h}_L = \frac{h_L}{D}, \quad \widetilde{A}_L = \frac{A_L}{D^2}, \quad 2.131$$

$$X^2 \left[ (\widetilde{V}_L \widetilde{D}_L)^{-n} \widetilde{V}_L^2 \frac{\widetilde{S}_L}{\widetilde{A}_L} \right] - \left[ (\widetilde{V}_G \widetilde{D}_G)^{-m} \widetilde{V}_G^2 \left( \frac{\widetilde{S}_G}{\widetilde{A}_G} + \frac{\widetilde{S}_1}{\widetilde{A}_L} + \frac{\widetilde{S}_1}{\widetilde{A}_G} \right) \right] - 4Y = 0 \quad 2.132$$

where

$$X^2 = \frac{\frac{4 C_L}{D} \left( \frac{\rho_L V_{SL} D}{\mu_L} \right)^{-n} \frac{\rho_L V_{SL}^2}{2}}{\frac{4 C_G}{D} \left( \frac{\rho_G V_{SG} D}{\mu_G} \right)^{-m} \frac{\rho_G V_{SG}^2}{2}} = \frac{-\left(\frac{dP}{dL}\right)_{SL}}{-\left(\frac{dP}{dL}\right)_{SG}} \quad 2.133$$

and

$$Y = \frac{(\rho_L - \rho_G) g \sin \theta_p}{\frac{4 C_G}{D} \left( \frac{\rho_G V_{SG} D}{\mu_G} \right)^{-m} \frac{\rho_G V_{SG}^2}{2}} = \frac{(\rho_L - \rho_G) g \sin \theta_p}{-\left(\frac{dP}{dL}\right)_{SG}} \quad 2.134$$

The following functional relations are required for the solution of the dimensionless equations in order to obtain the equilibrium liquid height.

$$\widetilde{A}_L = 0.25 \left[ \pi - \cos^{-1}(2\widetilde{h}_L - 1) + (2\widetilde{h}_L - 1) \sqrt{1 - (2\widetilde{h}_L - 1)^2} \right] \quad 2.135$$

$$\widetilde{A}_G = 0.25 \left[ \cos^{-1}(2\widetilde{h}_L - 1) - (2\widetilde{h}_L - 1) \sqrt{1 - (2\widetilde{h}_L - 1)^2} \right] \quad 2.136$$

$$\widetilde{S}_L = \pi - \cos^{-1}(2\widetilde{h}_L - 1) \quad 2.137$$

$$\widetilde{S}_G = \cos^{-1}(2\widetilde{h}_L - 1) \quad 2.138$$

$$\widetilde{S}_1 = \sqrt{1 - (2\widetilde{h}_L - 1)^2} \quad 2.139$$

$$\widetilde{V}_L = \frac{\widetilde{A}_P}{\widetilde{A}_L} \quad \text{and} \quad \widetilde{V}_G = \frac{\widetilde{A}_P}{\widetilde{A}_G} \quad 2.140$$

$$\widetilde{D}_L = \frac{4 \widetilde{A}_L}{\widetilde{S}_L} \quad \text{and} \quad \widetilde{D}_G = \frac{4 \widetilde{A}_G}{\widetilde{S}_G + \widetilde{S}_1} \quad 2.141$$

When the determination of the equilibrium liquid holdup has been determined, the gas-liquid flow pattern is predicted, and the resulting pressure gradient can be calculated from Equation 2.119 or 2.120 as both equations would yield the same result. It should be noted that the pressure gradient obtained using the Taitel and Dukler model is only valid for all flow conditions at which the stratified flow pattern exists. This constitutes one of the major limitations of the Taitel and Dukler (1976) model. Other mechanistic models have been developed by several investigators to calculate pressure gradients for other flow patterns namely Dispersed bubble, bubble, slug, and annular flow pattern (Hasan and Kabir, 1988; Ansari et al., 1990; Petalas and Aziz, 2000; Xiao et al., 1990; Barnea, 1987). The mass and momentum transfers between the gas and the liquid phases at different pipe inclinations are unique for each flow pattern prompting a distinctive modelling approach for the different flow patterns. For instance, slug flow hydrodynamics is complex with unsteady flow behaviour characteristics. It possesses a distinctive gas-liquid fluid configuration and complex velocity, liquid holdup and pressure distributions. This makes the prediction of the liquid holdup, pressure drop, heat transfer, and mass transfer difficult and challenging, hindering the development of accurate predictive methods.

Duckler and Hubbard (1975) carried out an experimental study to shed light on the mechanism and process of mass transfer for slug flow in horizontal and near horizontal pipes. Using a horizontal test section of 1.5-in id, 65ft long and equipped with fast response pressure transducers, an understanding of the slug flow mechanism was developed from an extensive visualization study including short exposure time still photographs, motion picture sequences at several speeds, and dye tracer work. From visual observations they outlined the stages at which slug flow develops in a pipe:

Liquid and gas flow simultaneously into a pipe with the liquid flowing as a stratified phase and the gas flowing above the liquid. When the gas-liquid velocities under which the slug flow pattern is attained, the liquid level rises, approaching the top of the pipe and waves begin to appear on the liquid surface. Eventually the liquid level bridges the pipe and momentarily blocks the gas flow. (See Figure 2.6A, B, and C). As soon as the bridging occurs, the liquid in the bridge is accelerated to the gas velocity. The liquid appears to be accelerated uniformly across its cross-section, thereby picking up all the slow-moving liquid ahead of it and accelerating it to slug velocity. (See Figure 2.6D.) As the slug travels down the pipe, the liquid is shed uniformly from its back forming a film region which decelerates rapidly from the slug velocity to a much lower velocity, due to the interfacial and wall shear stresses. The length of the slug stabilises as the slug is now picking up liquid at the same rate that it is shed. With the slug having a higher kinetic energy than that of the liquid film, the liquid film penetrates a distance into the slug before attaining the slug velocity, creating an eddy at the front of the slug which is essentially a mixing vortex. The length of the mixing eddy is the distance of penetration of the liquid film.

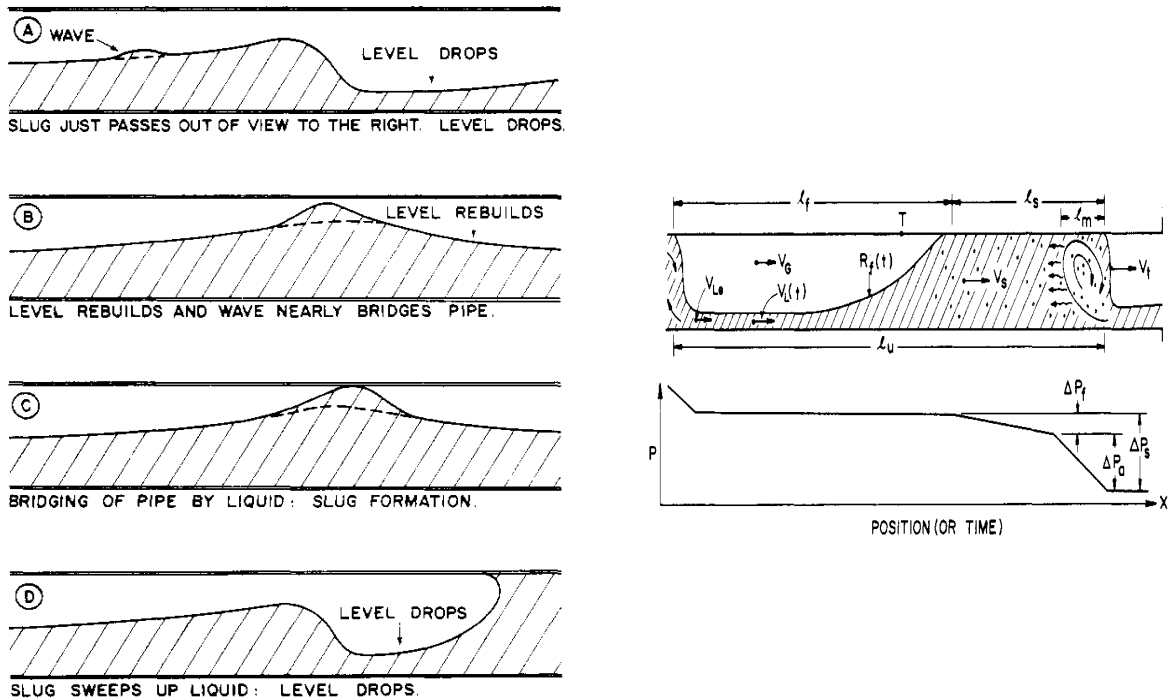


Figure 2.6: Process of formation of the slug flow pattern (Duckler & Hubbard, 1975)

Duckler and Hubbard (1975) developed a hydrodynamic model for a fully developed slug flow in pipes based on the observed flow dynamics and mechanism of the slug movement. The total pressure drop across a slug unit in a horizontal flow is the combination of the acceleration and frictional pressure drop. The acceleration pressure drop results from the acceleration of the slow moving liquid film to the slug velocity while the frictional pressure drop results from the wall shear stress. However, in the model development, the pressure drop of the gas phase flowing above the liquid film was neglected, only considering the slug body and the liquid film region.

Taitel and Barnea (1990) presented a pioneering comprehensive analysis for slug flow in pipes. The idea of the study was to extend the scope of the existing slug flow models and develop a unified model that accounts for horizontal, inclined upward and vertical upward slug flow. The observation of the slug flow mechanism suggested by the Dukler and Hubbard was adopted in the development of the model. However, some of the aspects of both models differ. For example, this

model recognised that the gas and the liquid phase in the slug body region may move at different velocities unlike the Dukler and Hubbard model that assumes a homogeneous no-slip flow in the slug body  $V_{Ls} = V_{Gs} = V_s$ . This gives the model a major advantage as it alleviates the error produced by assuming that both phases flow at the same velocity and calculating the fluid properties using the no-slip approach. Another great advantage of this model is that it can be applied to perform two-phase slug flow hydraulic calculations for a wider range of pipe inclination angles as most of the slug flow mechanistic models developed prior to this considered either only vertical upward, horizontal or inclined slug flow.

The translational velocity  $V_T$  coordinate system was used in the formulation of the model along with the basic assumption of steady state flow. In this coordinate system, the liquid and the gas phases can be expressed as flowing backwards at velocity of  $V_T - V_{Ls}$  and  $V_T - V_{Gs}$ , with respect to the coordinate system. This velocity is defined as the relative velocity and as the cross-sectional area of the liquid film behind the slug decreases, the relative velocity increases. Thus, it is possible to relate the velocities in the slug body region and the liquid film region to a given location in a fully developed slug unit. The significant advantage of using this coordinate system is that the flow variables become dependent on the local position in the pipe but independent of time. The mass flowrate  $W_L$  of the liquid in a slug unit can be obtained by integrating the liquid flow through a fixed pipe area over the time taken for the passage of a slug unit. The mass flowrate of the of the liquid phase can be expressed as

$$W_L = \left( V_{Ls} \rho_L A_P H_{Ls} t_s + \int_0^{T_f} V_{Lf} \rho_L A_P H_{Lf} dt \right) \frac{1}{t_u} \quad 2.142$$

The times taken for the entire slug unit  $t_u$ , slug body  $t_s$  and the liquid film region  $t_f$  to cross a given point in the pipe can be expressed in terms of the translational velocity as

$$t_u = \frac{L_u}{V_T} \quad t_s = \frac{L_s}{V_T} \quad t_f = \frac{L_f}{V_T} \quad 2.143$$

Substituting equation 2.143 and  $dt = dL/V_T$  into 2.142 and yields

$$W_L = V_{Ls} \rho_L A_P H_{Ls} \frac{L_s}{L_u} + \frac{1}{L_u} \int_0^{L_f} V_{Lf} \rho_L A_P H_{Lf} dL \quad 2.144$$

In order to determine the pressure drop, the hydrodynamics of the liquid film region would have to be carefully considered. A momentum balance of the phases in the liquid film region would be required to obtain profiles of the liquid film velocity and the liquid film holdup as there are a function of position and vary along the length of the slug in the pipe. The momentum equations for the liquid film and gas pocket is expressed in terms of the translational velocity coordinate system, respectively as

$$\rho_L v_f \frac{\partial v_f}{\partial L} = -\frac{\partial P}{\partial L} + \frac{\tau_{Lf} S_{Lf}}{A_{Lf}} - \frac{\tau_i S_i}{A_{Lf}} + \rho_L g \sin \theta_p - \rho_L g \cos \theta_p \frac{\partial h_{Lf}}{\partial L} \quad 2.145$$

and

$$\rho_G v_g \frac{\partial v_g}{\partial L} = -\frac{\partial P}{\partial L} + \frac{\tau_{Gf} S_{Gf}}{A_{Gf}} + \frac{\tau_i S_i}{A_{Gf}} + \rho_G g \sin \theta_p - \rho_G g \cos \theta_p \frac{\partial h_{Lf}}{\partial L} \quad 2.146$$

The relative velocities of the liquid and gas phase in the liquid film region is given as

$$v_f = V_T - V_{Lf} ; \quad v_g = V_T - V_{Gf} \quad 2.147$$

Applying a mass balance on a control volume bounded by a slug body with respect to the translational velocity coordinate system, the mass pickup/shedding rate can be obtained. In this coordinate system, the interface in liquid film region is assumed to be stationary and all the liquid flows backwards. The liquid film moves backwards at  $V_T - V_{Lf}$  and the liquid slug moves backward at  $V_T - V_{Ls}$ . The mass

flow rate backward is equivalent to the mass pickup/shedding rate  $x$ , which can be obtained by applying the liquid phase continuity equation to the control volume at the translational velocity coordinate system as

$$x = \rho_L A_P H_{Ls} (V_T - V_{Ls}) = \rho_L A_P H_{Lf} (V_T - V_{Lf}) \quad 2.148$$

The relative velocities of the liquid phase in the liquid film region,  $v_f$  can be determined from Equation 2.148 and in a similar approach, the relative velocity of the gas phase in the liquid film region,  $v_g$  can also be obtained.

$$v_f = (V_T - V_{Lf}) = \frac{(V_T - V_{Ls}) H_{Ls}}{H_{Lf}} \quad 2.149$$

$$v_g = (V_T - V_{Gf}) = \frac{(V_T - V_{Gs})(1 - H_{Ls})}{(1 - H_{Lf})} \quad 2.150$$

Combining Equations 2.145 through 2.150, rearranging and simplifying yields an ordinary differential equation for the liquid film height as a function of the local position in the liquid film region.

$$\frac{\partial h_{Lf}}{\partial L} = \frac{\frac{\tau_{Lf} S_{Lf}}{A_{Lf}} - \frac{\tau_{Gf} S_{Gf}}{A_{Gf}} - \tau_i S_i \left( \frac{1}{A_{Lf}} + \frac{1}{A_{Gf}} \right) + (\rho_L - \rho_G) g \sin \theta_p}{\rho_G v_g \frac{(V_T - V_{Gs})(1 - H_{Ls})}{(1 - H_{Lf})^2} \frac{\partial H_{Lf}}{\partial h_{Lf}} - \rho_L v_f \frac{(V_T - V_{Ls}) H_{Ls}}{H_{Lf}^2} \frac{\partial H_{Lf}}{\partial h_{Lf}} + (\rho_L - \rho_G) g \cos \theta_p} \quad 2.151$$

The differential Equation 2.151 can be solved numerically to obtain the liquid film profile,  $h_{Lf}(L)$  and the liquid film velocity profile,  $V_{Lf}(L)$ . The initial condition for the ODE is  $h_{Lf}(L=0) = h_s = H_{Ls} D$  corresponding to  $V_{Lf}(L=0) = V_T - V_{Ls}$ . The numerical integration is performed until the mass balance equation is satisfied,

yielding the length of the liquid film, the liquid film holdup and velocity just before the pickup point. (Shoham, 2005)

The change in the liquid film holdup with respect to the height of the liquid film can be determined from geometrical relationship as

$$\frac{\partial H_{Lf}}{\partial h_{Lf}} = \frac{4}{\pi D} \sqrt{1 - \left(2 \frac{h_{Lf}}{D} - 1\right)^2} \quad 2.152$$

The terms  $S_{Lf}$ ,  $S_{Gf}$ ,  $S_i$ ,  $A_{Lf}$ , and  $A_{Gf}$  can be determined from geometrical relationships as presented earlier in Equations 2.135 to 2.141.

The shear stresses in Equation 2.151 is expressed in terms of the actual velocity of the phases as

$$\tau_{Lf} = f_f \frac{\rho_L V_{Lf} |V_{Lf}|}{2} \quad 2.153$$

$$\tau_{Gf} = f_g \frac{\rho_G V_{Gf} |V_{Gf}|}{2} \quad 2.154$$

$$\tau_i = f_i \frac{\rho_G (V_{Gf} - V_{Lf}) |V_{Gf} - V_{Lf}|}{2} \quad 2.155$$

The friction factor between the liquid film and the pipe wall,  $f_f$  and the gas phase and the pipe wall,  $f_g$  can be obtained from the general Blasius correlation for smooth pipes,  $f = CRe^{-m}$  using the hydraulic diameter concept. The hydraulic diameter for the liquid film and the gas can is given as

$$d_{Lf} = \frac{4A_{Lf}}{S_{Lf}} \quad d_{Gg} = \frac{4A_{Gf}}{S_{Gf}} \quad 2.156$$

The following coefficients are utilised for the friction factor equation:  $C = 16$  and  $m = 1$  for laminar flow, and  $C = 0.046$  and  $m = 0.2$  for turbulent flow. For rough pipes, the following expression can be used to determine the friction factors of liquid or gas phases.

$$f = 0.001375 \left( 1 + \left[ 2 \times 10^4 \frac{\epsilon}{D} + \frac{10^6}{\text{Re}} \right]^{1/3} \right) \quad 2.157$$

The determination of the interfacial friction factor,  $f_i$  is more complex than that of the liquid or the gas phase friction factor. If the flow has a smooth interface, the interfacial friction factor is approximated as the gas phase friction factor i.e.  $f_i = f_g$ . If the flow exhibits a wavy interface, then a constant value of  $f_i = 0.014$  suggested for a stratified wavy flow can be used as the interfacial friction factor.

Due to the intermittent nature of slug flow in pipes, the local axial pressure drop is not constant and cannot be determined through a conventional approach. However, the axial pressure gradient of slug flow can be determined by obtaining the average pressure drop across a slug unit. Since the momentum fluxes in and out of the control volume of a slug flow is equivalent, the global pressure drop can be reduced to a force balance relationship as:

$$-\Delta P_u = \rho_u g \sin \theta_p L_u + \frac{\tau_s \pi D}{A_p} L_s + \int_0^{L_f} \frac{\tau_{Lf} S_{Lf} + \tau_{Gf} S_{Gf}}{A_p} dL \quad 2.158$$

Where

$$\rho_u = \rho_L H_{LA} + \rho_G (1 - H_{LA}) \quad 2.159$$

and the average liquid holdup of a slug unit  $H_{LA}$  is defined as

$$H_{LA} = \frac{V_T H_{Ls} - V_{Ls} H_{Ls} + V_{SL}}{V_T} \quad 2.160$$

From the Equation 2.158, it is evident that the pressure drop across a slug unit contains the gravitational pressure drop component and the frictional pressure drop component. The acceleration pressure drop component does not exist in its own form but has been accounted for the third term of the Equation 2.158.

Closure relationships are required in order to calculate the pressure drop across a slug unit. Some of the closure relationships as presented by (Shoham, 2005) are given in Table 2.7

Table 2.7: Closure relationships for mechanistic slug flow model for pipe flow

Parameter	Closure relationship
Translational velocity, $V_T$	$V_T = c_o V_M + 0.54 \sqrt{gD} \cos \theta_p + \sqrt{gD} \sin \theta_p,$
	$0^\circ \leq \theta_p \leq 90^\circ$
	For laminar flow $c_o = 2$ For turbulent flow $c_o = 1.2$
Gas bubble velocity in slug body $V_{Gs}$	$V_{Gs} = c_o V_M + 0.54 \left[ \frac{g\sigma(\rho_L - \rho_G)}{\rho_L^2} \right]^{0.25} H_{Ls}^2 \sin \theta_p$
	For laminar flow $c_o = 2$ For turbulent flow $c_o = 1.2$
	Horizontal flow: $H_{Ls} = \frac{1}{1 + \left( \frac{V_M}{8.66} \right)^{1.39}}$
Liquid holdup in the slug body $H_{Ls}$	Horizontal to upward inclined flow: $H_{Ls} = \exp[-(7.85 \times 10^{-3}\theta + 2.48 \times 10^{-6}Re_{Ls})]$
	$0^\circ \leq \theta_p \leq 90^\circ$
	$Re_{Ls} = \frac{\rho_L V_M D}{\mu_L}$
	Slug frequency, $u_s$
	$0^\circ \leq \theta_p \leq 11^\circ$
Slug length, $L_s$	$L_s = 30 D, \quad D \leq 2 \text{ in}$
	$\ln(L_s) = -25.4 + 28.5[\ln(D)]^{0.1}, \quad D > 2 \text{ in}$
	$D = \text{inches}, L_s \text{ in ft}$

### **2.3 Multiphase Gas – Liquid flow in annuli**

There are a lot of works regarding two-phase flow in pipes. However, their application to two-phase flow in annuli is limited due to the additional complexity of the flow dynamics generally encountered for flows in annuli geometries. Although some the early investigators had developed methods for predicting two-phase flow dynamics for annuli flows using the methods previously developed for two-phase flow in circular pipes by applying the hydraulic diameter concept, studies have shown that this approach often generates significant errors. For example, the error involved in predicting the friction factor in annuli pipes by applying the hydraulic diameter concept can vary between about 40 to 50 percent depending on the inner to outer pipe diameter ratio and the degree of eccentricity of the inner pipe (Caetano et al., 1992). These errors prompted the development of specific methods for the prediction of two-phase flow behaviour in annuli configurations by applying either some of the techniques developed for single phase flow in annuli, two-phase flow in circular pipes or a combination of both.

Sadatomi et al. (1982) studied the Taylor bubble rise velocity for two-phase flow in circular, rectangular, triangular and concentric annuli configurations. They reported that the Taylor bubble's shape differs from that of a circular-cap and varies in the range of an elliptical-cap to a parabolic-cap. The new shapes found were reported to provide faster bubble rising velocities when compared to flow without insertions which is a function of the particular flow geometry. In this study, flow pattern maps were developed for air-water vertical flows through the various circular and noncircular configurations considered by detecting the transition criteria between the different flow patterns. They concluded from the analysis of their experimental results that the flow geometry had little to no influence on the flow pattern transitions. However, they did not provide information on the factors that affects the flow pattern transitions.

Kelessidis and Dukler (1988) investigated the flow patterns in a vertical upward gas-liquid flow in a concentric and 50% eccentric annulus in order to examine the factors that influences the flow pattern transitions and propose methods to predict the flow pattern transition zones. The test section consisted of two acrylic pipes

which are eclectically non conducting. The outer diameter of the inner tube, and the inner diameter of the outer tube was 0.0508m and 0.0762m respectively. The flow pattern identification was achieved by mounting conductivity probes on the inner and outer pipe walls of the annular configuration.

The flow patterns observed in this study were the bubble flow, slug flow, churn flow and annular flow.

The flow pattern classification was accomplished by applying a probability density function (PDF) to the voltage-time traces obtained from the conductance probes. The voltage scale of the voltage-time trace signal  $V(t)$ , is divided into equal increments of width  $w$  and the time scale into equal increments of width  $\Delta T$  (Figure 2.7). During the observation period, if the voltage is seen within the range  $(v - w/2, v + w/2)$  for a total of  $n_i$  times, then, for a stationary time series, the PDF,  $p(v)$ , can be defined as

$$P(v) = \lim_{w \rightarrow 0} \frac{P[v, w]}{w} = \lim_{w \rightarrow 0} \frac{1}{w} \left( \lim_{T \rightarrow \infty} \frac{T_x}{T} \right) \quad 2.161$$

$P[v, w]$  is the probability distribution function and  $T_x = n_i \Delta T$ .

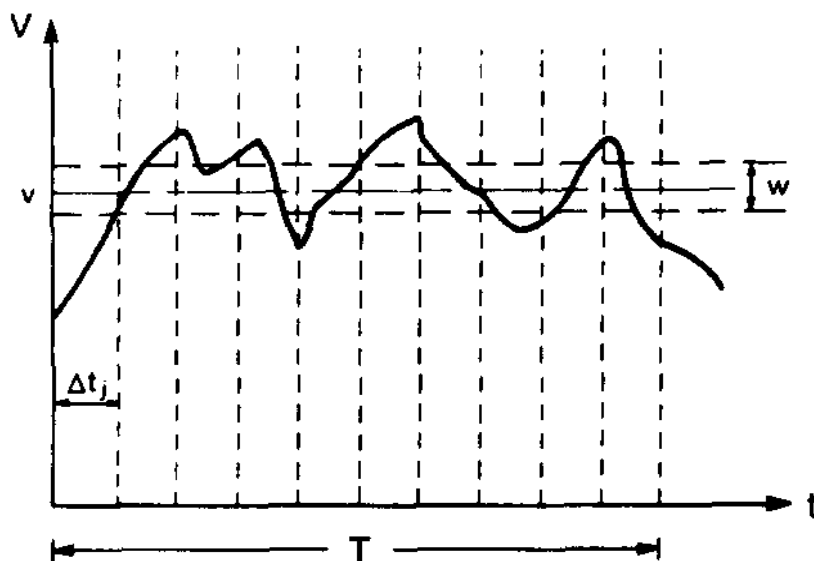


Figure 2.7: Voltage-time trace illustrating the estimation of the PDF (Kelessidis & Dukler, 1988)

PDF plots are generated from the signals obtained by the conductivity probes for the different flow patterns and flow pattern transitions. The PDF values are plotted against the normalized voltage values  $V/V_{\max}$ , where  $V_{\max}$  represents the maximum value of the voltage.

For the Bubble flow pattern, the PDF plot will show a distribution with a single peak near the maximum voltage as the conductivity probe will be exposed majorly to liquid the liquid phase and little of the gas phase. Hence, the  $\int P dv = 1$  for  $V/V_{\max} > 0.75$  (Figure 2.8). Two well-defined peaks exist in the PDF plot for the slug pattern. One of the peaks exists in the range of  $0.75 \leq V/V_{\max} \leq 1.0$  and the other has a maximum at zero with a range of  $V/V_{\max} \leq 0.25$ . For a fully developed slug flow it was suggested that the Taylor bubble must occupy at least 20% of the entire length of the column and the peak at the low voltage must have an integral  $> 0.2$ .

The churn flow pattern PDF displays a single peak at the low voltage region with its maximum voltage at zero position (Figure 2.9). The peak exists in the range  $0.75 \leq V/V_{\max} \leq 1.0$ . for the annular flow pattern, a single peak is observed at the zero-voltage position since the output of the conductivity probe is zero.

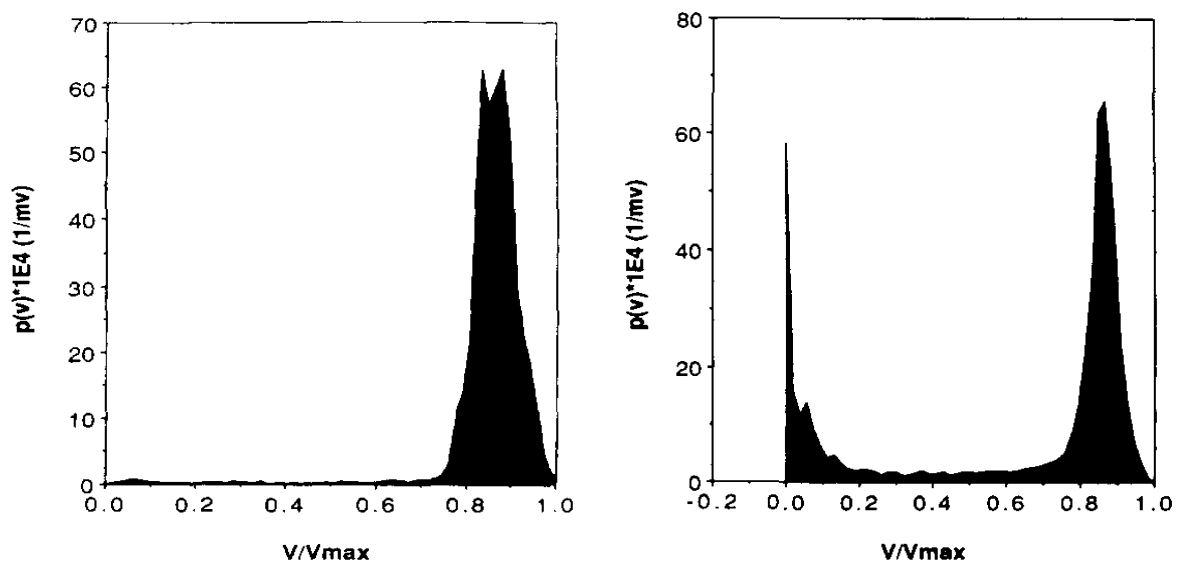


Figure 2.8: Example of PDF plots for the bubble (left) and slug flow pattern (right) (Kelessidis & Dukler, 1988).

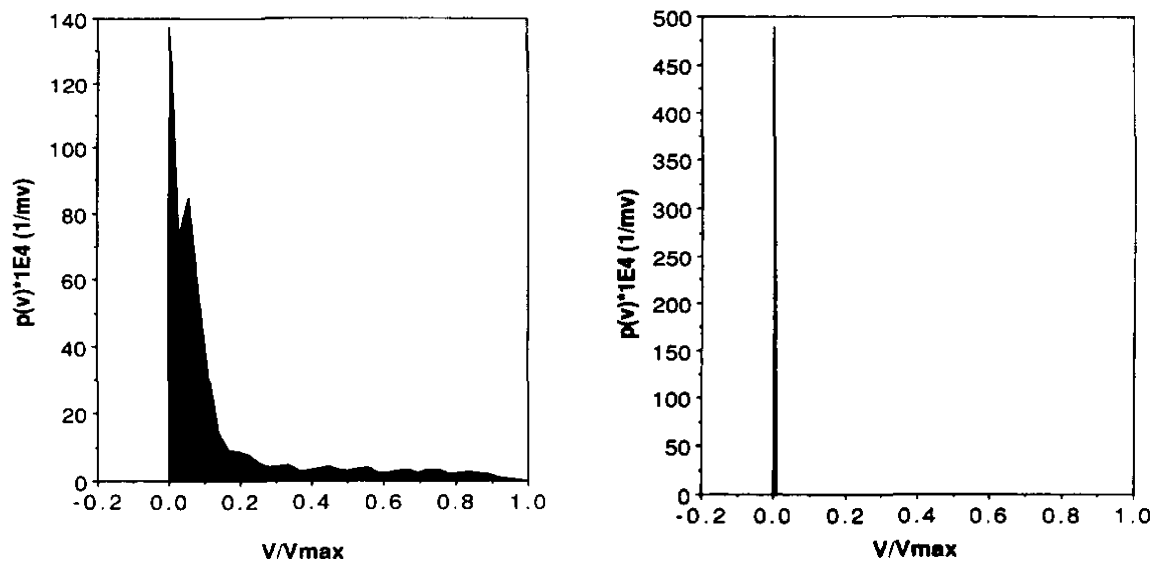


Figure 2.9: Example of PDF plots for the churn (left) and annular flow pattern (right) (Kelessidis & Dukler, 1988)

The transition between the investigated flow patterns were characterized in a similar approach based on the signal voltage peak values, the position of the peaks and the integral value of the PDF function. Mathematical models for flow pattern prediction were developed with an approach dependent on the study presented by Barnea et al, (1980) were they investigated how the void fractions and liquid and gas flowrates influence the transition criteria between the various flow patterns. Although only the 50% eccentricity was considered in this study, it was concluded from the analysis of the experimental data that the degree of eccentricity has little effect on the flow pattern transitions.

Caetano et al. (1992) experimentally and theoretically studied the upward gas-liquid flow through a concentric and fully eccentric annulus. The experimental setup consisted of a 16-m long vertical annulus with a 76.2-mm ID outer tube and a 42.2-mm OD inner tube. A comprehensive experimental data was obtained from the setup using air-water and air-kerosene mixtures over a wide range of flow conditions. A classification of the different flow patterns encountered for vertical flows in a concentric and eccentric annulus was performed along with the development of flow pattern maps based on the input superficial gas and liquid

velocities. Measurements of volumetric average liquid holdup and average total pressure gradient were obtained for each the different fluid mixtures and flow patterns for a wide range of flow conditions. Mechanistic models were developed for each of the existing two-phase annuli flow patterns to calculate important parameters like the average in-situ liquid holdup and pressure gradient of the flow. The development of the models was based on the physical phenomena of two-phase flow incorporated with annulus characteristics such as the casing and tubing sizes and eccentricity. In this study, it was shown from data analysis that the application of the hydraulic diameter concept for annuli configurations can be inaccurate especially when the flow has a low Reynolds number. It is common practice to predict friction factor for flow in noncircular conduits by applying the hydraulic diameter concept. However, this procedure should be limited to high Reynolds numbers, since unacceptable errors may occur for lower degrees of turbulence. This prompted the development of a more rigorous approach to calculate the friction factor and accurately predict the frictional pressure gradient in annuli under low or moderate degrees of turbulence.

Assuming that all annuli configurations have the same hydraulic diameter and Reynolds number, comparison of the friction factor behaviour in annuli can be made in terms of the pipe diameter ratio and the friction geometry parameter.

The fanning friction factor for laminar flow through a circular pipe is given by

$$f_p = \frac{F_p}{Re} = \frac{16}{Re} \quad 2.162$$

Where  $F_p$  represents the friction geometry parameter which has a constant value of 16 for pipe flow.

The friction factor for laminar flow of Newtonian fluids in a concentric annulus developed by Bird et al. (1976) was used to express the friction factor in terms of the friction geometry parameter and the annulus pipe diameter ratio as

$$f_{CA} = \frac{F_{CA}}{Re} = \frac{16}{Re} \frac{(1-K)^2}{\left[ \frac{1-K^4}{1-K^2} - \frac{1-K^2}{\ln(1/K)} \right]} \quad 2.163$$

The friction geometry parameter for a concentric annulus,  $F_{CA}$  can then be expressed as a function of the pipe diameter ratio,  $K_a = D_1/D_2$  as

$$F_{CA} = F_{CA}(K_a) = \frac{16(1-K_a)^2}{\left[ \frac{1-K_a^4}{1-K_a^2} - \frac{1-K_a^2}{\ln(1/K_a)} \right]} \quad 2.164$$

The equations to calculate the friction factor for a Newtonian laminar flow through an eccentric annulus,  $f_{EA}$  are present as follows:

$$f_{EA} = \frac{F_{EA}}{Re} = \frac{1}{Re} \frac{4(1-K_a)^2(1-K_a^2)}{\emptyset \sinh^4 \eta_o} \quad 2.165$$

The friction geometry parameter for an eccentric annulus expressed as a function of the pipe diameter ratio,  $K_a$  and the eccentricity,  $e$  is given as

$$F_{EA} = F_{EA}(K_a, e) = \frac{4(1-K_a)^2(1-K_a^2)}{\emptyset \sinh^4 \eta_o} \quad 2.166$$

$$\cosh \eta_i = \frac{K_a(1+e^2) + (1-e^2)}{2K_a e} \quad 2.167$$

$$\cosh \eta_o = \frac{K_a(1-e^2) + (1+e^2)}{2e} \quad 2.168$$

$$\emptyset = (\coth \eta_i - \coth \eta_o)^2 \left[ \frac{1}{\eta_o - \eta_i} - 2 \sum_{m=1}^{\infty} \frac{2m}{\exp(2m\eta_i) - \exp(2m\eta_o)} \right] + \frac{1}{4} \left( \frac{1}{\sinh^4 \eta_o} - \frac{1}{\sinh^4 \eta_i} \right) \quad 2.169$$

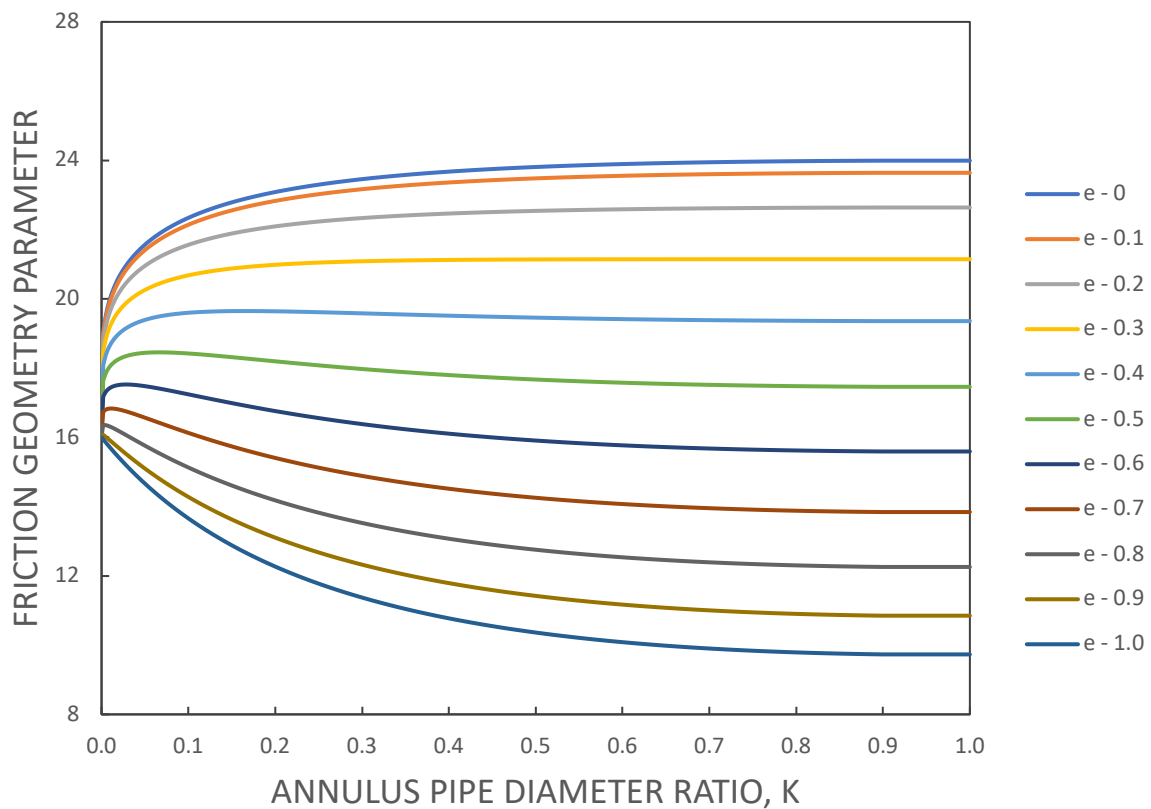


Figure 2.10: Friction geometry parameter for laminar flow in annuli and circular pipes

Figure 2.10 shows graphically the influence of the pipe diameter ratio and the eccentricity on the friction geometry parameter. The friction geometry parameter is a function of the pipe diameter ratio for a concentric annulus, a function of both the pipe diameter ratio and eccentricity for an eccentric annulus and is constant for a pipe flow. If the pipe diameter ratio is held constant, the friction geometry parameter decreases with an increase in eccentricity and as a result leads to a decrease in the friction factor and consequently a decrease in the frictional pressure gradient. The friction geometry parameter and the consequent friction factor for a pipe flow is always higher than of the annuli with high degrees of eccentricity. This again shows why it is highly probable to obtain inaccurate results when the application of the hydraulic diameter is used to predict the friction factor for annuli flow using standard or conventional single-phase pipe flow methods.

Friction factors for turbulent flows through a concentric and eccentric annulus was developed using a semi-empirical approach and compared to experimental data. The friction pressure drop was measured for single-phase turbulent water flow in concentric and fully eccentric annuli, and Fanning friction factors were calculated for each test using the developed friction factor equations. The friction factor equations for turbulent flow in a concentric and eccentric annulus is given respectively as:

$$\left\{ f_{CA} \left( \frac{F_P}{F_{CA}} \right)^{0.45 \exp[-(Re-3000)/10^6]} \right\}^{-1/2} \quad 2.170$$

$$= 4 \log \left\{ Re \left( f_{CA} \left( \frac{F_P}{F_{CA}} \right)^{0.45 \exp[-(Re-3000)/10^6]} \right)^{-1/2} \right\} - 0.40$$

$$\left\{ f_{EA} \left( \frac{F_P}{F_{EA}} \right)^{0.45 \exp[-(Re-3000)/10^6]} \right\}^{-1/2} \quad 2.171$$

$$= 4 \log \left\{ Re \left( f_{EA} \left( \frac{F_P}{F_{EA}} \right)^{0.45 \exp[-(Re-3000)/10^6]} \right)^{-1/2} \right\} - 0.40$$

The study showed that for the same hydraulic diameter, there is a significant difference between the annuli friction factor values when compared to that of a circular pipe. In turbulent flow in annuli, the difference between the measured and the predicted friction factor values decreases with an increase in the Reynolds number of the flow. Usually the friction factor for a concentric annulus is higher than for pipe flow; however, for a fully eccentric annulus the friction factor is lower than for pipe flow. This difference is greatly dependent on the annulus pipe diameter ratio and the degree of eccentricity.

Sunthakar et al. (2000) performed extensive experiments using a horizontal field-scale low-pressure flow loop (8" X 4.5", 90' long) to simulate the annuli flow of non-Newtonian fluids with or without drillpipe rotation. The liquids used were water and aqueous polymer solution (CMC+XCD+water), at flow rates in the range 75-360 gpm and air in the range 10-1000 scfm. The study involved the measurements of the pressure drop and average liquid holdup along the entire annular section, including the identification of the flow pattern by visual observation and the investigation of the effect of the gas-liquid input flowrates, fluid viscosity and drillpipe rotation on average liquid holdup and pressure drop. However, the drillpipe rotary speed considered in these experiments was 100 rpm. It was noted that the intermittent flow pattern was observed for a wide range of the tests carried out prompting the need to modify the available flow pattern transition criteria for two-phase annuli flows. For the flow of air-aqueous polymer solution fluids it was observed that the flow pattern appeared to be similar to that of the air-water fluids with or without the drillpipe rotation. Flow pattern maps developed by visual observations were compared to their model for flow pattern prediction which was developed by modifying the Taitel and Dukler (1976) based on the hydraulic diameter concept.

In this study, it was concluded that the frictional pressure drop for air-water annuli flow increased with the drillpipe rotation due to a turbulence effect caused by the rotating drillpipe while for the air-aqueous polymer solution flow, the effect of the drillpipe rotation was dependent on both the turbulent effect of the drillpipe and the shear-thinning effect of the fluid. Thus, the frictional pressure drop was found to either increase or decrease depending on the gas-liquid flow rates, the rheology of the fluid and the rotary speed of the drillpipe.

Lage and Time (2002) formulated a steady-state mechanistic model to predict the mixture behaviour for vertical two-phase flow in a concentric annulus. An experimental program was launched to obtain a wide variety of data by pumping air and water to form the two-phase mixture that simulated the gas injection through the drill string during underbalanced drilling operations. The flow pattern transition criteria were developed based on the underlying physics governing two-

phase flow mixture as presented by Taitel et al. 1980. Pressure gradient calculation models for slug and annular flow were developed by considering the mass balance between each of the phases and the friction factor model used was that suggested by Caetano et al. (1992). The proposed model was compared to measurements obtained from the experimental study, showing good agreement and was reported to have a better performance when evaluated by comparing its performance to the mechanistic model developed by Caetano et al. (1992) and the empirical model developed by Beggs and Brill (1973). Although the objective of this study was to develop a model to predict the behaviour of two-phase flow through an annulus during underbalanced drilling operations UBD, the application of the model to the drilling scenario is questionable as both the experimental and mathematical modelling were based on Newtonian air-water mixtures while the drilling fluid is practically a non-Newtonian fluid. For example, the friction factor used in the model was developed fundamentally for annuli Newtonian flows and cannot be applied directly to model the flow of non-Newtonian drilling fluid through the annuli.

Omurlu and Ozbayoglu (2007) conducted an experimental and theoretical study for two-phase modeling of liquid-air flow through horizontal fully eccentric annuli. The test section was 16ft long and made of acrylic casings and a steel drillpipe. Two pairs of annular geometrical configurations were used to simulate the flow of air and water mixtures and visually identify the prevailing flow pattern. They introduced the use of a representative diameter in order to characterize the fully eccentric annulus and reported that the use of this parameter was more accurate in predicting the flow pattern and pressure gradient when compared to the experimental data. The models presented for the calculation of the pressure gradients for the different flow patterns did not take into account the geometry of the annulus and once again are developed from methods designed for Newtonian flow through pipes.

Although a large number of experimental and theoretical work has been done on multiphase flow in annuli, most of the empirical or mechanistic models that has been presented for annuli flows have been developed by modifying the models that were initially developed for Newtonian two-phase flows in pipe. It has been

shown that the rheological behavior of non-Newtonian fluids differs to that of the Newtonian fluids. Thus, the application of the conventional methods developed for Newtonian fluids in predicting the behaviour of drilling fluid flow in annuli would definitely be inadequate and lead to inaccurate results as the drilling fluids exhibit a non-Newtonian behaviour. For drilling applications, there are a number of parameters that influence the behaviour of the fluid flow dynamics and would need to be taken into account when modeling the flow of non-Newtonian annuli drilling fluid flow.

Ettehadi and Ozbayoglu (2013) conducted an experimental study to investigate the effect of the changes in the gas and liquid rates, penetration rate, and drillpipe rotation speed on multiphase flow through horizontal and inclined annuli. The fluids used for the simulation of the drilling fluids were water to represent the liquid phase and air to represent the gaseous phase. It was observed that for a constant gas-liquid flowrate, the drillpipe rotation led to an increase in the total pressure gradient of the flow and for an inclined annulus, the pressure gradient is not affected when the drillpipe rotary speeds is higher than 80 rpm. It was also observed that for gas superficial velocity more than 20 ft/sec, the effect of drillpipe rotation speed is negligible due to high turbulence effects. They reported that for a horizontal eccentric annuli flow, increasing the gas velocity in the wellbore, lead to a relatively smaller change in the total pressure loss change when compared to the pressure gradient changes for the inclined configurations. This is because the frictional pressure gradient component is only effective term contributing to the total pressure gradient in the horizontal configuration whereas in the other configurations the frictional and gravitational components contribute to the total pressure gradient.

Nossen, et al. (2017) carried out a project involving experimental and numerical studies of the fundamental physics governing multiphase annuli flows. Their drive was to develop a method that could be applied to acquire reliable data and shed light on the physical understanding that can be used as a basis for developing reliable commercial models for prediction of the behaviour of multiphase flows in

annuli. The well flow loop constructed in this study was equipped with various instrumentation for measurement of flow details including gamma densitometers and X-ray computer tomography. Velocity profile measurements were obtained using LDA (Laser Doppler Anemometry). With this experimental setup, they were able to obtain measurements for the flow patterns, liquid holdup, phase distributions and annuli velocity profiles. The analysis of the data obtained from this study showed that the behavior of multiphase flow in pipes was different that of the annuli flow and concluded that this method of data acquisition can be beneficial in developing robust mechanistic models and limit the number of assumptions made due to the difficulty of obtaining detailed experimental data.

Ibarra et al. (2019) conducted a recent study to investigate two-phase flow through a concentric and fully eccentric annulus. The flow of gas-water and gas-oil were studied using high speed photography, differential pressure transducers, and a broad-beam gamma densitometer to characterize the flow the properties of the liquid phase, the inner pipe eccentricity and the inclination angle of the annulus. The first part of this study involved the identification of the flow patterns and the measurement of the average liquid holdup, the slip ratio and pressure gradient in the respective annular configurations. Flow pattern identification and mapping were achieved by collecting data with the help of visual observations from high-speed cameras and probability density function of the average liquid holdup obtained from the gamma densitometer. It was reported that the structure of the flow in the eccentric annulus was more stable than that of the concentric annuli and the observed trend can be attributed to the difference in velocity distribution of the flow between the concentric and eccentric annulus. The experimental data also showed that for the same flow conditions, the pressure gradient in the concentric annulus is higher than that of the eccentric annulus. The second part of this study involved the development of flow pattern transition algorithms and a mechanistic model to determine the pressure gradient for slug flow. The friction factor model for single-phase annular flows presented by Caetano et al. (1992) was modified to give a better performance for a wider range of the annulus pipe diameter ratio.

The friction factor for the concentric and eccentric can be expressed respectively as

$$f_{CA} = f_P F_{CA}^C \quad 2.172$$

$$f_{EA} = f_P F_{EA}^C \quad 2.173$$

The friction factor for laminar Newtonian flow in pipes is give as  $f_P = 16/Re$ , while the Zigrang and Sylvester (1982) friction factor correlation was suggested to be applied for Newtonian turbulent flow in pipes.

$$\frac{1}{\sqrt{f_P}} = -4 \log \left\{ \frac{2 \varepsilon/D_h}{3.7} - \frac{5.02}{Re} \log \left[ \frac{2 \varepsilon/D_h}{3.7} - \frac{5.02}{Re} \log \left( \frac{2 \varepsilon/D_h}{3.7} + \frac{13}{Re} \right) \right] \right\} \quad 2.174$$

Where the parameter  $\varepsilon$  represents the roughness of the pipe.

The friction geometry parameter for the concentric annuli was modified by introducing a correction factor  $K_o$

$$F_{CA} = K_o \frac{16(1 - K_a)^2}{\left[ \frac{1 - K_a^4}{1 - K_a^2} - \frac{1 - K_a^2}{\ln(1/K_a)} \right]} \quad 2.175$$

$$K_1 = 1 - |0.56 - K_a| \quad 2.176$$

$$K_o = \max(0.68, K_1) \quad 2.177$$

The parameter  $c = 1$  for laminar flow while for turbulent flow, the parameter is given by

$$c = 0.45 \exp[-(Re - 3000)/10^6] \quad 2.178$$

The prediction of the models was compared to the experimental data and was reported to show good agreement for both the concentric and the fully eccentric annulus. However, for the horizontal gas-liquid flow in the concentric annulus, the model was found to under predict the pressure gradient by an absolute average relative error of about 23%.

#### **2.4 Cuttings transport in drilling annuli**

One of the primary functions of the drilling fluid is efficient transportation of the drilled cuttings from the wellbore to the surface. This transport process is usually called the drilled cuttings transport and the ability of the drilling fluid to lift the drilled cuttings out of the wellbore is referred to as the carrying capacity of the drilling fluid. A poor hole cleaning process can lead to wellbore instability issues and may also lead to stuck pipe or an increased drag and torque on the drillstring which may possibly result in a twist-off pipe, incurring cost and an unwanted non-productive time. Understanding the cutting transport process itself relies on exercising the knowledge from three key areas namely, the flow characteristics of the drilling fluid flow through the annuli, the settling characteristics of the drilled cuttings, and the mechanism at which the drilled cuttings are being transported (Luo, 1988). Experimental and field reports have indicated that the effective hole cleaning process during drilling activities is a function of some important parameters that can be managed appropriately to optimise the overall drilling process. These parameters are the fluid flowrate, the fluid rheological and physical properties, and the cutting sizes. However, over the years, it has been reported that the wellbore geometry also have a strong influence on the hole cleaning efficiency so the main issue has been the development of a reliable method that adjusts the fluid properties and fluid circulation rates to suit the fixed design parameters such as wellbore inclination angle, drillpipe rotary speed, pipe eccentricity, etc, in order to have an optimum hole cleaning process.

Empirical and mechanistic cutting transport models have been published by various researchers in an attempt to provide solutions for the prediction of the cutting transport dynamics by taking into account the important parameters that influence the movement of cuttings in the wellbore annuli. Some of these models were developed with an idea of determining the minimum liquid flowrate that would be required prevent the cuttings from settling and forming a stationary bed at the bottom section of the annuli while some of the were developed with an idea of predicting the cuttings velocity from the simultaneous solution of the governing fluid-cuttings transport momentum equations.

Peden et al. (1990) were one of the early investigators that performed experiments in order to investigate the influence of drillpipe rotation and eccentricity (+50% and -50%) on the cutting transport process during drilling. A concept known as the minimum transport velocity MTV was adopted to characterise the cuttings transport efficiency, assuming that there is a critical annuli velocity above which the drilled cuttings is transported in suspension or rolling at the bottom of the wellbore annuli. Thus, the operational flow rate, used in the drilling hydraulics programme, should be able to generate an annular velocity that is at least equal to the minimum transport velocity and the lower the MTV required, the easier it is to achieve an effective hole cleaning operation. In an attempt to shed light on the factors responsible for the initiation of cutting movement in a wellbore annulus, they analysed the forces that act on a cutting lying at the bottom of a deviated wellbore annulus being transported in a drilling fluid. These forces are the lift forces, the drag forces, the frictional forces and the gravitational forces. The lift force is the force that tends to lift the cuttings into suspension in the annuli and is presumed to be generated due to two main reasons. The first reason is due to the asymmetric distribution fluid velocity around the cutting that creates an asymmetric pressure distribution around the cutting where a higher pressure exists on the lower surface than on the upper surface of the cutting. This creates a net upward force on the cuttings. The second reason is due to the instantaneous turbulent velocity fluctuations generated as a result of the turbulent flow regime.

It was deduced that the cuttings would be transported in by rolling/sliding at the low side of the wellbore annuli wall for conditions where the drag force acting on the particle in the direction of the flow is equal to or greater than the gravitational

force and the cuttings would be transported in the suspension regime, the lift force has to be greater than the gravitational force component perpendicular to the wellbore axis. The predictions obtained by minimum transport velocity (MTV) models were compared to their experimental results showing significant agreement for cuttings suspension. The minimum transport velocity models were previously developed by Luo (1988) where dimensional analysis was applied to the important parameters that influence the effective movement of cuttings in a wellbore annulus. Luo (1988) did not validate the models but recommended that the models should be validated with the results obtained from an experimental study.

Peden et al. (1990) presented several conclusions on how certain parameters influence the hole cleaning process. For the wellbore inclination angle, they concluded that this angle has a significant effect on hole cleaning and this effect was dependent on the mechanism of the cuttings transport considered. The worst scenario for hole cleaning was seen between 40° and 60° inclination angle for both cuttings rolling and suspension transport mechanisms. However, the specific angle where the worst hole cleaning is obtained appears to be dependent on a wide range of other parameters some of which are the fluid rheology properties, well geometry, cuttings sizes and drillpipe rotary speed. Pipe rotation reduces the minimum transport velocity for the cases of +50% eccentricity and no significant effect of drillpipe rotation was noticed for the cases of -50% eccentricity. The MTV required for smaller concentric annuli are lower than that required for the larger concentric annuli and for large annuli, pipe rotation has no significant effect on hole cleaning while the opposite effect occurs for smaller annuli types. An interesting conclusion drawn from this study was that the degree of turbulence of the flow strongly influences the hole cleaning efficiency leading to situations whereby water may require a lower MTV than a viscous fluid. However, even though this turbulence effect was highlighted, it was not considered in the model that was used to validate their experimental study or develop their computer model.

Clark and Bickham (1994) developed mechanistic models that could be applied to perform cuttings transport analysis throughout a drilling wellbore. When the

velocity of the drilling mud in the annuli is high enough, the drill cuttings are transported upward. This annular mud flowrate only needs to exceed the cuttings bed build-up conditions in the most sensitive areas the in the entire wellbore and as the annular mud velocity is continuously decreased, a point is reached where some cuttings are lost from the flow. They called this velocity the critical velocity required to effective clean the wellbore. From experimental flow loop tests, they identified the three significant patterns that describe the mechanisms for cuttings transport: the rolling, lifting and stationary bed pattern. They reported the prevailing cutting transport mechanism is highly dependent on the wellbore inclination angle. At high angles, the cutting transport mechanism is mainly the rolling pattern. At lower wellbore angles where the wellbore's complementary angle is greater than the cutting's angle of repose, cuttings are lifted from a churning fluidized bed. Whereas at near-vertical to vertical wellbore angles, the cuttings are uniformly distributed in the annuli and tend to settle downhole against the flowing mud. At high wellbore angles, a stationary cuttings bed is formed and accumulates in the lower part of the wellbore annuli when the wellbore's complementary angle is less than the cutting's angle of repose. However, if the wellbore complementary angle, is less than the angle of repose, the cuttings are either rolled or lifted from the bed surface. It was then inferred that the flowrate required to remove a stationary cuttings bed can be predicted if the dynamic forces acting on the bed can be calculated as a function of local fluid velocity in the annuli. It was assumed that the static forces acting on the cuttings are the buoyancy force, gravity force, and the plastic force due to the yield stress of the mud, while the dynamic forces acting on the cuttings are the lift force, drag force, and a pressure gradient force. These forces are assumed to act through the centre of gravity of the cuttings and the rheology of the drilling fluid is assumed to be governed by the Herschel-Bulkley rheological model. From a force balance analysis, the two equations were developed for the prediction of the critical velocity required to transport the cuttings via a lifting or rolling mechanism in the wellbore annuli. The model was compared to experimental and field data and was reported to produce favourable agreements. They concluded that these models can be used to reliably predict the cutting transport efficiency in a drilling wellbore as a function of the major drilling operating parameters. However, they admitted that the effect of the drillpipe eccentricity and the drillpipe rotation were not taken into consideration in the development and validation of these models even though

these parameters have been reported by earlier researchers to have a significant influence on the cutting transport efficiency.

A computational/numerical approach is another method that has been used for the prediction and modelling of cuttings transport in the drilling annuli. The drilled cuttings transport is modelled as a two-phase flow process. A dispersed cutting phase is assumed to be flowing simultaneously in a continuous liquid phase for a single-phase drilling fluid or in a continuous multiphase drilling fluid. For instance, in underbalanced drilling operations, the reservoir fluids (gas, oil or/and water) that flow into the wellbore due to the underbalance condition of the system are assumed to be combined with the drilling fluid as the continuous phase with uniform and homogeneous transport properties (Masuda, et al., 2000). The drilled cuttings are assumed to be under the influence of several forces that influences the annuli cuttings distribution, including the drag force, the lift force and the gravitational force. This modelling technique is commonly referred to as a two-layered or three-layered modelling approach, depending on the number of distinctive layers assumed to exist in the annuli flow. In the two-layered modelling approach, the flow is considered to be consisted of two-layers, where the upper layer consists of drilling fluid with a certain concentration of suspended cuttings and the lower layer is made of a stationary or moving cuttings bed (Li et al., 2007). In the three-layered modelling approach, the flow is considered to be consisted of three-layers in the annuli. The bottom layer is assumed to be a stationary cuttings bed, the middle layer is assumed to be a moving bed region while the upper layer is considered to be the cuttings suspension region. The distribution of the cuttings in the annuli varies with time and location. Thus, the multi-layered dynamic models can offer a theoretical basis for hole cleaning and drilling hydraulics modelling. This is usually based on the assumption that the cuttings and drilling fluids are incompressible and there is slippage between the cuttings and fluids in the suspension layer of the flow.

The multi-layered dynamic models are generally formulated with the idea that the behaviour of the drilling fluid and cuttings in the suspension layer are governed by their separate mass and momentum balance equations and each of the phases flow at separate velocities, which is believed to be the reason for the slippage between the drilling fluid phase and cuttings phase.

For the two-layered model, the general form of the transient conservation equations is derived by relating the mass accumulation in a differential volume of element to the net rate of mass inflow across the bounding interface.

The mass and momentum balance partial differential equations can be solved numerically to obtain the unknown variables, including the area of the cuttings bed, deposit bed velocity, cuttings concentration in the suspension layer, drilling fluid velocity and cuttings velocity in the suspension layer, and the annuli pressure gradient. However, a number of empirical correlations are required to describe the interphase interactions, cutting interactions (due to particle-particle collisions), and interactions between each of the distinctive layers and the physical boundary of the annuli. These empirical correlations are mainly derived from experimental investigation of the dynamics of particle-particle interactions and particle-fluid interactions during particle-fluid simultaneous flow in a conduit.

The empirical, numerical CFD and experimental methodology have been applied by various investigators to develop methods can be applied to predict the cutting transport behaviour and efficiency of hole cleaning during drilling activities. Although the actual method used by these researchers have differed in a lot of aspects, the effect of the major drilling parameters on the efficiency of hole cleaning published has shown similar trends. The key parameters that have been concluded to be the most dominant or controlling factor for the behaviour of cuttings in the drilling annuli. Literature has stated that these major parameters are the flowrate, annuli size, wellbore geometry, cutting size, drilling fluid viscosity, rate of penetration ROP, wellbore inclination angle, drillpipe rotation and the cutting and drilling fluid densities. The sensitivity of each of these parameters or a combination of a number of these parameters on hole cleaning have been studied by various researchers (Table 2.7) leading to the development of predictive models or guidelines to ensure an effective hole cleaning operation during drilling activities.

Gao and Young (1995) performed an analysis of field generated data along with a theoretical analysis for hole cleaning efficiency with an aim to develop a series of guidelines that can be applied to achieve an effective hole cleaning operation based on the sensitivity of some of the parameters that govern hole cleaning.

The major conclusions of the effect of the drilling parameters on the effectiveness of the hole cleaning aspect of a drilling operation obtained from literature has been summarised in this study. This summary has been arrived at by taking the similarities of the effect of each of the major drilling parameters as discovered and published by previous researchers or from field acquired data, from the past to this present time (Table 2.7). The effect of the major drilling parameters on hole cleaning are as follows:

#### Drilling fluid circulation rates:

The drilling fluid flowrate is the most important parameter that highly impacts the hole cleaning efficiency during drilling operations. There are two distinctly different mechanisms of cuttings transport that have been identified. The first is whereby the cuttings are transported by rolling or sliding along the low side wall of the annuli and the second is where the cuttings are transported by suspension in the flowing annuli drilling fluid. These two mechanisms have led to the definition of a minimum transport velocity MTV or critical velocity that is required to transport the cuttings via rolling or sliding at the bottom of the annuli and a minimum transport velocity MTV or critical velocity required to suspend the cuttings in the annuli. The flowrate of the drilling fluid must be high enough to generate an annuli velocity that exceeds at least the MTV or critical velocity for rolling in order to ensure an adequate hole cleaning operation. It is suggested that in order to prevent the formation of a stationary cuttings bed, a high flowrate as possible, that guarantees the MTV required for cutting suspension should be aimed for towards the optimisation of the hole cleaning efficiency.

#### Fluid rheology and flow regime:

The effect of the fluid rheology on the cutting transport is dependent on the drilling fluid flow regime. Increasing the drilling fluid viscosity can improve the cutting transport efficiency in the laminar flow regime. However, for the turbulent flow regime, reducing the viscosity may be favourable for cutting transport especially

in a deviated wellbore. The turbulent flow regime provides a better hole cleaning when the viscosity of the drilling fluid is relatively low and if the fluid viscosity is increased above a certain threshold, the laminar flow regime would be a lot more effective. Once a stationary cuttings bed is formed on the low side of the wellbore annuli, the MTV for cuttings suspension must be achieved if the drilling fluid has a high viscosity as it is difficult to remove the cuttings using a highly viscous fluid. However, with a low viscosity drilling fluid, the removal of the cuttings bed is far more efficient and strongly recommended.

Effect of wellbore inclination angle:

The effect of the wellbore inclination angle on hole cleaning efficiency is dependent on the prevailing cutting transport mechanism. The minimum transport velocity MTV required to suspend the cuttings in the annuli increases with an increase in the wellbore inclination angle. The minimum transport velocity MTV required to transport the cuttings in the rolling mechanism increases with an increase in the wellbore angle from the vertical until about a range of 40° to 60°. Thereafter, any further increase in the wellbore angle leads to a decrease in the minimum transport velocity MTV required to clean the hole.

Rate of penetration (ROP):

Drilling with a high ROP increases the concentration of the cuttings generated in the annuli which as a result reduces the ability of the drilling fluid to have an effective transport. An instantaneously high ROP should be avoided when drilling. It is favourable to minimise the ROP in order to improve the hole cleaning efficiency especially when drilling extended reach wells. The higher the rate of penetration, the higher the minimum transport velocity required to transport the cuttings out of the wellbore.

Drillpipe rotation:

The effect of the drillpipe rotation is dependent on the geometry of the wellbore and the rheology of the drilling fluid. In large annuli, drillpipe rotation has no

significant effect on the hole cleaning while for smaller annuli clearances, drillpipe rotation significantly improves cutting transport. The effect of pipe rotation is also dependent on the degree of eccentricity of the drillpipe in the annuli. The cutting transport efficiency is improved with drillpipe rotation for an eccentric annulus. However, for the concentric annuli, drillpipe rotation had a little or negligible effect on hole cleaning. Although the general reports from experimental and field studies have shown that drillpipe rotation improves cutting transport, some studies have reported that this effect is rheology dependent as they noticed a negligible effect when using water as the drilling fluid, but a significant improvement when using a viscous non-Newtonian fluid. In some studies, it was reported that the axial drillpipe rotation had an insignificant effect on the hole cleaning efficiency. However, if the drillpipe is rotated in an orbital manner, it can improve the hole cleaning for the cuttings rolling mechanism in a deviated wellbore. It is indicated that field operations data have shown that pipe rotation significantly improves the cutting transport efficiency in extended reach wells as a direct result of the orbital motion and sweeping effect of the drillpipe.

#### Cutting size:

Although almost all developed cutting transport models relate the MTV or critical velocity to the cutting size in a proportional manner that implies that the larger the cutting size, the more the difficulty for transportation, there have been reports that this phenomenon is not always the case. Depending on the drilling fluid viscosity, annuli velocity, and wellbore inclination angle, smaller cuttings may show more resistance to movement than the larger cuttings. Some reports have shown that smaller cuttings are harder to transport with water in horizontal wellbores where the transport of larger cuttings are relatively favourable. However, using a more viscous fluid presents the opposite results. Smaller cuttings are transported most efficiently in inclined wellbores when using low-viscosity fluids, while between 0° and 50° larger cuttings are transported most efficiently with high viscosity drilling fluids.

Table 2.8: Studies of the effect of the major drilling parameters on hole cleaning

Source	Method	Factors	Model	Major conclusions
Okrajni and Azar (1986)	Experimental Theoretical	Single-phase flow Fluid rheology Rpm	AM	The worst cuttings transport is experienced at inclination

		Hole angle Eccentricity		angles within the range of 40 to 45.
Gavignet and Sobey. (1989)	Theoretical	Single-phase flow	<b>TLM</b>	The criterion for the formation of a stationary bed is strongly dependent on drill pipe eccentricity and particle, pipe, and hole sizes
Ford et al. 1990	Experimental	Single-phase flow Fluid rheology Rpm Hole angle Cutting size Pipe size	--	Increasing the fluid viscosity decreases the MTV for both the cuttings rolling and suspension mechanisms when using the medium and highly viscous fluids. However, the MTV for both transport mechanisms was lower when using water than it was when using the medium viscosity fluid
Sifferman and Becker. (1992)	Experimental	Single-phase flow Flowrate Fluid rheology ROP Rpm Hole angle Cutting size	--	Drillpipe rotation reduces annular cuttings build-up under certain conditions and this effect is greater at inclination angles near horizontal, for small cuttings
Sanchez et al. (1999)	Experimental	Single-phase flow Rpm Hole angle	--	Pipe rotation has a significant effect on hole cleaning
Kamp and Rivero (1999)	Numerical	Flowrate ROP	<b>TLM</b>	At constant mud flowrate, the bed height increases as the rate of penetration increases
Doan et al. (2000)	Experimental Numerical	Two-phase flow Cuttings rate	<b>TLM</b>	Cuttings removal from annuli is highly dependent on the cuttings injection rate
Walker and Li (2000)	Experimental	Two-phase flow Particle size Fluid rheology Eccentricity	--	Fluid rheology plays an important role for solids transport. It is beneficial to pick up solids with a low viscosity fluid in turbulent flow but to maximize the carrying capacity a gel or a multiphase system should be used to transport the solids out of the wellbore
Cho et al. (2001)	Experimental Theoretical	Single-phase flow Hole angle	<b>TLM</b>	A highly viscous fluid reduces the cuttings-bed area and increases the pressure gradient under the same nominal annular velocity.
Bilgesu et al. (2002)	Numerical	Single-phase flow	<b>CFD</b>	The velocity in the annuli plays a major role in the effectiveness of hole cleaning.
Ozbayoglu and Miska (2003)	Experimental Theoretical	Two-phase flow	<b>THLM</b>	--
Yibing and Kuru (2004)	Numerical	Two-phase flow Fluid rheology	<b>TLM</b>	The quality of foam has an effect on the cutting transport

	Theoretical	ROP		efficiency. As the foam quality increases, the foam viscosity also increases, which is favourable for cuttings transport and vice versa.
Duan et al. (2006)	Experimental Theoretical	Single-phase flow Hole angle Rpm	<b>EM</b>	In horizontal pipes, smaller cuttings are more difficult to transport with water but easier with a viscous fluid. Improvement due to pipe rotation in the transport of small cuttings is two times that as seen for larger cuttings
Ozbayoglu et al. (2007)	Numerical Theoretical	Single-phase flow Hole angle ROP	<b>EM</b>	The major variable influencing the cuttings bed thickness is the shear stress acting on the cuttings bed surface.
Li et al. (2007)	Numerical	Single-phase flow Flowrate Fluid rheology eccentricity	<b>TLM</b>	A thicker mud will remove the cuttings at lower flow rates than that of a thin mud or water. However, Water will remove the cuttings more effectively if the sufficient pump capacity is available to pump the water at the required critical flow rate
Costa et al. (2007)	Numerical	Single-phase flow ROP	<b>TLM</b>	A decrease in ROP leads to a decrease in cuttings bed height
Duan et al. (2008)	Experimental Theoretical	Two-phase flow Rpm Eccentricity	<b>AM</b> <b>EM</b>	Pipe rotation significantly decreases cuttings concentration and pressure drop in a horizontal annulus during foam drilling.
Wang et al. (2010)	Numerical	Single-phase flow Rpm	<b>THLM</b>	The thickness of the cuttings bed decreases with an increase in flowrate and pipe rotation. Drillpipe rotation is one of the most effective practises for hole cleaning.
Li et al. (2010)	Numerical	Single-phase flow Rpm	<b>CFD</b>	Pipe rotation within the range of 80 to 120 rpm has a significant benefit on hole cleaning.
Wei et al. (2013)	Experimental Theoretical	Two-phase flow Rpm eccentricity	<b>EM</b>	In horizontal gas-liquid flow, depending on the fluid flowrate and viscosity, cuttings transport is mainly saltation, and the drillpipe rotation improves cuttings transport.
Cayeux et al. (2014)	Numerical	Single-phase flow Flowrate Rpm ROP	<b>CFD</b>	An increase in pipe rotation from 60 to 100 Rpm showed a significant improvement in cutting transport. The reduction of ROP is a viable option that benefits hole cleaning.

Xiaofeng et al. (2014)	Numerical Theoretical	Single-phase flow Flowrate Rpm Hole angle	<b>CFD</b> <b>EM</b>	Pipe rotation has a major influence on the distribution of cuttings in inclined annuli. Increasing pipe rotation speeds can significantly reduce cuttings volume and annular pressure drop at low or medium flow rates.
Gul et al. (2017)	Experimental	Two-phase flow Flowrate	--	The area of the cuttings bed decreases with an increase in liquid and gas flowrates. However, an increase in the liquid flowrate was found to be more effective.
Akhshik et al. (2015)	Numerical	Single-phase flow Flowrate Rpm ROP Hole angle	<b>CFD-</b> <b>DEM</b>	The transportation mechanism of particles is the suspension regime at low well inclination angles (near vertical), rolling regime at high inclination angles (near horizontal) and a combination of both medium inclination angles. Pipe rotation significantly decreases cuttings concentration
Pandya et al. (2020)	Experimental Theoretical	Single-phase flow Flowrate Hole angle Cuttings density	<b>EM</b>	The transport efficiency of solids is strongly dependent on the fluid rheological properties. Particle-transport mechanisms are highly influenced and vary depending on the wellbore inclination angle.
Zhang et al. (2020)	Numerical	Single-phase flow Flowrate Hole angle	<b>CFD</b>	The maximum height at which the cutting can be suspended to decreases with an increase in the cutting's diameter. This makes the cuttings more likely to form a bed at the lower region of the annuli
Erge and Van Oort. (2020)	Numerical Theoretical	Single-phase flow Fluid rheology Rpm eccentricity	<b>CFD</b>	Axial flow alone is not sufficient for effective hole cleaning, especially in the highly deviated and horizontal wells. In a fully eccentric annulus, without pipe rotation, cuttings will form a bed on the low side of the annuli even at elevated axial flow rates

### **2.4.1 Multiphase cutting transport in annuli**

In general, the models developed for cutting transport for drilling applications have been formulated based on an empirical, mechanistic or numerical methodology. However, their application to two-phase flow scenarios are questionable as the dynamics of solids transport in a multiphase fluid is flow pattern dependent which means that the ability of the multiphase fluids to transport solid particles is strongly influenced by the prevailing flow pattern of the flow (Oyeneyin, 2015). For instance, for underbalanced drilling operations, the intermittent and dispersed bubble flow pattern are more effective than the other flow patterns in terms of hole cleaning (Lage, et al., 2000).

The numerical two-layer or three-layer cutting transport modelling approach has recently gained a lot of popularity over the empirical or mechanistic cutting transport models mainly because it allows for the simultaneous solutions of cuttings moving in the different transport mechanisms, accounts for cutting-cutting physical interactions and can be applied to complex wellbore geometries. However, the direct application for simulation of cutting transport in two-phase flows has neglected the complex and transient nature posed by two-phase fluid flows in a conduit.

The multi-layered cutting transport modelling expresses the mass and momentum conservation equation for the two-phase fluid as if the fluid is homogeneous mixture with a no-slip effect where the gas and the liquid phases flow at the same velocities. The mechanism of mass, momentum and energy transfer between phases in a two-phase is highly dependent on the flow pattern (Guo, et al., 2007) and the prevailing flow pattern is dependent on a number of parameters amongst which is the fluid input flowrate, the geometry of the conduit and the physical properties of the fluid. In order to accurately perform numerical simulations for multiphase fluids with cuttings, the momentum and mass conservation equations must take into account the flow pattern transitions along with the momentum and mass conservation equations for the cuttings phase where the drag, lift and other dynamic or static forces acting on the drilled cuttings are also determined based on the local position in the annuli. This is important because the forces acting on the cuttings in the annuli would vary depending on the location of the cuttings in the annuli and the magnitude of this effect is strongly dependent on the flow pattern existing in the given section of the wellbore.

## **2.5 Summary of research gaps**

In order to develop a reliable method for the prediction of the dynamic behaviour of multiphase drilling fluid flow, it is important that the combined effect of the rheology of the drilling fluid, the wellbore geometry, as well as the other important drilling parameters are taken into consideration. The methods developed for the modelling of multiphase drilling fluid annuli flows have either been accomplished by modifying the models originally developed for two-phase flows in pipes using the hydraulic diameter concept or adopted the concept formulated for Newtonian two-phase flow in annuli. The drilling fluid is a non-Newtonian fluid that is shear dependent. Thus, its behaviour when flowing through the annuli is highly dependent on the physical conditions to which it is subjected to. Early researchers that studied the annuli flow of single-phase drilling fluids showed experimentally, numerically and from field data that the rheology of the drilling fluid combined with the other important drilling parameters as discussed in the literature, significantly impacts the dynamic behaviour of the flow, thereby influencing the drilling hydraulics and the hole cleaning efficiency during drilling activities. The current methods developed for the modelling of two-phase drilling fluid flow in annuli for oil well drilling applications have neglected the combined effect of the drilling fluid rheology with the major drilling parameters. If this leads to inaccurate or erroneous predictions for single-phase drilling fluid annuli flows, it can be deduced that the negligence of this effect would also lead to inaccurate predictions for two-phase drilling fluid annuli flows provided that the liquid phase of the drilling fluid possesses a non-Newtonian characteristic behaviour.

From the analysis of the previous studies that have been done on two-phase flows in annuli, it is evident that some of the results published have been conflicting in certain aspects. It has been established from literature that the effect of the drillpipe rotation on the velocity fields in the concentric annuli is negligible while for the eccentric annuli, the drillpipe rotation significantly redistributes the velocity fields and improves the flow in the stagnation zones or in the smaller region of the annuli. However, the results of the effect of the drillpipe rotation on the pressure drop in the concentric or eccentric annuli for both single-phase and two-phase flow has been conflicting and not generally or conclusively defined. While some studies have reported that the increase in drillpipe rotation decreases the pressure gradient, other studies have reported an increase in pressure gradient

or either an increase or a decrease in pressure gradient depending on the investigated flowing conditions. Another issue is that the currently developed models for the hydraulics of multiphase drilling fluid annuli flows have ignored the combined effects of the drilling fluid rheology, the eccentricity and the drillpipe rotation which significantly influences the accuracy for the prediction of the pressure drop.

Furthermore, cuttings transport predictions are essential for the planning of directional and horizontal drilling operations. An effective multiphase cuttings transport modelling is one of the essential components for the achievement of a successful underbalanced drilling operation. A poorly designed and/or executed UBD procedure can provoke deeper formation damage than that which may result from a properly planned and executed conventional overbalanced drilling operation (Bennion, et al., 1996). The current multi-layered cutting transport models developed for multiphase flow applications neglects the complex and transient nature of multiphase flow. The ability of a two-phase drilling fluid to transport cuttings effectively is highly dependent on the flow pattern along with a number of other drilling parameters. Negligence of the fluid flow pattern may lead to large prediction errors as the mechanism of mass, momentum and energy transfer between the phases are highly dependent on the flow pattern and hence the forces acting on the cuttings would be strongly influenced by this phenomenon.

This study aims to experimentally, theoretically and numerically investigate the dynamics of cuttings transport and the effect of the drillpipe rotation and eccentricity on the pressure gradient for drilling fluid annuli flow and develop reliable drilling hydraulic and cutting transport models that alleviate the inaccuracies posed by the current models. The flow patterns to be considered are the dispersed bubble, bubble, stratified flow and slug flow patterns, as these flow patterns most likely to be encountered for underbalanced or multiphase drilling operations (Mousavi, et al., 2008). The output of this research would provide methods that can be applied for multiphase drilling hydraulics calculations for wellbore pressure maintenance and models to optimise the cutting transport efficiency throughout the life of a drilling operation.

## Chapter 3

### Experimental study

A laboratory program was designed and conducted in order to simulate the flow of single-phase and multiphase fluids in a drilling annulus. An experimental rig was built at Robert Gordon University (RGU), consisting of various measurement equipment and a data acquisition system to acquire real-time experimental data. The experimental rig includes a horizontal and an inclined test sections and is designed to operate with a maximum gas flowrate of 28 m<sup>3</sup>/hr and a maximum liquid flowrate of 35 m<sup>3</sup>/hr. Single phase or multiphase (air and liquid) Newtonian or non-Newtonian water-based polymer mixtures with or without solid particles are flowed through a flow loop in order to imitate an oil well drilling process and study the fluid and cutting transport dynamics. The test sections are designed and constructed in a systematic manner to represent a concentric annulus and can be switched to represent an eccentric annulus when desired. Various concentrations of water-based polymer solutions were prepared, and rheological measurements were carried out using a rotational rheometer to obtain the shear stress to shear rate relationship. The liquid and gas flowrates required to establish the required flow patterns for the different experimental fluid types, section geometries and inclination angles were mapped out prior to the start of the experimental investigation and data acquisition phase. The flow patterns considered for the experimental study are the dispersed bubble, bubble, stratified flow and slug flow patterns, as these are the flow patterns that have been reported to mostly occur during underbalanced or multiphase drilling operations. Prior to commissioning the experimental rig, the measuring equipment were calibrated and tested along with the data acquisition systems, to ensure that accurate data was generated, and measurement errors were minimised.

The main aim of the experimental study was to create a single-phase or multiphase drilling scenario and physically investigate the combined effects of fluid rheology, eccentricity and drillpipe rotation on real-time drilling hydraulics and cutting transport mechanism and efficiency. The experiments conducted provided an experimental database that was used for the verification and validation of the empirical correlations and mechanistic models that were developed in this study.

### 3.1 Test fluids

The drilling fluid used during oil-well drilling operations possess mostly a non-Newtonian rheological behaviour. Thus, experiments performed to investigate the behaviour of flow of drilling fluids through the annuli must make use of non-Newtonian fluid mixtures to produce a similar effect. In other to reproduce the pseudoplastic behaviour of the drilling fluid, polymer solutions prepared with concentrations of 0.1% and 0.5% Xanthan Gum (XG) in water were used in this experimental study. This was done by adding the required amount of the Xanthan Gum (XG) into distilled water in the mixing/storage tanks and vigorously agitating the mixture until the solute is completely dissolved in the mixture. At several points during the experiments, fluid samples were taken from the tank and tested to determine the rheological properties of the testing fluid and provide the certainty of repeatability. These rheological measurements (shear stress to shear strain relationship) are carried out using a Brookfield Viscometer. Figure 3.1 presents a plot of the shear stress to shear rate data obtained for the test fluids used in this experimental study.

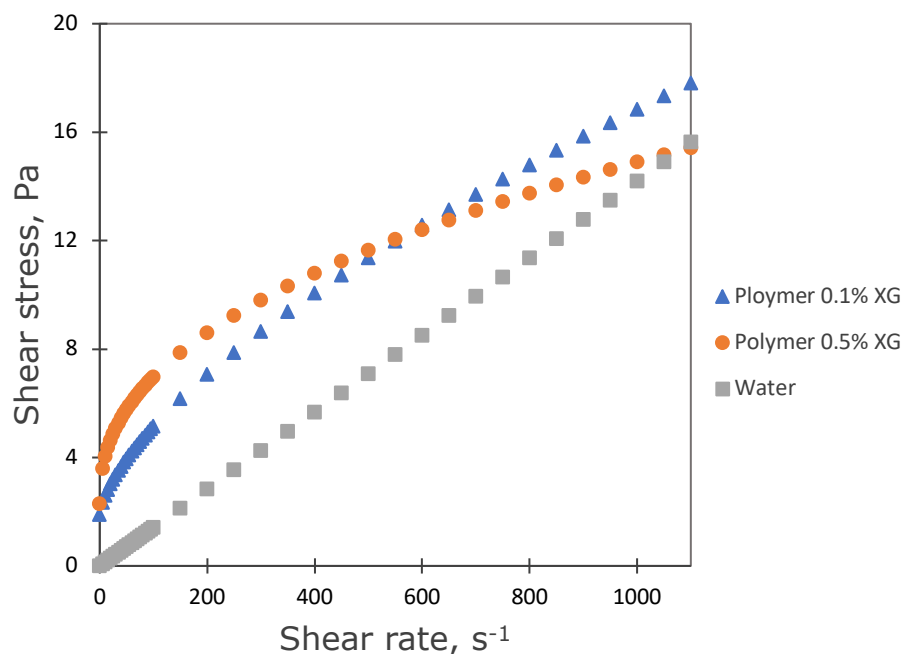


Figure 3.1: Shear stress versus shear rate data for the test fluids

### 3.1.1 Determination of rheological parameters

To obtain the rheological parameters of the water-based Xanthan Gum (XG) polymer mixtures, a nonlinear regression was performed on the shear stress to shear strain relationship generated for each of the polymer solutions. The shear stress to shear strain data was best fitted to the appropriate rheological models (Equations 2.1-2.6) using a systematic computational method explained as follows:

A modified golden search iterative method and non-linear regression analysis was performed simultaneously to obtain the rheological parameters ( $\tau_0$ ,  $K$ , and  $n$ ) of the polymer mixtures from their shear stress to shear strain relationship data. The procedure is based on the prediction of the appropriate yield stress value that best fits the rheological data obtained using the Brookfield Viscometer. The golden search iterative method is an iterative process used to determine the minimum or maximum of a given function within a certain domain. This adopted iterative method involves the selection of a lower bound shear stress value  $\tau_L$  and an upper bound shear stress value  $\tau_U$ , with the assumption that the optimum yield shear stress value lies within  $\tau_L$  and  $\tau_U$ . Two yield stress values,  $\tau_1$  and  $\tau_2$  are calculated from the upper and lower bound shear stress values, and a non-linear regression is performed on the data using both values. The correlation coefficients  $R^2$  obtained using  $\tau_1$  and  $\tau_2$  are then compared, and if the convergence criterion is not met, either the upper or the lower limit value is changed and passed on to the next iterative process. This process is repeated until the correlation coefficient,  $R^2$  obtained using  $\tau_1$  and  $\tau_2$  form the current upper and lower bound yield stress values converges to the same value (Figure 3.2), thereby yielding the yield stress  $\tau_0$  as well as the flow behaviour index,  $n$  and the consistency index,  $K$  of the fluid.

The equations used to predict the yield stress values at every iteration can be expressed as:

$$\tau_1 = \tau_L + G_R (\tau_U - \tau_L) \quad 3.1$$

$$\tau_2 = \tau_U - G_R (\tau_U - \tau_L) \quad 3.2$$

The parameter  $G_R$  in Equations 3.1 and 3.2 is referred to as the golden ratio and is approximately equal to 0.618.

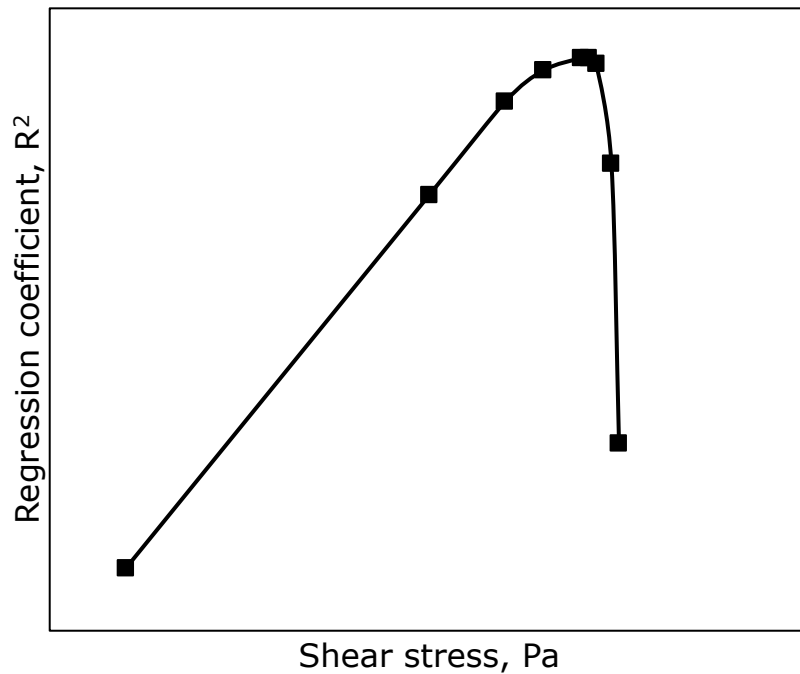


Figure 3.2: Variation of correlation coefficient with assumed values of yield stress

The steps involved in the computation algorithm used to determine the rheological parameters of the experimental testing fluids is explained as follows:

1. Store the data of the shear stress to shear rate relationship of the polymer mixture in a matrix  $T$  of  $n$  rows and two columns
2. Guess a value for the upper  $\tau_U$  and lower limit  $\tau_L$  (in this study, an initial guess of zero for the lower limit value  $\tau_L = 0$  was used and the initial guess for the upper limit value was the minimum shear stress value in the matrix  $T$ ,  $\tau_L = \tau_{\min}$ )
3. Compute  $\tau_1$  and  $\tau_2$  using equations 3.1 and 3.2
4. Subtract  $\tau_1$  from all the shear stress values in matrix  $T$  and store results in another matrix  $T1$

5. Subtract  $\tau_2$  from all the shear stress values in matrix T and store results in another matrix T2
6. Perform non-linear regression on both matrix T1 and T2 to obtain the correlation coefficients  $R^2_1$  and  $R^2_2$  respectively
7. If  $R^2_1 < R^2_2$ , set upper limit equal to  $\tau_1$ ,  $\tau_U = \tau_1$  else if  $R^2_1 > R^2_2$ , set lower limit equal to  $\tau_2$ ,  $\tau_L = \tau_2$
8. Repeat steps 3 to 7 until  $R^2_1$  and  $R^2_2$  converges to the same value yielding  $\tau_1 = \tau_2 = \tau_0$ . The slope and intercept from the non-linear regression yields the parameters n and K.

A script written in MATLAB for the computation of the rheological parameters of the experimental testing fluids using this developed computation algorithm is presented in the appendix A. The rheological parameters for the test fluids used in this experimental study are presented in the Table 3.1.

Table 3.1: Rheological parameters for experimental test fluids

Fluid type	Phases	K(Pa s <sup>n</sup> )	n	$\tau_0$ (Pa)
1	Water	0.014	1.002	0
3	Polymer (0.1% XG)	0.1566	0.66	1.88
5	Polymer (0.5% XG)	0.6461	0.43	2.29

Table 3.2: Experimental test fluid types

Fluid type	Phase type	Contents
1	Single-phase	Water
2	Two-phase	Water + air
3	Single-phase	Polymer (0.1% XG)
4	Two-phase	Polymer (0.1% XG) + air
5	Single-phase	Polymer (0.5% XG)
6	Two-phase	Polymer (0.5% XG) + air

The fluid types used for the experimental study are summarised in the Table 3.2. In this study the numbers 1 to 6 would be used to represent the fluid types used in an experimental run depending on the types and rheological characteristics of the phases that make up the testing fluid.

### 3.2 Model drilled cuttings

Solid materials were used in this experimental study to represent the drilled cuttings with the aim of studying the transport mechanism of cuttings in wellbore annuli and investigating the effect of the major drilling parameters on cuttings transport efficiency. Plastic and glass beads of different, sizes, weight and concentrations were used to simulate the cuttings in a wellbore annulus (Figure 3.3b). This offered a significant benefit of providing a clearer system, enabling the visibility of the cutting transport dynamics to be more effective. Another added advantage of using the plastic beads is they can be retrieved, cleaned and re-used for other experimental runs. A sieve tank (Figure 3.3a) was designed and constructed and connected to the drain outlet of the mixing/storage tanks. A mesh size of 0.9mm apertures were used to ensure that all the particles used in the experiments were captured prior to the disposal of the experimental fluids. The retrieved particles are then washed with water and sorted using a sieve shaker to prepare them for the next experimental runs.



Figure 3.3: (a) solids separation tank and (b) glass and plastic beads

Table 3.3 presents some of the properties of the particles used to simulate the cutting transport in this experimental study.

Table 3.3: Types of the particles used in experimental study

Particle	Colour	Shape	Size, mm	Density, Kg/m <sup>3</sup>
1	Red	Spherical	3 - 4	950
2	White	Spherical	3 - 8.5	500
3	Light Green	Spherical	2.5 - 3.7	2100
4	Dark Green	Spherical	2.20 - 2.4	1500
5	Blue	Spherical	1.25 - 1.65	2000

### 3.3 Experimental rig design and setup

A multiphase flow rig, capable of simulating both single-phase and two-phase fluid flow in concentric and eccentric annuli geometries was designed and constructed to conduct this experimental study. The flow loop consists of transparent test sections that enables the visual observations of the two-phase gas-liquid flow patterns and particle transport mechanism under various experimental conditions. Each annular test section has an outer diameter of 0.1440 m, an inner pipe diameter of 0.0885m. Figure 3.5 shows an illustration of the entire experimental unit used to run tests and acquire experimental data.

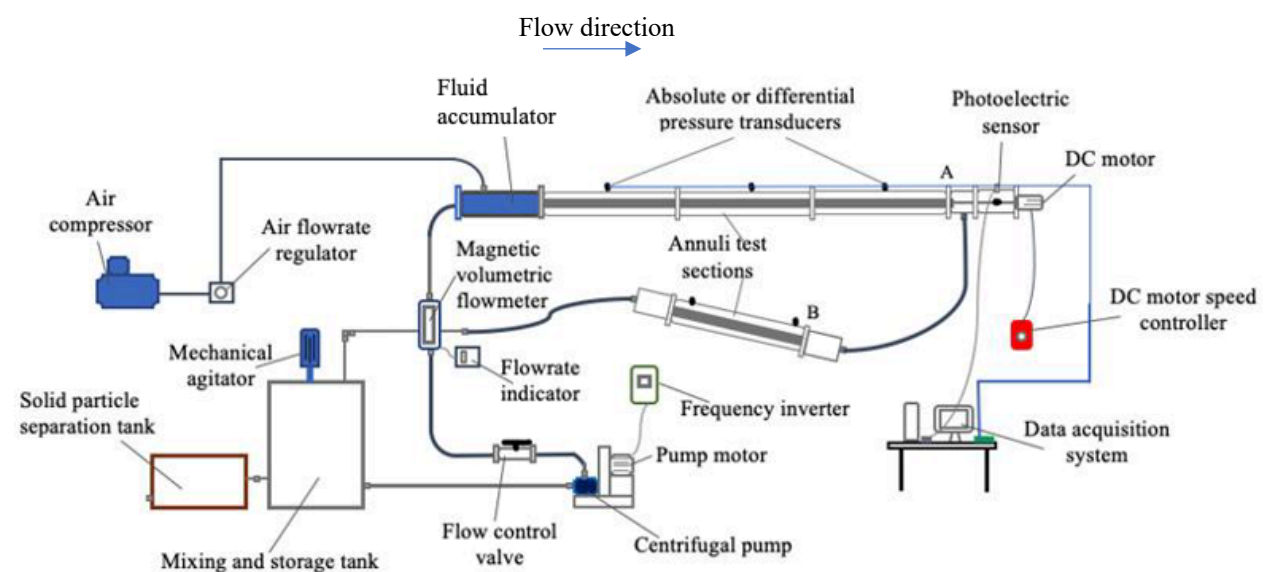


Figure 3.4: Schematic diagram of the experimental unit

The main components of the experimental unit are described in the following sections.

#### 3.3.1 Test sections

The experimental unit is composed of two annular test sections made of a 144mm outer diameter acrylic glass tube and an 88 mm diameter inner Acrylonitrile Butadiene Styrene ABS pipe. The Figure 3.1 shows the acrylic glass tube and the inner ABS pipe. The ABS pipes are completely sealed at both ends to prevent the flow or accumulation of fluids through inner pipe. One of the test sections is mounted in a horizontal orientation and is approximately 14ft long. The outer test

section is mounted on an erected plane in which the inclination angle can be set and varied at will.

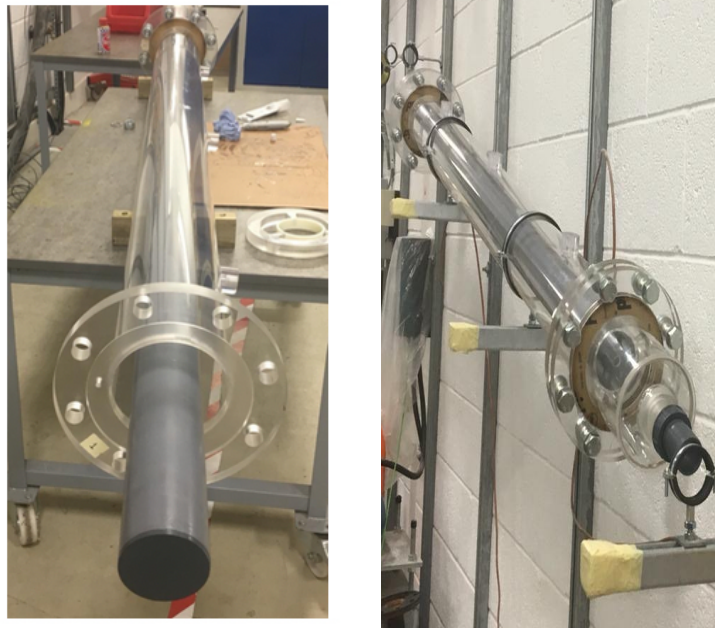


Figure 3.5: Acrylic glass tube and ABS pipe used to construct a concentric/eccentric annulus test section

The use of the transparent acrylic glass tube offers some significant benefit of being able to visually observe the prevailing gas-liquid flow patterns, the cutting transport mechanism and the point in time where the cuttings begin to settle at the low side of the annuli to form a stationary bed. The inner pipe is fitted into flanges to position them centrally in the acrylic glass tube. Either concentric and eccentric holes are bored into the flanges to allow for the inner pipe to be positioned concentrically or eccentrically ( $e = 0.7$ ). Roller ball bearings are fitted into the flanges to enable the inner pipe to rotate readily about its axis (Figure 3.7). A steel pipe fluid accumulator was installed upstream of the test sections in order to stabilise and create a timely fully developed flow. A non-return valve is installed on the steel pipe and connected to the gas line from a gas compressor. When multiphase gas-liquid flow is desired, the two phases are introduced simultaneously and mixed in the steel pipe containing the baffle plates before flowing into the test sections.

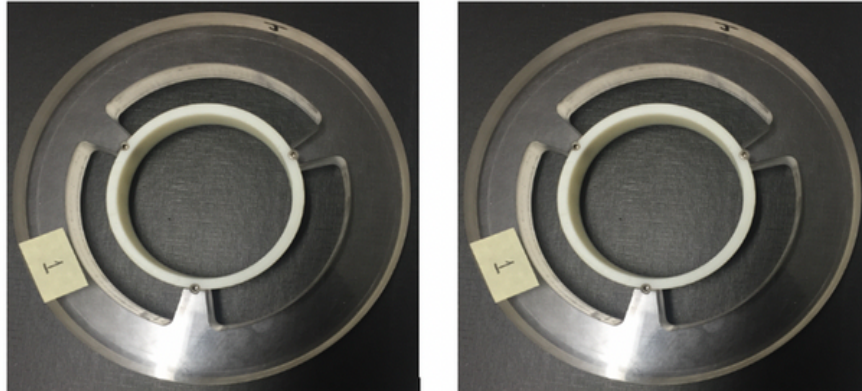


Figure 3.6:Concentric and eccentric flanges

In order to maintain the bearings, it is required that they are lubricated at regular intervals and this lubrication is important process in preventing the failure of the bearings. When the experimental unit is assembled, there is no access to bearings, so the maintenance processes are only possible if the rig is dismantled. The use of the sealed bearings provided a solution to this issue as they are already lubricated by the manufacturer and require no further lubrication. Another major advantage of using the sealed bearings is that the seals prevent the entry of solid particles when performing cutting transport experiments thereby reducing the chances of mechanical wear and tear and favouring the lifespan of the bearings.

### **3.3.2 Pressure transducer**

Absolute and differential pressure transducers were connected to the test sections to obtain pressure measurements. While the absolute pressure transducers were used to obtain the pressure readings at local points in the test sections, the differential transducers were used to obtain the pressure difference between two points in the test sections. The absolute pressure transducers are in the range of 0 to 7bar while the differential pressure transducers are in the range of -25 to 25mbar.

### **3.3.3 Flow meter**

The magnetic inductive flowmeter was selected as an option to measure the flowrate of the liquids. The magnetic inductive flowmeter consists of a transmitter and a converter which exist separately but are connected to one another by cables forming a functional unit. The converter has an analog output and can also be provided optionally with a pulse output. The analog output supplies an electric current in the standard signal 0 to 4 to 20mA, which is proportional to the fluid flowrate, and is designed to meet the requirements for control, indication and recording as well as other measurement applications. The converter is the equipment that converts an electrode voltage into an output signal which is proportional to the flowrate.

The transmitter operates with no moving parts, consists of a meter tube, electromagnets, reference core and measuring electrodes and measures the mass or volume flow rate of electrically conductive liquids in pipes. When electrically conductive products flow through the transmitter, a voltage is induced that is tapped off by the electrodes which are insulated against the meter tube. The induced measure voltage is proportional to the mean velocity of the flow.

Flowrate measurements using the magnetic inductive flowmeter offer some major advantages. The transmitter has no moving parts and therefore can be operated with little or no maintenance, the flow is not altered as there is no expansion or contraction of the meter tube and thus constitutes no pressure loss on the flow, flowrate measurements for high or low conductivity liquids are straight forward due to high input resistance of the converter, possess a high degree of measurement accuracy

### **3.3.4 DC motor**

A DC motor is connected to the inner pipe with a metal shaft to enable the inner pipe to rotate about its axis in the annulus (Figure 3.7). The motor has a rated torque of 4.2Nm and operates to a maximum rotary speed of 159rpm. In order to regulate the speed of the motor, and thus the speed of the inner pipe in the annulus, the motor is connected to a low voltage DC motor speed controller. The

DC motor speed controller is used to vary the supply voltage to the motor thereby enabling the increase or decrease in the speed of the inner pipe to the desired rpm value.

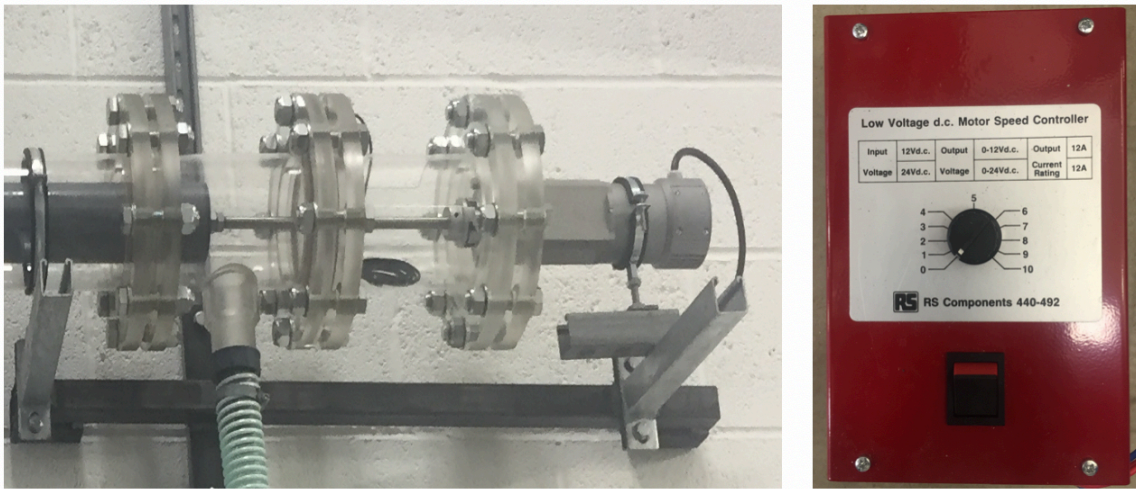


Figure 3.7:DC motor connected to inner pipe and the motor speed controller

### 3.3.5 Photoelectric sensor

A cylindrical photoelectric sensor was used to determine the rotary speed rpm of the inner pipe in the annulus. The sensor is a retro-reflective photoelectric sensor that has both the transmitter and receiver contained within the same housing but require a reflector opposite to the sensor. The photoelectric sensor is placed just above the area of the shaft where the reflective tape is located (Figure 3.8). The reflector bounces the light beam back to the transmitter until an object breaks the beam. When the light beam is broken a voltage is outputted from the device. The times at which these voltages are detected can be used to determine the frequency and thus, the speed of the rotating inner pipe.

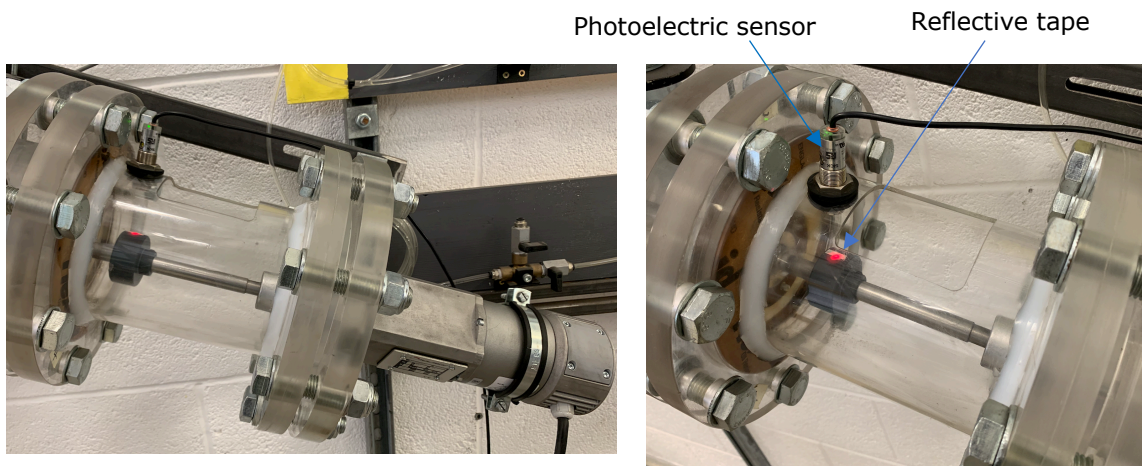


Figure 3.8:Photoelectric sensor and reflector tape arrangement

### 3.3.6 Data acquisition system

The data acquisition system is composed of a computer and two data acquisition devices from National instruments. The DAQ devices which are the NI SCB-68 E series and the USB-6009 are used to obtain real-time data from the experimental rig (Figure 3.9). A LabVIEW software is installed on the computer and a virtual instrument program is written in other to display and acquire the desired data from the key experimental rig equipment and sensors such as the pump, the absolute and differential pressure transducers, the photoelectric sensors (inner pipe rotary speed, rpm) and the liquid and gas flow meters.

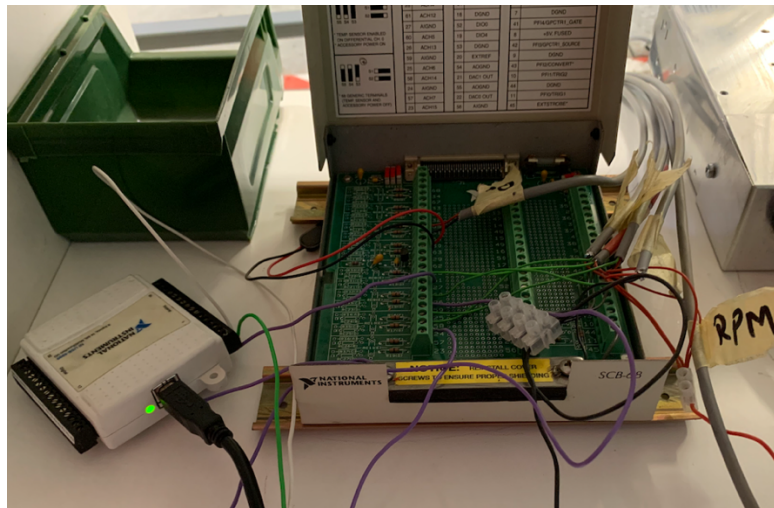


Figure 3.9: Data acquisition devices

### 3.4 Calibration of experimental rig

In order to ensure that the experimental data obtained from the experimental rig are reliable, the equipment were calibrated and tested to ensure that the measured readings were accurate, and the errors imposed by the device or equipment were minimised.

#### 3.4.1 Pressure transducers

The absolute and differential pressure transducers were calibrated using a Druck pressure calibrator obtained from SCOTIA Instrumentation Ltd (Figure B.1). In order to mitigate obtaining erroneous readings during experimental tests, it is

important to ensure that at a given pressure, all the pressure transducers installed on the experimental rig outputs the same voltage. This may not always be the case as each of the transducers has a certain range of accuracy or manufactured error. To calibrate the pressure transducers, the transducers are connected to the Druck pressure calibrator and wired to the DAQ device and thus, the LabVIEW software. Once a given pressure is supplied from the Druck to the pressure transducers, the voltage output from the transducer is converted to pressure in the LabVIEW virtual instrument program and recorded. This process is repeated three times for each transducer and an average of all the readings are taken to improve the calibration accuracy. After the process has been completed, a regression analysis is performed on the pressure readings to obtain pressure correction equations for all the transducers. These pressure correction equations are written into the main LabVIEW virtual instrument program to ensure that the transducers output the same voltage readings for a given or applied pressure. Figure B.2 and B.3 show an example of the calibration plot of one of the absolute and differential pressure transducers that were calibrated and installed on the experimental rig.

#### **3.4.2 Fluid flow meter**

The readings obtained from the liquid flow meter was checked manually to ensure that the flowrate reading display in LabVIEW front panel was accurate. This was accomplished by running the pump and flowing water from the mixing tanks, through the flow loop with the return line flowing back to the tanks. A plastic container of 10 litres in volume was placed at the outlet of the flow loop and the time taken for the container to be filled completely with water was recorded. As the system had no mass accumulation, the actual flowrate of the liquid experimental rig was deduced and compared to the values received from the liquid flow meter. Figure B.4 shows a comparison of the flowmeter readings to the measured liquid flowrate readings. From the plot it is clear that the flowmeter readings are quite accurate and require no adjustments.

### **3.5 Data acquisition techniques**

A LabVIEW software is used together with the NI SCB-68 E series and the USB-6009 DAQ devices to obtain data from the experimental unit. The NI SCB-68 E series offered an advantage of having a relatively larger board surface area and has 8 different analog input channels that can be used for instrumentation, making it possible to connect a total of 16 devices. The pressure transducers, pump and flowmeters were connected to the SCB-68 E series DAQ device while the photoelectric sensor was connected to the USB-6009 DAQ device. Separate LabVIEW virtual instrument programs were written to obtain and process the data generated by the DAQ devices. Figure B.5 shows the front panel design for pressure and flowrate data acquisition.

#### **3.5.1 Pressure readings**

The absolute and differential pressure transducers are connected to the SCB-68 E series DAQ device and real-time data is obtained simultaneously from all the transducers during experimental runs. The pressure correction equations derived from the transducer calibration process is incorporated into the LabVIEW program to ensure that all the transducers are operating in the same plane, and errors are minimised. Two-phase flow mixtures are transient and highly turbulent, and the pressure drop across the annuli sections is dependent on the transient in-situ liquid hold up and the gas-liquid flow patterns amongst other parameters. This means that the differential pressure readings from the transducers would vary significantly for a given experimental run with constant gas-liquid flowrate. In order to account for this effect, a sub VI LabVIEW program is included to take the average of the differential pressure readings over the period of time for the experimental run. Figure 3.10 shows the Block diagram design for pressure data acquisition.

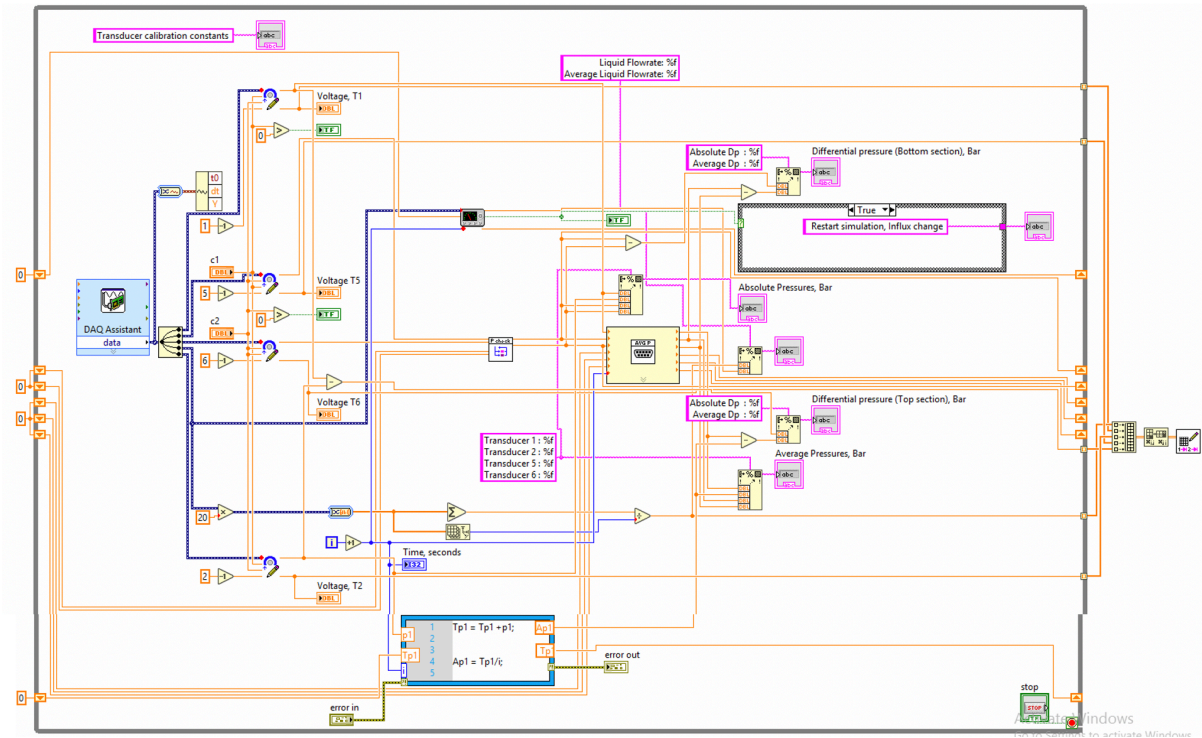


Figure 3.10: LabVIEW block diagram for pressure to flowrate data acquisition

### 3.5.2 Rotary speed of the inner pipe

The photoelectric sensor was used to obtain the information of the rotary speed of the inner ABS pipe in the annuli test sections. A reflective tape cut to a size that is a lot smaller than the circumference of the rotating shaft, is placed on the rotating shaft connected to the motor. When the shaft is rotated, and the reflective tape comes across the sensor the light beam produced by the sensor is broken and an impulse voltage is outputted from the device and obtained by the USB-6009 DAQ device. The frequency at which the photoelectric sensor outputs the impulse signal can be used to calculate the instantaneous rotation speed  $\omega_t$  of the inner pipe using the following relationships:

$$F_t = \frac{1}{(T_j - T_{j-1})} \quad 3.3$$

$$\omega_t = 60 \times F_t$$

3.4

where  $T_j$  and  $T_{j-1}$  are the times at which the current and the previous impulse voltages were obtained respectively.

A precaution to note is that depending on the width of the reflector tape, the RPM of the inner pipe can be greatly overestimated. This error is significantly pronounced at lower rotary speeds where the reflector tape takes more time to rotate past the sensors beam. Thus, the sensor would output multiple impulse voltage signals during one revolution of the shaft, rendering the rotary speed calculations invalid. This can be corrected by ensuring that once an impulse voltage signal is generated by the sensor, every other voltage signal is ignored until a zero-voltage signal is obtained. This would ensure that only one impulse voltage signal is obtained for one revolution of the inner pipe, making the instantaneous rotary speed calculations highly accurate. Figure 3.11 shows the Block diagram design for the inner pipe rotary speed data acquisition.

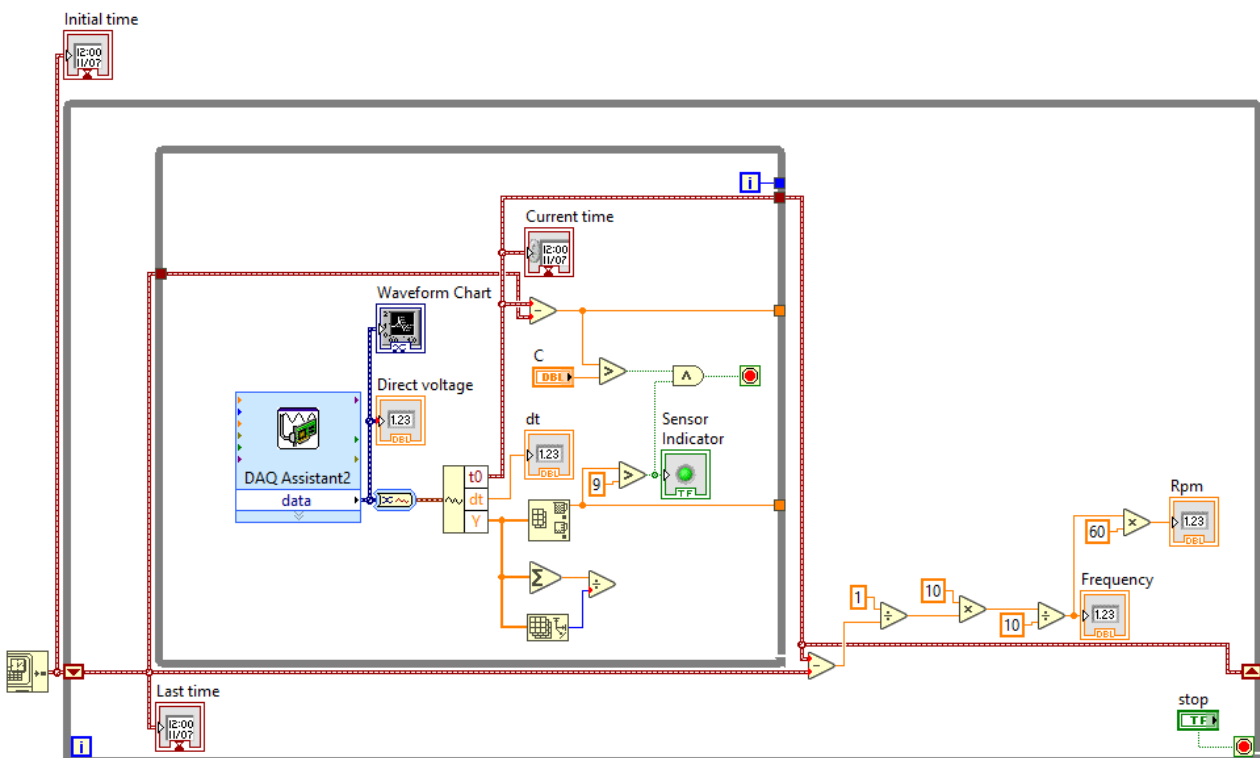


Figure 3.11: LabVIEW block diagram for inner pipe rotary speed calculation

### 3.6 Experimental test procedures

The operational ranges for the test conditions explored is presented in Table 3.4.

Table 3.4: Operational parameters for experimental tests

Parameters	Value range
Eccentricity	0 and 0.7
Rotation	0 to 150 rpm
Angle	0 - 30°
Air flowrate	0 to 28 m <sup>3</sup> /hr
Liquid flowrate	0 to 35 m <sup>3</sup> /hr

The following procedures are used for the experimental investigation and data acquisition involving the fluid flow hydraulics and cutting transport dynamics in the concentric or eccentric annuli, with or without inner pipe rotation.

#### 3.6.1 Single-phase flow

This section highlights the experimental procedures used when the testing fluids are of fluid types 1, 3 and 5. This procedure is the same for when the experimental rig is setup as a concentric or an eccentric annulus. The experimental procedures are as follows:

1. Prepare testing fluid in the mixing/storage tanks
2. Power on the flowmeter, pressure transducer, photoelectric sensor
3. Start-up data acquisition system
4. Switch on the pump
5. Adjust the controller to set the liquid flowrate to the desired value
6. Switch on DC motor and set inner pipe rotation speed to the desired Rpm
7. Start recording data
8. As soon as the readings stabilise, adjust motor speed controller to change the rpm values and take readings until data for all the rotary speeds are recorded.
9. Switch off the DC motor
10. Re-adjust the controller to set the liquid flowrate to the next desired value
11. Repeat steps 6 – 10 until the required data has been acquired.

### **3.6.2 Single-phase flow with solid particles**

This section highlights the experimental procedures used when the testing fluids of fluid types 1, 3 and 5 are mixed homogeneously with solid particles. This procedure is the same for when the experimental rig is setup as a concentric or an eccentric annulus. The experimental procedures are as follows:

1. Prepare testing fluid in the mixing/storage tanks
2. Switch on the mechanical agitators
3. Add solid particles until the required solid-liquid volumetric concentration is reached
4. Power on the flowmeter, pressure transducer, photoelectric sensor
5. Start-up data acquisition system
6. Switch on the pump.
7. Adjust the controller to set the flowrate to the desired value
8. Switch on DC motor and set inner pipe rotation speed to the desired Rpm
9. Start high-speed camera to record the flow dynamics in the test section
10. Start recording data
11. Adjust motor speed controller to change the Rpm values and take readings until data for all the rotary speeds are recorded.
12. Switch off high-speed camera
13. Switch off the DC motor
14. Re-adjust the controller to set the flowrate to the next desired value
15. Repeat steps 8 – 14 until the required data has been acquired.

### **3.6.3 Two-phase flow**

This section highlights the experimental procedures used when the testing fluids are of fluid types 2, 4 and 6. This procedure is the same for when the experimental rig is setup as a concentric or an eccentric annulus. The experimental procedures are as follows:

1. Prepare testing fluid in the mixing/storage tanks
2. Power on the flowmeter, pressure transducer, photoelectric sensor
3. Start-up data acquisition system

4. Switch on the pump and air supply
5. Adjust the controller to set the liquid flowrate to the desired value
6. Adjust the gas controller to set the air flowrate to the desired value
7. Start high-speed camera to record the flow dynamics in the test section
8. Switch on DC motor and set inner pipe rotation speed to the desired Rpm
9. Start recording data
10. As soon as the readings stabilise, adjust motor speed controller to change the rpm values and take readings until data for all the rotary speeds are recorded.
11. Switch off high-speed camera
12. Switch off the DC motor
13. Re-adjust the controller to set the liquid flowrate to the next desired value
14. Re-adjust the gas controller to set the air flowrate to the next desired value
15. Repeat steps 7 – 14 until the required data has been acquired.

#### **3.6.4 Two-phase flow with solid particles**

This section highlights the experimental procedures used when the testing fluids of fluid types 2, 4 and 6 are mixed homogeneously with solid particles. This procedure is the same for when the experimental rig is setup as a concentric or an eccentric annulus. The experimental procedures are as follows:

1. Prepare testing fluid in the mixing/storage tanks
2. Switch on the mechanical agitators
3. Add solid particles until the required solid-liquid volumetric concentration is reached
4. Power on the flowmeter, pressure transducer, photoelectric sensor
5. Start-up data acquisition system
6. Switch on the pump and air supply.
7. Adjust the controller to set the flowrate to the desired value
8. Adjust the gas controller to set the air flowrate to the desired value
9. Switch on DC motor and set inner pipe rotation speed to the desired Rpm
10. Start high-speed camera to record the flow dynamics in the test section
11. Start recording data

12. Adjust motor speed controller to change the Rpm values and take readings until data for all the rotary speeds are recorded.
13. Switch off high-speed camera
14. Switch off the DC motor
15. Re-adjust the controller to set the liquid-solids flowrate to the next desired value
16. Re-adjust the gas controller to set the air flowrate to the next desired value
17. Repeat steps 9 – 16 until the required data has been acquired.

## Chapter 4

### Mathematical modelling of multiphase flow in annuli

#### 4.1 Reynolds number for annuli flow of non-Newtonian fluids

The prediction of the pressure loss in either single phase or two-phase flow in the drilling annuli requires the generalisation of a Reynolds number which is dependent on the rheological characteristics of the drilling fluid. The Reynolds number for fluid flow in any geometrical configuration can be interpreted as the ratio of inertial forces to viscous forces. This is a dimensionless number that allows for the estimation of the transition from laminar to turbulent flow conditions and is also used as a criterion for dynamic similitude. This means that if two geometrical configurations with different diameters, different flowrates or different fluid properties have the same dimensionless numbers, they are classified as dynamically similar.

The relationship between the friction factor and the Reynolds number for laminar isothermal flow of Newtonian fluids in cylindrical ducts can be expressed as follows:

$$\frac{f}{2} = \frac{\xi}{\text{Re}} \quad 4.1$$

The relationship between the friction factor and the frictional pressure gradient is given as

$$\frac{f}{2} = \frac{\tau_w}{\rho v^2} = \frac{dp}{dL} \frac{D_h}{4\rho v^2} \quad 4.2$$

and the Reynolds number for Newtonian fluid flow is

$$\text{Re} = \frac{\rho v D_h}{\mu} \quad 4.3$$

For non-Newtonian fluids the rheological models are shear rate dependent and there exists an apparent or effective viscosity that is highly dependent on not just the forces applied to the fluid, but the rheological properties of the fluid. Thus, the

determination of the Reynolds number for non-Newtonian fluids cannot be performed through the conventional approach applied to obtain the Reynolds number for the Newtonian annuli flows.

Metzner and Reed (1955) solved the momentum equations using the Power law model (Equation 2.1) to develop a generalised Reynolds number. They analytically obtained a relationship between the friction factor and the Reynolds number for a fully developed laminar flow in a pipe. This generalised Reynolds number when multiplied by the friction factor, produced the same result as the one given by a Newtonian fluid.

$$\text{Re} = \frac{\rho v^{2-n} D_h^n}{K \phi(n)^n \xi^{n-1}} \quad 4.4$$

The parameter  $\xi$  in the Equation 4.4 is the product of the friction factor and the Reynolds number for a Newtonian fluid under laminar flow conditions. The function  $\phi(n)$  is a hyperbolic function of the flow behaviour index which is largely dependent on the conduit geometry. This hyperbolic function may be represented generally in the following form

$$\phi(n) = \frac{un + 1}{(u + 1)n} \quad 4.5$$

where  $u$  is a geometrical parameter that is dependent on the cross-section the conduit and  $n$  is the flow behaviour index of the fluid. The geometrical parameter  $u$  is defined by

$$u = \frac{24}{\xi} \quad 4.6$$

Metzner and Reed defined the parameter  $\xi = 8$  for flow in circular ducts and  $\xi = 12$  for flow through infinite plates.

The Reynolds number derived using the Power law model cannot be used to characterise the Bingham plastic or the Herschel-Bulkley drilling fluids as these fluids have different rheological properties to that of the Power law drilling fluids. In this study, the generalised Reynolds number for the Bingham plastic or the Herschel-Bulkley drilling fluids are derived as the Power law theory is not capable of describing the viscosity characteristics of fluids with different rheological properties.

For non-Newtonian drilling fluids, the wall shear stress  $\tau_w$  in the equation has to be calculated by the appropriate viscosity law using the Equations 2.1-2.6. Since the shear rate is defined as the negative gradient of the velocity profile, the wall shear stress can be obtained if the expression of the velocity gradient is considered at the wall of the annuli pipe. For a Herschel-Bulkley drilling fluid, the shear stress at the wall of the annuli pipe can be expressed as

$$\tau_w = \tau_o + K \left( -\frac{dv}{dr} \right)_w^n \quad 4.7$$

For incompressible fully developed 2D flows of liquids with a rate-dependent viscosity, the calculation of shear rate is more complex because unlike that of Newtonian fluids the velocity profile is not parabolic. The true wall shear rate can be found using the Weissenberg-Rabinowitsch-Mooney (WRM) equation expressed for flow through a slit as

$$\left( -\frac{dv}{dr} \right)_w = \frac{1}{3} \left( -\frac{dv}{dr} \right)_{aw} \left[ 2 + \frac{1}{m} \right] \quad 4.8$$

The term  $(-dv/dr)_{aw}$  represents the apparent shear rate while the constant  $m$  is the gradient of the log-log plot of the shear stress against the shear rate and may be expressed as:

$$m = \frac{d \ln(\tau_w)}{d \ln(-dv/dr)_{aw}} = \frac{d \ln(\tau_w)}{d \ln(\gamma_{aw})} \quad 4.9$$

The constant  $m$  can be determined by the differentiation (chain rule) of the logarithmic expression as follows

$$m = \frac{d \ln(\tau_w)}{d \ln(\gamma_{aw})} = \frac{d \ln(\tau_o + K \gamma_{aw}^n)}{d \ln(\gamma_{aw})} \quad 4.10$$

$$m = \frac{d}{d \ln(\gamma_{aw})} \ln(\tau_o + K e^{n \ln(\gamma_{aw})}) \quad 4.11$$

$$m = \frac{n K \gamma_{aw}^n}{\tau_o + K \gamma_{aw}^n} \quad 4.12$$

The apparent shear rate at the wall of the annuli in the case of a Newtonian fluid flow can be expressed as

$$\gamma_{aw} = \left(-\frac{dv}{dr}\right)_{aw} = \frac{12v}{D_h} \quad 4.13$$

Substituting Equation 4.13 into Equation 4.8 and 4.12 and simplifying the result yields the final expression for the shear rate at the wall of the annuli as

$$\left(-\frac{dv}{dr}\right)_w = \left(\frac{2m+1}{3m}\right) \left(\frac{12v}{D_h}\right) \quad 4.14$$

$$m = \frac{n K \left(\frac{12v}{D_h}\right)^n}{\tau_o + K \left(\frac{12v}{D_h}\right)^n} \quad 4.15$$

Using Equation 4.14, the shear stress at the wall of the drilling annuli yields

$$\tau_w = \tau_o + K \left(\frac{2m+1}{3m}\right)^n \left(\frac{12v}{D_h}\right)^n \quad 4.16$$

For fluid flow through parallel plates, where  $\xi = 12$ , the relationship between the friction factor and the Reynolds number from Equation 4.1 can be written as

$$Re = \frac{24}{f} \quad 4.17$$

From Equation 4.2 and 4.16, the friction factor  $f$  can be expressed as

$$f = \frac{2\tau_w}{\rho v^2} = \frac{2 \left( \tau_o + K \left(\frac{2m+1}{3m}\right)^n \left(\frac{12v}{D_h}\right)^n \right)}{\rho v^2} \quad 4.18$$

Thus, the Reynolds number that characterises the flow of Herschel-Bulkley drilling fluids,  $Re_{HB}$  in a drilling annulus can be expressed as

$$Re_{HB} = 24 \frac{\rho v^2}{2 \left( \tau_o + K \left(\frac{2m+1}{3m}\right)^n \left(\frac{12v}{D_h}\right)^n \right)} \quad 4.19$$

This Equation for  $Re_{HB}$  can be expressed in the generalised form as

$$Re_{HB} = \frac{\rho v D_h}{\frac{\tau_o D_h}{12v} + K \left( \frac{2m+1}{3m} \right)^n \left( \frac{12v}{D_h} \right)^{n-1}} \quad 4.20$$

From Equation 4.20, it can be deduced that the equation for the effective or apparent viscosity of the Herschel-Bulkley drilling fluid for annuli flows is

$$\mu_{HB} = \frac{\tau_o D_h}{12v} + K \left( \frac{2m+1}{3m} \right)^n \left( \frac{12v}{D_h} \right)^{n-1} \quad 4.21$$

For a Power law fluid where the yield stress is zero  $\tau_o = 0$ , the constant  $m$  becomes equal to the flow behaviour index of the fluid,  $m = n$ . Thus, the Reynolds number and effective viscosity of the Power law drilling fluid can be expressed respectively as

$$Re_{PL} = \frac{\rho v D_h}{K \left( \frac{2m+1}{3m} \right)^n \left( \frac{12v}{D_h} \right)^{n-1}} \quad 4.22$$

$$\mu_{PL} = K \left( \frac{2m+1}{3m} \right)^n \left( \frac{12v}{D_h} \right)^{n-1} \quad 4.23$$

For drilling fluids described by the Bingham plastic rheological model, the shear stress at the annuli wall can be expressed from Equation 2.3 as

$$\tau_w = \tau_y + \mu_p \left( -\frac{dv}{dr} \right)_w \quad 4.24$$

$$\tau_w = \tau_y + \mu_p \left( \frac{2m+1}{3m} \right) \left( \frac{12v}{D_h} \right) \quad 4.25$$

Following the procedures as explained above, the constant  $m$  for the Bingham plastic fluid can be expressed as

$$m = \frac{\mu_p \left( \frac{12v}{D_h} \right)}{\tau_y + \mu_p \left( \frac{12v}{D_h} \right)} \quad 4.26$$

The Reynolds number for the Bingham plastic drilling fluid flow in the annuli  $Re_{BP}$ , can then be derived as follows

$$f = \frac{2\tau_w}{\rho v^2} = \frac{2 \left( \tau_y + \mu_p \left( \frac{2m+1}{3m} \right) \left( \frac{12v}{D_h} \right) \right)}{\rho v^2} \quad 4.27$$

$$Re_{BP} = \frac{\rho v D_h}{\frac{\tau_y D_h}{12v} + \mu_p \left( \frac{2m+1}{3m} \right)} \quad 4.28$$

Thus, the effective viscosity of the Bingham plastic drilling fluid can be expressed as

$$\mu_{BP} = \frac{\tau_y D_h}{12v} + \mu_p \left( \frac{2m+1}{3m} \right) \quad 4.29$$

## **4.2 Friction factor for laminar flow of non-Newtonian fluids**

The literature review in chapter 2 has indicated that the theoretical methods adopted for the calculation of the frictional pressure gradient for non-Newtonian fluid flows in the annuli have either neglected the effects of eccentricity, fluid rheology or drillpipe rotation. The friction factors determined with the concept of the friction geometry parameter has been applied for the determination of the frictional pressure gradient especially for two-phase flow. The friction geometry parameter has been developed for Newtonian fluid flow in the concentric and eccentric annuli and cannot be applied directly for the determination of the friction factor for non-Newtonian fluid flow. Another major concern is that these methods have neglected the drillpipe rotation effect and the shear thinning characteristics of the non-Newtonian drilling fluid, both of which are known to have a significant impact on the drilling hydraulics from field data and experimental reports. However, a vigorous treatment of the helical flow fields is possible for any annulus configuration and would be developed from the solution of the continuity equation. This section presents new methods for the determination of the friction factor for the concentric and eccentric annuli, with or without drillpipe rotation.

In a situation whereby a fluid flows through the annular space between the drillpipe and the casing during drilling operations, the drillpipe might be rotated at a certain angular velocity while the casing or borehole well is stationary. The motion of the fluid through the annuli would be purely due to the axial pressure gradient because the centrifugal force in the radial direction, produced by the rotary motion of the fluid, is compensated by the pressure and gravitational force in the radial direction and hence would not contribute to the motion of the fluid. The drilling fluid flow in this situation would move in a helical path creating the existence of an axial and tangential velocity component due to the rotation of the drillpipe. The equation of motion in the cylindrical coordinates (Equations 2.7-2.10) can be simplified to obtain two major equations that can describe the helical flow of fluids in the annuli. These equations can be expressed in terms of the axial and tangential shear stress gradients as

$$-\rho \frac{v_\theta^2}{r} = \rho g_r - \frac{\partial P}{\partial r} - \frac{1}{r} \frac{\partial \tau_{r\theta}}{\partial \theta}$$

$$\rho \frac{v_\theta}{r} \frac{\partial v_\theta}{\partial \theta} = \rho g_\theta - \frac{1}{r} \frac{\partial P}{\partial \theta} - \frac{1}{r^2} \frac{\partial}{\partial r} (r^2 \tau_{\theta r}) + \frac{1}{r} \frac{\partial \tau_{\theta\theta}}{\partial \theta} \quad 4.30$$

$$\rho \frac{v_\theta}{r} \frac{\partial v_z}{\partial \theta} = \rho g_z - \frac{\partial P}{\partial z} - \frac{1}{r} \frac{\partial}{\partial r} (r \tau_{zr}) + \frac{1}{r} \frac{\partial \tau_{z\theta}}{\partial \theta}$$

For concentric annuli helical flows, the flow is a function of  $r$  and does not vary in the radial direction  $\theta$ . Thus, these systems of equations can be simplified to yield

$$\frac{1}{r^2} \frac{\partial}{\partial r} (r^2 \tau_{\theta r}) = 0 \quad 4.31$$

$$\rho g_z - \frac{\partial P}{\partial z} - \frac{1}{r} \frac{\partial}{\partial r} (r \tau_{zr}) = 0 \quad 4.32$$

The first two terms in the Equation 4.32 can be combined and expressed as a modified pressure gradient ( $\partial P_m / \partial z$ )

$$\frac{\partial P_m}{\partial z} - \frac{1}{r} \frac{\partial}{\partial r} (r \tau_{zr}) = 0 \quad 4.33$$

The integration of these equations yields the equations for the axial  $\tau_{zr}$  and tangential  $\tau_{\theta r}$  shear stresses for fluid flow in a conduit, expressed respectively as

$$\tau_{zr} = \frac{\partial P_m}{\partial z} \frac{r}{2} + \frac{C_z}{r} \quad 4.34$$

$$\tau_{\theta r} = \frac{C_{\omega}}{r^2} \quad 4.35$$

The constants  $C_z$  and  $C_{\omega}$  in the axial and tangential shear stress equations are constants of integration.

#### 4.2.1 Generalised rheology model

A rheology model referred to as the generalised rheology model in this study, is used in the development of the methods for the prediction of the friction factors for non-Newtonian annuli flows. This generalised rheology model expresses the shear stress to shear rate relationship for the drilling fluid as

$$\tau = \tau_{\epsilon} + \epsilon \gamma^n \quad 4.36$$

The apparent viscosity may then be expressed as:

$$\mu_a = \frac{\tau_{\epsilon}}{\gamma} + \epsilon \gamma^{n-1} \quad 4.37$$

The constants  $\tau_{\epsilon}$ ,  $\epsilon$ , and  $n$  are the yield stress, consistency index, and flow behaviour index of the drilling fluid. This generalised model represents drilling fluids with the rheological behaviour described by the Power law, Bingham plastic or the Herschel-Bulkley rheology, depending on the input constants to the model. Table 4.1 shows the input constants dependent on the drilling fluid type.

Table 4.1: Constants for the generalised rheology model

Fluid rheology type	$\tau_\epsilon$	$\epsilon$	n
Newtonian	$\tau_\epsilon = 0$	$\epsilon = \mu$	$n = 1$
Power law (shear thinning)	$\tau_\epsilon = 0$	$\epsilon = K$	$n < 1$
Bingham plastic	$\tau_\epsilon = \tau_y$	$\epsilon = \mu_p$	$n = 1$
Herschel-Bulkley (shear thinning)	$\tau_\epsilon = \tau_o$	$\epsilon = K$	$n < 1$

Following this concept, a generalised Reynolds number for the drilling fluid annuli flow can be expressed as

$$Re_{Gen} = \frac{\rho v D_h}{\frac{\tau_\epsilon D_h}{12v} + \epsilon \left(\frac{2m+1}{3m}\right)^n \left(\frac{12v}{D_h}\right)^{n-1}} \quad 4.38$$

$$m = \frac{n \epsilon \left(\frac{12v}{D_h}\right)^n}{\tau_\epsilon + \epsilon \left(\frac{12v}{D_h}\right)^n} \quad 4.39$$

#### 4.2.2 Annuli shear stress and velocity profiles

When the drillpipe is rotated, the drilling fluid would experience a multi-directional shear force that creates the helical movement of the fluid. Thus, the shear stress to shear rate relationship, which is the fluid rheology model, must be represented in a tensor form. The magnitude of the shear rate for a multi-directional shear flow can be expressed in the cylindrical coordinate system as

$$|\gamma^2| = 2 \left[ \left(\frac{\partial v_r}{\partial r}\right)^2 + \left(\frac{1}{r} \frac{\partial v_\theta}{\partial \theta} + \frac{v_r}{r}\right)^2 + \left(\frac{\partial v_z}{\partial z}\right)^2 \right] + \left(\frac{1}{r} \frac{\partial v_z}{\partial \theta} + \frac{\partial v_\theta}{\partial z}\right)^2 + \left[\frac{1}{r} \frac{\partial v_r}{\partial \theta} + r \frac{\partial}{\partial r} \left(\frac{v_\theta}{r}\right)\right]^2 + \left(\frac{\partial v_z}{\partial r} + \frac{\partial v_r}{\partial z}\right)^2 \quad 4.40$$

For a concentric annulus, assuming that the axial and tangential velocity component ( $v_z$  and  $v_\theta$ ), existing in the helical flow are constant in the axial z-direction, and vary in the radial r-direction, the magnitude of the shear rate can be simplified to yield

$$|\gamma^2| = \left( r \frac{\partial}{\partial r} \left( \frac{v_\theta}{r} \right) \right)^2 + \left( \frac{\partial v_z}{\partial r} \right)^2 \quad 4.41$$

$$|\gamma| = \sqrt{\left( r \frac{\partial \omega}{\partial r} \right)^2 + \left( \frac{\partial v_z}{\partial r} \right)^2} \quad 4.42$$

where  $v_\theta = \omega r$

In the case where there is no drillpipe rotation and the drilling fluid flow is purely in the axial direction, the shear rate equation reduces to the conventional or general form for a 2D fluid flow  $\gamma = \partial v_z / \partial r$ . Similarly, the magnitude of the shear stress for the helical flow of fluids can be expressed as

$$|\tau| = \sqrt{\tau_{zr}^2 + \tau_{\theta r}^2} \quad 4.43$$

Adopting the form of the Newtonian model, the axial and tangential shear stresses may be expressed in form of their velocity gradients as:

$$\tau_{\theta r} = \mu_a \left( r \frac{\partial \omega}{\partial r} \right) \quad 4.44$$

$$\tau_{zr} = -\mu_a \left( \frac{\partial v_z}{\partial r} \right) \quad 4.45$$

The apparent viscosity of the drilling fluid subjected to a helical flow pattern, using the general model in Equation 4.37 and 4.42 is derived as follows:

$$\mu_a = \frac{\tau_\epsilon}{|\gamma|} + \epsilon |\gamma|^{n-1} \quad 4.46$$

$$\mu_a = \frac{\tau_\epsilon}{\left| \sqrt{\left( r \frac{\partial \omega}{\partial r} \right)^2 + \left( \frac{\partial v_z}{\partial r} \right)^2} \right|} + \epsilon \left| \sqrt{\left( r \frac{\partial \omega}{\partial r} \right)^2 + \left( \frac{\partial v_z}{\partial r} \right)^2} \right|^{n-1} \quad 4.47$$

Using Equation 4.44 and 4.45, the apparent viscosity equation can be further simplified to yield

$$\mu_a = \left[ \frac{\epsilon |\tau_{\theta r}^2 + \tau_{zr}^2|^{\frac{n-1}{2}}}{1 - \frac{\tau_\epsilon}{|\tau_{\theta r}^2 + \tau_{zr}^2|^{\frac{1}{2}}}} \right]^s \quad 4.48$$

where  $s = 1/n$

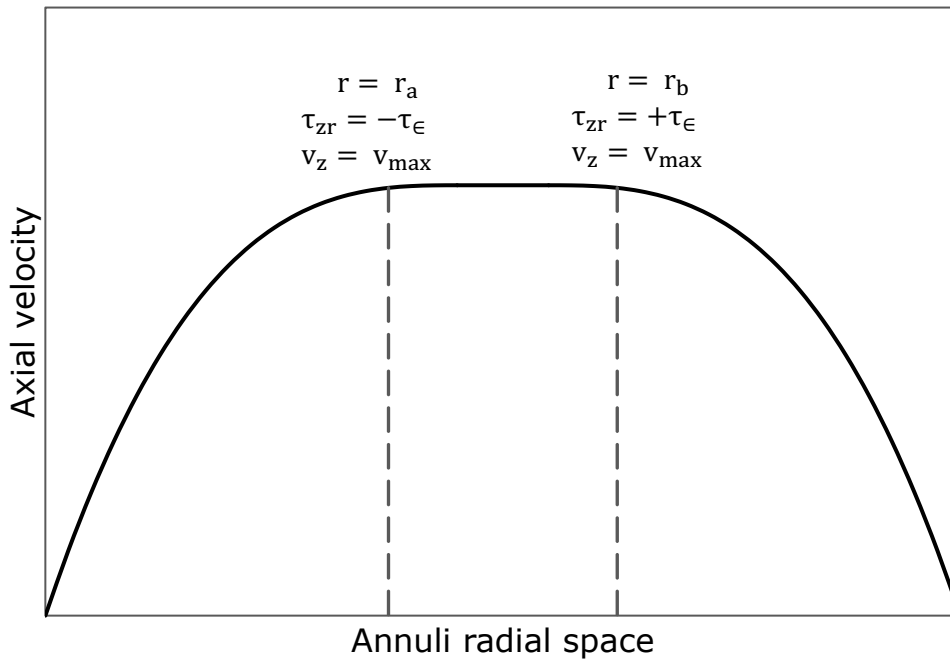


Figure 4.1: Annuli velocity profile of a non-Newtonian with a yield stress

Figure 4.1 shows the shape of the velocity profile for a fully developed annuli flow of non-Newtonian drilling fluids that possess a yield stress. For fluids with a yield stress to flow through the annuli, the axial pressure force must produce a shear stress that exceeds the yield stress  $\tau_{\epsilon}$ . Thus, as the fluid flows through the annuli, there is a region of the fluid that does not shear and the fluid elements in this region, move at the local maximum velocity. This unsheared region of the fluid is referred to as the unsheared plug. In the derivation of the shear stress and velocity profiles, the points that mark the boundaries of the unsheared plug in the radial direction are signified as the points  $r = r_a$  and  $r = r_b$  as shown in Figure 4.1. For the Herschel-Bulkley drilling fluid the shear stress at point  $r = r_a$  is equal to the negative value of the yield stress  $\tau_{zr} = -\tau_{\epsilon} = -\tau_0$  while the shear stress at the point  $r = r_b$  is equal to the positive value of the yield stress  $\tau_{zr} = +\tau_{\epsilon} = +\tau_0$ . Likewise, for the Bingham plastic fluid, the shear stresses at the points  $r = r_a$  and  $r = r_b$  are equal to the negative and positive value of the Bingham yield stress respectively  $\tau_{zr} = -\tau_{\epsilon} = -\tau_y$  and  $\tau_{zr} = +\tau_{\epsilon} = +\tau_y$ . The Power law fluid does not possess a yield stress and hence does not have the region of an unsheared plug in the annuli. In the axial velocity profile of the Power law fluid, the local maximum velocity exists at the point  $r_a = r_b$  and the shear stress at this point is zero  $\tau_{zr} =$

$\tau_{\epsilon} = 0$ . The width of the unsheared plug can be determined by considering a force balance of the pressure force being equal to the shear force in the region of the plug. The pressure force acts on the cross-sectional area of the plug, while the shear force, which is equal to the yield stress times the surface area of the plug, acts on the inner and outer surfaces of the plug. Performing this force balance over a differential length  $\partial z$  of the plug, yields the equation for the width of the plug as:

$$\pi(r_b^2 - r_a^2) \frac{\partial P_m}{\partial z} \partial z = 2\pi(r_b + r_a)\tau_{\epsilon} \partial z \quad 4.49$$

$$r_b - r_a = \frac{2\tau_{\epsilon}}{\frac{\partial P_m}{\partial z}} \quad 4.50$$

$$\tau_{\epsilon} = \frac{1}{2} \frac{\partial P_m}{\partial z} (r_b - r_a) \quad 4.51$$

It is obvious that the width of the plug depends on just the axial pressure gradient and the yield stress value of the fluid and is independent of the size of the annuli. However, in an eccentric annulus, the width of the unsheared plug and the position of the local maximum velocity varies across the angular direction of the annuli. Thus, the points  $r = r_a$  and  $r = r_b$  are a function of the angle  $\theta$  hence the shear stress and velocity profiles vary across the angular direction of the annuli and are direct functions of the angle  $\theta$ . To account for this phenomenon, the annuli can be represented by an infinite number of concentric annuli with variable outer radii  $r_2^{\epsilon}$  as shown in Figure 4.2.

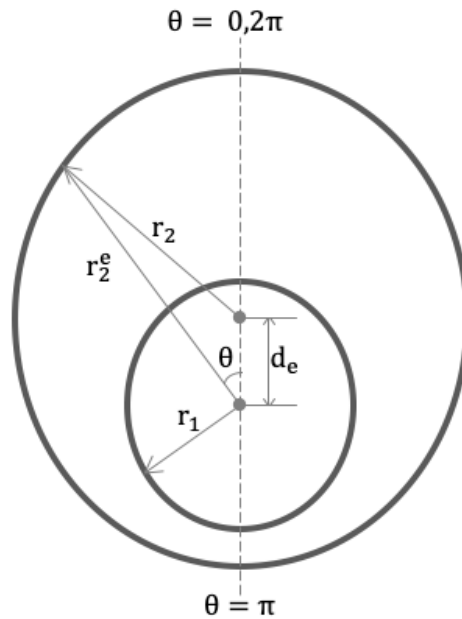


Figure 4.2: Eccentric annulus with a variable outer radius

The outer radius of the eccentric annulus is a function of the angle  $\theta$  and the eccentricity  $e$  and can be determined with the following equations:

$$r_2^e = d_e \cos \theta + \sqrt{r_2^2 - (d_e \sin \theta)^2} \quad 4.52$$

$$d_e = (r_2 - r_1)e \quad 4.53$$

By using this concept, the line  $r_1$  to  $r_2^e$  represents the distance from the inner pipe to the outer pipe of a given concentric annuli and hence the mechanical equations for the flow do not vary with  $\theta$  but only varies along the radial direction  $r$ . For this reason, the equations for the concentric annuli can be used to obtain a solution for the flow in the eccentric annuli.

The axial shear stress profile at a given angular position in the annuli may be obtained by applying the boundary conditions to Equation 4.34 that  $\tau_{zr} = -\tau_\epsilon$  at  $r = r_a$  and inserting the Equation 4.51 to the result to yield:

$$\tau_{zr}(\theta, r) = \frac{1}{2} \frac{\partial P_m}{\partial z} \left[ \left( r - \frac{r_a^2}{r} \right) - \frac{r_a(r_b - r_a)}{r} \right] \quad r_1 \leq r \leq r_a \quad 4.54$$

Similarly, from the boundary condition that  $\tau_{zr} = +\tau_\epsilon$  at  $r = r_b$ , the axial shear stress profile is

$$\tau_{zr}(\theta, r) = \frac{1}{2} \frac{\partial P_m}{\partial z} \left[ \left( r - \frac{r_b^2}{r} \right) + \frac{r_b(r_b - r_a)}{r} \right] \quad r_b \leq r \leq r_2^e \quad 4.55$$

where  $r_a = f(\theta, e)$  and  $r_b = f(\theta, e)$ .

Substituting the axial and tangential shear stress equations into the Equation 4.48 yields the equations for the annuli viscosity profile as:

$$\mu_a(\theta, r) = \frac{\left[ \left( \frac{C_\omega}{r^2} \right)^2 + \left( \frac{1}{2} \frac{\partial P_m}{\partial z} \left[ \left( r - \frac{r_a^2}{r} \right) - \frac{r_a(r_b - r_a)}{r} \right] \right)^2 \right]^{\frac{n-1}{2}}}{1 - \frac{\tau_\epsilon}{\left[ \left( \frac{C_\omega}{r^2} \right)^2 + \left( \frac{1}{2} \frac{\partial P_m}{\partial z} \left[ \left( r - \frac{r_a^2}{r} \right) - \frac{r_a(r_b - r_a)}{r} \right] \right)^2 \right]^{\frac{1}{2}}}} \quad 4.56$$

Inserting the shear stress profile equations into Equation 4.45 and integrating the results with the appropriate boundary conditions produces the velocity profile equation for fluid flow in the concentric and eccentric annulus, with or without drillpipe rotation. In the region of  $r_1 \leq r \leq r_a$ , the axial velocity of the fluid increases with an increase in  $r$ , so the axial velocity gradient can either be greater than or equal to 0,  $\partial v_z / \partial r \geq 0$ . Conversely, in the region of  $r_b \leq r \leq r_2^e$ , the axial velocity gradient is either zero or a negative value as the fluid velocity decreases with an increase in  $r$ . In the region of the maximum axial velocity or the plug region  $r_a \leq r \leq r_b$ , the axial velocity gradient is equal to zero  $\partial v_z / \partial r = 0$ . The velocity gradients or shear rate equations are thereby given as

$$\frac{\partial v_z}{\partial r} = \frac{1}{2\mu_a(\theta, r)} \frac{\partial P_m}{\partial z} \left[ \left( \frac{r_a^2}{r} - r \right) + \frac{r_a(r_b - r_a)}{r} \right] \quad r_1 \leq r \leq r_a \quad 4.57$$

$$\frac{\partial v_z}{\partial r} = 0 \quad r_a \leq r \leq r_b \quad 4.58$$

$$\frac{\partial v_z}{\partial r} = \frac{1}{2\mu_a(\theta, r)} \frac{\partial P_m}{\partial z} \left[ \left( r - \frac{r_b^2}{r} \right) + \frac{r_b(r_b - r_a)}{r} \right] \quad r_b \leq r \leq r_2^e \quad 4.59$$

Integrating Equation 4.57 and applying the no-slip boundary condition that  $v_z(\theta, r) = 0$ , at the drillpipe wall  $r = r_1$  yields the axial velocity profile:

$$v_z(\theta, r) = \frac{1}{2} \frac{\partial P_m}{\partial z} \int_{r_1}^r \frac{1}{\mu_a(\theta, r)} \left[ \left( \frac{r_a^2}{r} - r \right) + \frac{r_a(r_b - r_a)}{r} \right] dr \quad r_1 \leq r \leq r_a \quad 4.60$$

Similarly, integrating Equation 4.59 while applying the no-slip boundary condition that  $v_z(\theta, r) = 0$ , at the drillpipe wall  $r = r_2^e$  yields:

$$v_z(\theta, r) = \frac{1}{2} \frac{\partial P_m}{\partial z} \int_r^{r_2^e} \frac{1}{\mu_a(\theta, r)} \left[ \left( r - \frac{r_b^2}{r} \right) + \frac{r_b(r_b - r_a)}{r} \right] dr \quad r_b \leq r \leq r_2^e \quad 4.61$$

In the region  $r_a \leq r \leq r_b$ ,  $v_z(\theta, r) = v_z(\theta, r_a) = v_z(\theta, r_b) = v_{z\max}(\theta)$

The angular velocity profile may be derived from Equation 4.44 as follows

$$\frac{\partial \omega}{\partial r} = \frac{1}{\mu_a(\theta, r)} \frac{C_\omega}{r^3} \quad 4.62$$

Integrating the above equation and applying the boundary condition that the angular velocity is maximum at the drillpipe wall,  $\omega = \omega_{\max}$  at  $r = r_1$  we can arrive at:

$$\omega(\theta, r) = \omega_{\max} - C_{\omega}(\theta, r) \int_{r_1}^r \frac{dr}{\mu_a(\theta, r) r^3} \quad 4.63$$

The volume flow rate for the generalised drilling fluid flow through the concentric and eccentric annulus with or without drillpipe rotation annulus can be expressed by integrating the velocity distribution over the entire annulus region while applying the appropriate boundary conditions:

$$Q = \int_0^{2\pi} \int_{r_1}^{r_2^e} v_z(\theta, r) r \, dr d\theta \quad 4.64$$

Substituting the equations for the axial velocity profiles into Equation 4.63, the equation for the volume flow rate becomes:

$$\begin{aligned} Q = & \frac{1}{4} \frac{\partial P_m}{\partial z} \int_0^{2\pi} (r_a^2 - r^2) \int_{r_1}^{r_a} \frac{1}{\mu_a(\theta, r)} \left[ \left( \frac{r_a^2}{r} - r \right) + \frac{r_a(r_b - r_a)}{r} \right] dr d\theta \\ & + \frac{1}{4} \frac{\partial P_m}{\partial z} \int_0^{2\pi} (r_a^2 - r_b^2) \int_{r_1}^{r_a} \frac{1}{\mu_a(\theta, r)} \left[ \left( \frac{r_a^2}{r} - r \right) + \frac{r_a(r_b - r_a)}{r} \right] dr d\theta \\ & + \frac{1}{4} \frac{\partial P_m}{\partial z} \int_0^{2\pi} (r^2 - r_b^2) \int_{r_b}^{r_2^e} \frac{1}{\mu_a(\theta, r)} \left[ \left( r - \frac{r_b^2}{r} \right) + \frac{r_b(r_b - r_a)}{r} \right] dr d\theta \end{aligned} \quad 4.65$$

The constant  $C_{\omega}(\theta, r)$  can be determined by applying the no-slip boundary condition that  $\omega = 0$  at the outer wall of the annulus  $r = r_2^e$ , thereby arriving at:

$$C_{\omega}(\theta, r) = \frac{\omega_{\max}}{\int_{r_1}^{r_2^e} \frac{dr}{\mu_a(\theta, r) r^3}} \quad 4.66$$

The following function can be used to determine the radial position  $r_a = f(\theta, e)$  and  $r_b = f(\theta, e)$ .

$$f(r_a, r_b) = \int_{r_1}^{r_a} \frac{1}{\mu_a(\theta, r)} \left[ \left( \frac{r_a^2}{r} - r \right) + \frac{r_a(r_b - r_a)}{r} \right] dr$$

$$- \int_{r_b}^{r_2^e} \frac{1}{\mu_a(\theta, r)} \left[ \left( r - \frac{r_b^2}{r} \right) + \frac{r_b(r_b - r_a)}{r} \right] dr \quad 4.67$$

Due to the complexity of these fluid flow equations, there is currently no method by which an analytical resolution or simplification can be derived towards the solution of the fluid flow equations. Thus, these equations, must be solved simultaneously using numerical integration and iterative methods. However, special iterative methods should be applied in other to reduce the computational cost of the solution. From the solution of these fluid flow equations, Figures 4.3 to 4.8 are presented to show the combined effect of drillpipe rotation and eccentricity on the fluid velocities for a non-Newtonian drilling fluid flowing through a concentric and eccentric annulus. The inner and outer pipe sizes used for this case study are 40mm and 80mm respectively and the fluid rheological parameters were selected from public domain to represent a Power law drilling fluid. The parameters for the Power law fluid were  $\tau_{\epsilon} = 0, Pa$ ,  $\epsilon = 0.096, Pa s^n$  and  $n = 0.75$ , while for the Herschel-Bulkley fluid a yield stress of  $\tau_{\epsilon} = 0.5, Pa$  was included to the parameters in order to simulate the behaviour of the Herschel-Bulkley drilling fluid. The drilling fluid flowrate for both fluid types was  $6.696 m^3/h$ , the eccentricity value was  $e = 0.7$  and the drillpipe rotary speeds were varied from 0 to 300 rpm.

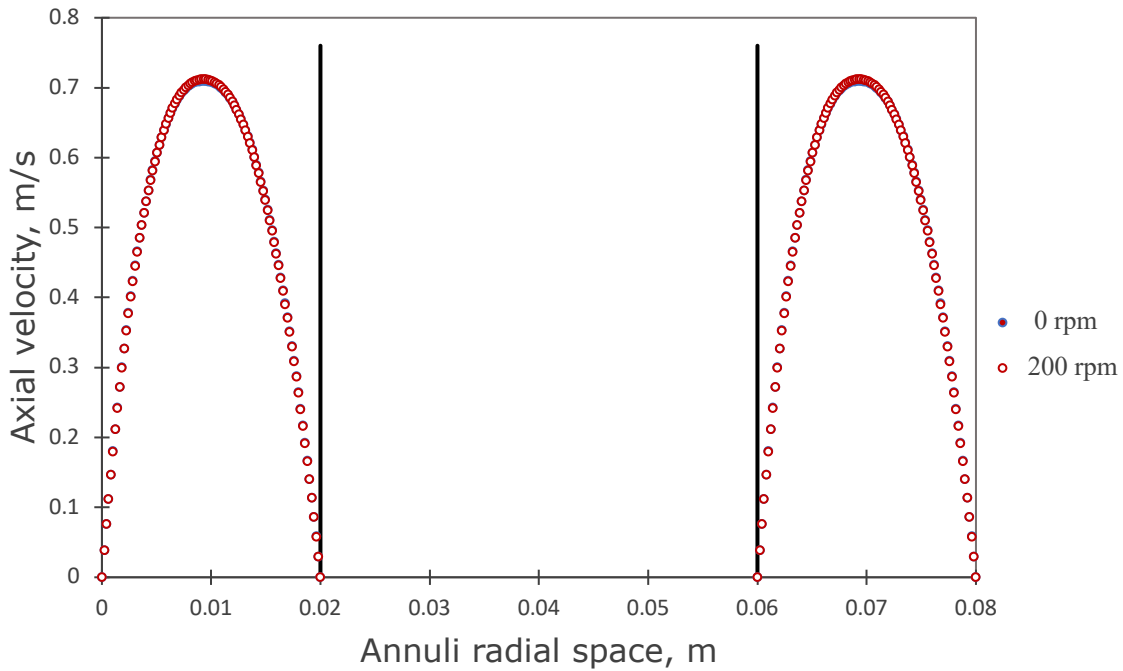


Figure 4.3: Axial velocity profiles for the Power law fluid flow in the concentric annulus with drillpipe rotation

The axial velocity fields existing in the angular position  $\theta = 0$  and  $\theta = \pi$  are determined in order to theoretically examine the combined effect of drillpipe rotary speeds and eccentricity in the drilling annuli. For an eccentric annulus geometry, the angular position  $\theta = 0$  represents the largest region of the annuli while the position  $\theta = \pi$  is the region with the smallest radial distance from the drillpipe wall to the outer pipe.

The results obtained for the case of the concentric annulus  $e = 0$  shows that when the drilling fluid flowrate is held constant, an increase in the drillpipe rotary speed has very little or no effect on the annuli axial velocity distribution and there is no change in the axial velocity in the angular direction (Figure 4.3). For the Power law fluid, the radial position  $r = r_a = r_b$  is the location where the local maximum axial velocity exists across the angular direction of the annuli. For the eccentric annulus  $e = 0.7$  without the drillpipe rotation, the axial velocity at the angular position  $\theta = 0$  significantly increases, while the axial velocity at the angular position  $\theta = \pi$  decreases to become a region of relatively very little fluid flow or near stagnancy (Figure 4.4). At this region of low fluid flow in the eccentric

annulus, the drill cuttings may tend to accumulate to form a stationary cuttings bed.

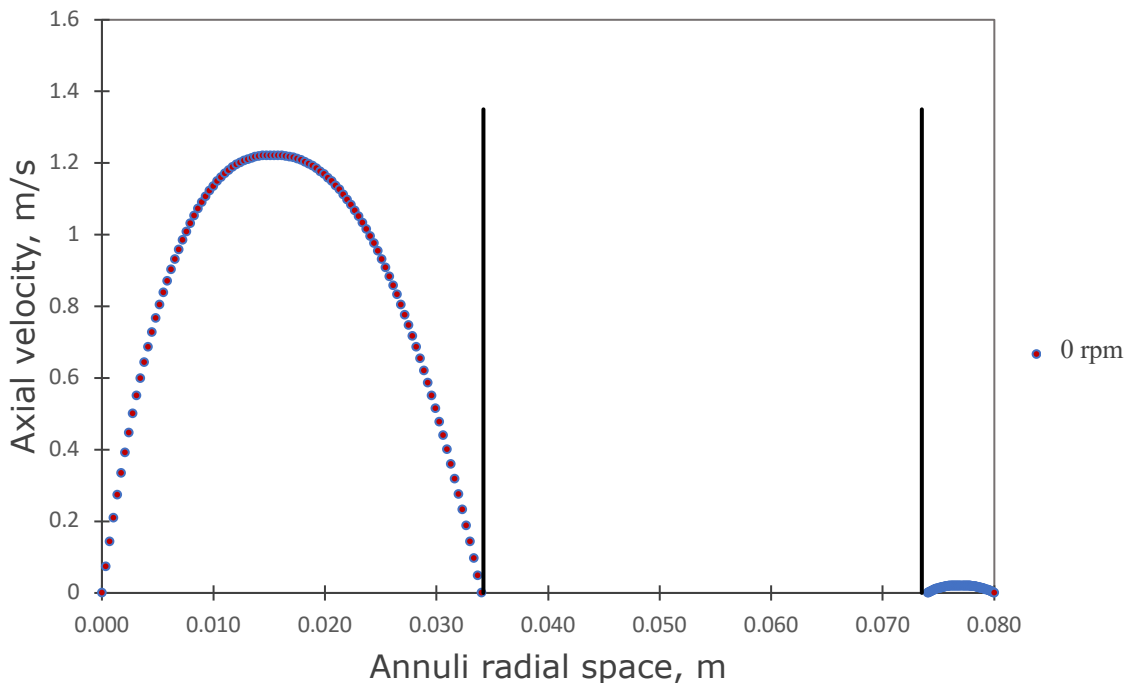


Figure 4.4: Axial velocity profiles for the Power law fluid flow in the eccentric annulus with drillpipe rotation

Figures 4.5 and 4.6 show the effect of drillpipe rotation on the axial velocity for the angular position  $\theta = 0$  and  $\theta = \pi$  respectively. When the flowrate is held constant, an increase in the pipe rotary speed leads to a slight decrease in the axial velocity in the angular position  $\theta = 0$  and a significant increase in the axial velocity in the angular position  $\theta = \pi$ . The axial velocity at the other angular positions in the annuli also either increase or decrease with increase in drillpipe rotation, depending on the radial distance from the drillpipe to the outer pipe and the local apparent viscosity of the fluid. These results explain why the eccentric annulus has been reported in literature to encourage the accumulation of drill cuttings at the bottom of the annuli and why drillpipe rotation may significantly improve the cutting transport or prevent the formation of a stationary bed.

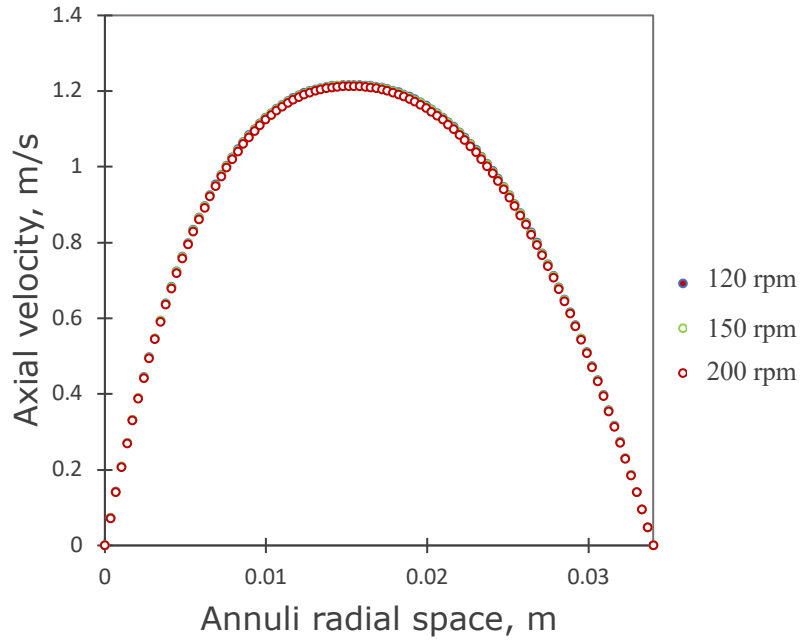


Figure 4.5: Effect of drillpipe rotation on the axial velocity at the largest region of the eccentric annulus for the Power law fluid flow

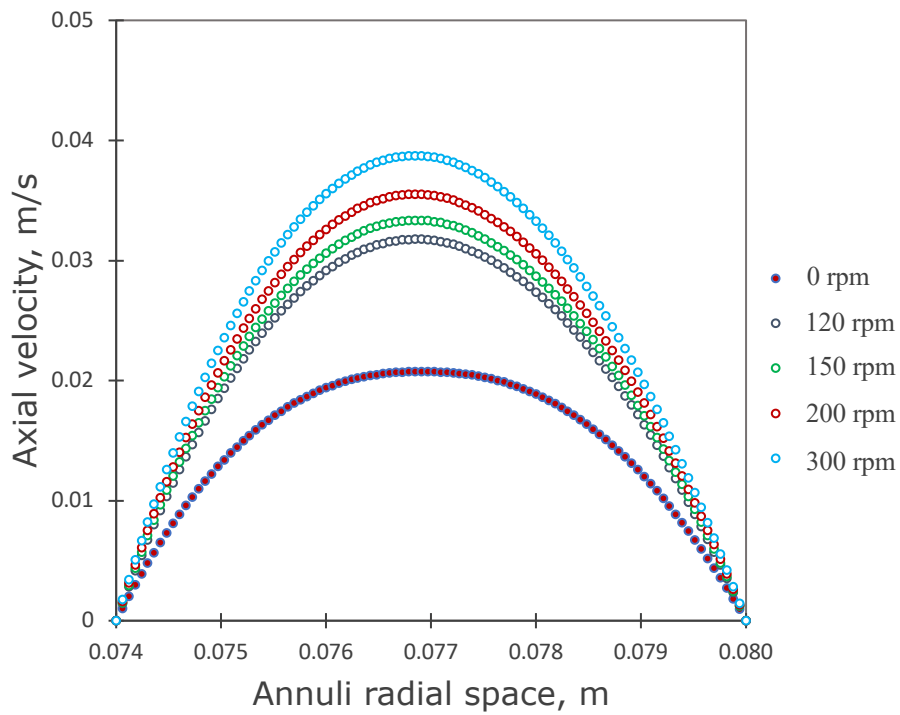


Figure 4.6: Effect of drillpipe rotation on the axial velocity at the smallest region of the eccentric annulus for the Power law fluid flow

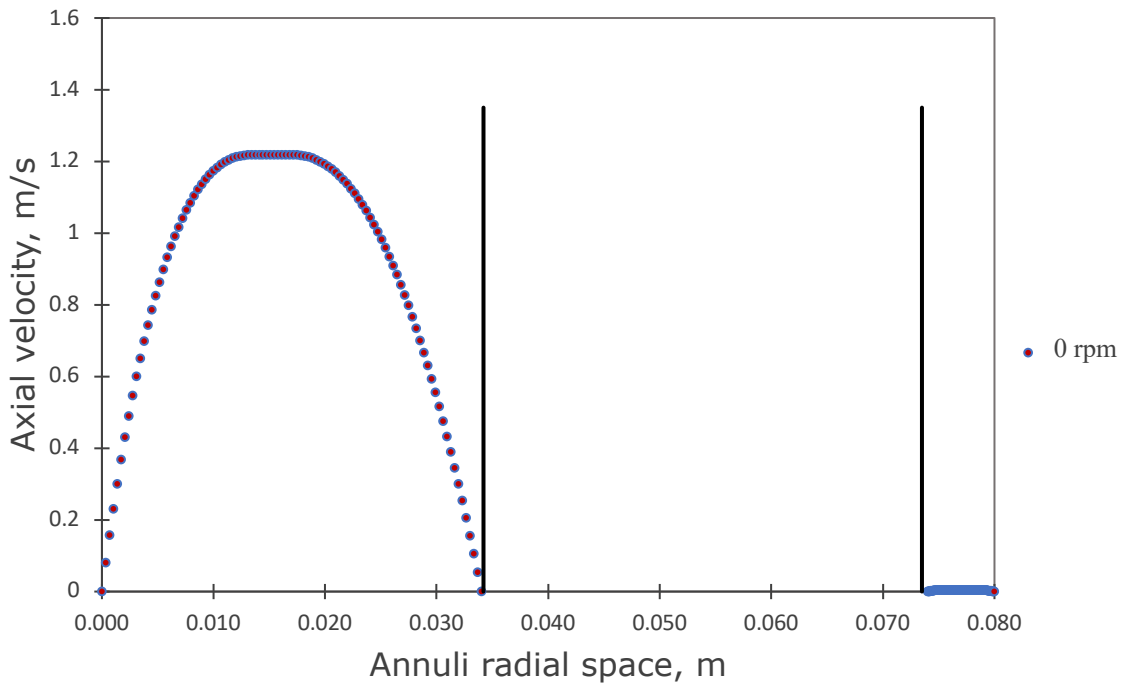


Figure 4.7: Axial velocity profiles for the Herschel-Bulkley fluid flow in the eccentric annulus with drillpipe rotation

Figure 4.7 shows the axial velocity for the Herschel-Bulkley fluid flow in the eccentric annulus. Similarly, for the Power law fluid flow in the eccentric annulus, the axial velocity in the largest region in the annulus largely increases while that of the smallest region decreases to an almost no flow zone. It is obvious that the reason for this is that the resistance of flow between the layers of the fluid are greater in the smaller region than the enlarged region of the annuli, leading to a disproportionate distribution of the velocity fields across the annulus. The increase in the drillpipe rotary speed leads to an increase in the axial velocity of the fluid at the region where there is relatively very little flow in the eccentric annulus for the Herschel-Bulkley fluid. From Figures 4.6 and 4.8, it can be deduced that drillpipe rotation can improve the fluid flow in the smallest region of the eccentric annuli by over 50% for a Power law or Herschel-Bulkley non-Newtonian drilling fluid. However, even though the drillpipe rotation may tend to improve the cuttings transport efficiency, the effect of drillpipe rotation on the annuli pressure gradient must be considered simultaneously in order to manage wellbore pressures.

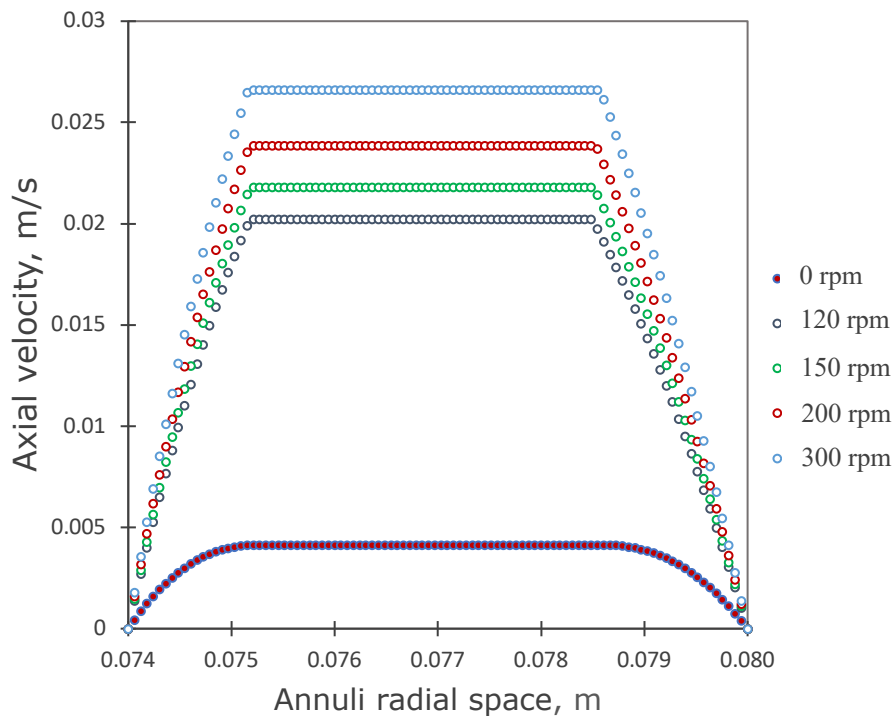


Figure 4.8: Effect of drillpipe rotation on the axial velocity at the smallest region of the eccentric annulus for the Herschel-Bulkley fluid flow.

### 4.3 Friction geometry parameter

The friction factor for fluid flow through annuli configurations has been calculated using the friction geometry parameter obtained from the analytical solution of the continuity equation and equations of motion for fully developed Newtonian steady state axial fluid flow. For the eccentric annuli, analytical solutions using the bipolar coordinate system has also been obtained for Newtonian axial fluid flow under steady state assumptions.

These analytical solutions cannot be applied to obtain solutions for non-Newtonian Concentric/Eccentric laminar fluid flows especially in a helical annulus. However, a vigorous treatment of the helical flow fields is possible for any annulus configuration and has been developed from the solution of the continuity equation and the general momentum equations governing fluid flow.

The fanning friction factor for a concentric/eccentric annulus with or without rotation, considering the generalized non-Newtonian fluid flow can be expressed as:

$$f = \frac{F_{\pi}}{Re_{Gen}} \quad 4.68$$

The generalised Reynolds number  $Re_{Gen}$  for the drilling fluid annuli flow can be obtained from Equations 4.38 and 4.39, the parameter  $F_{\pi}$  in Equation 4.68 represents the annuli geometry parameter and the frictional pressure gradient for single phase drilling fluid flow in a concentric/eccentric annulus, with or without drillpipe rotation can then be calculated from:

$$\frac{dP}{dL} = \frac{2f\rho v^2}{D_h} \quad 4.69$$

From the solution of the governing equations for non-Newtonian fluid flow, the friction geometry parameter for the concentric and eccentric annulus, with or without drillpipe rotation, the annuli geometry parameter can be obtained from the following equations

$$\begin{aligned} S_{\pi} = & \int_0^{\pi} (r_a^2 - r^2) \int_{r_1}^{r_a} \frac{1}{\mu_a(\theta, r)} \left[ \left( \frac{r_a^2}{r} - r \right) + \frac{r_a(r_b - r_a)}{r} \right] r dr d\theta \\ & + \int_0^{\pi} (r_a^2 - r_b^2) \int_{r_1}^{r_a} \frac{1}{\mu_a(\theta, r)} \left[ \left( \frac{r_a^2}{r} - r \right) + \frac{r_a(r_b - r_a)}{r} \right] r dr d\theta \\ & + \int_0^{\pi} (r^2 - r_b^2) \int_{r_b}^{r_2^e} \frac{1}{\mu_a(\theta, r)} \left[ \left( r - \frac{r_b^2}{r} \right) + \frac{r_b(r_b - r_a)}{r} \right] r dr d\theta \end{aligned} \quad 4.70$$

$$I_{\omega f} = 4S_{\pi}\mu_{Gen} \quad 4.71$$

$$F_{\pi} = \frac{\pi(d_2 + d_1)D_h^3}{I_{\omega f}} \quad 4.72$$

$$\mu_{Gen} = \frac{\tau_{\epsilon}D_h}{12v} + \epsilon \left( \frac{2m+1}{3m} \right)^n \left( \frac{12v}{D_h} \right)^{n-1} \quad 4.73$$

$$m = \frac{n \in \left( \frac{12v}{D_h} \right)^n}{\tau_{\epsilon} + \epsilon \left( \frac{12v}{D_h} \right)^n}$$

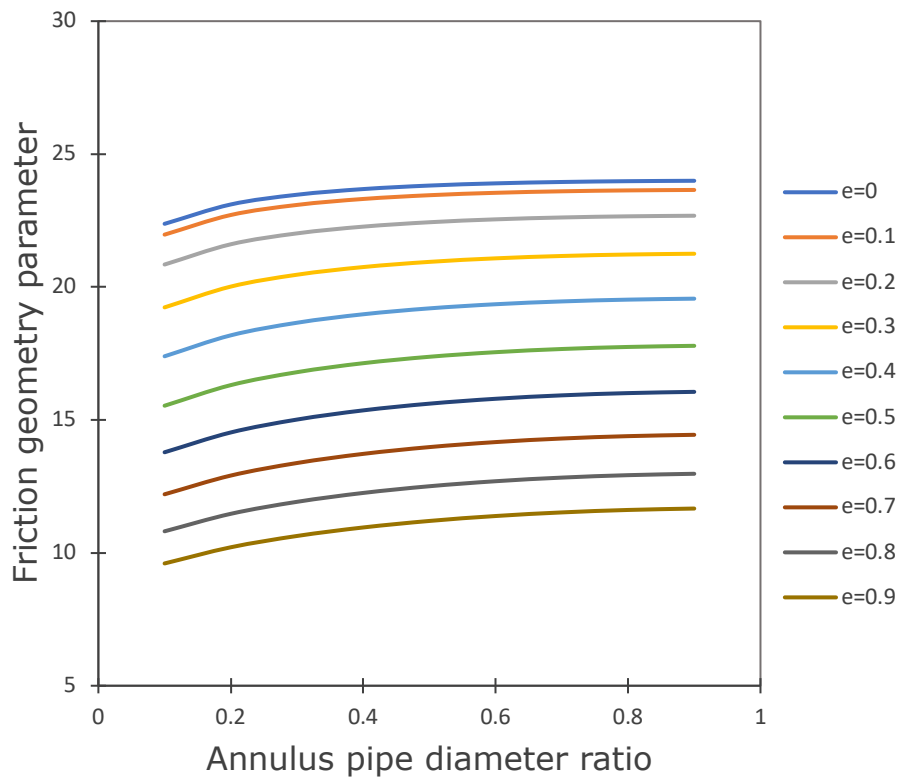


Figure 4.9: Friction geometry parameter plot ( $n = 0.75$ )

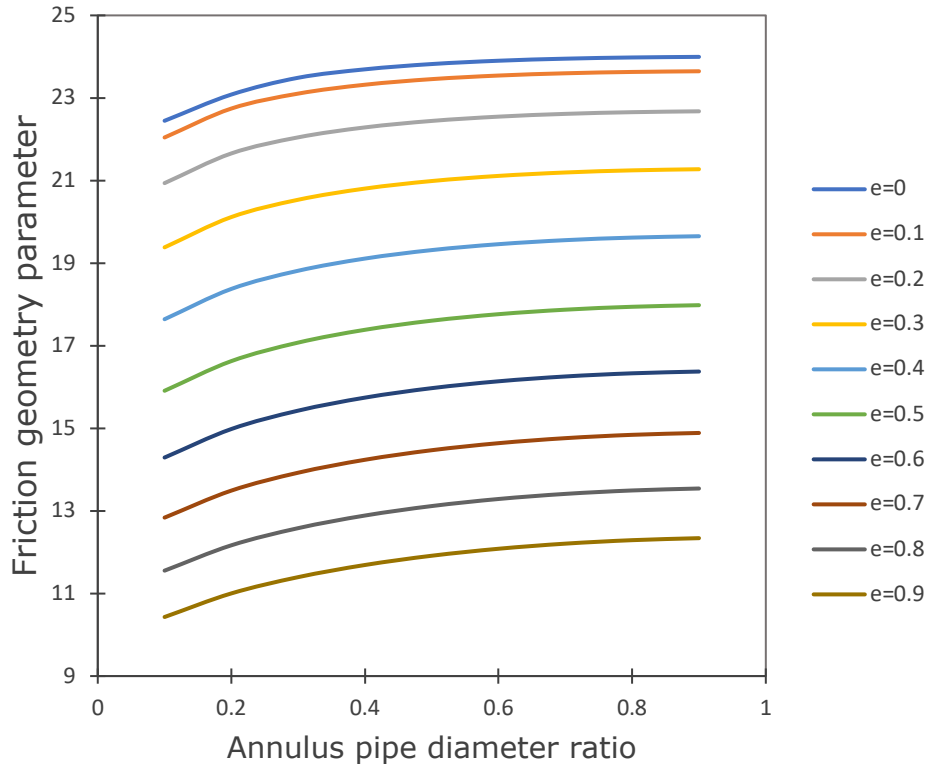


Figure 4.10:Friction geometry parameter plot ( $n = 0.55$ )

Figures 4.9 and 4.10 show that the friction geometry parameter for non-Newtonian annuli fluid flow is significantly dependent on the flow behaviour index and the flow rate of fluid. For the Herschel-Bulkley fluid, the friction geometry parameter is not only dependent on just the flow behaviour index and fluid flow rate but is also dependent on the yield stress of the fluid. This emphasises why the friction geometry parameter developed for the Newtonian annuli fluid flow cannot be applied to calculate the friction factor for non-Newtonian annuli fluid flow.

Table 4.2:Input parameters for sample calculations

<b>Input</b>	
Outer wall/casing diameter, m	0.08
Drillpipe diameter, m	0.04
Flow rate, $\text{m}^3/\text{h}$	6.7
Fluid density $\text{kg}/\text{m}^3$	800
Consistency index, $\text{pa}\cdot\text{s}^n$	0.096
Flow behaviour index	0.75

The friction geometry parameter values obtained from the newly developed analytical model was compared the that which was suggested by Caetano et al. (1992) for the friction geometry parameter for laminar flow of Newtonian fluids in annuli (Table 4.3). The results showed that values matched perfectly with an absolute error of  $\pm 0$ .

Table 4.3: Friction geometry parameter values for Newtonian fluid flow at different pipe diameter ratios in the concentric annuli ( $e = 0$ ).

Pipe diameter ratio	Friction geometry parameter ( $e = 0$ )	
	Caetano et al. (1992)	New analytical model
0.1	22.3430	22.3430
0.2	23.0881	23.0881
0.3	23.4612	23.4612
0.4	23.6783	23.6783
0.5	23.8125	23.8125
0.6	23.8970	23.8970
0.7	23.9495	23.9495
0.8	23.9801	23.9801
0.9	23.9956	23.9956

Furthermore, sample calculations for the pressure gradient in annuli flows, performed using the data given in Table 4.2 were compared to the pressure gradient obtained using Hacıislamoglu and Langlinais (1990) empirical correlation (Equation 2.28 and 2.29) which has been applied by various studies to calculate the pressure gradient in an eccentric annulus. Hacıislamoglu and Langlinais (1990) claimed that their empirical correlation has an accuracy of  $\pm 5\%$  and is valid for eccentricities from 0 to 0.95, pipe diameter ratios of 0.3 to 0.9 and flow behaviour indices of 0.4 to 1.0. However, the comparison of the analytical model showed a maximum deviation of about 7%. The Hacıislamoglu and Langlinais (1990) empirical correlation was developed for Power law non-Newtonian annuli fluid flow and cannot be applied for annuli flow of non-Newtonian fluids with other rheological characteristics. However, the new model can be applied to calculate the frictional pressure gradient for the laminar flow of Power law, Bingham plastic and Herschel-Bulkley drilling fluids in a concentric and eccentric annulus, with or without drillpipe rotation.

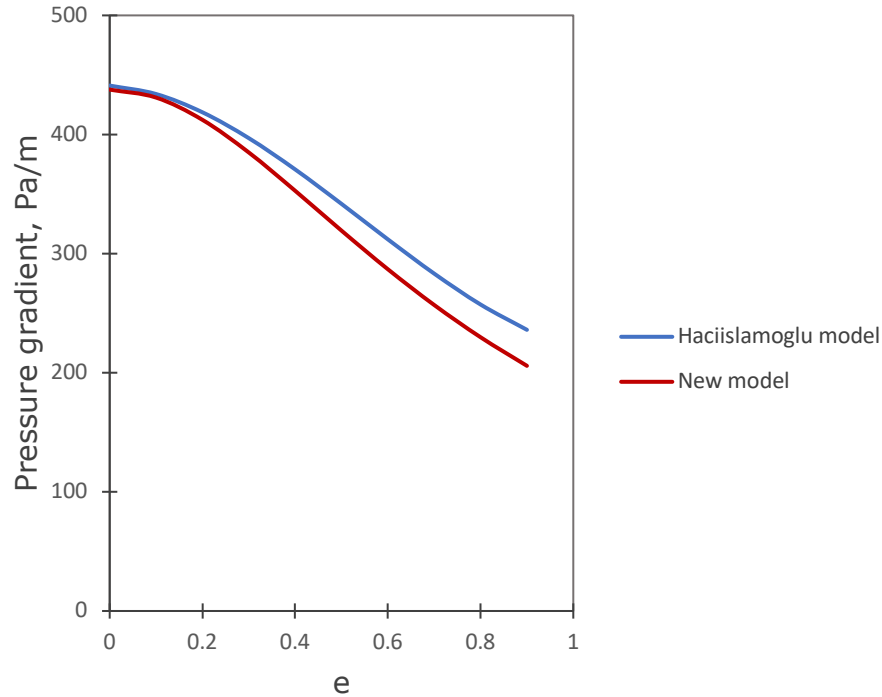


Figure 4.11: Pressure gradient versus eccentricity

Figure 4.12 and 4.13 shows the trends of the friction geometry parameter for the helical flow of non-Newtonian Power law fluid flow in the eccentric annuli. It can be seen that the friction geometry parameter for non-Newtonian fluid flow decreases with an increase with drillpipe rotary speed. However, for low annulus pipe diameter ratios, the effect of the drillpipe rotation on the friction geometry parameter is insignificant. This is mainly because the axial force is a lot more dominant than the tangential force due to the large annular gap between the drillpipe and the outer wall/casing. Thus, the fluid in the annuli is subjected to a low tangential shear rate, resulting in a relatively lower effect on the axial pressure gradient. For larger pipe diameter ratios, the tangential shear rate due to the drillpipe rotation is higher as the annular gap between the drillpipe and the outer wall/casing reduces. At very high annulus pipe diameter ratios, the effect of drillpipe rotation on the friction geometry parameter becomes less significant.

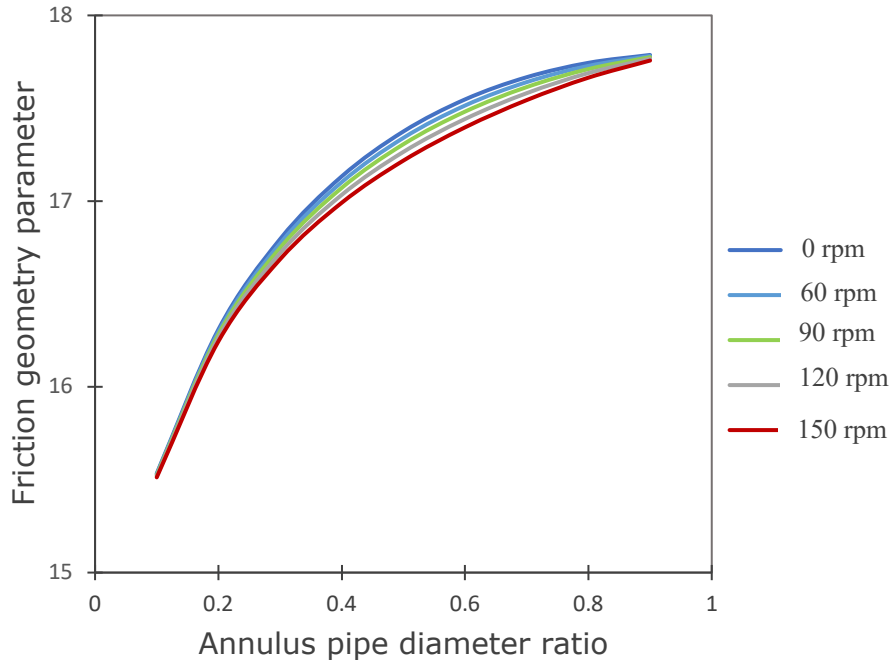


Figure 4.12: Effect of drillpipe rotation on the friction geometry parameter ( $e = 0.5, n = 0.75$ )

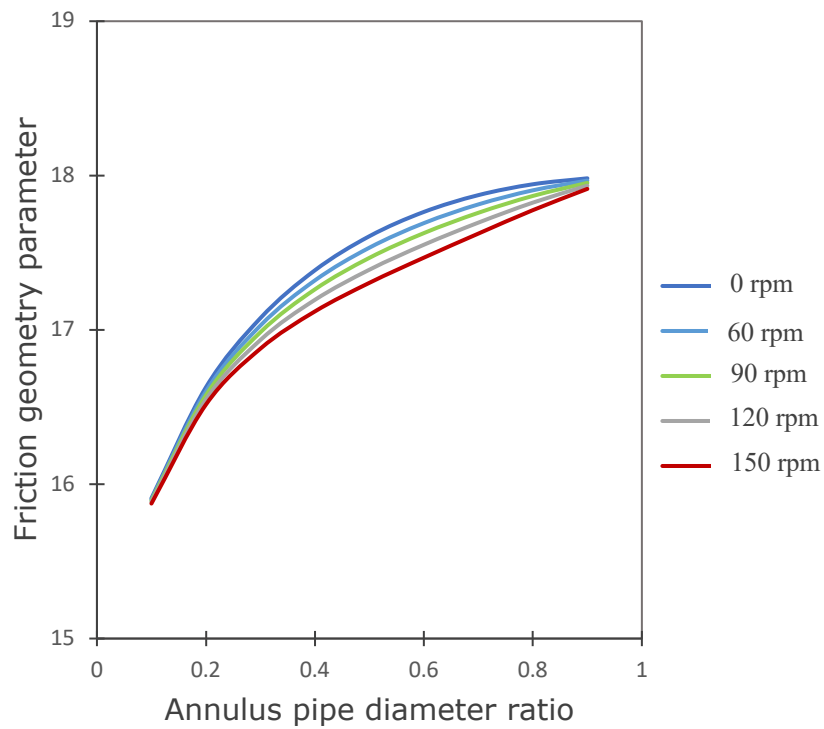


Figure 4.13: Effect of drillpipe rotation on the friction geometry parameter ( $e = 0.5, n = 0.55$ )

#### 4.4 Friction factor for turbulent flow of non-Newtonian fluids

There is no rigorous or exact method available for the prediction of the friction factor for annuli or pipe flows under turbulent flowing conditions till date. However, the friction factor for single phase turbulent flows can be predicted from the application of three main methods: The empirical approach, semi-empirical approach and the universal velocity distribution (Caetano, et al., 1992).

The semi-empirical approach involves the use of experimental data for turbulent flow in combination with characteristics of laminar flow in the same noncircular configuration. An example of this prediction category is the procedure of Gunn and Darling (1963). An important conclusion by Gunn and Darling is that the similarity existing between friction factors for circular and noncircular configurations in the laminar region is also accompanied by a similarity in the turbulent region. Using dimensional analysis, they showed that for turbulent flow in noncircular sections, the following functional dependency for friction factor exists.

$$f = \phi \left( \text{Re}, \frac{F_C}{F_{NC}} \right) \quad 4.74$$

The term  $\frac{F_C}{F_{NC}}$  is the ratio of the friction geometry parameters for circular and noncircular conduits. The friction factor is inversely proportional to the ratio  $\frac{F_C}{F_{NC}}$  at low Reynolds number and independent of the ratio at high Reynolds number.

In this study, the Gunn and Darling (1963) method is applied to predict the friction factor for Non-Newtonian turbulent flows through the annuli, by modifying the method suggested by Caetano et al (1992) for Newtonian fluid flow through a concentric and eccentric annulus. This method has been reported to be beneficial for turbulent friction factor predictions due to its simplicity and good performance (Brill & Mukherjee, 1999).

The non-Newtonian turbulent friction factor with or without drillpipe rotation for a concentric and eccentric annulus may be predicted from the following equations using the generalised Reynolds number  $\text{Re}_{\text{Gen}}$  for the drilling fluid annuli flow and

the friction geometry parameter for laminar steady state flow through the annuli.

$$\left(f\left(\frac{16}{F_{\pi}}\right)^A\right)^{-0.5} = 4 \log\left(\text{Re}_{\text{Gen}} \left[f\left(\frac{16}{F_{\pi}}\right)^A\right]^{0.5}\right) - 0.4 \quad 4.75$$

$$A = 0.45e^{[-(\text{Re}_{\text{Gen}}-3000)/10^6]} \quad 4.76$$

#### 4.5 Multiphase drilling hydraulics modelling

When two or more phases flow simultaneously in through annuli configurations, the flow behaviour a lot more complex than that of the single-phase flow. The phases separate and the shear stresses at the pipe wall are different for each phase due to the differences in their densities and viscosities. For liquid and gas flows, the expansion of the highly compressible gas phase with decreasing pressure increases the in-situ volumetric flow rate of the gas. As a result, the liquid and gas phases do not travel at the same velocity in the pipe. For upward flow, the less dense and less viscous gas phase tends to flow faster than the liquid phase, while for downward flows, the liquid phase flows faster than the gas phase. This phenomenon, generally referred to as slippage, significantly influences the pressure gradient in the annuli and has to be taken into account when performing pressure gradient predictions. Different flow patterns can exist in the drilling annulus as a result of the large pressure and temperature changes the fluids encounter. The prevailing flow pattern has a significant influence on the pressure and temperature gradients in the annuli as the buoyancy, turbulence and surface tension forces vary significantly with fluid flow rates, wellbore sizes, inclination angle, and fluid properties of the phases that make up the drilling fluid. Thus, the ability to predict the flow pattern as a function of the drilling parameters is of primary importance for wellbore pressure management. Many empirical correlations have been developed to predict the flow pattern, slippage between phases and the frictional pressure gradient for pipes and annuli configurations.

However, these approaches often present major disadvantages due to the high degree of empiricism applied towards the predicting of the fluid flow behaviour. In this study, a mechanistic approach that relies on the fundamental mechanisms that govern multiphase flow of fluids in annuli, has been applied to develop flow pattern specific models that rely much less on empirical correlations. Mechanistic models have been developed for the Dispersed bubble, bubble, stratified and slug flow patterns as these flow patterns have been reported to be most likely encountered in a drilling wellbore. Flow pattern prediction techniques used in this study are similar to the methods presented by Caetano, et al., (1992) for annuli flows. The drilling hydraulics models for each of the flow patterns have been developed as detailed in the following sections by exploiting the fundamental physics governing two-phase flow in a conduit.

### **Model development**

The basis for virtually all computations involving fluid flow in annuli is the conservation of mass, momentum and energy. Application of these principles permits the prediction of pressure and temperature changes with respect to time and space across an entire drilling wellbore. The conservation of mass in a control volume can be expressed as:

$$\frac{\partial \rho}{\partial t} + \frac{\partial \rho V}{\partial L} = 0 \quad 4.77$$

For a steady state flow, it is assumed that there is no accumulation and the mass of fluid flowing into the system is equal to the mass of fluid flowing out. The Equation 4.77 then becomes

$$\frac{\partial \rho V}{\partial L} = 0 \quad 4.78$$

From this expression it is evident that for a steady state flow,  $\rho v = \text{constant}$ .

The conservation of linear momentum for single phase flow through an annulus can be expressed as:

$$\frac{\partial \rho v}{\partial t} + \frac{\partial \rho V^2}{\partial L} = -\frac{\partial P}{\partial L} - \frac{\tau \pi D_h}{A} - \rho g \sin \theta_p \quad 4.79$$

$$D_h = d_2 - d_1 \quad 4.80$$

$$\tau = \frac{f \rho V^2}{2} \quad 4.81$$

Combining the Equations 4.78 and 4.79 to eliminate the rate of accumulation of linear momentum and assuming steady state flow yields:

$$\frac{\partial P}{\partial L} = -\frac{\partial \rho V^2}{\partial L} - \frac{\tau \pi D_h}{A} - \rho g \sin \theta_p \quad 4.82$$

Equation 4.82 shows that the pressure gradient is made up three main components namely: the frictional component, acceleration or kinetic component, and the elevation component. For multiphase flow, the prediction of the pressure gradient requires the analysis of each of these components as a function of the prevailing flow pattern.

#### 4.5.1 Pressure drop for dispersed bubble flow

The dispersed bubble flow pattern occurs at low to medium gas superficial gas velocities with high superficial liquid velocities. The flow pattern is discontinuous gas phase which is distributed as spherical discrete bubbles in a continuous liquid phase. The discrete gas bubbles do not exhibit significant slippage through the liquid phase. Thus, the dispersed bubble flow can be treated as a no-slip homogeneous mixture flow as it is assumed that the liquid and gas flow at the mixture velocity. The mixture properties of the drilling fluid may be determined from the following relationships:

$$V_m = V_{SL} + V_{SG} \quad 4.83$$

$$\lambda_L = \frac{V_{SL}}{V_{SL} + V_{SG}} \quad 4.84$$

$$\rho_m = \rho_L \lambda_L + \rho_G (1 - \lambda_L) \quad 4.85$$

$$\mu_m = \mu_L \lambda_L + \mu_G (1 - \lambda_L) \quad 4.86$$

The annuli pressure gradient for the dispersed bubble flow pattern, determined based on the mixture properties of the drilling fluid can be expressed as:

$$\frac{\partial P}{\partial L} = - \frac{\partial \rho V_m^2}{\partial L} - \frac{\tau_s \pi D_h}{A} - \rho_m g \sin \theta_p \quad 4.87$$

$$\tau_s = \frac{f_m \rho_m V_m^2}{2} \quad 4.88$$

$$Re_m = \frac{\rho_m V_m d_h}{\mu_m} \quad 4.89$$

The liquid viscosity  $\mu_L$  is set as the generalised non-Newtonian viscosity for the drilling fluid  $\mu_{Gen}$  and the friction factor  $f_m$ , is determined by the method presented in Section 4.3 and 4.4.

#### 4.5.2 Pressure drop for bubble flow

The pressure gradient calculation for the Bubble flow pattern is similar to that of the dispersed bubble flow pattern but slippage between the phases is taken into account and the in-situ liquid holdup  $H_L$  is used instead of the no-slip holdup.

$$\rho_b = \rho_L H_L + \rho_G (1 - H_L) \quad 4.90$$

$$\mu_b = \mu_L H_L + \mu_G (1 - H_L) \quad 4.91$$

### 4.5.3 Pressure drop for stratified flow

Stratified flow occurs when the simultaneous flow of liquid and gas in a pipe is stable. The liquid height and pressure gradient can be obtained by assuming equilibrium stratified flow is attained for a set of given flow conditions: the liquid and gas flowrates, the annulus size and eccentricity, rpm, and the physical properties of the phases. This is carried out by applying a momentum balance of all the phases in a differential control volume. For a steady state stratified flow, it is assumed that there is little or no acceleration so the rate of change of momentum across the control volume is neglected.

The momentum balance for the liquid and gas phases in a drilling annulus can be expressed as:

$$-\frac{dP}{dL} + \frac{\tau_{Lw}S_{Lw}}{A_L} + \frac{\tau_{Lp}S_{Lp}}{A_L} - \frac{\tau_i S_i}{A_L} + \rho_L g \sin \theta_p = 0 \quad 4.92$$

$$-\frac{dP}{dL} + \frac{\tau_{Gw}S_{Gw}}{A_G} + \frac{\tau_{Gp}S_{Gp}}{A_G} + \frac{\tau_i S_i}{A_G} + \rho_G g \sin \theta_p = 0 \quad 4.93$$

Substituting Equation 4.92 into Equation 4.93 thereby eliminating the pressure gradient term, yields a combined momentum equation that is implicit for the equilibrium liquid height in the annulus.

$$\frac{\tau_{Lw}S_{Lw}}{A_L} + \frac{\tau_{Lp}S_{Lp}}{A_L} - \frac{\tau_{Gw}S_{Gw}}{A_G} - \frac{\tau_{Gp}S_{Gp}}{A_G} - \tau_i S_i \left( \frac{1}{A_L} + \frac{1}{A_G} \right) + (\rho_L - \rho_G)g \sin \theta_p = 0 \quad 4.94$$

When the combined momentum equation has been satisfied, the pressure gradient can then be obtained from the momentum equations of either the liquid or the gas phase as both equations would yield the same result.

#### **4.5.4 Pressure drop for slug flow**

Intermittent flow exists over a vast range of liquid and gas flowrates in horizontal, vertical and inclined pipe configurations. It is the flow pattern found to be dominant in upward inclined flows. The process of slug flow possesses a complex hydrodynamic behaviour making liquid hold up, pressure drop and mass transfer predictions difficult due to its unsteady nature. In order to perform accurate hydraulic calculations for slug flow in a concentric/eccentric drilling annulus it is important to understand the flow mechanism. As presented by Duckler and Hubbard (1975) as gas and liquid flow at velocities under which slug velocities take place, the liquid level decelerates leading to an increase in liquid level approaching the top of the pipe. Eventually the liquid bridges the pipe temporarily blocking the flow of the gas and forming a gas pocket and liquid slug zone. The liquid is accelerated uniformly across its cross-section picking up the slow-moving liquid film in its front and accelerating it to the slug velocity. At the same time the liquid is shed from the back of the slug as the gas pocket pushes into it creating the liquid film region. Assuming a steady state flow, the pickup rate is equal to the shedding rate and since the slug is picking up liquid at the same rate that it is shed, the length of the slug stabilizes.

The slug flow model development is based on the study presented by Taitel and Barnea (1990) to predict pressure drop across a slug unit in a horizontal and upward inclined pipe flow. The fundamentals have been adopted here and modified to develop mechanistic models for the determination of the pressure gradient for Intermittent flow in the concentric and eccentric annuli.

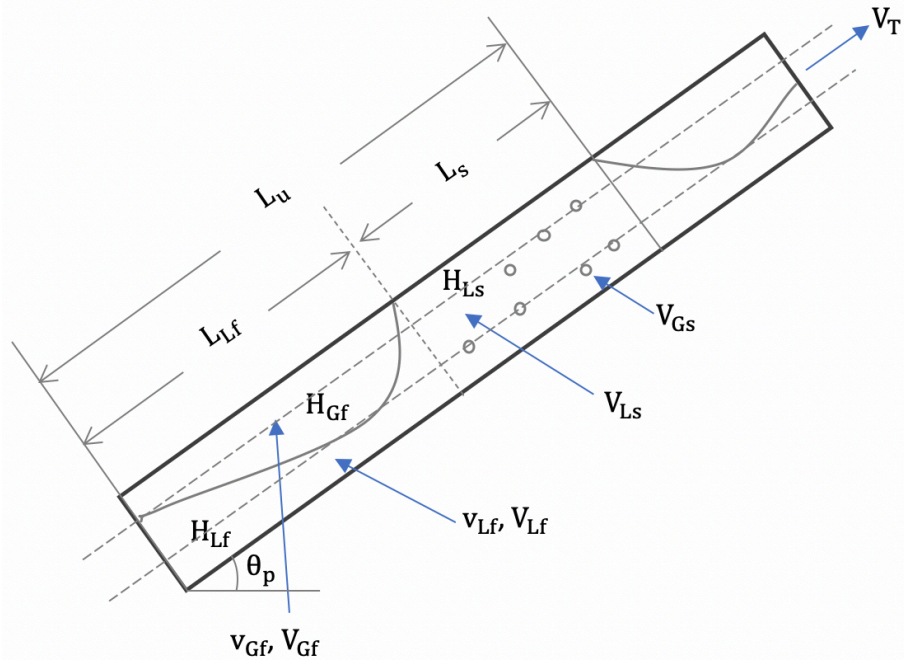


Figure 4.14: Configuration of a fully developed in an inclined wellbore annulus

The liquid and gas flowrates in a control volume containing the liquid slug and liquid-film/gas pocket region can be expressed respectively as:

$$Q_L = V_{Ls}A_{Ls} + v_{Lf}A_{Lf} \quad 4.95$$

$$Q_G = V_{Gs}A_{Gs} + v_{Gf}A_{Gf} \quad 4.96$$

The time taken for the slug unit, the liquid slug region and the liquid-film/gas pocket region to cross a given point in the wellbore annulus can be expressed in terms of the translational velocity:

$$t_u = \frac{L_u}{V_T} \quad t_s = \frac{L_s}{V_T} \quad t_{Lf} = \frac{L_{Lf}}{V_T} \quad 4.97$$

Where the length of a fully developed slug unit is given by:  $L_u = L_s + L_{Lf}$

From Equation 4.95 and 4.97 the liquid volume in the slug unit can be expressed as:

$$Q_L t_u = V_{Ls} A_{Ls} t_s + V_{Lf} A_{Lf} t_{Lf} \quad 4.98$$

$$Q_L - V_{Ls} A_{Ls} \frac{L_s}{L_u} - V_{Lf} A_{Lf} \frac{L_{Lf}}{L_u} = 0 \quad 4.99$$

Considering that the liquid level is not constant throughout the length of the liquid-film/gas pocket region

$$Q_L - V_{Ls} A_{Ls} \frac{L_s}{L_u} - \int_0^{L_{Lf}} \frac{V_{Lf} A_{Lf}}{L_u} \partial L_{Lf} = 0 \quad 4.100$$

The Liquid film velocity can be obtained from the mass balance due to the pickup rate of the liquid film in the front of the slug as follows.

$$(V_T - V_{Ls}) H_{Ls} = (V_T - V_{Lf}) H_{Lf} \quad 4.101$$

$$V_{Lf} = V_T - \frac{(V_T - V_{Ls}) H_{Ls}}{H_{Lf}} \quad 4.102$$

$$Q_L - V_{Ls} A_{Ls} \frac{L_s}{L_u} - \int_0^{L_{Lf}} \left( V_T - \frac{(V_T - V_{Ls}) H_{Ls}}{H_{Lf}} \right) \frac{A_{Lf}}{L_u} \partial L_{Lf} = 0 \quad 4.103$$

$$Q_L - V_{Ls} A_{Ls} + \frac{V_T A_{Ls} L_{Lf}}{L_u} - \frac{V_T A}{L_u} \int_0^{L_{Lf}} H_{Lf} \partial L_{Lf} = 0 \quad 4.104$$

The area and holdup of the liquid film is a function of the liquid height. Since the liquid height varies along the length of the liquid-film/gas pocket region, the area of the liquid film would correspondingly vary across the film length. The area of the liquid film in a concentric and eccentric annulus can be obtained from geometrical relationships.

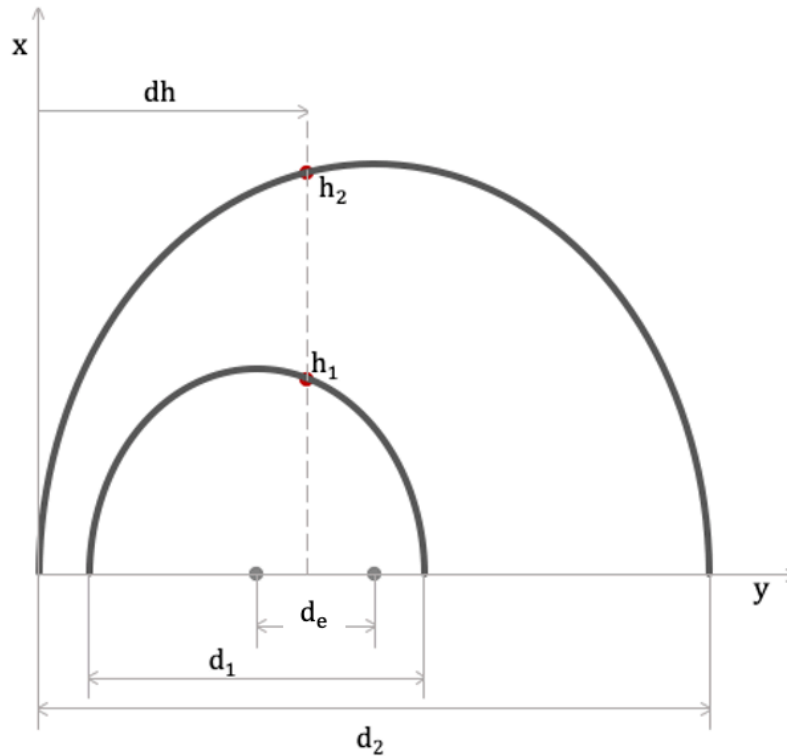


Figure 4.15: Annulus geometry schematic for rate of change of liquid area with height

Unlike pipe flow, the liquid height and holdup for annuli flows cannot be determined with the conventional approach as there exist an inner pipe inside the outer pipe. Again, the liquid height may be influenced by the eccentricity of the inner drillpipe because for the same liquid area, the liquid height in a concentric annulus may be different from that of the eccentric annulus, the effect being dependent on the degree of eccentricity of the annuli geometry. To account for this effect a new model is developed to determine the liquid height and liquid holdup for a concentric and eccentric annulus.

From the schematic diagram (Figure 4.15), the area of the liquid film in a concentric or eccentric annulus can be obtained by considering the gradient of the area of the liquid film (area of the shaded portion) in the annulus. Using

geometrical relationships and taking half of the annulus configuration, the rate of change of the area of the liquid film is derived as:

$$\frac{dA_{Lf}}{dy} = 2 \left[ \left( \frac{d_2^2}{4} - \left( \frac{d_2}{2} \sin \alpha_2 \right)^2 \right)^{1/2} - \left( \frac{d_1^2}{4} - \left( \frac{d_1}{2} \sin \alpha_1 \right)^2 \right)^{1/2} \right] \quad 4.105$$

The geometric positions  $h_2$  and  $h_1$  in Figure 4.15 can be expressed respectively as:

$$h_2 = \frac{d_2}{2} + \frac{d_2}{2} \sin \alpha_2 \quad 4.106$$

$$h_1 = \frac{d_2}{2} - d_e + \frac{d_1}{2} \sin \alpha_1 \quad 4.107$$

Since the positions  $h_2$  and  $h_1$  are both equal to the liquid film height,  $h_2 = h_1 = h_{Lf}$  the following relationships can be derived

$$\sin \alpha_2 = \frac{2h_{Lf} - d_2}{d_2} \quad \sin \alpha_1 = \frac{2h_{Lf} - d_2 + 2d_e}{d_1} \quad 4.108$$

From Equations 4.105 to 4.108, the expression for the area of the liquid in a concentric or eccentric annulus can be expressed as:

$$A_{Lf} = 2 \int_0^{h_{Lf}} \left[ \left( \frac{d_2^2}{4} - \left( \frac{1}{2} (2h_{Lf} - d_2) \right)^2 \right)^{1/2} - \left( \frac{d_1^2}{4} - \left( \frac{1}{2} (2h_{Lf} - d_2 + 2d_e) \right)^2 \right)^{1/2} \right] dh_{Lf} \quad 4.109$$

$$d_e = \frac{1}{2} (d_2 - d_1)e$$

Equation 4.109 is solved analytically to yield the following rigorous equations for the area of the liquid film:

$$X1 = \frac{d_2^2}{4} \sin^{-1} \left( \frac{2h_{Lf} - d_2}{d_2} \right) - \frac{d_1^2}{4} \sin^{-1} \left( \frac{2h_{Lf} - d_2 + 2d_e}{d_1} \right) \quad 4.110$$

$$X2 = \frac{1}{2} \left( (2h_{Lf} - d_2)(h_{Lf}d_2 - h_{Lf}^2)^{1/2} + (d_2 - 2d_e - 2h_{Lf}) \left[ (d_2 - 2d_e)h_{Lf} - h_{Lf}^2 + \frac{1}{4}5d_1^2 - \left( \frac{1}{2}(d_2 - 2d_e) \right)^2 \right]^{1/2} + \frac{1}{4}\pi d_2^2 \right) \quad 4.111$$

$$X3 = \frac{1}{2}(d_2 - 2d_e) \left( \frac{1}{4}d_1^2 - \left( \frac{1}{2}(d_2 - 2d_e) \right)^2 \right)^{1/2} + \frac{1}{4}d_1^2 \sin^{-1} \left( \frac{d_2 - 2d_e}{d_1} \right) \quad 4.112$$

Summation of the of the Equations 4.110, 4.111 and 4.112 yields the area of the liquid film in a concentric or eccentric annulus.

$$A_{Lf} = X1 + X2 + X3 \quad 4.113$$

Thus, the liquid holdup in the liquid-film/gas pocket region can then be calculated from:

$$H_{Lf} = \frac{4(X1 + X2 + X3)}{\pi(d_2^2 - d_1^2)} \quad 4.114$$

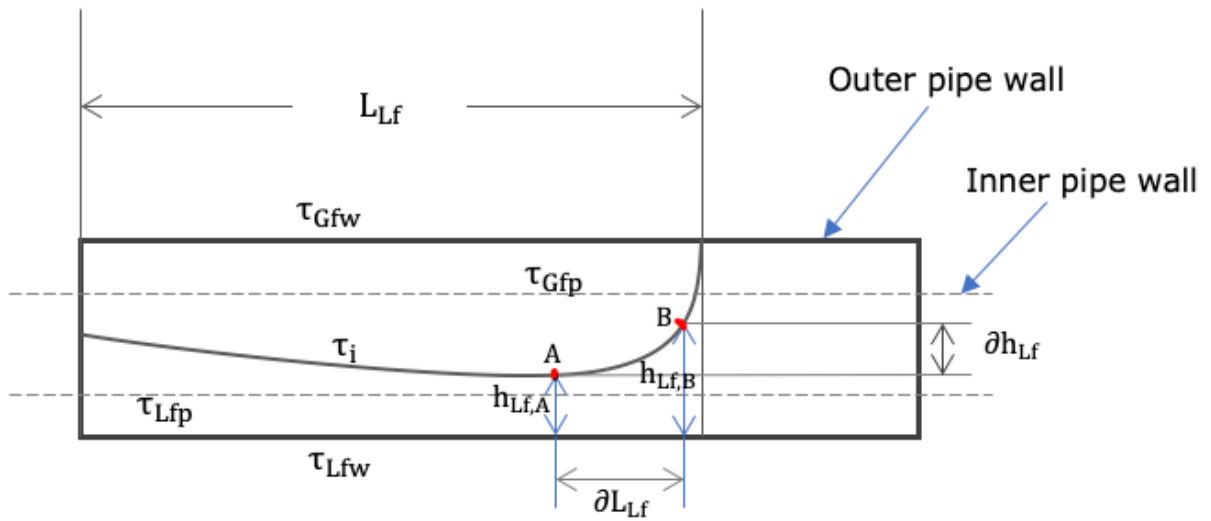


Figure 4.16: Change in the liquid film height with distance in the liquid film region

The steady state slug flow pattern differs significantly from the other flow patterns as the fluids tend to accelerate creating a change in the liquid height of film with length (Figure 4.16). This phenomenon clearly influences the axial pressure gradient and must be accounted for in the governing equations used to describe the slug flow behaviour.

The conservation of momentum equations for the liquid film and gas pocket in the drilling annulus can be expressed as

$$-\frac{\partial P}{\partial L} + \rho_L v_{Lf} \frac{\partial v_{Lf}}{\partial L} + \frac{\tau_{Lfw} S_{Lfw}}{A_{Lf}} + \frac{\tau_{Lfp} S_{Lfp}}{A_{Lf}} - \frac{\tau_i S_i}{A_{Lf}} + \rho_L g \sin \theta_p - \rho_L g \cos \theta_p \frac{\partial h_{Lf}}{\partial L} = 0 \quad 4.115$$

$$-\frac{\partial P}{\partial L} + \rho_G v_{Gf} \frac{\partial v_{Gf}}{\partial L} + \frac{\tau_{Gfw} S_{Gfw}}{A_{Gf}} + \frac{\tau_{Gfp} S_{Gfp}}{A_{Gf}} + \frac{\tau_i S_i}{A_{Gf}} + \rho_G g \sin \theta_p - \rho_G g \cos \theta_p \frac{\partial h_{Lf}}{\partial L} = 0 \quad 4.116$$

The relative velocities to the translational velocity are used as the analysis is carried out in the translational-velocity coordinate system assuming that the interface between the liquid film and the gas is stationary. The relative velocities of the liquid film and gas are given as:

$$v_{Lf} = V_T - V_{Lf} ; \quad v_{Gf} = V_T - V_{Gf} \quad 4.117$$

Using Equations 4.101 and 4.102, the relative velocity of the liquid film can be expressed as:

$$v_{Lf} = \frac{(V_T - V_{Ls})H_{Ls}}{H_{Lf}} \quad 4.118$$

Similarly, from the mass balance of the gas phase in the liquid-film/gas pocket region, the relative velocity of the gas may then be expressed as follows:

$$(V_T - V_{Gs})(1 - H_{Ls}) = (V_T - V_{Gf})(1 - H_{Lf}) \quad 4.119$$

$$v_{Gf} = \frac{(V_T - V_{Gs})(1 - H_{Ls})}{(1 - H_{Lf})} \quad 4.120$$

The change in the relative velocities with length is a function of the hold-up of the liquid film and can be expressed as:

$$\frac{\partial v_{Lf}}{\partial L} = \frac{\partial v_{Lf}}{\partial H_{Lf}} \times \frac{\partial H_{Lf}}{\partial h_{Lf}} \times \frac{\partial h_{Lf}}{\partial L} \quad 4.121$$

$$\frac{\partial v_{Gf}}{\partial L} = \frac{\partial v_{Gf}}{\partial H_{Lf}} \times \frac{\partial H_{Lf}}{\partial h_{Lf}} \times \frac{\partial h_{Lf}}{\partial L} \quad 4.122$$

$$\frac{\partial v_{Lf}}{\partial H_{Lf}} = \frac{(V_T - V_{Ls})H_{Ls}}{H_{Lf}^2} \quad 4.123$$

$$\frac{\partial v_{Gf}}{\partial H_{Lf}} = \frac{(V_T - V_{Gs})(1 - H_{Ls})}{(1 - H_{Lf})^2} \quad 4.124$$

Substituting Equation 4.116 into Equation 4.115 thereby eliminating the pressure gradient term and applying Equation 4.121 through 4.124, the gradient of the change in liquid height with wellbore length yields

$$\begin{aligned} & \frac{\partial h_{Lf}}{\partial L} \\ &= \frac{\frac{\tau_{Lfw} S_{Lfw}}{A_{Lf}} + \frac{\tau_{Lfp} S_{Lfp}}{A_{Lf}} - \frac{\tau_{Gfw} S_{Gfw}}{A_{Gf}} - \frac{\tau_{Gfp} S_{Gfp}}{A_{Gf}} - \tau_i S_i \left( \frac{1}{A_{Lf}} + \frac{1}{A_{Gf}} \right) + (\rho_L - \rho_G) g \sin \theta_p}{\rho_G v_{Gf} \frac{(V_T - V_{Gs})(1 - H_{Ls})}{(1 - H_{Lf})^2} \frac{\partial H_{Lf}}{\partial h_{Lf}} - \rho_L v_{Lf} \frac{(V_T - V_{Ls}) H_{Ls}}{H_{Lf}^2} \frac{\partial H_{Lf}}{\partial h_{Lf}} + (\rho_L - \rho_G) g \cos \theta_p} \end{aligned} \quad 4.125$$

Equation 4.125 has to be integrated numerically to yield the liquid film profile  $h_{Lf}(L)$ , and also to determine the liquid holdup and liquid film velocity distributions. The boundary condition for integrating the first-order differential equation is  $h_{Lf}(L = 0) = h_{Lf0}$  corresponding to  $v_{Lf}(L = 0) = V_T - V_{Ls}$ . Before starting the numerical integration, the boundary condition is obtained by first solving Equation 4.126 to obtain  $h_{Lf0}$

$$f(h_{Lf0}) = \frac{H_{Ls} \pi (d_2^2 - d_1^2) - 4(X1 + X2 + X3)}{\pi (d_2^2 - d_1^2)} \quad 4.126$$

The numerical integration is performed while checking that Equation 4.104 is satisfied. Once the mass balance is satisfied the integration is stopped yielding the length of the liquid film in the liquid-film/gas pocket region.

The interfacial, outer wall and drillpipe shear stresses of the gas and liquid phases are expressed in terms of the actual phase velocities rather than the relative

velocities used in the momentum equations. This is because the translational velocity coordinate system is nonaccelerating hence the force is invariant.

$$\tau_{Lfw} = f_{Lfw} \frac{\rho_L V_{Lf} |V_{Lf}|}{2} \quad 4.127$$

$$\tau_{Gfw} = f_{Gfw} \frac{\rho_G V_{Gf} |V_{Gf}|}{2} \quad 4.128$$

$$\tau_i = f_i \frac{\rho_G (V_{Gf} - V_{Lf}) |V_{Gf} - V_{Lf}|}{2} \quad 4.129$$

$$\tau_{Lfp} = \frac{f_{Lfp} \rho_L V_{Lf} |V_{Lf}|}{2} \quad 4.130$$

$$\tau_{Gfp} = \frac{f_{Gfp} \rho_G V_{Gf} |V_{Gf}|}{2} \quad 4.131$$

The friction factors in the equations above are determined using the hydraulic diameters expressed as follows:

$$d_{Lfw} = \frac{4A_{Lf}}{S_{Lfw}} \quad d_{Gfw} = \frac{4A_{Gf}}{S_{Gfw}} \quad 4.132$$

$$d_{Lfp} = \frac{4A_{Lf}}{S_{Lfp}} \quad d_{Gfp} = \frac{4A_{Gf}}{S_{Gfp}} \quad 4.133$$

Due to the intermittent nature of slug flow, the local axial pressure drop is not constant. Thus, it is practical to determine the average pressure drop and

corresponding pressure gradient across a slug unit. The pressure drop across a slug unit can be calculated by performing a global force and momentum balance across a given slug unit in an annulus. The global pressure drop across a slug unit can be expressed as:

$$\Delta P_u = \rho_u g \sin \theta_p L_u + \frac{\tau_s \pi D_h}{A} L_s + \int_0^{L_{Lf}} \frac{\tau_{Lfw} S_{Lfw} + \tau_{Lfp} S_{Lfp} + \tau_{Gfw} S_{Gfw} + \tau_{Gfp} S_{Gfp}}{A} dL \quad 4.134$$

$$\rho_u = \rho_L H_{LA} + \rho_G (1 - H_{LA}) \quad 4.135$$

$$\tau_s = \frac{f_s \rho_s V_m^2}{2} \quad 4.136$$

$$\rho_s = \rho_L H_{Ls} + \rho_G (1 - H_{Ls}) \quad 4.137$$

The first term in Equation 4.134 represents the gravitational component of the pressure drop while the second and third represent the frictional pressure drop component in the slug body region and the liquid-film/gas pocket region. The pressure gradient is given as:

$$-\frac{dP}{dL} = \frac{-\Delta P_u}{L_u} \quad 4.138$$

The average liquid holdup  $H_{LA}$  in a slug unit can generally be expressed as:

$$H_{LA} = H_{Ls} \frac{L_s}{L_u} + H_{Lf} \frac{L_{Lf}}{L_u} \quad 4.139$$

Since the liquid holdup in the film is not constant along the length of the liquid-film/gas pocket region, the average liquid holdup should then be expressed as:

$$H_{LA} = H_{Ls} \frac{L_s}{L_u} + \frac{1}{L_u} \int_0^{L_{Lf}} H_{Lf} \partial L_{Lf} \quad 4.140$$

$$\int_0^{L_{Lf}} H_{Lf} \partial L_{Lf} = H_{LA}L_u - H_{LS}L_s \quad 4.141$$

Substituting Equation 4.141 into Equation 4.104 and rearranging yields a simplified equation for the average liquid holdup in a slug unit, thereby avoiding the integral term.

$$Q_L - V_{LS}AH_{LS} + \frac{V_TAH_{LS}L_{Lf}}{L_u} - \frac{V_TA}{L_u}(H_{LA}L_u - H_{LS}L_s) = 0 \quad 4.142$$

$$H_{LA} = \left( Q_L - V_{LS}AH_{LS} + \frac{V_TAH_{LS}L_{Lf}}{L_u} + \frac{V_TAH_{LS}L_s}{L_u} \right) \frac{1}{V_TA} \quad 4.143$$

$$H_{LA} = \frac{V_{SL} - V_{LS}H_{LS} + V_TH_{LS}}{V_T} \quad 4.144$$

#### 4.6 Geometric and Closure relationships

In order to obtain solutions from the developed hydraulic models, the simultaneous calculations of the gas-liquid interface length and the wetted perimeter of the gas and the liquid phases are required. These geometrical parameters, as shown in the Figure 4.17 are mainly functions of the gas-liquid input parameters, the wellbore annuli sizes and the degrees of eccentricity of the drillpipe. Analytical equations have been developed in this study to compute the gas-liquid interface length and the wetted perimeter of the gas and the liquid phases directly from input parameters. These equations are presented as follows:

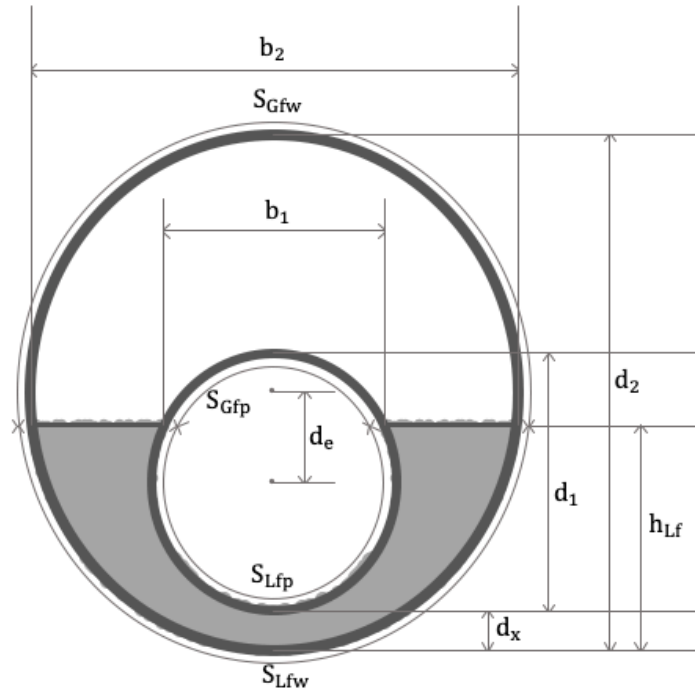


Figure 4.17: Schematic showing the annuli geometric parameters

The gas-liquid interface length  $S_i$  :

$$S_i = b_2 - b_1 \quad 4.145$$

$$S_i = d_2 \sin\left(\frac{\alpha_2}{2}\right) - d_1 \sin\left(\frac{\alpha_1}{2}\right) \quad 4.146$$

$$\alpha_2 = 2 \cos^{-1}\left(\frac{d_2 - h_{Lf}}{d_2}\right) \quad \alpha_1 = 2 \cos^{-1}\left(\frac{d_1 - h_b}{d_1}\right) \quad 4.147$$

$$h_b = h_{Lf} - d_x \quad 4.148$$

$$d_x = \frac{d_2}{2} - \left(\frac{2d_e + d_1}{2}\right) \quad 4.149$$

$$S_i = d_2 \sin\left[\cos^{-1}\left(\frac{d_2 - 2h_{Lf}}{d_2}\right)\right] - d_1 \sin\left[\cos^{-1}\left(\frac{d_1 - 2(h_{Lf} - d_x)}{d_1}\right)\right] \quad 4.150$$

Wetted perimeter of the gas phase on the drillpipe and wellbore wall/casing respectively:

$$S_{Gfp} = \pi d_1 - d_1 \cos^{-1} \left( \frac{d_1 - 2(h_{Lf} - d_x)}{d_1} \right) \quad 4.151$$

$$S_{Gfw} = \pi d_2 - d_2 \cos^{-1} \left( \frac{d_2 - 2h_{Lf}}{d_2} \right) \quad 4.152$$

Wetted perimeter of the liquid phase on the drillpipe and wellbore wall/casing respectively:

$$S_{Lfw} = d_2 \cos^{-1} \left( \frac{d_2 - 2h_{Lf}}{d_2} \right) \quad 4.153$$

$$S_{Lfp} = d_1 \cos^{-1} \left( \frac{d_1 - 2(h_{Lf} - d_x)}{d_1} \right) \quad 4.154$$

### **Translational velocity:**

The slug flow model was developed by subjecting the annuli gas-liquid flow to the translational velocity coordinate system in which for a steady state system, the gas and the liquid phases were expressed as flowing backwards with respect to the coordinate system. The translational velocity is the sum of the drift velocity of a gas bubble, which is equivalent to the velocity of a Taylor bubble in a stagnant liquid, plus the contribution of the mixture velocity in the preceding slug. The equation for the translational velocity of may be written as:

$$V_T = 1.2V_m + V_D \quad 4.155$$

The drift velocity for vertical flow  $V_{D,v}$ , based on potential flow analysis and the studies of Davies and Taylor (1950) and Dumitrescu (1943) was expressed as:

$$V_{D,v} = 0.345 [g D]^{0.5} \quad 4.156$$

Several studies reported that drift velocity also occurs for horizontal flows due to the difference in hydrostatic head between the liquid film and the nose of the Taylor bubble. Based on the analysis of Benjamin (1968), the drift velocity for horizontal flows may be expressed as:

$$V_{D,H} = 0.54 [g D]^{0.5} \quad 4.157$$

Bendiksen (1984) observed that the drift velocity for horizontal flows was larger than that of the vertical. He reported that as the inclination angle decreased from the vertical, the drift velocity increased until a maximum value was attained at about the 30° inclination angle from the horizontal. Further decrease in the inclination angle resulted in a drop of the drift velocity. They proposed a correlation for the drift velocity as a function of the inclination angle, by summing up a component of the drift velocity for horizontal and vertical flows to yield:

$$V_D = V_{D,H} \cos \theta_p + V_{D,v} \sin \theta_p, \quad 0^\circ \leq \theta_p \leq 90^\circ \quad 4.158$$

Based on the study of Sadatomi et al. (1982), Caetano et al. (1992) recommended that the equi-periphery diameter  $D_{Ep}$  should be used as the characteristic dimension of the annuli instead of the hydraulic diameter. The equi-periphery diameter of the drilling annuli is the sum of the drillpipe diameter and the wellbore/casing diameter:

$$D_{Ep} = d_1 + d_2 \quad 4.159$$

From Equations 4.155 to 4.159, the final form of the translational velocity may be expressed as:

$$V_T = 1.2V_m + 0.54 \sqrt{g D_{Ep} \cos \theta_p} + 0.345 \sqrt{g D_{Ep} \sin \theta_p} \quad 4.160$$

The gas velocity in the slug body  $V_{Gs}$  may be obtained from the following equation

$$V_{Gs} = 1.2V_m + 1.53 \left[ \frac{(\rho_L - \rho_G) g \sigma}{\rho_L^2} \right]^{0.25} H_{Ls}^{0.5} \sin \theta_p \quad 4.161$$

#### 4.7 Chapter summary

The review of previous studies showed the several studies have provided conflicting views on the effect of the inner pipe rotation on the pressure drop in the concentric or eccentric annuli for both single-phase and two-phase flow. While some studies have reported that the increase in drillpipe rotation decreases the pressure losses, other studies have reported an increase in pressure losses or either an increase or a decrease in pressure losses for annuli flows. While the friction geometry parameter developed for flow of Newtonian fluids through the annuli has been applied by some studies in the past to perform frictional pressure gradient calculations for non-Newtonian fluid flows through the annuli, This chapter revealed that unlike the Newtonian annuli flow, the friction geometry parameter for non-Newtonian annuli flows are dependent on the combined effect of the rheological properties of the fluid, inner pipe rotary speed and the eccentricity of the inner pipe. To account for these issues, the following analytical equations were developed and presented for the evaluation of annuli fluid dynamics and pressure losses in the concentric or eccentric annuli with and without inner pipe rotation:

1. Generalised Reynolds number and effective viscosity equations valid for annuli flow of both Newtonian and non-Newtonian (Power law, Bingham plastic and Yield power law) fluids were derived from fundamental principles and presented (Section 4.1)
2. New friction geometry parameter equations valid for both Newtonian and non-Newtonian flows were analytically developed (Equation 4.68 to 4.73). Analytical velocity and shear stress profile equations were derived (Section 4.2.2) and laminar and turbulent friction factor equations that take in account the combined effect of the fluid rheology, fluid circulation rate, pipe eccentricity and inner pipe rotary speed were presented (Equation 4.75 and 4.76). The output of these equations was compared favourably to that suggested by Caetano et al. (1992) for Newtonian fluids (Table 4.3) and Hacıislamoglu and Langlinais (1990) (Figure 4.11)

Furthermore, for two-phase gas-liquid fluids, in addition to combined effect of the aforementioned parameters, it is required that the gas-liquid fluid flow pattern is taken into account in order to accurately predict the pressure losses experienced by both Newtonian and non-Newtonian annuli flows. Section 4.5 presents details of the development of different flow pattern dependent models valid for the Dispersed bubble, bubble, stratified and slug flow patterns. New equations to determine the liquid height and area, which is valid for any level of pipe eccentricity was developed by applying a novel concept (Equation 4.110 to 4.114). In addition, flow pattern dependent geometric relationships necessary for the prediction of the pressure loss in the concentric and eccentric annuli were also derived and presented in section 4.6.

## Chapter 5

### Cuttings transport modelling

A successful drilling operation requires that the drilled cuttings being generated are effectively transported with the aid of the drilling fluid, through the annulus of the wellbore to the surface. Inefficient hole cleaning during drilling may cause several problems such as increased torque and drag, stuck pipe, high hydraulic requirements, poor wellbore pressure management, lost circulation or complete loss of wellbore. Literature in chapter two shows that hole cleaning is dependent on a number of important parameters that govern the cutting transport dynamics in a wellbore and these parameters have been selectively investigated by several researchers with the aim of developing fundamental theories that could be used to explain the cuttings transport phenomenon. Empirical and mechanistic cutting transport models have been developed using the concept of the critical velocity required to ensure that cuttings are mobile in the annuli or with the concept of the multi-layered model with an assumption that cuttings are transported in several distinctive layers with each layer having a different cutting transport mechanism. However, multiphase flow characteristics have been ignored when applying these concepts in the modelling or flow dynamics predictions for multiphase drilling fluids. During underbalanced drilling operations, the drilling fluid is a multiphase fluid composed of a liquid and a gas phase either due to the intentional introduction of the gas from the surface or the influx of gas or other fluids from the subsurface formations into the wellbore. Multiphase drilling fluid flow in annuli is accompanied by transient flow patterns that significantly influence the hole cleaning efficiency of the drilling program. The mass, momentum and energy transfer between the phases in the multiphase flow are different to that of the single-phase flow and the forces acting on the cuttings in the wellbore are reliant on the prevailing flow pattern in the annuli. While some flow patterns are favourable for cuttings transport the others are known to have a higher tendency to affect the cuttings transport dynamics and encourage the settling of the cuttings to form a stationary bed at the low side of the annuli. Thus, it is important to take into consideration the flow pattern along with the other relevant drilling parameters when performing cutting transport modelling for multiphase drilling fluid annuli flow. In this chapter, the concept of the minimum transport velocity

has been used to develop models that can be used to predict the minimum annuli velocity required to ensure that the cuttings in the wellbore are mobile and entrained in the flow. Furthermore, a flow pattern dependent multi-layered modelling approach has been applied to develop mechanistic models using the principles of conservation of mass and linear momentum to determine the axial pressure gradient in a drilling wellbore.

### **5.1 Concept of minimum transport velocity**

When the flowrate in the annuli is below the minimum threshold required to transport the cuttings out of the wellbore, the cuttings would fall to the low side of the annuli and form a stationary bed. This gives rise to the concept of the minimum transport velocity MTV, which can be referred to as the critical velocity that must exist in the annuli in order to prevent the formation of a stationary bed and ensure that the cuttings are transported effectively. The idea behind this concept is based on the modelling of the critical annuli velocity as a function of the major drilling parameters that have either been proven from field reports or from experimental studies to have a significant influence on the cutting transport efficiency during drilling activities. However, the fundamental knowledge of the transport mechanism of fluid-solids mixtures in horizontal, vertical and inclined pipes or annuli has to be considerably understood and applied towards the establishment of the critical annuli velocity. There are a number of patterns that can be formed in a conduit when transporting fluid-solids mixtures. These cutting transport patterns have been generally classified as suspension, moving bed and stationary bed patterns in order to simplify the solution to the problem. The pressure gradient experienced by the flow in the annuli is also highly dependent on the mechanism on which the cuttings entrained in the drilling fluids are being transported. Thus, the concept of the minimum transport velocity is not only required to ensure the cuttings are being transported effectively but is very useful to determine the annuli pressure gradient, which is an important factor for wellbore pressure management. The lower the MTV, the higher the tendency to achieve an annular velocity that would effectively clean the wellbore during drilling. The knowledge of the MTV is beneficial in the aspect of designing the

operational conditions used in the drilling hydraulics programme in order to optimise cost and efficiency.

### **5.1.1 Initiation of cutting movement**

There are various forces that act on a cutting in the wellbore annuli. These forces are a function of the annuli velocity and properties of the drilling fluid in which the cuttings are entrained. These forces are responsible for the movement or settling of the cuttings and govern the mechanism by which the cuttings are being transported in the annulus. At a relatively low fluid flowrate, the annuli velocity is insufficient relative to the cuttings velocity to keep the cuttings hence the cuttings will settle towards the bottom of the annulus to form a stationary bed, thereby reducing the cross-section area of the flow and increasing the annuli fluid velocity in available flowing region.

This process takes place until an equilibrium point is reached at which the fluid velocity is high enough to maintain the remaining cuttings in suspension and the increase in the height of the stationary bed existing at the bottom side of the annuli stops. If the drilling fluid flowrate is gradually increased, the height of the stationary bed will be gradually reduced as more cuttings would be lifted into suspension region and a moving bed region may be formed, where a certain concentration of the cutting slides along the top of the stationary bed. However, there exists a vertical concentration gradient across the annuli space where most of the cuttings tend to move in the lower half of suspension region. A sufficient and further increase in the fluid velocity would lead to the movement of the stationary bed at the bottom of the annuli and a cuttings suspension region above the moving bed region. Eventually, when the annuli velocity is sufficiently high, the moving bed will disappear, and all the cuttings will be transported in suspension. The forces responsible for the transition between the cutting transport mechanisms are the drag lift, buoyancy, frictional and gravitational forces.

The lift force is the force that tends to lift the cuttings into suspension in the annuli while the drag force which is due to the viscous drag of the fluid acting on the surface of the cutting, tends to move the cuttings in the direction of the flow.

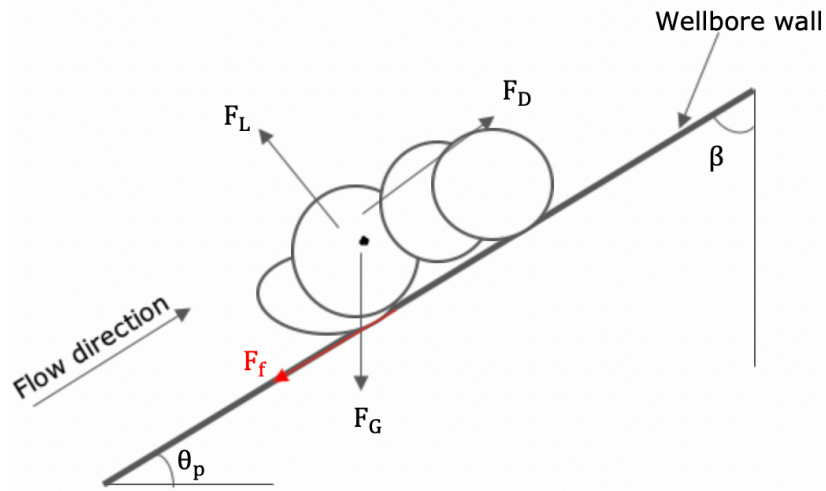


Figure 5.1: Forces acting on cutting particles in an inclined wellbore annulus

The lift and drag force can be expressed respectively as:

$$F_L = C_{cL} A_{cL} \frac{\rho_f v_p^2}{2} \quad 5.1$$

$$F_D = C_{cD} A_{ce} \frac{\rho_f v_p^2}{2} \quad 5.2$$

where  $A_{cL}$  is the projected area of the particle in the direction normal to the flow,  $A_{ce}$  is the projected area of the upper exposed portion of the particle,  $C_{cL}$  is the cutting lift coefficient,  $C_{cD}$  is the drag coefficient of the cutting and  $v_p$  represents the velocity of the fluid in the location of the cutting.

The frictional and gravitational force acts against the movement of the cuttings and has to be overcome before the cuttings can be transported. The frictional and gravitational force may be expressed as:

$$F_f = f_s F_G \quad 5.3$$

$$F_G = V_c (\rho_c - \rho_f) g \quad 5.4$$

$f_s$  is the friction coefficient between the cuttings and the annular wall under the wet condition and  $V_c$  represents the volume of the cutting.

In a horizontal or inclined wellbore, the cuttings may roll or slide along the bottom wall of the annuli so the total resistance force acting on the cuttings is the sum of the gravitational force and the frictional force between the cuttings and the wellbore wall. The total resistant force to the cuttings movement in the annuli be obtained as follows:

$$F_f = f_s F_G \sin \beta \quad 5.5$$

$$F_G = V_c (\rho_c - \rho_f) g \cos \beta \quad 5.6$$

$$F_R = V_c (\rho_c - \rho_f) g [\cos \beta + f_s \sin \beta] \quad 5.7$$

Under the action of the drag force of the drilling fluid, the cuttings may be transported in the direction of the flow as a moving bed by rolling or sliding along the surface of the annular wall. For this action to occur, the drag force has to be greater than or equal to the total resistance force acting against the cutting. This condition may be expressed as:

$$C_{cD} A_{ce} \frac{\rho_f V_p^2}{2} \geq V_c (\rho_c - \rho_f) g [\cos \beta + f_s \sin \beta] \quad 5.8$$

Similarly, the cuttings would be transported in the suspension pattern if the lift force is strong enough to overcome the gravitational force acting against the cutting:

$$C_{cL} A_{cL} \frac{\rho_f v_p^2}{2} \geq V_c (\rho_c - \rho_f) g \sin \beta \quad 5.9$$

### 5.1.2 Factors affecting cutting transport

From the force balance analysis on a cutting in the wellbore annuli, it can be deduced that if the annuli fluid velocity is below the minimum transport velocity MTV required to keep the cuttings suspended, the cuttings would fall towards the bottom of the annuli wall. However, the cuttings would be transported as a moving bed if the drilling fluid velocity is less than the minimum transport velocity required to suspend the cuttings but greater than the minimum transport velocity that is needed to roll or slide the cuttings along the bottom of the wellbore. If the drilling fluid velocity is below the minimum transport velocity MTV required to transport the cuttings as a moving bed, the cutting would form a stationary bed at the bottom of the wellbore annuli.

Based on these assumptions and the force balance analysis, the critical condition for initiating the cuttings suspension or rolling movement may be obtained by defining the minimum transport velocity MTV as a function of the major parameters that govern cutting transport. The minimum transport velocity for rolling and suspension can be defined respectively by the following functions:

$$V_{MR} = f(\rho_f, \rho_c, d_c, d_x, \mu_f, g(\rho_c - \rho_f)[f_s \sin \beta + \cos \beta]) \quad 5.10$$

$$V_{MS} = f(\rho_f, \rho_c, d_c, d_x, \mu_f, g(\rho_c - \rho_f)\sin\beta) \quad 5.11$$

Based on this concept, minimum transport velocity models for transporting drilled cuttings in suspension and rolling/sliding at the low side of the wellbore annulus were developed from dimensional analysis using the Buckingham pi theorem. The developed models for the minimum transport velocity MTV are given in the final form as:

Rolling:

$$V_{MR} = A \frac{\mu_f}{d_c \rho_f} \left[ \frac{d_c^3 \rho_f g (\rho_c - \rho_f) [\cos \beta + f_s \sin \beta]}{\mu_f^2} \right]^B \left[ \frac{d_x}{d_c} \right]^C \quad 5.12$$

Suspension:

$$V_{MS} = E \frac{\mu_f}{d_c \rho_f} \left[ \frac{d_c^3 \rho_f g (\rho_c - \rho_f) \sin \beta}{\mu_f^2} \right]^F \left[ \frac{d_x}{d_c} \right]^G \quad 5.13$$

For a fully eccentric annulus, the distance between the drillpipe and the borehole wall is zero so the above MTV equations cannot be used to predict the minimum velocity as there is no fluid located in the lowest region of the annulus. A parameter  $A_e$  which represents 1% of the wellbore area from the bottom of the wellbore is suggested in this study for determining the minimum transport velocity in the fully eccentric annulus. However, the average velocity in the area  $A_e$  would have to be computed from CFD numerical simulations or obtained from experimental investigation. The models for the minimum transport velocity MTV for rolling and suspension for the fully eccentric annuli are:

Rolling:

$$V_{MR} = B_1 \frac{\mu_f}{d_c \rho_f} \left[ \frac{d_c^3 \rho_f g (\rho_c - \rho_f) [\cos \beta + f_s \sin \beta]}{\mu_f^2} \right]^{B_2} \left[ \frac{A_e}{d_c^2} \right]^{B_3} \quad 5.14$$

Suspension:

$$V_{MS} = E_1 \frac{\mu_f}{d_c \rho_f} \left[ \frac{d_c^3 \rho_f g (\rho_c - \rho_f) \sin \beta}{\mu_f^2} \right]^{E_2} \left[ \frac{A_e}{d_c^2} \right]^{E_3} \quad 5.15$$

where  $B_1, B_2, B_3, E_1, E_2$  and  $E_3$  are the coefficients which should be evaluated based on numerical or experimental data.

The fluid properties used for the minimum transport velocity predictions are those which are existing at the bottom of the wellbore annuli where the cuttings are most likely to settle and form a stationary bed. The fluid density  $\rho_f$  and viscosity  $\mu_f$  in the MTV equations are the dependent on the multiphase flow pattern in the annuli. This is more reason why the flow pattern is important in cutting transport optimisation as the fluids located in the lowest region in the annuli is a function of the prevailing flow pattern.

## 5.2 Multi-layered model development

The pressure gradient in the wellbore annuli flowing with a multiphase drilling fluid is significantly dependent on the gas-liquid flow pattern and the cuttings transport mechanism. A stationary bed is formed in the annuli when the drilling fluid velocity is below the minimum transport velocity to keep the cuttings in the moving bed regime. The stationary bed height increases, thereby increasing the annuli fluid velocity until the point is reached where the oncoming cuttings have enough forces to keep them in suspension or in motion as a moving bed. This reduction in area

and the vertical concentration gradient of the cuttings have an impact on the hydraulics of the system. There are three layers that could be formed in the annulus during the drilling operation (Figure 5.2): a suspension layer where the cuttings are transported in suspension, a moving bed layer where the cuttings are moving as a bed either on the bottom pipe wall or on top of the stationary bed, and a stationary bed layer. One, two or three of these layers can occur simultaneously in the wellbore annuli depending on the flowing or operating conditions.

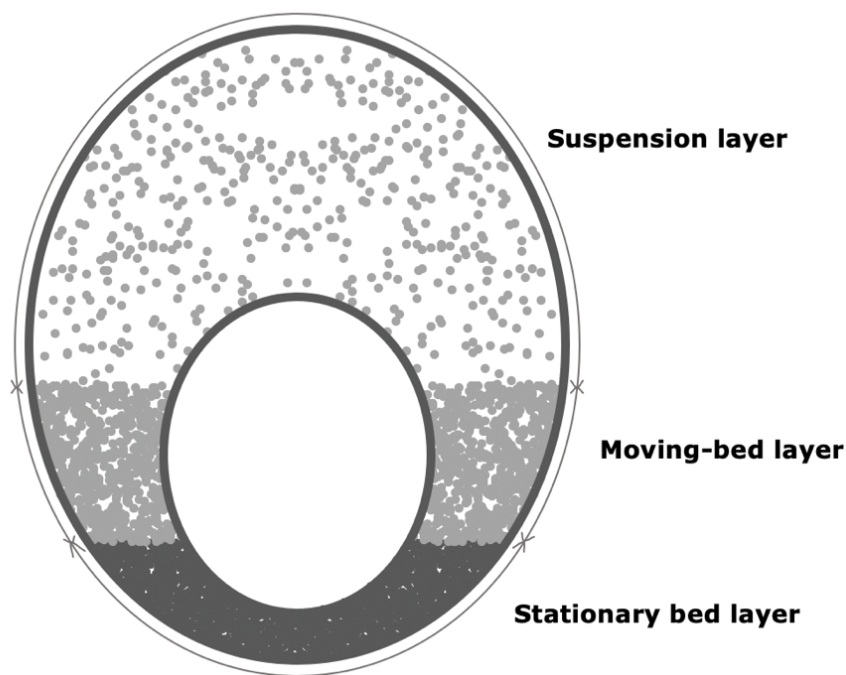


Figure 5.2: Configuration of the three-layered cutting transport mechanism in wellbore annuli

The area of the flow can be obtained from the following relationships:

$$Q = A_{\text{flow}} V_f \tag{5.16}$$

$$A_{\text{flow}} = \frac{Q}{V_f} \tag{5.17}$$

$$V_f = \max(V_{avg}, V_{MR}) \quad 5.18$$

$$A_a = A_b + A_{flow} = \frac{\pi(d_2^2 - d_1^2)}{4} \quad 5.19$$

The area of the stationary cutting bed in a concentric or eccentric annulus can be expressed as:

$$\frac{dA}{2} = \int_{y=0}^{y=h} [(r_2^2 - (r_2 \sin \alpha_2)^2)^{1/2} - (r_1^2 - (r_1 \sin \alpha_1)^2)^{1/2}] dy \quad 5.20$$

The approach for the formulation of the stationary bed equation is similar to the method derived in chapter 4. Equations 4.110 to 4.113 can be used to calculate the area of the stationary bed by substituting the bed height. The bed height in a concentric or eccentric annulus can be obtained from the following function:

$$f(h) = \frac{A_b}{2} - \int_{y=0}^{y=h} \left[ \left( \frac{d_2^2}{4} - \left( \frac{d_2}{2} \sin \left( \frac{2h - d_2}{d_2} \right) \right)^2 \right)^{1/2} - \left( \frac{d_2^2}{4} - \left( \frac{d_2}{2} \sin \left( \frac{2h - d_2 + e(d_2 - d_1)}{d_2} \right) \right)^2 \right)^{1/2} \right] dh \quad 5.21$$

In this mathematical model development, the multiphase gas-liquid flow pattern is taken into consideration with the cuttings transport mechanism, making this a major improvement from the previously developed multi-layered models. The mass, momentum and energy conservations for multiphase flowing fluids in conduits are flow pattern dependent; therefore, the model development using the governing conservation equations needs to be flow pattern specific. The model development is based on the assumption that the drilling activity is carried out at operating conditions where the suspension, moving bed and stationary bed layers are formed simultaneously in the annulus.

### 5.2.1 Dispersed bubble flow

Assuming that the flow is steady-state and there is no slip between the cuttings and fluid phase. The continuity equation for the cuttings and the fluid phase in a given control volume may be written as:

Cuttings phase:

$$\frac{\partial(\rho_p C_1 A_1 V_1)}{\partial L} + \frac{\partial(\rho_p C_2 A_2 V_2)}{\partial L} + \frac{\partial(\rho_p C_3 A_3 V_3)}{\partial L} = 0 \quad 5.22$$

Drilling fluid phase:

$$\frac{\partial(\rho_f(1 - C_1)A_1V_1)}{\partial L} + \frac{\partial(\rho_f(1 - C_2)A_2V_2)}{\partial L} + \frac{\partial(\rho_f(1 - C_3)A_3V_3)}{\partial L} = 0 \quad 5.23$$

Integrating the continuity equations across the control volume, and acknowledging that the stationary bed is not moving  $V_3 = 0$ , the mass balance of the cuttings and the fluid phase can then be expressed as:

Cuttings phase:

$$\rho_p C_1 A_1 V_1 + \rho_p C_2 A_2 V_2 = \rho_p C_p A V_m \quad 5.24$$

Drilling fluid phase:

$$\rho_m (1 - C_1) A_1 V_1 + \rho_m (1 - C_2) A_2 V_2 = \rho_m (1 - C_p) A V_m \quad 5.25$$

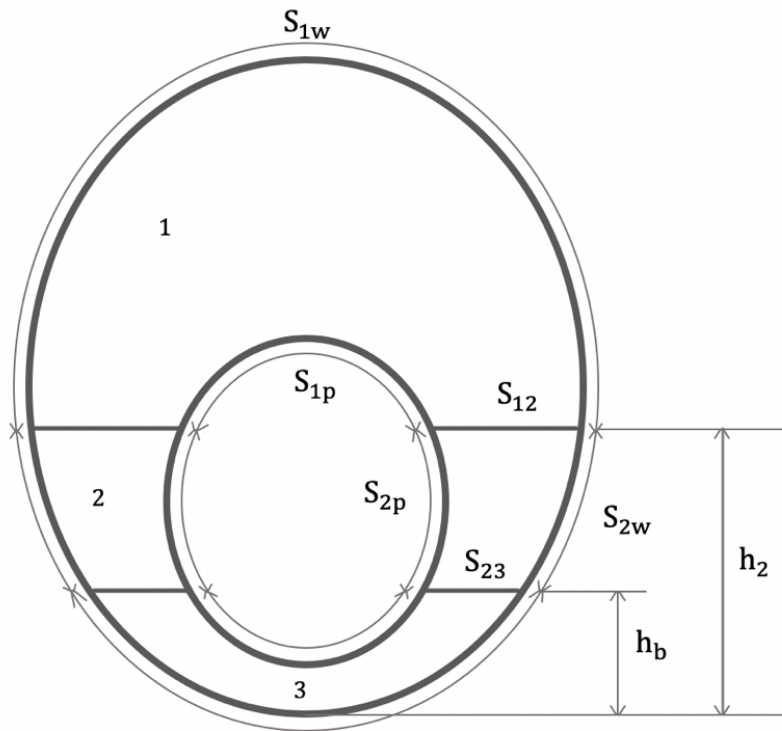


Figure 5.3: Schematic diagram of the three-layer model for dispersed bubble flow

The momentum equations can be obtained from considering the sum of the forces acting on each of the layers (Figure 5.3):

Suspension layer:

$$-\frac{dP}{\partial L} + \frac{\tau_{1w}S_{1w}}{A_1} + \frac{\tau_{1p}S_{1p}}{A_1} - \frac{\tau_{12}S_{12}}{A_1} + \rho_1 g \sin \theta_p = 0 \quad 5.26$$

Moving bed layer:

$$-\frac{dP}{\partial L} + \frac{\tau_{2w}S_{2w}}{A_2} + \frac{\tau_{2p}S_{2p}}{A_2} + \frac{\tau_{12}S_{12}}{A_2} + \frac{\tau_{23}S_{23}}{A_2} + \rho_2 g \sin \theta_p = 0 \quad 5.27$$

The mixture density for each of the layers are given as:

$$\rho_1 = \rho_m(1 - C_1) + \rho_p C_1 \quad 5.28$$

$$\rho_2 = \rho_m(1 - C_1) + \rho_p C_2 \quad 5.29$$

where  $\rho_m$ , defined by the Equation 4.85, is the gas-liquid mixture density.

The wetted perimeters required for the solution of these equations are dependent on the height of the stationary bed  $h_b$  and the height of the suspension-moving bed interface  $h_2$ . The functions for the wetted perimeters derived solely from wellbore geometry and trigonometry are given as:

$$S_{12} = d_2 \sin \left[ \cos^{-1} \left( \frac{d_2 - 2h_2}{d_2} \right) \right] - d_1 \sin \left[ \cos^{-1} \left( \frac{d_1 - 2(h_2 - d_x)}{d_1} \right) \right] \quad 5.30$$

$$S_{23} = d_2 \sin \left[ \cos^{-1} \left( \frac{d_2 - 2h_b}{d_2} \right) \right] - d_1 \sin \left[ \cos^{-1} \left( \frac{d_1 - 2(h_b - d_x)}{d_1} \right) \right] \quad 5.31$$

$$S_{1p} = \pi d_1 - d_1 \cos^{-1} \left( \frac{d_1 - 2(h_2 - d_x)}{d_1} \right) \quad 5.32$$

$$S_{1w} = \pi d_2 - d_2 \cos^{-1} \left( \frac{d_2 - 2h_2}{d_2} \right) \quad 5.33$$

$$S_{3w} = d_2 \cos^{-1} \left( \frac{d_2 - 2h_b}{d_2} \right) \quad 5.34$$

$$S_{3p} = d_1 \cos^{-1} \left( \frac{d_1 - 2(h_b - d_x)}{d_1} \right) \quad 5.35$$

$$S_{2w} = \pi d_2 - S_{1w} - S_{3w} \quad 5.36$$

$$S_{2p} = \pi d_1 - S_{1p} - S_{3p} \quad 5.37$$

The cross-sectional area of each of the layers can be computed using Equations 4.110 to 4.113 as a function of the interfacial heights  $h_2$  and  $h_b$ :

$$A_1 = A_a - (X_1(h_2) + X_2(h_2) + X_3(h_2)) \quad 5.38$$

$$A_b = X_1(h_b) + X_2(h_b) + X_3(h_b) \quad 5.39$$

$$A_2 = A_a - A_1 - A_b \quad 5.40$$

In order to obtain a solution, Equations 5.24 to 5.40 would have to be solved simultaneously using an iterative technique.

### 5.2.2 Stratified flow

The vertical cuttings concentration in stratified flow pattern is different to that which is experienced by the dispersed bubble flow pattern. When the stratified gas-liquid flow is formed in the wellbore annuli, the cuttings would fall to the liquid phase flowing below the gas phase due to density differences. This leads to the formation of 4 distinctive layers in the annuli where the suspension and moving bed layers are embedded in the liquid phase alone (Figure 5.4). The layer one

only contains all of the gas phase, hence the velocity of the layer 1 can be expressed as a function of the input gas flowrate into the wellbore from:

$$V_1 = \frac{Q_G}{A_1} \quad 5.41$$

Since there are no cuttings traveling in the gas phase in layer 1, the material balance for the cuttings and the liquid phase in the layer 2 and 3 may be expressed as:

Cuttings phase:

$$\rho_c C_2 A_2 V_2 + \rho_c C_3 A_3 V_3 = \rho_c C_c Q_L \quad 5.42$$

Drilling fluid phase:

$$\rho_L (1 - C_2) A_2 V_2 + \rho_L (1 - C_3) A_3 V_3 = \rho_L (1 - C_c) Q_L \quad 5.43$$

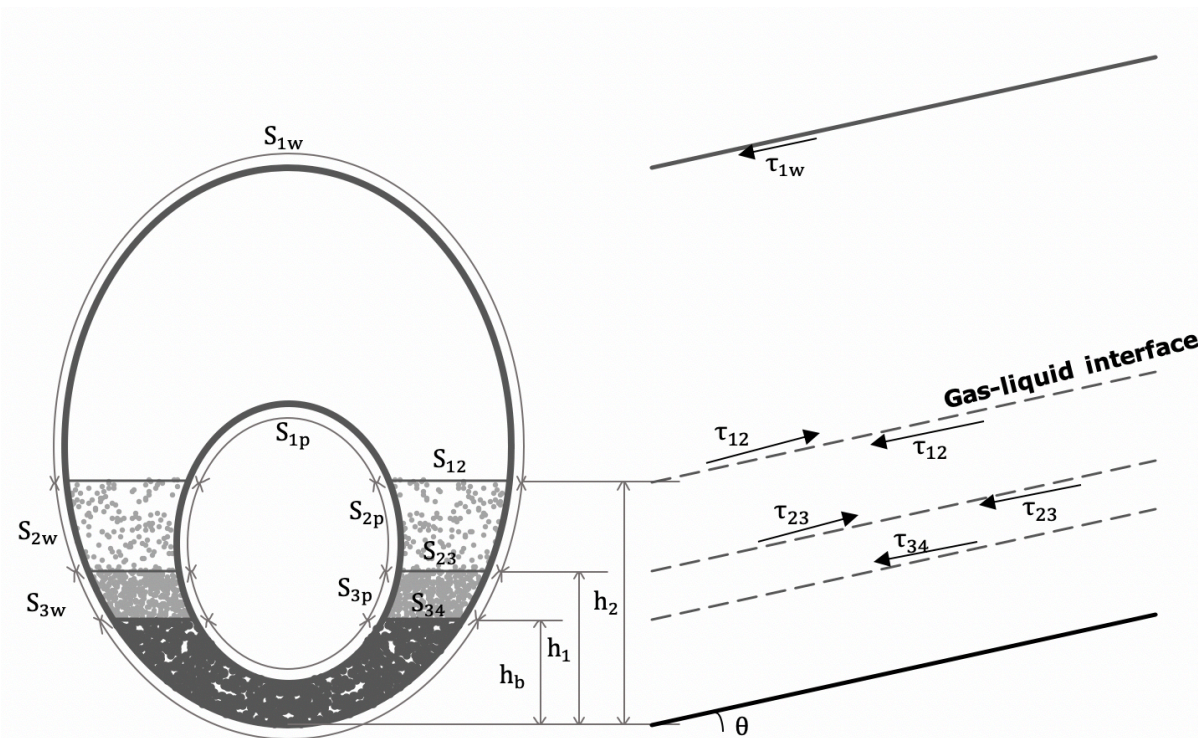


Figure 5.4: Schematic diagram of the four-layer model for stratified (gas, liquid and cuttings) flow

The momentum equations obtained from considering the sum of the forces acting on each of the layers may be expressed as:

Layer 1: Gas phase

$$-\frac{dP}{\partial L} + \frac{\tau_{1w}S_{1w}}{A_1} + \frac{\tau_{1p}S_{1p}}{A_1} - \frac{\tau_{12}S_{12}}{A_1} + \rho_1 g \sin \theta_p = 0 \quad 5.44$$

Layer 2: Suspension layer (Liquid phase)

$$-\frac{dP}{\partial L} + \frac{\tau_{2w}S_{2w}}{A_2} + \frac{\tau_{2p}S_{2p}}{A_2} + \frac{\tau_{12}S_{12}}{A_2} - \frac{\tau_{23}S_{23}}{A_2} + \rho_2 g \sin \theta_p = 0 \quad 5.45$$

Layer 3: Moving bed layer (Liquid phase)

$$-\frac{dP}{\partial L} + \frac{\tau_{3w}S_{3w}}{A_3} + \frac{\tau_{3p}S_{3p}}{A_3} + \frac{\tau_{23}S_{23}}{A_3} + \frac{\tau_{34}S_{34}}{A_3} + \rho_3 g \sin \theta_p = 0 \quad 5.46$$

The density of the layer 1 is the density of the gas phase as only the gas phase is flowing in this layer. Thus, the in-situ density for each of the layers are given as:

$$\rho_1 = \rho_G \quad 5.47$$

$$\rho_2 = \rho_L(1 - C_2) + \rho_p C_2 \quad 5.48$$

$$\rho_3 = \rho_L(1 - C_3) + \rho_p C_3 \quad 5.49$$

The wetted perimeters required for the solution of the stratified flow momentum equations are not only dependent on the height of the stationary bed  $h_b$  and the height of the suspension-moving bed interface  $h_1$ , but is also dependent on the height of the gas-liquid interface  $h_2$ . The functions required to compute the wetted perimeters derived from the wellbore geometry can be expressed as:

$$S_{12} = d_2 \sin \left[ \cos^{-1} \left( \frac{d_2 - 2h_2}{d_2} \right) \right] - d_1 \sin \left[ \cos^{-1} \left( \frac{d_1 - 2(h_2 - d_x)}{d_1} \right) \right] \quad 5.50$$

$$S_{23} = d_2 \sin \left[ \cos^{-1} \left( \frac{d_2 - 2h_1}{d_2} \right) \right] - d_1 \sin \left[ \cos^{-1} \left( \frac{d_1 - 2(h_1 - d_x)}{d_1} \right) \right] \quad 5.51$$

$$S_{34} = d_2 \sin \left[ \cos^{-1} \left( \frac{d_2 - 2h_b}{d_2} \right) \right] - d_1 \sin \left[ \cos^{-1} \left( \frac{d_1 - 2(h_b - d_x)}{d_1} \right) \right] \quad 5.52$$

$$S_{1p} = \pi d_1 - d_1 \cos^{-1} \left( \frac{d_1 - 2(h_2 - d_x)}{d_1} \right) \quad 5.53$$

$$S_{1w} = \pi d_2 - d_2 \cos^{-1} \left( \frac{d_2 - 2h_2}{d_2} \right) \quad 5.54$$

$$S_{3w} = d_2 \cos^{-1} \left( \frac{d_2 - 2h_1}{d_2} \right) - S_{4w} \quad 5.55$$

$$S_{4w} = d_2 \cos^{-1} \left( \frac{d_2 - 2h_b}{d_2} \right) \quad 5.56$$

$$S_{3p} = d_1 \cos^{-1} \left( \frac{d_1 - 2(h_1 - d_x)}{d_1} \right) - S_{4p} \quad 5.57$$

$$S_{4p} = d_1 \cos^{-1} \left( \frac{d_1 - 2(h_b - d_x)}{d_1} \right) \quad 5.58$$

$$S_{2w} = \pi d_2 - S_{1w} - S_{3w} - S_{4w} \quad 5.59$$

$$S_{2p} = \pi d_1 - S_{1p} - S_{3p} - S_{4p} \quad 5.60$$

The cross-sectional area of each of the layers can be computed using a similar approach to that which was used in the dispersed bubble flow pattern. The functions required for determining the area of the layers may be expressed as:

$$A_1 = A_a - (X_1(h_2) + X_2(h_2) + X_3(h_2)) \quad 5.61$$

$$A_b = X_1(h_b) + X_2(h_b) + X_3(h_b) \quad 5.62$$

$$A_3 = (X_1(h_1) + X_2(h_1) + X_3(h_1)) - A_b \quad 5.63$$

$$A_2 = A_a - A_1 - A_3 - A_b \quad 5.64$$

The wall and interfacial shear stresses in the mathematical models can be determined respectively from the following equations:

$$\tau_i = \frac{f_i \rho_i V_i^2}{2} \quad 5.65$$

$$\tau_{ij} = \frac{f_i \rho_i (V_i - V_j)^2}{2} \quad 5.66$$

where subscripts i and j indicate the position of the layers in the annulus.

### 5.2.3 Slug flow

The cutting transport modelling for the slug flow pattern is relatively more complex than that of the other flow patterns. This is because there is not only the formation of several vertical layers due to the disparities in the cutting transport mechanism, but also two separate regions in the axial direction, where the phase configuration and the fluid shearing forces differ significantly. As explained in detail in Chapter 4, a fully developed slug unit is composed of the axial movement of a slug body accompanied by a liquid-film/gas pocket region. In the slug unit, if the drilling fluid annuli velocity in the slug body is below the minimum transport velocity required to keep the cuttings mobile, this would lead to the formation of a stationary cuttings bed and the flow of the oncoming liquid-film/gas pocket region over the stationary bed. The process of slug flow on its own in a conduit possesses a complex hydrodynamic behaviour making predictions difficult due to its unsteady nature and the fluid forces or conservation of momentum in the slug body differs to that which exists in the liquid-film/gas pocket region. The fluid configuration of a fully developed slug flow containing cuttings with formation of the different cutting transport mechanisms can be observed from the Figure 5.5.

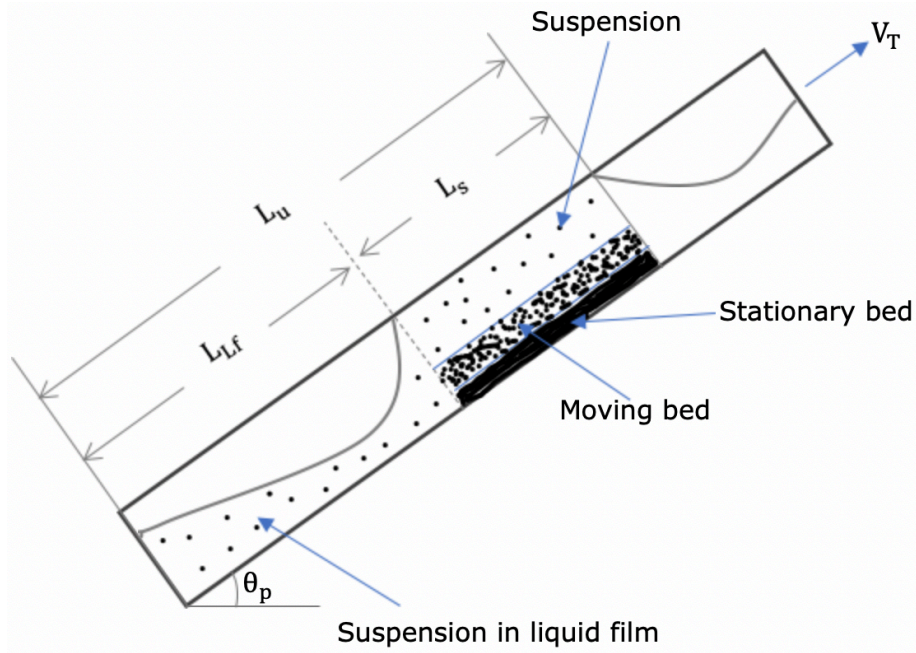


Figure 5.5: A fully developed slug flow with different cutting transport mechanisms in an inclined wellbore annulus

The material balance of the cutting gas and fluid phase in the entire fully developed slug unit may be expressed as:

Cuttings phase:

$$\rho_c C_1 A_1 V_1 L_s + \rho_c C_2 A_2 V_2 L_s + \rho_c C_{Lf} A_{flow} \int_0^{L_{Lf}} V_{Lf} H_{Lf} \partial L_{Lf} = \rho_c C_c A_a V_m L_u \quad 5.67$$

Drilling fluid phase:

$$\begin{aligned} & \rho_s (1 - C_1) A_1 V_1 L_s + \rho_s (1 - C_2) A_2 V_2 L_s + \\ & \rho_L (1 - C_{Lf}) A_{flow} \int_0^{L_{Lf}} V_{Lf} H_{Lf} \partial L_{Lf} + \rho_G A_{flow} \int_0^{L_{Lf}} V_{Gf} (1 - H_{Lf}) \partial L_{Lf} \\ & = \rho_m (1 - C_c) A_a V_m L_u \end{aligned} \quad 5.68$$

### Slug body region:

The mass and momentum balance equations in the slug body region of the fully developed slug unit are similar to that of the dispersed bubble flow. In the slug body region, the cuttings can be both or either in suspension or mobile as a moving bed. The momentum equations for the suspension and moving-bed layer may be expressed as:

Suspension layer:

$$-\frac{dP}{\partial L}_s + \frac{\tau_{1w}S_{1w}}{A_1} + \frac{\tau_{1p}S_{1p}}{A_1} - \frac{\tau_{12}S_{12}}{A_1} + \rho_1 g \sin \theta_p = 0 \quad 5.69$$

Moving bed layer:

$$-\frac{dP}{\partial L}_s + \frac{\tau_{2w}S_{2w}}{A_2} + \frac{\tau_{2p}S_{2p}}{A_2} + \frac{\tau_{12}S_{12}}{A_2} + \frac{\tau_{23}S_{23}}{A_2} + \rho_2 g \sin \theta_p = 0 \quad 5.70$$

The mixture density for each of the layers are given as:

$$\rho_1 = \rho_s(1 - C_1) + \rho_p C_1 \quad 5.71$$

$$\rho_2 = \rho_s(1 - C_1) + \rho_p C_2 \quad 5.72$$

The parameters and procedures for the solution of the equations here are the same as that required for the dispersed bubble flow pattern. However, the fluid density in the slug body  $\rho_s$  is obtained as a function of the liquid hold up in the slug body  $H_{Ls}$  and not the input or no-slip liquid hold.

$$\rho_s = \rho_L H_{Ls} + \rho_G(1 - H_{Ls}) \quad 5.73$$

### Liquid-film/gas pocket region:

The faster flowing slug body moving behind the slower liquid film overruns and picks up the liquid in the liquid film and accelerates it to the slug velocity. The acceleration of the liquid film is accompanied with a change in the height of the liquid film, the liquid hold-up, the velocity of the liquid film and the interfacial and wall shear stresses in the axial direction of the flow. The cuttings flowing in the liquid-film/gas pocket region are only located in the liquid film due to density differences, so the cuttings benefit from the acceleration of the liquid film, keeping them in suspension. Figure 5.6 shows the geometric configuration of the liquid film/gas pocket region which contains the gas layer on top, a liquid region with cuttings suspension and stationary bed.

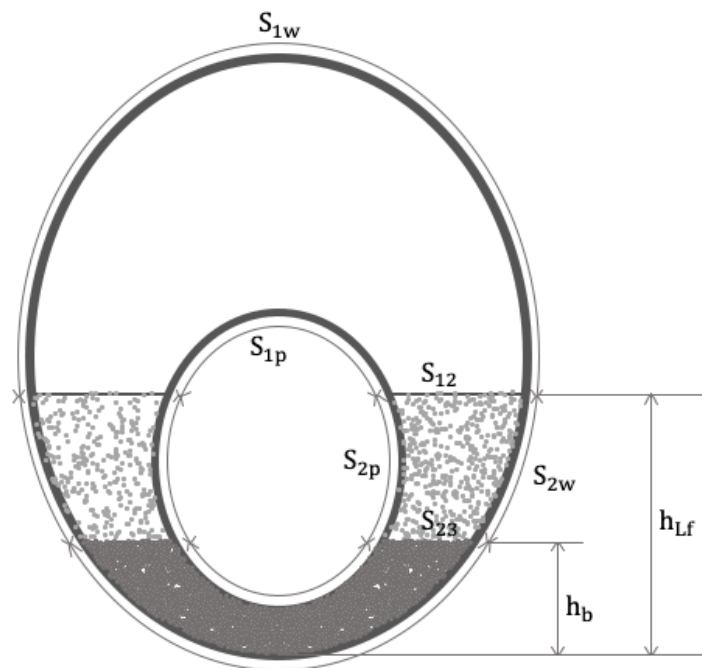


Figure 5.6: Schematic diagram of the mathematical model for liquid film/gas pocket region

The liquid film hydrodynamics analysis in the translational velocity co-ordinate system permits the respective expression of the conservation of momentum equations for the gas pocket and the liquid film in the drilling annulus as:

Layer 1: Gas pocket

$$-\frac{\partial P}{\partial L} + \rho_G v_{Gf} \frac{\partial v_{Gf}}{\partial L} + \frac{\tau_{1w} S_{1w}}{A_{Gf}} + \frac{\tau_{1p} S_{1p}}{A_{Gf}} + \frac{\tau_{12} S_{12}}{A_{Gf}} + \rho_G g \sin \theta_p - \rho_G g \cos \theta_p \frac{\partial h_{Lf}}{\partial L} = 0 \quad 5.74$$

Layer 2: Liquid film and drilled cuttings

$$\begin{aligned} -\frac{\partial P}{\partial L} + \rho_{Lfc} v_{Lf} \frac{\partial v_{Lf}}{\partial L} + \frac{\tau_{2w} S_{2w}}{A_{Lf}} + \frac{\tau_{2p} S_{2p}}{A_{Lf}} - \frac{\tau_{12} S_{12}}{A_{Lf}} + \frac{\tau_{23} S_{23}}{A_{Lf}} \\ + \rho_{Lfc} g \sin \theta_p - \rho_{Lfc} g \cos \theta_p \frac{\partial h_{Lf}}{\partial L} = 0 \end{aligned} \quad 5.75$$

The relative velocities of the liquid film and gas are given as:

$$v_{Lf} = V_T - V_{Lf} \quad \text{and} \quad v_{Gf} = V_T - V_{Gf} \quad 5.76$$

$\rho_{Lfc}$ , is the mixture density of the liquid and the cuttings in the liquid film, given as:

$$\rho_{Lfc} = \rho_L(1 - C_{Lf}) + \rho_c C_{Lf} \quad 5.77$$

Substituting Equation 5.74 into Equation 5.75 to eliminate the pressure gradient term and applying similar methods detailed in Chapter 4 for a fully developed slug flow, yields an ordinary differential equation for the change in the liquid film height in the axial direction.

$$\frac{\partial h_{Lf}}{\partial L} = \frac{\frac{\tau_{2w}S_{2w}}{A_{Lf}} + \frac{\tau_{2p}S_{2p}}{A_{Lf}} - \frac{\tau_{1w}S_{1w}}{A_{Gf}} - \frac{\tau_{1p}S_{1p}}{A_{Gf}} + \frac{\tau_{23}S_{23}}{A_{Lf}} - \tau_{12}S_{12} \left( \frac{1}{A_{Lf}} + \frac{1}{A_{Gf}} \right) + (\rho_{Lfc} - \rho_G)g \sin \theta_p}{\rho_G V_{Gf} \frac{(V_T - V_{Gs})(1 - H_{Ls})}{(1 - H_{Lf})^2} \frac{\partial H_{Lf}}{\partial h_{Lf}} - \rho_{Lfc} V_{Lf} \frac{(V_T - V_{Ls})H_{Ls}}{H_{Lf}^2} \frac{\partial H_{Lf}}{\partial h_{Lf}} + (\rho_{Lfc} - \rho_G)g \cos \theta_p} \quad 5.78$$

$$\frac{\partial H_{Lf}}{\partial h_{Lf}} = 2 \frac{\left[ \left( \frac{d_2^2}{4} - \left( \frac{1}{2}(2h_b - d_2) \right)^2 \right)^{1/2} - \left( \frac{d_1^2}{4} - \left( \frac{1}{2}(2h_b - d_2 + 2d_e) \right)^2 \right)^{1/2} \right]}{A_{flow}} \quad 5.79$$

Equation 5.78 has to be integrated numerically and iteratively following the procedures explained in Section 4.5.4 for slug flow to yield the length of the liquid film with the solution for the simultaneous flow of cuttings and gas-liquid fluids flow with a slug flow pattern. Before starting the numerical integration, the boundary condition is obtained by first solving the Equation 5.80 to obtain  $h_{Lf0}$ , where  $h_{Lf}(L = 0) = h_{Lf0}$  corresponds to  $v_{Lf}(L = 0) = V_T - V_{Ls}$

$$f(h_{Lf0}) = H_{Ls} - \frac{X1(h_{Lf0}) + X2(h_{Lf0}) + X3(h_{Lf0}) - A_b}{A_{flow}} \quad 5.80$$

Once the mass balance is satisfied the integration (Equation 4.104) is stopped yielding the length of the liquid film in the liquid-film/gas pocket region  $L_f$ . The total annuli pressure drop experienced by the flow can be obtained from the global force and momentum balance across the entire slug unit. The global pressure drop across a slug unit can be written as the summation of the pressure drop in the slug body region and the pressure drop in the liquid film region. The average density

of the fluids in the liquid-film/gas pocket region can be determined from the flowing equation:

$$\rho_{LFA} = \frac{\rho_{Lfc}}{L_{Lf}} \int_0^{L_{Lf}} H_{Lf} \partial L_{Lf} + \frac{\rho_G}{L_f} \int_0^{L_{Lf}} (1 - H_{Lf}) \partial L_{Lf} \quad 5.81$$

The total annuli pressure drop across a slug unit can be obtained from the global force and momentum balance across the given slug unit. The global pressure drop across a slug unit can be written as the summation of the pressure drop in the slug body region and the pressure drop in the liquid film region yielding:

$$\Delta P_u = \left( \frac{dP}{dL} \right)_s L_s + \rho_{LFA} g \sin \theta_p L_{Lf} + \int_0^{L_{Lf}} \frac{\tau_{2w} S_{2w} + \tau_{2p} S_{2p} + \tau_{1w} S_{1w} + \tau_{1p} S_{1p} + \tau_{23} S_{23}}{A_a - A_b} dL \quad 5.82$$

The velocity of the moving bed region,  $V_{MB}$  for all the flow patterns may be obtained by considering the forces acting on the cuttings in the wellbore. To initiate cutting movement, the forces moving the cuttings must be equal to or greater than the forces resisting its movement ( $F_D + F_L \geq F_G - F_B$ ). From the force balance analysis, the velocity of the moving bed  $V_{MB}$  may be expressed as (Cho, et al., 2002):

$$V_{MB} = \sqrt{\frac{0.13g(\rho_c - \rho_f) \left[ \frac{d_{mb}}{d_c} C_{mb} \sin \beta \right] [1 + 1.73 \tan \theta_p] \sin \beta}{\rho_f [0.165C_D + 0.098C_L]}} \quad 5.83$$

where  $d_{mb}$  and  $C_{mb}$ , represent the diameter and cutting concentration of the moving bed layer respectively.

The wall and drillpipe shear stresses for both Newtonian and non-Newtonian fluid flow should be obtained from the knowledge of the friction geometry parameter of the annuli (Equation 4.68 to 4.76). The Interfacial friction factors may be determined from the following equations:

Gas-liquid interface:

$$\frac{1}{\sqrt{f_i}} = 3.48 - 4 \log \left[ \frac{\gamma(V_i - V_{i+1})^2 f_i}{gD_{hi}} + \frac{9.35}{Re_i \sqrt{f_i}} \right] \quad 5.84$$

$$\gamma = 0.1 - 0.5$$

Suspension-moving bed interface:

$$\frac{1}{\sqrt{2f_i}} = -0.86 \ln \left[ \frac{\frac{d_p}{D_{hi}}}{3.7} + \frac{2.51}{Re_i \sqrt{2f_i}} \right] \quad 5.85$$

Moving bed-stationary bed interface:

$$f_i = \frac{0.046}{Re_i^{0.2}} \quad 5.86$$

The hydraulic diameters and Reynolds number for each of the layers formed in the annuli can be determined from the following equations:

Layer1:

$$D_{h1} = \frac{4A_1}{S_{1w} + S_{1p} + S_{12}} \quad Re_1 = \frac{\rho_1 V_1 D_{h1}}{\mu_1} \quad 5.87$$

Layer2:

$$D_{h2} = \frac{4A_2}{S_{2w} + S_{2p} + S_{23}} \quad Re_2 = \frac{\rho_2 V_2 D_{h2}}{\mu_2} \quad 5.88$$

Layer3:

$$D_{h3} = \frac{4A_3}{S_{3w} + S_{34} + S_{3p}} \quad Re_2 = \frac{\rho_3 V_3 D_{h3}}{\mu_3} \quad 5.89$$

### **5.3 Chapter summary**

The current multi-layered cutting transport models presented in literature for two-phase gas-liquid fluid flow applications considers the cutting transport mechanism but ignores transient gas-liquid fluid flow patterns. The ability of a two-phase drilling fluid to transport cuttings effectively during drilling operations is largely dependent on the fluid flow pattern and the prevailing cutting transport mechanism. The fluid flow pattern has to be adequately taken into consideration when evaluating the cuttings transport efficiency in order to avoid large prediction errors. In this chapter, the forces responsible for the movement of particles were analysed and the concept of the minimum transport velocity was applied to develop mathematical models to predicts the criteria required to transport the cuttings in the different particle transport mechanisms (Equation 5.12 to 5.15). New mathematical gas-liquid fluid flow pattern dependent multi-layered models were developed and presented for the different cuttings transport mechanisms in the bubble, dispersed bubble, stratified and slug gas-liquid flow patterns for the first time (Section 5.2). These models are valid for both Newtonian and non-Newtonian fluids and any level of pipe eccentricity.

This provides a new and reliable method that can be implemented to evaluate cuttings transport efficiency and perform wellbore hydraulics calculations for UBD operations.

## Chapter 6

### Numerical CFD methodology

The technique of computational fluid dynamics CFD was applied to perform transient simulations of single-phase and multiphase fluid flow in a concentric and eccentric annulus with or without inner pipe rotation. For an incompressible isothermal flow of a fluids whose effective viscosity is highly dependent on the strain rate tensor, the modelling of the fluid flow can be described using the continuity equations of mass and momentum. In order to obtain the velocity and pressure fields in the domain, a mathematical Finite-Volume approach was employed by dividing the flow domain into several control volumes and applying the conservation principles of mass and momentum to the cells of each control volume by numerically integrating the governing conservation equations across the faces bounding the control volume. For the simulation of multiphase (gas-liquid flows), the one fluid approach where a single set of equations for the entire flow domain is solved and the differences in the material properties of the different fluids and the interfacial phenomena is accounted for. The interface between the fluids was tracked by representing the boundaries between the fluids by marker points and constructed using a marker function onto a fixed grid. The methods of using marker points to represent the interface between the fluids is generally referred to as the front-tracking method. The standard way to integrate the governing momentum equations is by applying the projection method. This is done by obtaining a temporal velocity field that is non divergence-free and correcting the velocities by finding the pressure that ensures that the velocity fields are divergence-free. The governing momentum equation excluding other forces can be expressed as:

$$\frac{\partial \mathbf{u}}{\partial t} + \nabla \cdot \mathbf{u}\mathbf{u} = -\frac{1}{\rho} \nabla P + \frac{\mu}{\rho} \nabla^2 \mathbf{u} + \mathbf{g} \quad 6.1$$

Assuming that the flow is incompressible, the density of each fluid particle remains constant as the fluid particle moves with the flow hence the conservation of mass equation for the flow is expressed as follows:

$$\frac{D\rho}{Dt} = \frac{\partial\rho}{\partial t} + \mathbf{u} \cdot \nabla\rho = 0 \quad 6.2$$

$$\nabla \cdot \mathbf{u} = 0 \quad 6.3$$

The integration in time of the Equation 6.1 using the projection method involves the splitting of the process into two major steps. In the first step which is referred to as the predictor step, a temporal velocity field  $\mathbf{u}^t$  is computed without the consideration of the pressure fields with the following equation:

$$\frac{\mathbf{u}^t - \mathbf{u}^n}{\Delta t} = -\nabla \cdot \mathbf{u}^n \mathbf{u}^n + \frac{\mu}{\rho^n} \nabla^2 \mathbf{u}^n + \mathbf{g} \quad 6.4$$

$\mathbf{u}^n$  is the velocity at the current time step.

In the second step - the projection step, the correct velocity fields at the next time step  $\mathbf{u}^{n+1}$  is obtained by including the pressure gradient. However, the required pressure gradient has to be obtained in a manner that ensures that the corrected velocities are divergence-free. The projection equation may be expressed as:

$$\frac{\mathbf{u}^{n+1} - \mathbf{u}^t}{\Delta t} = -\frac{1}{\rho^n} \nabla P^{n+1} \quad 6.5$$

The addition of the Equation 6.4 and 6.5 yields a numerical approximation to the Equation 6.1, where the change in the velocity with time has been approximated using a method of first-order accuracy. The pressure gradient has no equation and has to be determined through an iterative approach. To ensure that the pressure obtained makes the final velocity divergence free at the end of a next time step, the divergence of the Equation 6.5 is taken and expressed as:

$$\frac{\nabla \cdot \mathbf{u}^{n+1} - \nabla \cdot \mathbf{u}^t}{\Delta t} = \nabla \cdot \left( -\frac{1}{\rho^n} \nabla P^{n+1} \right) \quad 6.6$$

From the conservation of mass Equation 6.3, the final velocity at the next time step should be in such a way that

$$\nabla \cdot \mathbf{u}^{n+1} = 0 \quad 6.7$$

Substituting the equation 6.7 into the Equation 6.6 yields the pressure gradient that can be used to project the final velocity at the next time  $\mathbf{u}^{n+1}$  as:

$$\nabla \cdot \left( \frac{1}{\rho^n} \nabla P^{n+1} \right) = \frac{\nabla \cdot \mathbf{u}^t}{\Delta t} \quad 6.8$$

In this study a MATLAB code was developed to perform transient simulations of single-phase and multiphase Newtonian and non-Newtonian fluid flow through a concentric and eccentric annulus and to numerically investigate the effect of combined effect of the inner pipe rotation and eccentricity on the flow dynamics and wellbore hydraulics.

### 6.1 Discretisation of governing equations

This section presents the discretisation of the Equations 6.4 to 6.8 for a concentric and eccentric annular geometry with the aim of obtaining the pressure and velocity fields in the annuli while considering the combined effect of inner pipe rotation and eccentricity. The annuli geometry is divided into several small control volumes and the with the application of the Gauss-divergence theorem, the governing equations are integrated in time and space across the faces of a control volume to obtain general discretised equations that can be applied to all the control volumes existing within the flow domain. However, separate or special treatments

are required at the boundaries or walls of the domain where the inlet and boundary conditions are specified.

### 6.1.1 Concentric annuli $e = 0$

The Navier-Stokes equation for flow through the concentric annulus was discretized using the cylindrical coordinate system. One of the major problems involved in the design of numerical methods for the solution of the Navier-Stokes equation is the development of an appropriate discrete form of the incompressibility constraint. In order to avoid numerical instabilities, a numerical scheme that preserves the global conservation of mass, momentum and energy has to be developed. The numerical scheme developed in this study is based fundamentally on the projection method. This method basically involves the breakup of the partial differential in time of the velocity field into two halves where one part is driven by advection and diffusion and the other by the differential pressure. A structured and staggered mesh was used to obtain the numerical solution for the flow through the concentric annulus where all the spatial derivatives for the pressure, velocity and density fields are approximated on a staggered grid system. In the staggered grid system, the density and other material properties are stored at the pressure nodes while the velocities are stored at locations usually shifted by half of the grid size. The main advantage of using the staggered grid system is that it prevents the appearance of unphysical behaviors referred to as checkerboard solutions. The control volumes are designed in such a way that the axial direction is referred to as the k-direction and

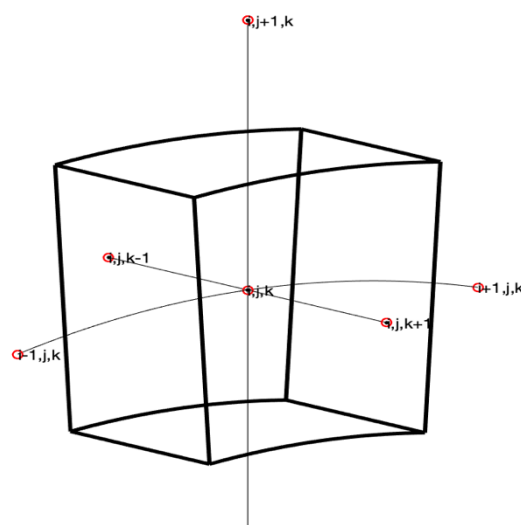


Figure 6.1 Control volume in cylindrical coordinates

the radial and angular directions are referred to as the i and j directions respectively (Figure 6.1).

Figure 6.2 shows an example of a three-dimensional control volume in the cylindrical coordinate system where the pressure and other material properties of the fluid is allocated to the center of the control volume and the velocities are assumed to exist at the boundaries of the control volume. The conservation of mass and momentum equations for fluid flow in the cylindrical coordinates may be expressed as:

$$\frac{1}{r} \frac{\partial(rv_r)}{\partial r} + \frac{1}{r} \frac{\partial(v_\theta)}{\partial \theta} + \frac{\partial(v_z)}{\partial z} = 0 \quad 6.9$$

$$\begin{aligned} r: \rho \left( \frac{\partial v_r}{\partial t} + v_r \frac{\partial v_r}{\partial r} + \frac{v_\theta}{r} \frac{\partial v_r}{\partial \theta} - \frac{v_\theta^2}{r} + v_z \frac{\partial v_r}{\partial z} \right) \\ = \rho g_r - \frac{\partial P}{\partial r} + \mu \left[ \frac{1}{r} \frac{\partial}{\partial r} \left( r \frac{\partial v_r}{\partial r} \right) + \frac{1}{r^2} \frac{\partial^2 v_r}{\partial \theta^2} + \frac{\partial^2 v_r}{\partial z^2} - \frac{v_r}{r^2} - \frac{2}{r^2} \frac{\partial v_\theta}{\partial \theta} \right] \end{aligned} \quad 6.10$$

$$\begin{aligned} \theta: \rho \left( \frac{\partial v_\theta}{\partial t} + v_r \frac{\partial v_\theta}{\partial r} + \frac{v_\theta}{r} \frac{\partial v_\theta}{\partial \theta} + \frac{v_r v_\theta}{r} + v_z \frac{\partial v_\theta}{\partial z} \right) \\ = \rho g_\theta - \frac{1}{r} \frac{\partial P}{\partial \theta} + \mu \left[ \frac{1}{r} \frac{\partial}{\partial r} \left( r \frac{\partial v_\theta}{\partial r} \right) + \frac{1}{r^2} \frac{\partial^2 v_\theta}{\partial \theta^2} + \frac{\partial^2 v_\theta}{\partial z^2} + \frac{2}{r^2} \frac{\partial v_r}{\partial \theta} - \frac{v_\theta}{r^2} \right] \end{aligned} \quad 6.11$$

$$z: \rho \left( \frac{\partial v_z}{\partial t} + v_r \frac{\partial v_z}{\partial r} + \frac{v_\theta}{r} \frac{\partial v_z}{\partial \theta} + v_z \frac{\partial v_z}{\partial z} \right)$$

6.12

$$= \rho g_z - \frac{\partial P}{\partial z} + \mu \left[ \frac{1}{r} \frac{\partial}{\partial r} \left( r \frac{\partial v_z}{\partial r} \right) + \frac{1}{r^2} \frac{\partial^2 v_z}{\partial \theta^2} + \frac{\partial^2 v_z}{\partial z^2} \right]$$

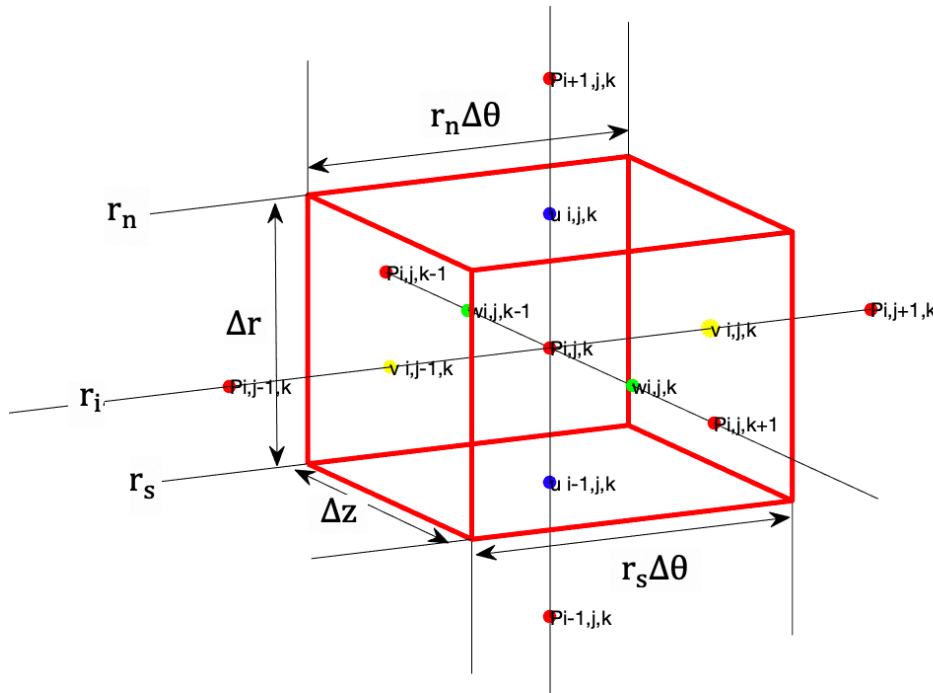


Figure 6.2: Control volume showing the location of the pressure and velocity fields in cylindrical coordinates

Figure 6.2 shows the positions where the velocity components and the pressure points are located. The red points denote the pressure points at the center of each control volume while the green, blue and yellow points, represented by the symbols  $w$ ,  $u$  and  $v$  denote the positions where the axial, radial and tangential velocities ( $u_z, u_r, u_\theta$ ) are located respectively.

The divergence of a velocity field  $\mathbf{u}$  which is a measure of the rate at which the field diverges can be measured by considering the flux out of an enclosed surface. Where  $\mathbf{n}$  is the outward normal on the faces or boundaries of the volume  $V = r dr d\theta dz$ , approximating the Equation 6.7 by performing an integration over the edges of the control volume in the Figure 6.2 yields:

$$\nabla \cdot \mathbf{u} = \frac{\sum_{f=1}^n \iint_{S_f} (\mathbf{u} \cdot \mathbf{n}) dS_f}{\iiint_V r dr d\theta dz} \quad 6.13$$

$$\begin{aligned} \nabla \cdot \mathbf{u}^{n+1} = & \frac{(u_{r_{i,j,k}}^{n+1} r_n - u_{r_{i-1,j,k}}^{n+1} r_s) \Delta\theta \Delta z}{r_i \Delta r \Delta\theta \Delta z} + \frac{(u_{\theta_{i,j,k}}^{n+1} - u_{\theta_{i,j-1,k}}^{n+1}) \Delta r \Delta z}{r_i \Delta r \Delta\theta \Delta z} \\ & + \frac{(u_{z_{i,j,k}}^{n+1} - u_{z_{i,j,k-1}}^{n+1}) r_i \Delta r \Delta\theta}{r_i \Delta r \Delta\theta \Delta z} = 0 \end{aligned} \quad 6.14$$

$$\frac{(u_{r_{i,j,k}}^{n+1} r_b - u_{r_{i-1,j,k}}^{n+1} r_a)}{r_i \Delta r} + \frac{(u_{\theta_{i,j,k}}^{n+1} - u_{\theta_{i,j-1,k}}^{n+1})}{r_i \Delta\theta} + \frac{(u_{z_{i,j,k}}^{n+1} - u_{z_{i,j,k-1}}^{n+1})}{\Delta z} = 0 \quad 6.15$$

$$r_n = \frac{1}{2}(r_{i+1} + r_i) \quad 6.16$$

$$r_s = \frac{1}{2}(r_i + r_{i-1}) \quad 6.17$$

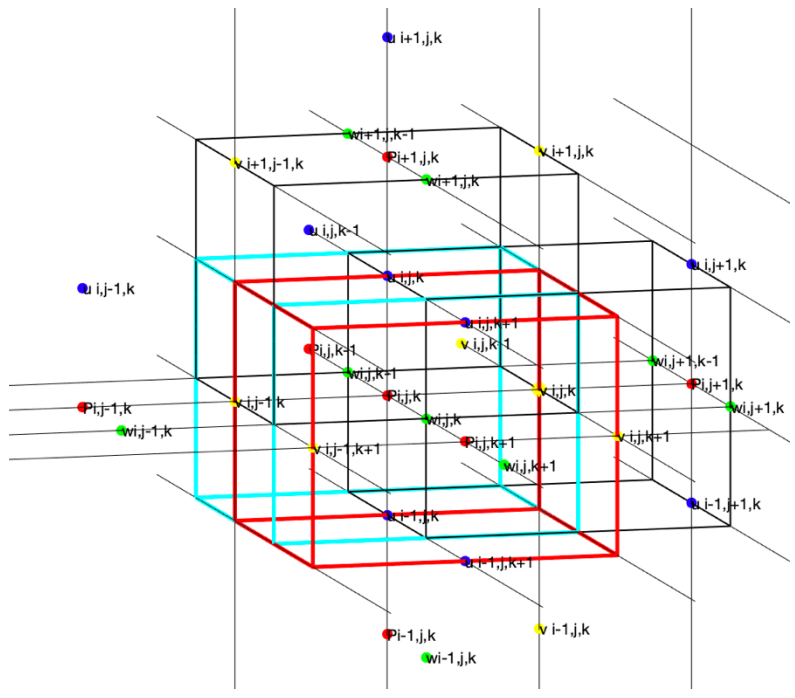


Figure 6.3: Control volume staggered by half a mesh in the axial direction

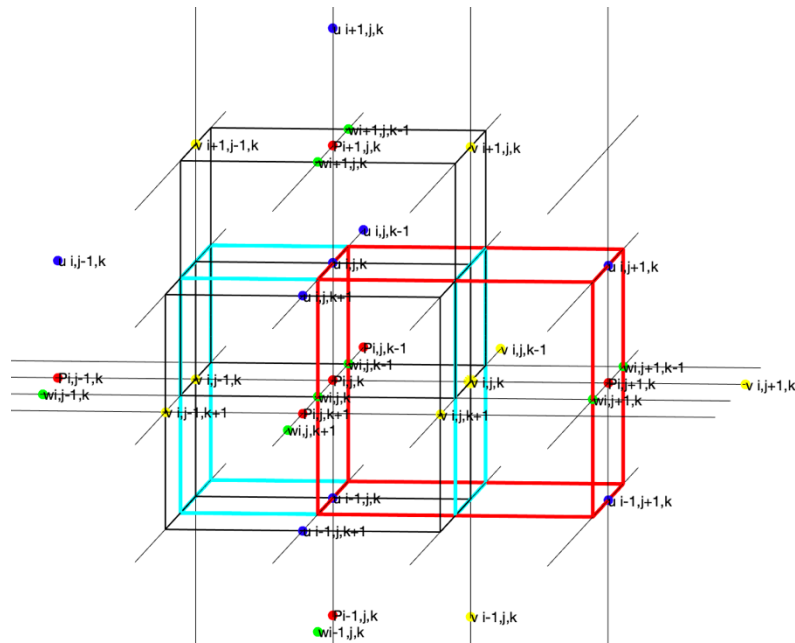


Figure 6.4: Control volume staggered by half a mesh in the angular direction

In the staggered grid mesh, separate control volumes are defined for the axial, tangential and radial components of the velocity. The axial velocity control volume is displaced by half a mesh in the axial direction while the control volumes for the

tangential and radial velocities are displaced by half a mesh in the tangential and radial directions respectively.

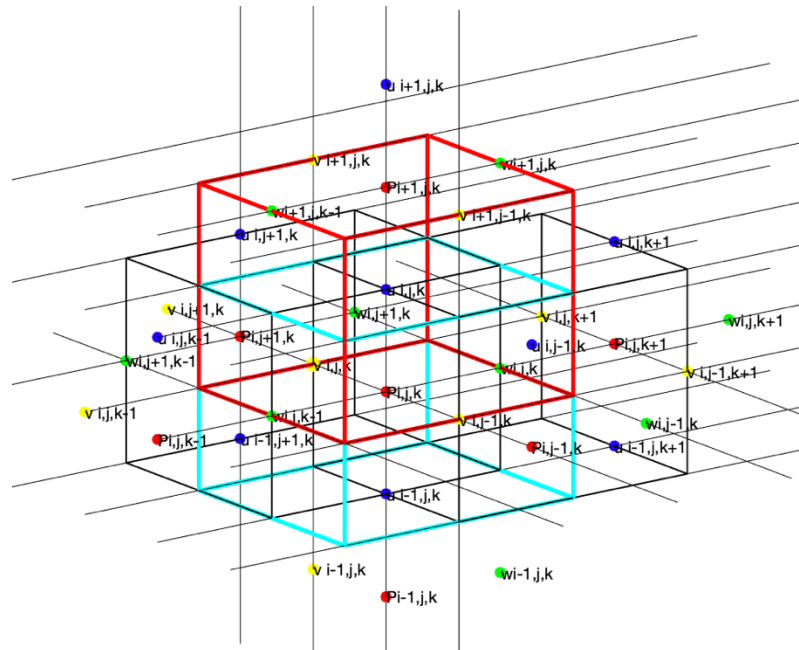


Figure 6.5: Control volume staggered by half a mesh in the radial direction

Figure 6.3 to 6.5 shows an example of the staggered grid system where the control volumes are staggered axial by half a mesh in the all the directions. The blue line represents the boundaries of the main control volume while the red line represents the boundaries of the staggered control volume in the axial, radial or tangential direction.

Equations 6.4 and 6.5 are integrated across the faces of the staggered control volumes in order to obtain an approximation of the velocity fields in the annuli domain. The integration of the Equation 6.5 across the faces of each of the staggered control volumes yields the equations for the correction velocities that are required at the faces of the pressure control volume as shown in Figure 6.2. The equations for the radial, tangential and axial correction velocities may be expressed as:

$$u_r^{n+1} = u_r^t{}_{i,j,k} + \frac{\Delta t}{\rho_{r1}} \left[ \frac{(P_{i+1,j,k} r_{i+1} - P_{i,j,k} r_i)}{r_n \Delta r} - \frac{(P_{i+1,j,k} + P_{i,j,k})}{2r_n} \right] \quad 6.18$$

$$u_r^{n+1}{}_{i-1,j,k} = u_r^t{}_{i-1,j,k} + \frac{\Delta t}{\rho_{r2}} \left[ \frac{(P_{i,j,k} r_i - P_{i-1,j,k} r_{i-1})}{r_s \Delta r} - \frac{(P_{i,j,k} + P_{i-1,j,k})}{2r_s} \right] \quad 6.19$$

$$u_\theta^{n+1} = u_\theta^t{}_{i,j,k} + \frac{\Delta t}{\rho_{\theta 1}} \frac{(P_{i,j+1,k} - P_{i,j,k})}{r_i \Delta \theta} \quad 6.20$$

$$u_\theta^{n+1}{}_{i,j-1,k} = u_\theta^t{}_{i,j-1,k} + \frac{\Delta t}{\rho_{\theta 2}} \frac{(P_{i,j,k} - P_{i,j-1,k})}{r_i \Delta \theta} \quad 6.21$$

$$u_z^{n+1} = u_z^t{}_{i,j,k} + \frac{\Delta t}{\rho_{z1}} \frac{(P_{i,j,k+1} - P_{i,j,k})}{\Delta z} \quad 6.22$$

$$u_z^{n+1}{}_{i,j,k-1} = u_z^t{}_{i,j,k-1} + \frac{\Delta t}{\rho_{z2}} \frac{(P_{i,j,k} - P_{i,j,k-1})}{\Delta z} \quad 6.23$$

The pressure in the Equations 6.18 to 6.23 has to be determined in such a way that the incompressibility constraint induced by the Equation 6.14 is satisfied. There is no equation for the pressure, so the pressure is determined using an iterative technique which is the most computationally expensive part of simulations regarding incompressible fluid flows. The pressure equation can be derived by substituting Equations 6.18 to 6.23 into the Equation 6.15 to obtain the pressure located in the centre of a control volume:

$$\begin{aligned}
P_{i,j,k}^\infty = & \left[ \frac{1}{r_i \Delta r^2} \left( \frac{P_{i+1,j,k} r_{i+1}}{\rho_{r1}} + \frac{P_{i-1,j,k} r_{i-1}}{\rho_{r2}} \right) + \frac{1}{2r_i \Delta r} \left( \frac{P_{i-1,j,k}}{\rho_{r2}} - \frac{P_{i+1,j,k}}{\rho_{r1}} \right) \right. \\
& \left. \frac{1}{(r_i \Delta \theta)^2} \left( \frac{P_{i,j+1,k}}{\rho_{\theta1}} + \frac{P_{i,j-1,k}}{\rho_{\theta2}} \right) + \frac{1}{\Delta z^2} \left( \frac{P_{i,j+1,k}}{\rho_{z1}} + \frac{P_{i,j-1,k}}{\rho_{z2}} \right) - S_{i,j,k} \right] \\
& \left[ \frac{1}{\Delta r^2} \left( \frac{1}{\rho_{r1}} + \frac{1}{\rho_{r2}} \right) + \frac{1}{2r_i \Delta r} \left( \frac{1}{\rho_{r1}} - \frac{1}{\rho_{r2}} \right) + \frac{1}{(r_i \Delta \theta)^2} \left( \frac{1}{\rho_{\theta1}} + \frac{1}{\rho_{\theta2}} \right) \right. \\
& \left. + \frac{1}{\Delta z^2} \left( \frac{1}{\rho_{z1}} + \frac{1}{\rho_{z2}} \right) \right]^{-1}
\end{aligned} \tag{6.24}$$

$$S_{i,j,k} = \frac{1}{\Delta t} \left[ \frac{(u_{r,i,j,k}^t r_n - u_{r,i-1,j,k}^t r_s)}{r_i \Delta r} + \frac{(u_{\theta,i,j,k}^t - u_{\theta,i,j-1,k}^t)}{r_i \Delta \theta} + \frac{(u_{z,i,j,k}^t - u_{z,i,j,k-1}^t)}{\Delta z} \right] \tag{6.25}$$

The local fluid densities in the centre of the staggered control volumes where the velocities are located is required in order to apply the Equations 6.14 to 6.20. since the fluid densities are not defined at location, the fluid density can be obtained using a linear interpolation of the densities located in the centre of the unstaggered or pressure control volume as:

$$\rho_{z1} = \frac{1}{2} (\rho_{i,j,k+1}^n + \rho_{i,j,k}^n) \tag{6.26}$$

$$\rho_{z2} = \frac{1}{2} (\rho_{i,j,k}^n + \rho_{i,j,k-1}^n) \tag{6.27}$$

$$\rho_{\theta1} = \frac{1}{2} (\rho_{i,j+1,k}^n + \rho_{i,j,k}^n) \tag{6.28}$$

$$\rho_{\theta 2} = \frac{1}{2}(\rho_{i,j,k}^n + \rho_{i,j-1,k}^n) \quad 6.29$$

$$\rho_{r1} = \frac{1}{2}(\rho_{i+1,j,k}^n + \rho_{i,j,k}^n) \quad 6.30$$

$$\rho_{r2} = \frac{1}{2}(\rho_{i,j,k}^n + \rho_{i-1,j,k}^n) \quad 6.31$$

In order to improve the computational times for the iterative pressure solver the successive over relaxation SOR method was applied by taking a weighted average between the pressures obtained from the previous iteration  $P^{\alpha-1}_{i,j,k}$  and the pressure obtained from the current iteration  $P^{\alpha}_{i,j,k}$  to calculate the update pressure in the control volume yielding the following equation:

$$P^{\alpha+1}_{i,j,k} = \omega_p P^{\alpha}_{i,j,k} + (1 - \omega_p)P^{\alpha-1}_{i,j,k} \quad 6.32$$

The term  $\omega_p$  is referred to as the relaxation parameter. This parameter has to be chosen carefully to establish a compromise between an accelerated convergence and stability. The range of the relaxation parameter used in this study was 1.2-1.5.

The diffusion and advection term in the Navier-Stokes equation (Equation 6.10 to 6.12) can be discretised in a similar manner by integrating the terms over the faces bounding the control volume. The numerical approximation to the advection term denoted by A and the diffusion term denoted by D can be obtained using the Gauss-divergence theorem by converting the volume integral into a surface integral where the contribution of each of the faces bounding the control volume are summed up. The axial, tangential and radial advection and diffusion equations were derived as follows:

$$u_{\theta r}^n = \frac{1}{2} \left[ \left( \frac{u_{\theta}^n{}_{i,j-1,k} + u_{\theta}^n{}_{i,j,k}}{2} \right) + \left( \frac{u_{\theta}^n{}_{i+1,j,k} + u_{\theta}^n{}_{i+1,j-1,k}}{2} \right) \right] \quad 6.33$$

$$u_{zr}^n = \frac{1}{2} \left[ \left( \frac{u_z^n{}_{i,j,k-1} + u_z^n{}_{i,j,k}}{2} \right) + \left( \frac{u_z^n{}_{i+1,j,k} + u_z^n{}_{i+1,j,k-1}}{2} \right) \right] \quad 6.34$$

$$u_{r\theta}^n = \frac{1}{2} \left[ \left( \frac{u_r^n{}_{i,j+1,k} + u_r^n{}_{i,j,k}}{2} \right) + \left( \frac{u_r^n{}_{i-1,j,k} + u_r^n{}_{i-1,j+1,k}}{2} \right) \right] \quad 6.35$$

$$u_{z\theta}^n = \frac{1}{2} \left[ \left( \frac{u_z^n{}_{i,j,k-1} + u_z^n{}_{i,j,k}}{2} \right) + \left( \frac{u_z^n{}_{i,j+1,k} + u_z^n{}_{i,j+1,k-1}}{2} \right) \right] \quad 6.36$$

$$u_{rz}^n = \frac{1}{2} \left[ \left( \frac{u_r^n{}_{i,j,k+1} + u_r^n{}_{i,j,k}}{2} \right) + \left( \frac{u_r^n{}_{i-1,j,k} + u_r^n{}_{i-1,j,k+1}}{2} \right) \right] \quad 6.37$$

$$u_{\theta z}^n = \frac{1}{2} \left[ \left( \frac{u_{\theta}^n{}_{i,j,k+1} + u_{\theta}^n{}_{i,j,k}}{2} \right) + \left( \frac{u_{\theta}^n{}_{i,j-1,k} + u_{\theta}^n{}_{i,j-1,k+1}}{2} \right) \right] \quad 6.38$$

$$\begin{aligned} (A_z^n)_{i,j,k} = & u_{rz}^n \left[ \frac{\left( \frac{u_z^n{}_{i+1,j,k} + u_z^n{}_{i,j,k}}{2} \right) r_n - \left( \frac{u_z^n{}_{i,j,k} + u_z^n{}_{i-1,j,k}}{2} \right) r_s}{r_i \Delta r} - \frac{u_z^n{}_{i,j,k}}{r_i} \right] \\ & + \frac{u_{\theta z}^n}{r_i \Delta \theta} \left[ \left( \frac{u_z^n{}_{i,j+1,k} + u_z^n{}_{i,j,k}}{2} \right) - \left( \frac{u_{\theta}^n{}_{i,j,k} + u_{\theta}^n{}_{i,j-1,k}}{2} \right) \right] \\ & + \frac{u_z^n{}_{i,j,k}}{\Delta z} \left[ \left( \frac{u_z^n{}_{i,j,k+1} + u_z^n{}_{i,j,k}}{2} \right) - \left( \frac{u_z^n{}_{i,j,k} + u_z^n{}_{i,j,k-1}}{2} \right) \right] \end{aligned} \quad 6.39$$

$$\begin{aligned}
(D_z^n)_{i,j,k} = & \frac{\mu}{\rho_{z1}} \left\{ \frac{1}{r_i \Delta r} \left[ \frac{[u_{z,i+1,j,k}^n r_{i+1} - u_{z,i,j,k}^n r_i]}{r_n \Delta r} - \left( \frac{u_{z,i+1,j,k}^n + u_{z,i,j,k}^n}{2r_n} \right) \right] r_n \right. \\
& - \frac{1}{r_i \Delta r} \left[ \frac{[u_{z,i,j,k}^n r_i - u_{z,i-1,j,k}^n r_{i-1}]}{r_s \Delta r} - \left( \frac{u_{z,i,j,k}^n + u_{z,i-1,j,k}^n}{2r_s} \right) \right] r_s + \\
& \left. \frac{u_{z,i,j,k+1}^n - 2u_{z,i,j,k}^n + u_{z,i,j,k-1}^n}{\Delta z^2} + \frac{u_{z,i,j+1,k}^n - 2u_{z,i,j,k}^n + u_{z,i,j-1,k}^n}{(r_i \Delta \theta)^2} \right\}
\end{aligned} \tag{6.40}$$

$$\begin{aligned}
(A_\theta^n)_{i,j,k} = & u_{r\theta}^n \left[ \frac{\left( \frac{u_{\theta,i+1,j,k}^n + u_{\theta,i,j,k}^n}{2} \right) r_n - \left( \frac{u_{\theta,i,j,k}^n + u_{\theta,i-1,j,k}^n}{2} \right) r_s}{r_i \Delta r} - \frac{u_{\theta,i,j,k}^n}{r_i} \right] \\
& + \frac{u_{\theta,i,j,k}^n}{r_i \Delta \theta} \left[ \left( \frac{u_{\theta,i,j+1,k}^n + u_{\theta,i,j,k}^n}{2} \right) - \left( \frac{u_{\theta,i,j,k}^n + u_{\theta,i,j-1,k}^n}{2} \right) \right] + \frac{u_{\theta,i,j,k}^n u_{r\theta}^n}{r_i} \\
& + \frac{u_{z\theta}^n}{\Delta z} \left[ \left( \frac{u_{\theta,i,j,k+1}^n + u_{\theta,i,j,k}^n}{2} \right) - \left( \frac{u_{\theta,i,j,k}^n + u_{\theta,i,j,k-1}^n}{2} \right) \right]
\end{aligned} \tag{6.41}$$

$$\begin{aligned}
(D_{\theta}^n)_{i,j,k} = & \frac{\mu}{\rho_{\theta 1}} \left\{ \frac{1}{r_i \Delta r} \left[ \frac{u_{\theta}^n{}_{i+1,j,k} r_{i+1} - u_{\theta}^n{}_{i,j,k} r_i}{r_n \Delta r} - \left( \frac{u_{\theta}^n{}_{i+1,j,k} + u_{\theta}^n{}_{i,j,k}}{2r_n} \right) \right] r_n \right. \\
& - \frac{1}{r_i \Delta r} \left[ \frac{u_{\theta}^n{}_{i,j,k} r_i - u_{\theta}^n{}_{i-1,j,k} r_{i-1}}{r_s \Delta r} - \left( \frac{u_{\theta}^n{}_{i,j,k} + u_{\theta}^n{}_{i-1,j,k}}{2r_s} \right) \right] r_s + \\
& \frac{u_{\theta}^n{}_{i,j,k+1} - 2u_{\theta}^n{}_{i,j,k} + u_{\theta}^n{}_{i,j,k-1}}{\Delta z^2} + \frac{u_{\theta}^n{}_{i,j+1,k} - 2u_{\theta}^n{}_{i,j,k} + u_{\theta}^n{}_{i,j-1,k}}{(r_i \Delta \theta)^2} \\
& \left. - \frac{u_{\theta}^n{}_{i,j,k}}{r_i^2} + \frac{2}{r_i^2} \left[ \frac{\left( \frac{u_{\theta}^n{}_{i,j+1,k} + u_{\theta}^n{}_{i-1,j+1,k}}{2} \right) - \left( \frac{u_{\theta}^n{}_{i,j,k} + u_{\theta}^n{}_{i-1,j,k}}{2} \right)}{\Delta \theta} \right] \right\}
\end{aligned} \tag{6.42}$$

$$\begin{aligned}
(A_r^n)_{i,j,k} = & u_{r,i,j,k}^n \left[ \frac{\left( \frac{u_{r,i+1,j,k} + u_{r,i,j,k}^n}{2} \right) r_{i+1} - \left( \frac{u_{r,i,j,k} + u_{r,i-1,j,k}^n}{2} \right) r_i}{r_n \Delta r} - \frac{u_{r,i,j,k}^n}{r_n} \right] \\
& + \frac{u_{\theta r}^n}{r_n \Delta \theta} \left[ \left( \frac{u_{r,i,j+1,k} + u_{r,i,j,k}^n}{2} \right) - \left( \frac{u_{r,i,j,k} + u_{r,i,j-1,k}^n}{2} \right) \right] - \frac{(u_{\theta r}^n)^2}{r_n} \\
& + \frac{u_{zr}^n}{\Delta z} \left[ \left( \frac{u_{r,i,j,k+1} + u_{r,i,j,k}^n}{2} \right) - \left( \frac{u_{r,i,j,k} + u_{r,i,j,k-1}^n}{2} \right) \right]
\end{aligned} \tag{6.43}$$

$$\begin{aligned}
(D_r^n)_{i,j,k} = & \frac{\mu}{\rho r_1} \left\{ \frac{1}{r_n \Delta r} \left[ \frac{u_{r,i+1,j,k}^n r_{n+1} - u_{r,i,j,k}^n r_n}{r_{i+1} \Delta r} - \left( \frac{u_{r,i+1,j,k}^n + u_{r,i,j,k}^n}{2r_{i+1}} \right) \right] r_{i+1} \right. \\
& - \frac{1}{r_n \Delta r} \left[ \frac{u_{r,i,j,k}^n r_n - u_{r,i-1,j,k}^n r_s}{r_i \Delta r} - \left( \frac{u_{r,i,j,k}^n + u_{r,i-1,j,k}^n}{2r_i} \right) \right] r_i + \\
& \frac{u_{r,i,j,k+1}^n - 2u_{r,i,j,k}^n + u_{r,i,j,k-1}^n}{\Delta z^2} + \frac{u_{r,i,j+1,k}^n - 2u_{r,i,j,k}^n + u_{r,i,j-1,k}^n}{(r_i \Delta \theta)^2} - \frac{u_{r,i,j,k}^n}{r_n^2} \\
& \left. - \frac{2}{r_n^2} \frac{\left[ \left( \frac{u_{\theta,i,j,k}^n + u_{\theta,i+1,j,k}^n}{2} \right) - \left( \frac{u_{\theta,i+1,j-1,k}^n + u_{\theta,i,j-1,k}^n}{2} \right) \right]}{\Delta \theta} \right\} \quad 6.44
\end{aligned}$$

where  $r_{n+1} = r_n + \Delta r$

### 6.1.2 Eccentric annuli $e > 0$

In the eccentric annular geometry, a different approach was developed to solve the governing fluid flow equations due to the non-orthogonality of the generated mesh. If a structured grid is used to mesh the eccentric annuli geometry and one of the faces of the control volumes located near the boundaries is aligned to the walls of the domain, the radial position of the centroids and vertex nodes of the control volumes in the angular and radial direction of the domain. From Figure 6.6, where  $x = r \cos \theta$  and  $y = r \sin \theta$ , the point  $r_{i,j,k} \neq r_{i+1,j,k}$  and  $r_{i,j+1,k} \neq r_{i+1,j+1,k}$  since the radial position of these nodes are functions of their angular position. Thus, the volume of a cell in the domain bounded by these points cannot be determined from the equation  $V = r dr d\theta dz$  and the equations discretised for the concentric annuli in cylindrical coordinates cannot be applied directly to obtain solutions in the eccentric annuli.

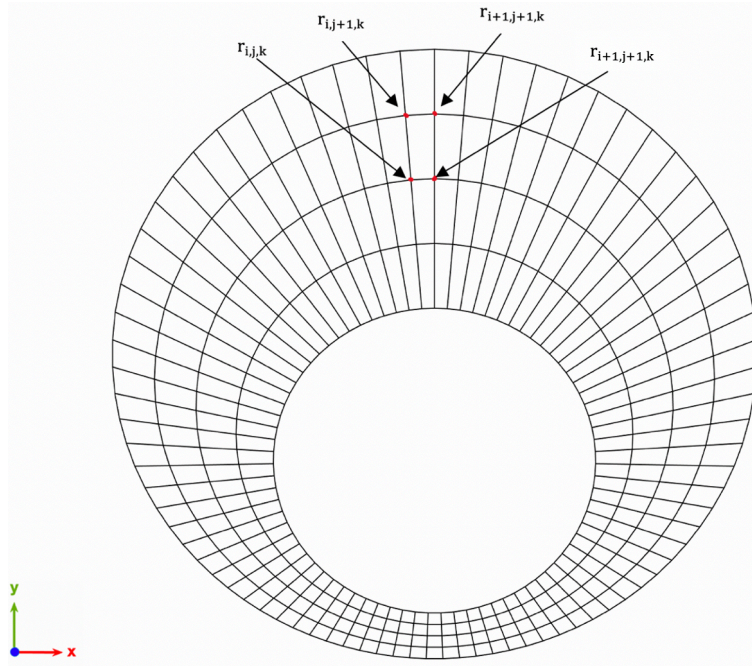


Figure 6.6: x-y plane of the control volumes for a structured mesh in the annuli

In order to obtain solutions for the governing equations in the eccentric annuli structured mesh, the cartesian velocity system was used where the axial tangential and radial components of the outward unit normal vector  $\mathbf{n}$  are non-zero on majority of the faces bounding the control volumes. Since the control volumes are comprised of a set of discrete planar faces, the volume of each of the cells can be determined by performing a surface integral over the discrete faces using the following equations:

$$x_f = \frac{1}{A_f} \int x \, dA$$

$$y_f = \frac{1}{A_f} \int y \, dA \tag{6.45}$$

$$z_f = \frac{1}{A_f} \int z \, dA$$

$$V_i = \sum_{f=1}^{N_{f,i}} n_{x,f} x_f A_f \tag{6.46}$$

In order to mitigate the numerical precision errors when determining the volume of a cell regardless of the shape or orientation, it is customary to take an average of the volumes obtained using the three components of the outward unit normal summed over the faces of the control volume. Thus, the volume of a cell in the domain may be expressed as:

$$V_i = \frac{1}{3} \left( \sum_{f=1}^{N_{f,i}} n_{x,f} x_f A_f + \sum_{f=1}^{N_{f,i}} n_{y,f} y_f A_f + \sum_{f=1}^{N_{f,i}} n_{z,f} z_f A_f \right) \quad 6.47$$

Where  $x_f$ ,  $y_f$  and  $z_f$  are the coordinates of the centroid of the faces of the control volume

The collocated grid method was applied towards the discretisation of the governing equations for the eccentric annuli. In the method, unlike the staggered grid method, all the components of the velocity and the material properties of the flow are located at every node in the annuli domain. However, in order to avoid errors or instabilities due to checkerboard oscillations, a technique referred to as momentum interpolation is applied at the faces of control volumes in the domain. The solution of the Navier-Stokes equation involves three major procedures in which are the calculation of a temporal velocity field, obtaining of the pressure fields using an iterative technique and the velocity correction step.

The temporal velocity field is obtained from the Equation 6.4 as

$$\mathbf{u}^t = \mathbf{u}^n + \Delta t \left[ -\nabla \cdot \mathbf{u}^n \mathbf{u}^n + \frac{\mu}{\rho^n} \nabla^2 \mathbf{u}^n + \mathbf{g} \right] \quad 6.48$$

While the pressure fields are obtained from the conservation of mass equation by performing an integration over the faces of the control volume and substituting the Equation 6.50 into the equation 6.49.

$$\nabla \cdot \mathbf{u}^{n+1} = \frac{1}{V_i} \sum_{f=1}^{N_{f,i}} \mathbf{u}_f \cdot \mathbf{n}_f A_f \quad 6.49$$

$$\mathbf{u}_f = \mathbf{u}_f^t - \frac{\Delta t}{\rho_f^n} \nabla P^{n+1} \quad 6.50$$

The temporal velocities at the face centroid of a cell is obtained by interpolating between the cell centroid values and the neighbouring cell that share the face using the Equation 6.51.

$$\mathbf{u}_f^t = \mathbf{u}_i^t w_f + (1 - w_f) \mathbf{u}_{Nc}^t \quad 6.51$$

where  $w_{f,i}$  is the cell to face interpolation function

Each of the terms in the governing equations are integrated using the Gauss-divergence theorem expressed by the following equations:

$$\nabla \mathbf{u} = \frac{1}{V_i} \int_{CV} \nabla \mathbf{u} \partial V = \frac{1}{V_i} \int_{CS} \mathbf{u} \cdot \mathbf{n} \partial A_f = \frac{1}{V_i} \sum_{f=1}^{N_{f,i}} \mathbf{u}_f \cdot \mathbf{n}_f A_f \quad 6.52$$

$$\nabla^2 \mathbf{u} = \frac{1}{V_i} \int_{CV} \nabla^2 \mathbf{u} \partial V = \frac{1}{V_i} \int_{CS} \nabla \mathbf{u} \cdot \mathbf{n} \partial A_f = \frac{1}{V_i} \sum_{f=1}^{N_{f,i}} \nabla \mathbf{u}_f \cdot \mathbf{n}_f A_f \quad 6.53$$

Even though this method has been described to be developed for fluid flow simulations in the eccentric annuli, it can also be applied directly for the fluid flow simulations in the concentric annuli. For non-Newtonian fluid flow simulations in the concentric and eccentric annuli, the viscosity of the fluid is not a constant and varies across the annuli domain as a function of local shear rate of the fluid. To account for the rheology of the non-Newtonian fluid, the viscosity of the fluid at

every cell or face in the flow domain is calculated according to the Equations 4.40 and 4.46.

The approximation of the spatial derivatives was second-order accurate and in order to keep the simulations stable, time-step limitations are required as a result of the algorithm being explicit. The criteria employed to ensure that the diffusion is large enough to keep the advection stable requires the step size  $\Delta t$ , is bounded by the following relationship:

$$\Delta t \leq \frac{2\mu}{\rho(\mathbf{u} \cdot \mathbf{u})} \quad 6.54$$

A second-order time integration scheme was implemented by obtaining two first order time steps and taking the average between the current and the previous results to improve the accuracy and stability of the simulations. Thus, the fluid properties and velocities in the flow domain were obtained using a second order forward in time integration. Assuming a function  $h$  exists in the flow domain, the time integration of  $h$  is given as:

$$h^* = h^n + \Delta t \left( \frac{dh}{dt} \right)^n \quad 6.55$$

$$h^{n+1} = h^n + \frac{\Delta t}{2} \left( \left( \frac{dh}{dt} \right)^n + \left( \frac{dh}{dt} \right)^* \right) \quad 6.56$$

## 6.2 Geometry and mesh generation

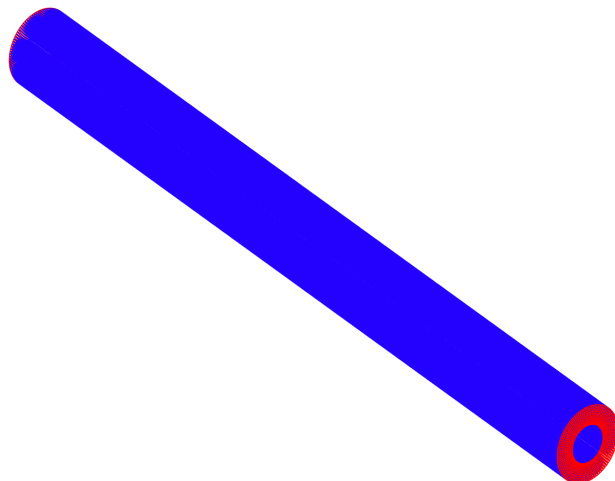
A mesh generation algorithm was developed to map the annuli geometry as a function of the distance between the midpoint of the inner pipe and the outer pipe wall and the angular position. The coordinates of the grid points in the structured mesh within the domain of the annuli can be defined by the following functions:

$$r_{i,j,k} = (r_2 - r_1)e \cos(\theta_{i,j,k}) + \sqrt{r_2^2 - ((r_2 - r_1)e \sin(\theta_{i,j,k}))^2} \quad 6.57$$

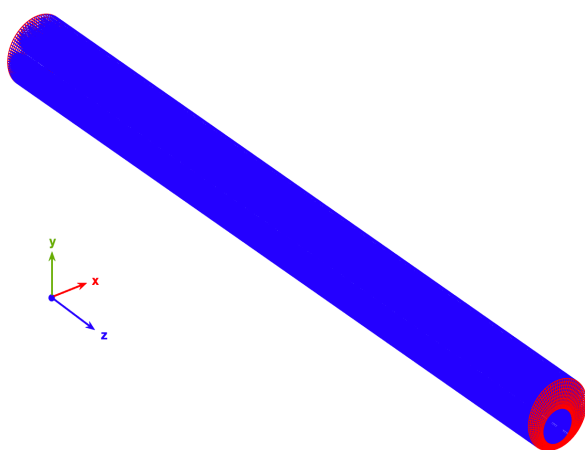
$$x_{i,j,k} = r_{i,j,k} \cos(\theta_{i,j,k}) \quad 6.58$$

$$y_{i,j,k} = r_{i,j,k} \sin(\theta_{i,j,k}) \quad 6.59$$

$$z_{i,j,k} = dz(k - 1) \quad 6.60$$



Concentric,  $e = 0$



Eccentric,  $e = 0.7$

Figure 6.7: Concentric and eccentric annuli geometry and mesh for fluid flow simulations

The size of the inner and outer pipe diameter is 0.088m and 0.144m respectively. Adequate boundary conditions are required at the walls of the annuli to ensure that the simulations produce accurate and stable results. Dirichlet boundary conditions are applied to the inlet face and inner and outer walls of the geometry while Neumann boundary conditions are applied to the exit or outflow face of the geometry. The nodes that are located on the red face (left face) of the geometry are set to be equal to the inlet velocity while the on nodes that are located on the outflow face (right face), the condition  $\nabla \mathbf{u} = 0$  is satisfied. Due to the no-slip effect on the walls, the axial, radial and tangential velocities at the walls are set to zero. In conditions where the inner pipe is rotating, the tangential velocity on the walls of the inner pipe is set according to the equation  $V_{\theta} = \omega r$ . However, the tangential velocity on the outer pipe is set equal to zero. Separate equations are however needed for the cells close to the boundaries of the domain in order to enforce of the boundary conditions and satisfy the governing equations. These equations were obtained using the same procedures outlined in the previous sections.

### 6.2.1 Mesh independence study

A mesh independence test was carried out to ensure that the numerical solution obtained was independent of the resolution of the mesh (Figure 6.8).

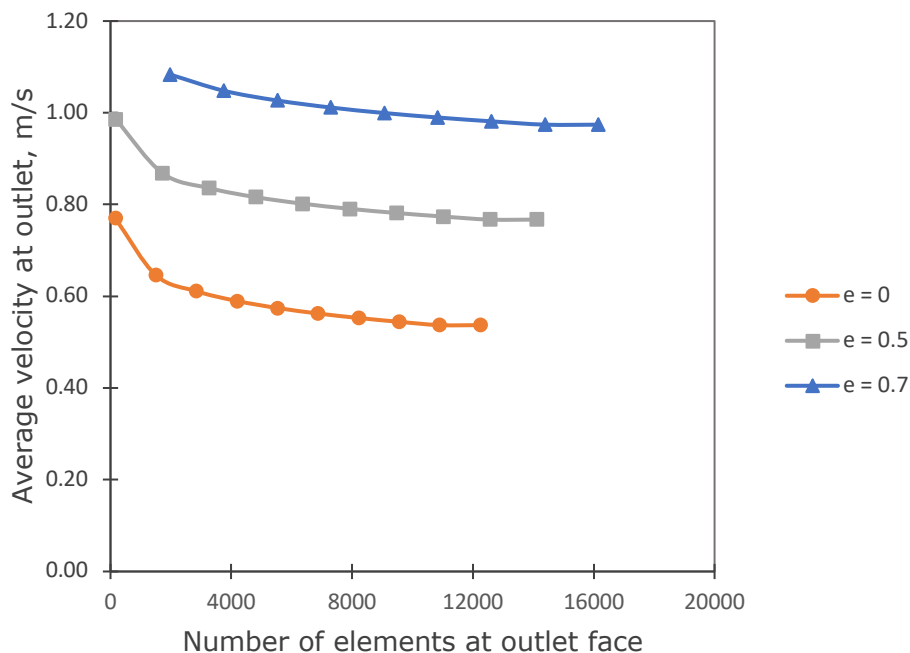


Figure 6.8: Mesh independence test

This was done by monitoring the average velocity at the outlet face of the domain while ensuring convergence criteria is met. The simulation was run with an initial mesh size until a convergence of residual error of  $10^{-4}$  is reached. The average velocity at the outlet face is obtained and the simulation is run again after the mesh has been refined. After the residual error of  $10^{-4}$  is attained, the average velocity obtained is compared to that of the previous simulation. This procedure is repeated until the difference between the values are within a minimum tolerance of about 1%. Figure 6.8 presents the results of the mesh independence tests carried out for different pipe eccentricities.

### 6.3 Single-phase flow simulations

The results of the simulation of single-phase Newtonian and non-Newtonian fluid flow in the concentric and eccentric annuli are presented and analysed in this section. The rheological parameters used to characterise the non-Newtonian fluids is presented in Table 6.1.

Table 6.1: Rheological parameters of the different fluid types

Fluid type	Rheology	$\epsilon, \text{Pas}^n$	$n$	$\tau_{\epsilon}, \text{Pa}$
A	Powerlaw	0.094	0.62	0
B	Herschel Bulkerly	0.154	0.75	0.55
C	Herschel Bulkerly	0.643	0.44	1.5
D	Newtonian	0.0054	1	0

The velocity fields were extracted from certain positions in the axial direction of the flow domain. The distribution of the velocity fields across the annuli geometry is shown in the Figures 6.9 – 6.14. Figures 6.9 and 6.10 show the velocity fields for the Newtonian and non-Newtonian fluid in the concentric annuli respectively. When the flow is fully developed, the tangential velocity introduced by the inner pipe rotation had no influence on the distribution of the velocity in the concentric annuli for both the Newtonian and non-Newtonian fluids. However, for the non-Newtonian fluid, the rotation of the inner pipe had a little but insignificant effect on the velocity fields. The inner pipe rotation when the flow is fully developed, led to a slight reduction in the axial pressure gradient in the concentric annulus for the non-Newtonian fluid. For a fully developed Newtonian fluid flow in the

concentric annuli, no significant influence on the axial pressure gradient was observed.

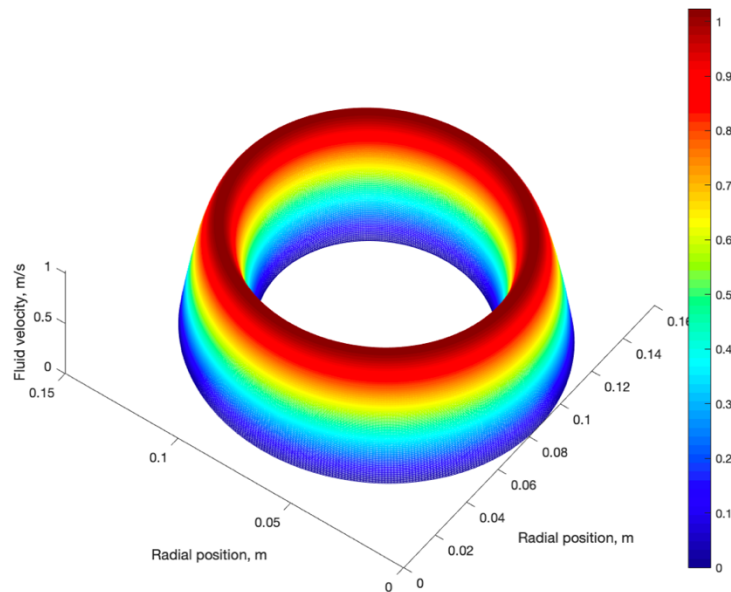


Figure 6.9: Velocity fields in the concentric annulus ( $Q = 12\text{m}^3/\text{h}$ ,  $\epsilon = 0.0054$ ,  $n = 1$ ,  $\tau_\epsilon = 0$ )

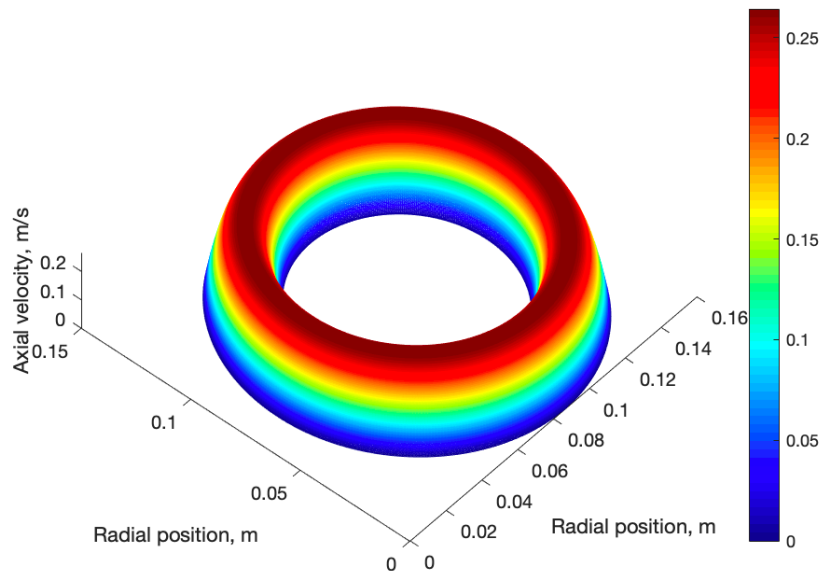


Figure 6.10: Velocity fields in the concentric annulus ( $Q = 7\text{m}^3/\text{h}$ ,  $\epsilon = 0.094$ ,  $n = 0.62$ ,  $\tau_\epsilon = 0$ )

The distribution of the velocity fields in the eccentric annulus is highly dependent on the degree of eccentricity of the annuli geometry. It can be seen from Figures 6.11 - 6.13 that as the eccentricity increases, the velocity in the bottom region of the annuli reduces significantly. This reduction in the flow in the bottom region of the annuli increases the tendency for cuttings to settle and form a stationary bed during drilling activities. While the rotation of the inner pipe has no significant effect on the velocity fields for a fully developed Newtonian fluid flow in the eccentric annuli, the inner pipe rotation influences that of the non-Newtonian fluids and redistributes the velocity fields thereby improving the fluid velocity at the bottom region of the annuli (Figure 6.14). The reason for this is that the viscosity of the non-Newtonian fluid reduces with the effect of rotation due to its shear thinning properties. The distribution of the velocity fields is also highly dependent on the rheological properties of the fluid. The fluids that possess a yield stress tends to form a different shape with more areas in the annuli having a relatively higher velocity than that of power law fluids (Figure 6.13).

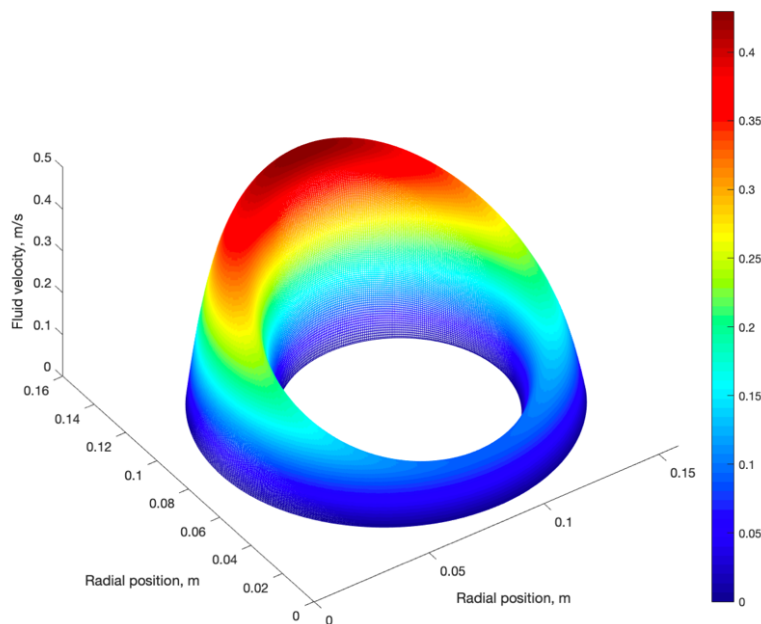


Figure 6.11: Velocity fields in the eccentric annulus,  $e = 0.3$  ( $Q = 7\text{m}^3/\text{h}$ ,  $\epsilon = 0.094$ ,  $n = 0.62$ ,  $\tau_\epsilon = 0$ )

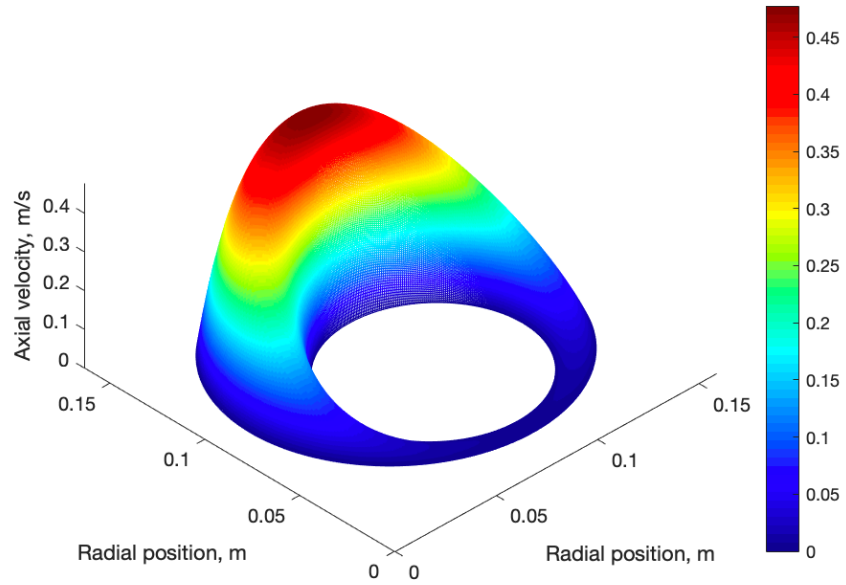


Figure 6.12: Velocity fields in the eccentric annulus,  $e = 0.7$  ( $Q = 7\text{m}^3/\text{h}$ ,  $\epsilon = 0.094$ ,  $n = 0.62$ ,  $\tau_\epsilon = 0$ )

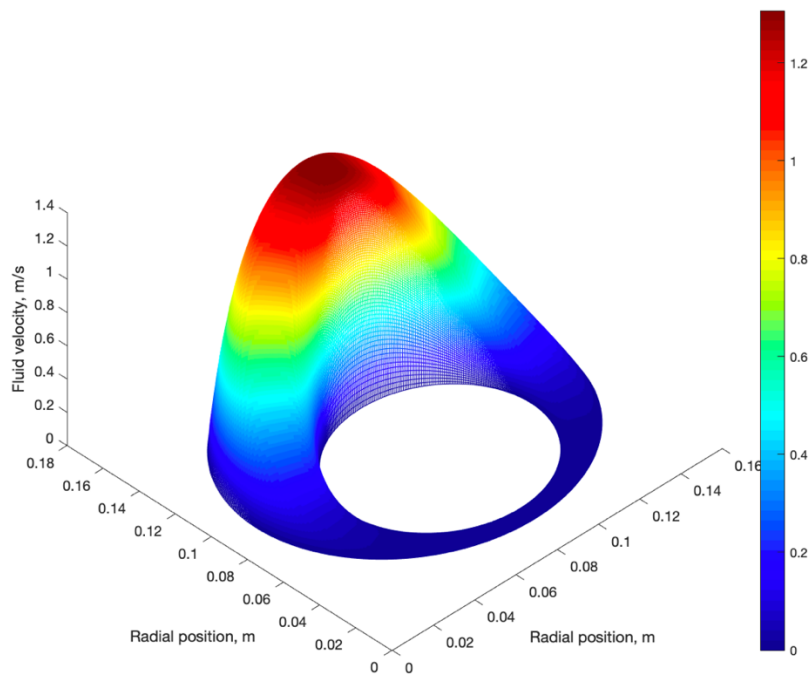


Figure 6.13: Velocity fields in the eccentric annulus,  $e = 0.7$  ( $Q = 7\text{m}^3/\text{h}$ ,  $\epsilon = 0.643$ ,  $n = 0.44$ ,  $\tau_\epsilon = 1.5$ )

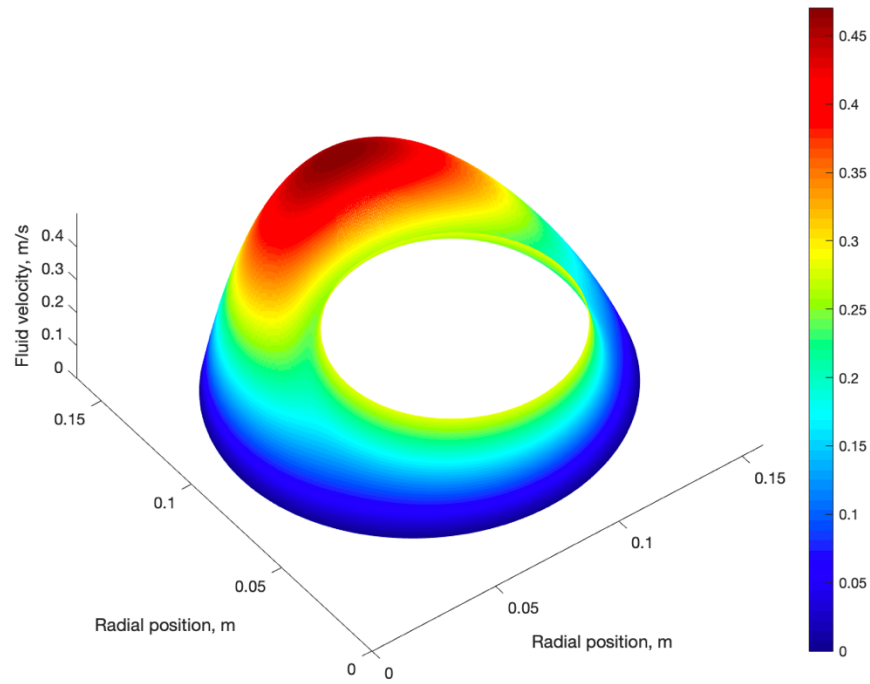


Figure 6.14: Improvement in fluid velocity in the bottom region of the eccentric annuli with inner pipe rotation

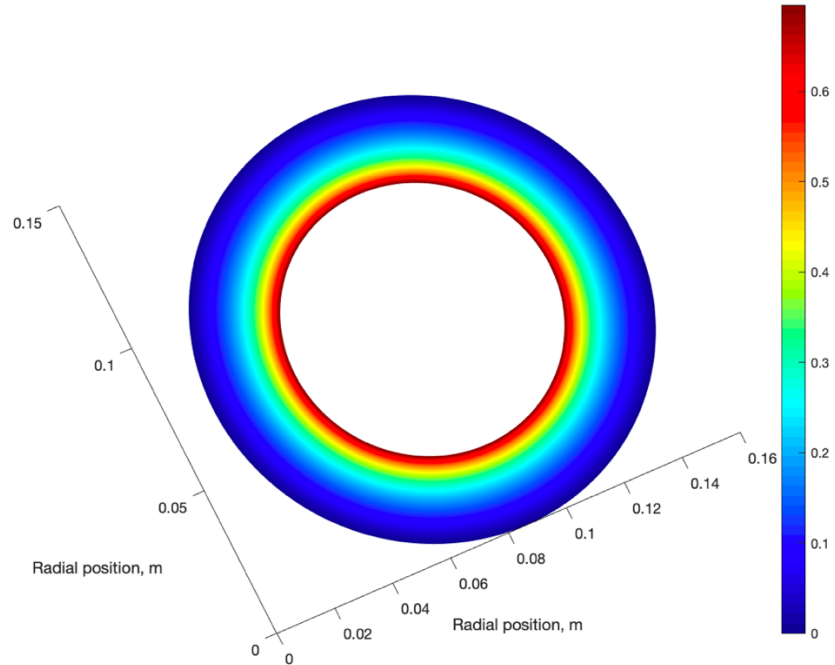


Figure 6.15: Tangential velocity field in the concentric annuli ( $e = 0$ , rpm = 150)

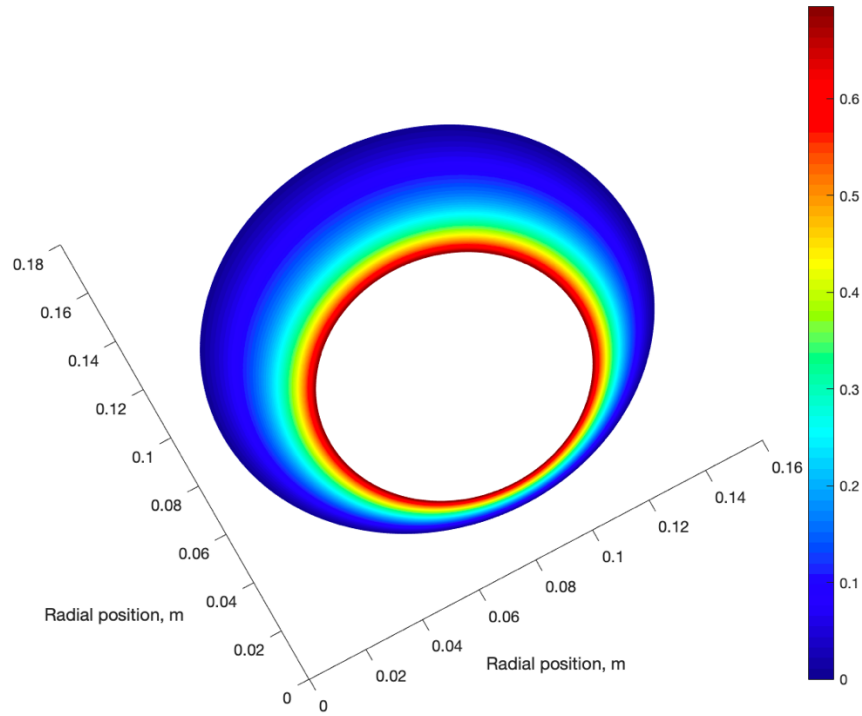


Figure 6.16: Tangential velocity field in the eccentric annuli ( $e = 0.7$ , rpm = 150)

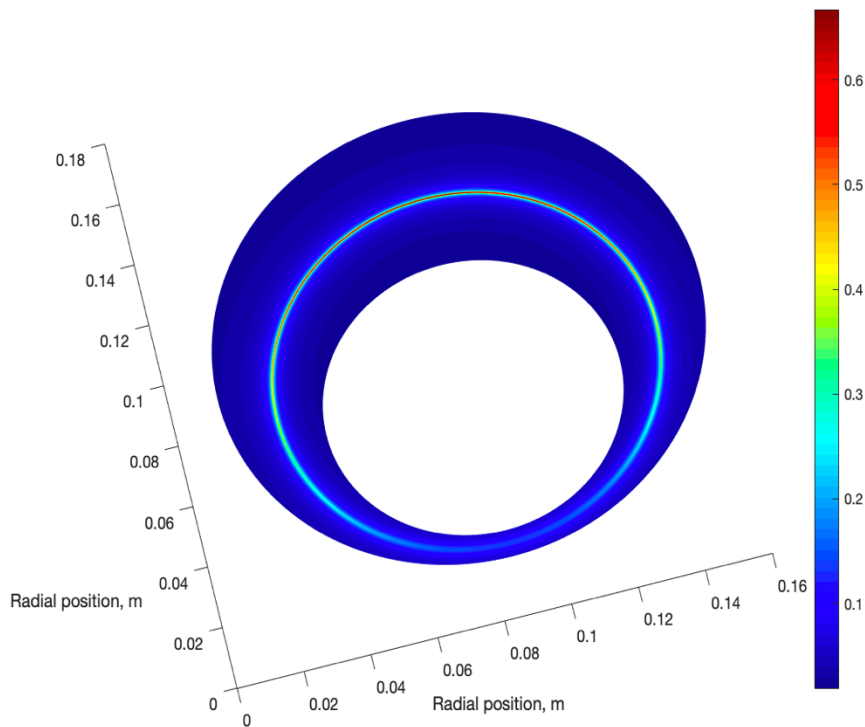


Figure 6.17: Fluid viscosity field in the eccentric annuli ( $e = 0$ , rpm = 0)

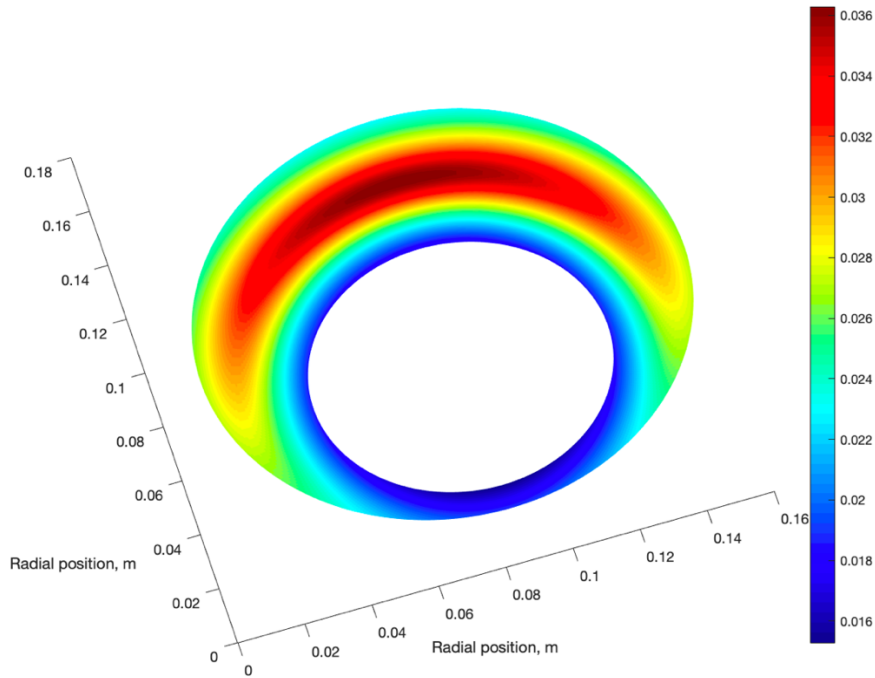


Figure 6.18: Fluid viscosity in eccentric annuli ( $e = 0$ , rpm = 150)

The Tangential velocity produced due to the inner pipe rotation is seen to be maximum at the inner pipe wall and reduces in the radial direction in the annuli (Figure 6.15 and 6.16). Thus, the shear rate of the fluid is dependent on its local position in the annuli. The viscosity of the non-Newtonian fluid being shear dependent is highly dependent on the eccentricity of the inner pipe and the rotation speed of the inner pipe. Figures 6.17 and 6.18 shows that the when the inner pipe is rotated, the viscosity of the fluid reduces significantly with the viscosity of the fluid close to the inner pipe and the bottom region of the annuli showing a larger viscosity reduction that the other areas in the eccentric annuli. Thus, this is the reason why the inner pipe rotation redistributes the fluid velocity and improves the flow in the bottom region of the eccentric annuli.

The axial pressure gradient was also seen to reduce with an increase in the inner pipe rotation in the eccentric annuli for a fully developed flow. This leads to the conclusion that under the flow conditions numerically investigated, when the flow rate of the fluid is held constant and the flow is fully developed, the axial pressure gradient decreases with inner pipe rotation. Table 6.2 presents the summary of

the results of the simulations carried out to investigate the effect of eccentricity and inner pipe rotation of the hydraulics of non-Newtonian fluid flow for an annular geometry with the inner and outer pipe diameter of 0.04m and 0.08m respectively.

Table 6.2: Results of numerical simulation for the different fluid types

Fluid type	Wellbore Eccentricity, E	Drillpipe speed, Rpm	Flowrate, m <sup>3</sup> /h	Pressure gradient Pa/m
A	0	0	3	140.98
	0	60	3	139.55
	0	80	3	138.63
	0	120	3	136.44
B	0	0	7	803.29
	0	60	7	801.63
	0	80	7	800.47
	0	120	7	797.50
A	0.7	0	3	84.69
	0.7	60	3	83.67
	0.7	80	3	83.14
	0.7	120	3	81.96
	0.7	0	7	143.83
	0.7	60	7	142.72
	0.7	80	7	142.46
	0.7	120	7	141.84
B	0.7	0	7	479.49
	0.7	60	7	477.53
	0.7	80	7	476.59
	0.7	120	7	474.48
	0.7	0	3	279.12
	0.7	60	3	274.64
	0.7	80	3	272.67
	0.7	120	3	268.59
C	0	0	7	409.36
	0	60	7	369.20
	0	90	7	348.23
	0	150	7	318.03
	0.5	0	9	336.23
	0.5	60	9	315.45
	0.5	120	9	289.43
	0.7	0	7	260.05
	0.7	60	7	242.34
	0.7	90	7	231.04
	0.7	150	7	213.45

## 6.4 Two phase flow

In this study, the main aim of the numerical simulation of two-phase (gas-liquid) fluid flow in the concentric and eccentric annuli is to investigate the combined effect of inner pipe rotation and eccentricity on the prevailing flow pattern for both Newtonian and non-Newtonian fluids. For the multiphase flow simulations using the one-fluid approach, when the governing equations are solved at every cell in the domain, the interface between different fluids is identified and tracked by a marker function. The front tracking method was applied to move the interface between the fluids and reconstruct the density of the fluids based on the location of the interface. In the one-fluid approach, a single-set of the governing equations are solved for the entire flow domain and the differences between the material properties of the fluids are accounted for. The boundary or interface of the fluids is represented by delta ( $\delta$ ) functions that are discretised and approximated along with the Navier-Stokes equations for fluid flow. The phases in the annuli are represented by a step function  $C$  which is equal to 1 in the cells where the liquid phase is located, equal to 0 where the gas phase is located and equal to a nonzero value of the gradient of the step function at the interface between the fluids.

### 6.4.1 Fluid density field

For gas-liquid flow through the concentric and eccentric annuli domain, the density of the fluid at every cell in the domain may be obtained from the following equation:

$$\rho_f(x, y, z) = \rho_L C(x, y, z) + \rho_G (1 - C(x, y, z)) \quad 6.61$$

The gradient of the density field can then be obtained from:

$$\nabla \rho_f = \rho_L \nabla C - \rho_G \nabla C = (\rho_L - \rho_G) \nabla C = \Delta \rho_f \nabla C \quad 6.62$$

$$\nabla \rho_f = \Delta \rho_f \delta(n) \mathbf{n} \quad 6.63$$

In order to transfer the quantity from the front element to the grid points, it is required that the transferred gradient is conserved. While the gradient of the density on the front element is expressed as a gradient per unit area, the gradient of the density in the cells is expressed as the gradient per unit volume. The discrete form of the gradient of the density at the cell centres in the flow domain may be obtained using the following equations:

$$\int_{CV} \nabla \rho_f \partial V = \int_{CS} \Delta \rho_f \delta(n) \mathbf{n} \partial s \quad 6.64$$

$$(\nabla \rho_f)_{i,j,k} = \sum_I \Delta \rho_f \mathbf{n} w_{i,j,k} \frac{\Delta s_I}{V_i} \quad 6.65$$

The term  $\Delta s_I$  represents the area of the front element at the interface of the fluids and  $w_{i,j,k}$  is the weight that is used to determine the actual value of the gradient shared between the neighbouring cells. Other similar quantities such a surface tension that exist at the interface between the fluids can be added to the grid from the front using this same approach. It is required that the total number of the weights used must sum up to unity:

$$\sum_i w_{i,j,k} = 1 \quad 6.66$$

#### 6.4.2 Interface tracking

The front that represents the interface between the fluids is moved with the flow by determining the velocity of the fluids at the local position where the front element exists with the domain. After the Navier-Stokes equation has been solved and the velocity fields have been obtained the interface or marker point velocities are obtained by interpolation from the grid points that surrounding the location

where each of the front elements are enclosed within the flow domain (Figure 6.19).

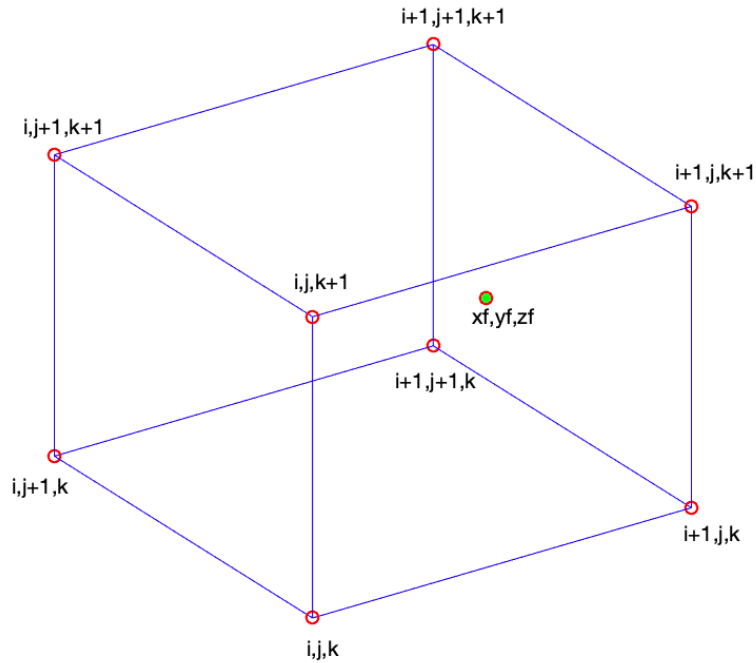


Figure 6.19: Interpretation of the location of the centroid of a front element within a fixed grid

Considering Figure 6.19, if the grid points surrounding the front is known, the velocity of the front  $\mathbf{u}_f(x_f, y_f, z_f)$  can be determined from the following equations:

$$\begin{aligned}
 \mathbf{u}_f = & \mathbf{u}_{i,j,k}W_{i,j,k} + \mathbf{u}_{i+1,j,k}W_{i+1,j,k} + \mathbf{u}_{i,j,k+1}W_{i,j,k+1} + \mathbf{u}_{i+1,j,k+1}W_{i+1,j,k+1} \\
 & + \mathbf{u}_{i,j+1,k}W_{i,j+1,k} + \mathbf{u}_{i,j+1,k+1}W_{i,j+1,k+1} + \mathbf{u}_{i+1,j+1,k}W_{i+1,j+1,k} \\
 & + \mathbf{u}_{i+1,j+1,k+1}W_{i+1,j+1,k+1}
 \end{aligned} \tag{6.67}$$

Here the weights are determined as volume fractions from the following equations:

$$w_{i,j,k} = \frac{(x_{i+1,j,k} - x_f)(y_{i,j+1,k} - y_f)(z_{i,j,k+1} - z_f)}{\Delta x \Delta y \Delta z} \quad 6.68$$

$$w_{i+1,j,k} = \frac{(x_f - x_{i,j,k})(y_{i,j+1,k} - y_f)(z_{i,j,k+1} - z_f)}{\Delta x \Delta y \Delta z} \quad 6.69$$

$$w_{i,j,k+1} = \frac{(x_{i+1,j,k} - x_f)(y_{i,j+1,k} - y_f)(z_f - z_{i,j,k})}{\Delta x \Delta y \Delta z} \quad 6.70$$

$$w_{i+1,j,k+1} = \frac{(x_f - x_{i,j,k})(y_{i,j+1,k} - y_f)(z_f - z_{i,j,k})}{\Delta x \Delta y \Delta z} \quad 6.71$$

$$w_{i,j+1,k} = \frac{(x_{i+1,j,k} - x_f)(y_f - y_{i,j,k})(z_{i,j,k+1} - z_f)}{\Delta x \Delta y \Delta z} \quad 6.72$$

$$w_{i,j+1,k+1} = \frac{(x_{i+1,j,k} - x_f)(y_f - y_{i,j,k})(z_f - z_{i,j,k})}{\Delta x \Delta y \Delta z} \quad 6.73$$

$$w_{i+1,j+1,k} = \frac{(x_f - x_{i,j,k})(y_f - y_{i,j,k})(z_{i,j,k+1} - z_f)}{\Delta x \Delta y \Delta z} \quad 6.74$$

$$w_{i+1,j+1,k+1} = \frac{(x_f - x_{i,j,k})(y_f - y_{i,j,k})(z_f - z_{i,j,k})}{\Delta x \Delta y \Delta z} \quad 6.75$$

After the velocity of the front has been calculated the new position of the interface at the next time step  $x_f^{n+1}$  can be determined from its position at the current time step  $x_f^n$  using an explicit first-order integration in time:

$$x_f^{n+1} = x_f^n + u_f^n \Delta t \quad 6.76$$

$$y_f^{n+1} = y_f^n + v_f^n \Delta t \quad 6.77$$

$$z_f^{n+1} = z_f^n + w_f^n \Delta t \quad 6.78$$

Although there are other ways to determine the weights that are used for the smoothing of the front element unto the grid, the method derived here has been checked to be highly accurate and can be applied with confidence. In general, this concept does not just apply to solving for the density fields in a fixed grid for multiphase flow simulations. It can also be applied to solving for the volumetric fraction of the phases following the same procedures as described for the gradient of the density fields. The volumetric fraction in the cells where only liquid is present would be set equal to 1, the volumetric fraction in the cells where only gas is present would be set to 0 while the cells where the interface is present would receive a nonzero value obtained from the front element.

A simple 2D simulation was developed for a pipe flow of single-phase water and two-phase air and water in the stratified flow pattern using the interface tracking mechanism. The marker function for the interface was modelled according to the Taitel and Dukler (1976) liquid height model for stratified gas-liquid flow (Equations 2.143 to 2.164). Figure 6.20 shows the transient tracking of the interface between the fluids through the pipe domain:

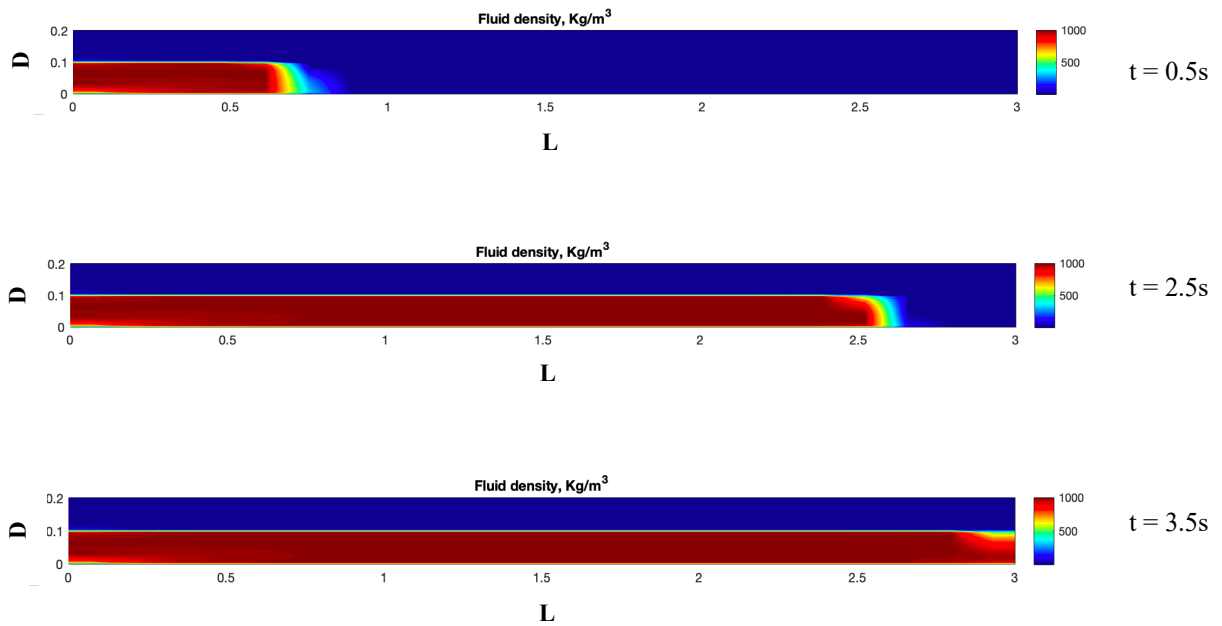


Figure 6.20: Air-water stratified flow density field using the interface tracking method

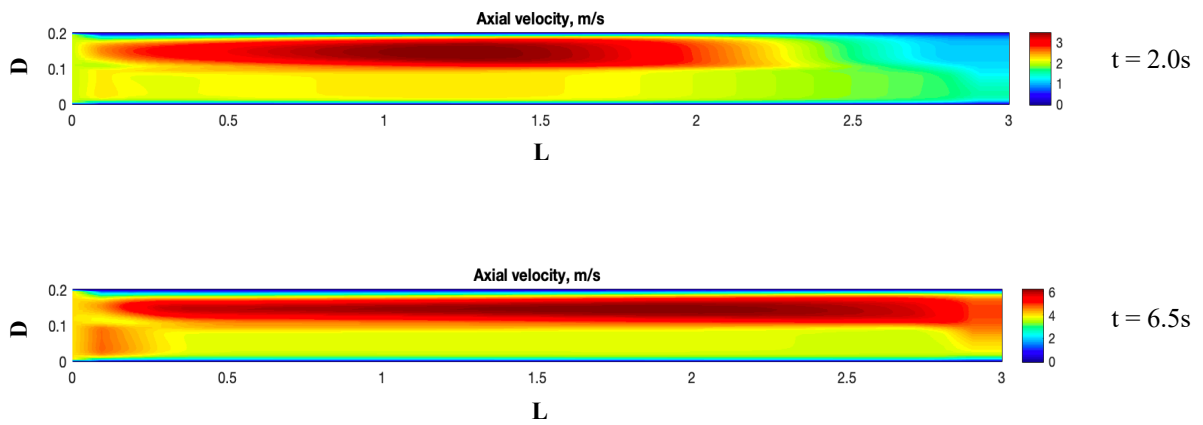


Figure 6.21: Air-water stratified flow velocity field using the interface tracking method

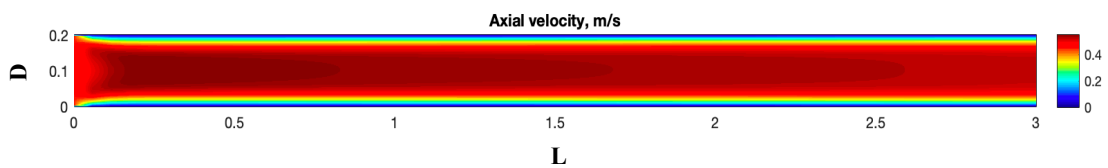


Figure 6.22: Velocity field for 2D single phase pipe flow simulation

It can be seen that while the velocity field has a symmetrical pattern in the pipe for the single-phase flow (Figure 6.22), the two-phase stratified flow results show that the velocity in the pipe is highly dependent on the flow pattern formed in a conduit. In the stratified flow pattern, the gas phase at the top flows faster than the liquid phase at the bottom due to the difference in fluid properties (Figure 6.21). This sheds light on the reason why the velocity profile for single phase flow is not valid for performing cutting transport calculations for multiphase flow with the main reason being that the velocity distribution in the annuli is dependent on the prevailing flow pattern.

### 6.4.3 Effect of rpm and eccentricity on flow pattern

In order to investigate the effect of the inner pipe rotation and eccentricity on flow pattern dynamics, the marker function is first initialised based on theoretical modelling for two-phase flow through the annuli, then the interface is tracked in the flow at the proceeding time steps. The inner pipe speed used in this simulation varied from 0-150rpm and the inlet parameters were set based on the flow pattern being investigated.

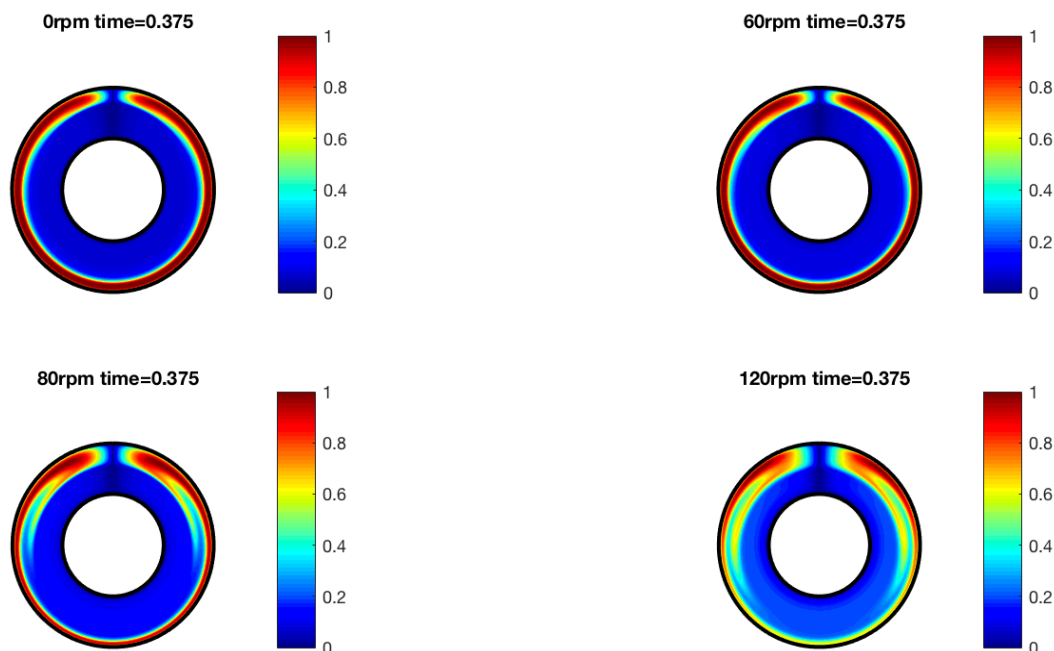


Figure 6.23: Effect of drillpipe rotation on annular flow in the concentric annuli

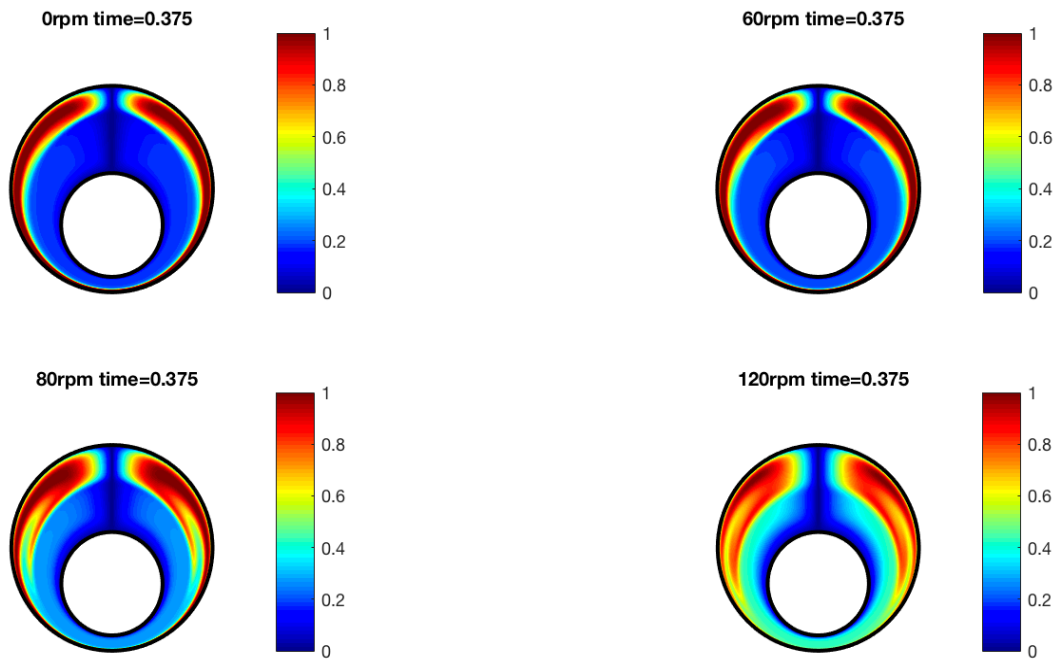


Figure 6.24: Effect of drillpipe rotation on annular flow in the eccentric annuli

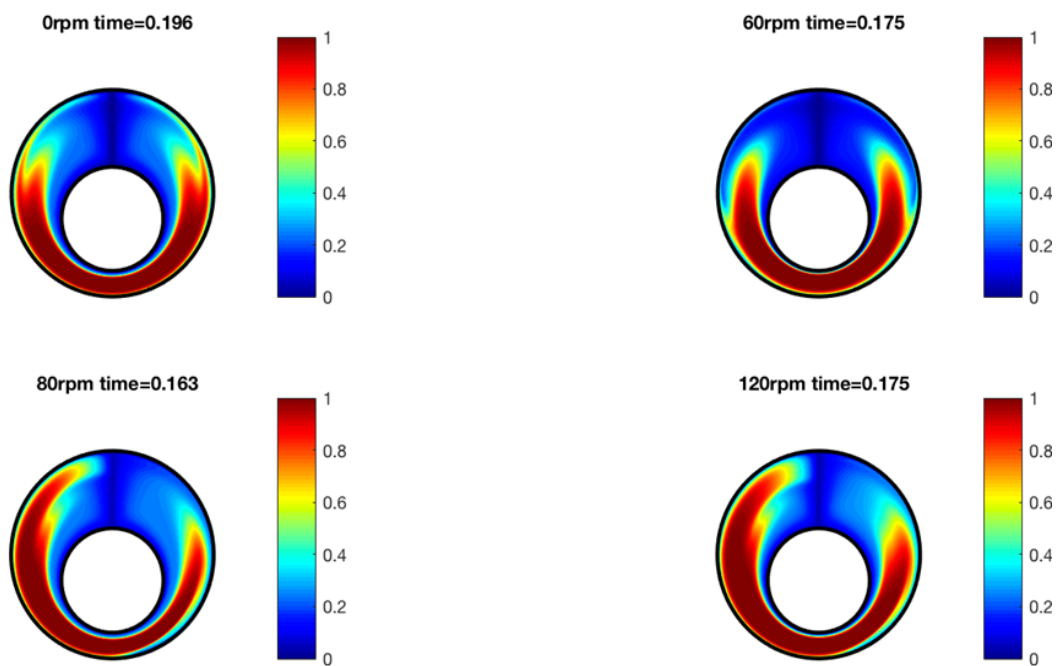


Figure 6.25: Effect of drillpipe rotation on slug flow in the eccentric annuli

Under the range of inner pipe speeds investigated, the combined effect of inner pipe rotation and eccentricity influenced the phase distribution across the annuli domain. However, the rotation of the inner pipe did not alter the interface in a manner that will lead to a transition from one flow pattern to the other for both the Newtonian and non-Newtonian fluids. Some of the results showing the flow patterns are presented in Figures 6.23 - 6.25. The illustration shows that although the drillpipe rotation affects the flow pattern, the axial force is more dominant than the tangential force exerted on the flow hence the flow pattern transitions were not obtained for rotary speeds investigated ( $\text{rpm} \leq 150$ ). It is fair to conclude that the prevailing flow pattern for two-phase drilling fluid flow in a concentric and eccentric annulus with or without inner pipe rotation ( $\text{rpm} \leq 150$ ), is majorly dependent on the flowrates and properties of the drilling fluid. For the flow pattern transition to occur, the drillpipe speed would have to generate a force that dominates the axial force of the flow. However, it is important to note that in situations where the fluid properties are pressure/temperature dependent, the change in pressure gradient due to the inner pipe rotation can alter the fluid properties. This condition may alter the in-situ fluid flowrates at certain locations in the wellbore annuli which can lead to a transition from one flow pattern to the other.

## **6.5 Validation of mathematical modelling**

For two-phase flow through the annuli, the distribution of the velocity fields like the single-phase flow is influenced by the degree of eccentricity of the annuli. For any flow pattern, the velocity of the fluids in the region with the reduced gap in the annuli will generally have a lower average velocity than the region with the increased gap. This is a factor that can largely affect the tendency of cuttings to be transported effectively with the drilling fluids out of the wellbore during drilling. Although inner pipe rotation can improve the velocity fields in the regions with low average velocities, for multiphase flow, this improvement is dependent on the flow pattern in the annuli. Generally, the impact of inner pipe rotation on the axial annuli velocity fields for single-phase flow is a lot more significant than that of two-phase. The reason for this is that some of the flow patterns that exist in two-phase flow occur under highly turbulent conditions. Thus, the impact of the axial

force pushing the flow in the axial direction is a lot more dominant than the tangential force generated by the rotating inner pipe and like for single-phase flow, there is a maximum inner pipe rotation speed after which the influence of the tangential velocity on the axial flow becomes insignificant. Figures 6.21 and 6.22 show that the velocity distribution for two-phase flow in conduit is flow pattern dependent so the impact of inner pipe rotation and eccentricity on the velocity fields and cutting transport must also be flow pattern dependent. In order to perform cutting transport simulations or theoretical calculations for two-phase flow conditions, it is required that the flow pattern is taken into consideration.

The pressure gradient results obtained from the simulation for single-phase non-Newtonian flow in concentric and eccentric annuli with or without the inner pipe rotation were compared to the pressure gradient values obtained using the theoretical model for friction factor derived in Chapter 4. Figures 6.26 and 6.27 shows the comparison of the numerical and theoretical pressure gradient data obtained at several input flowrates for both the concentric and eccentric annulus with and without inner pipe rotation.

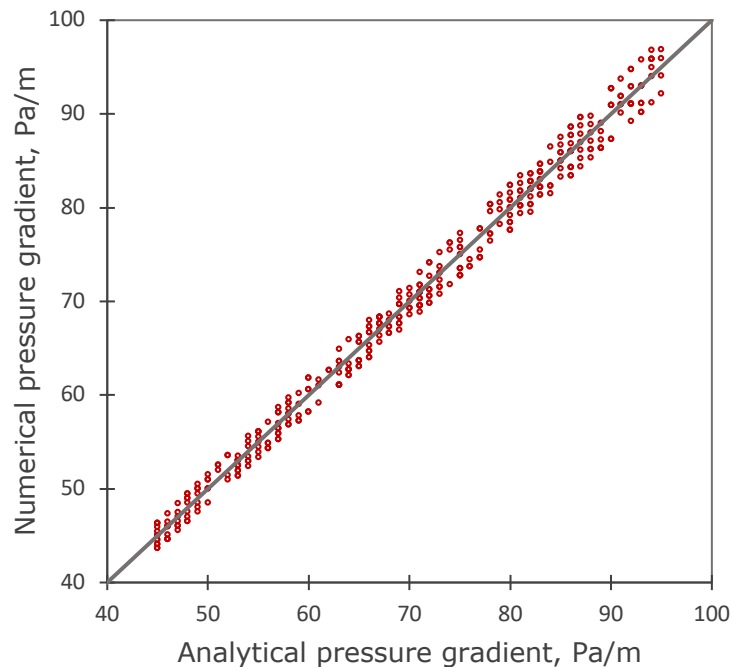


Figure 6.26: Comparison of the numerical and theoretical pressure gradient data (Fluid type A)

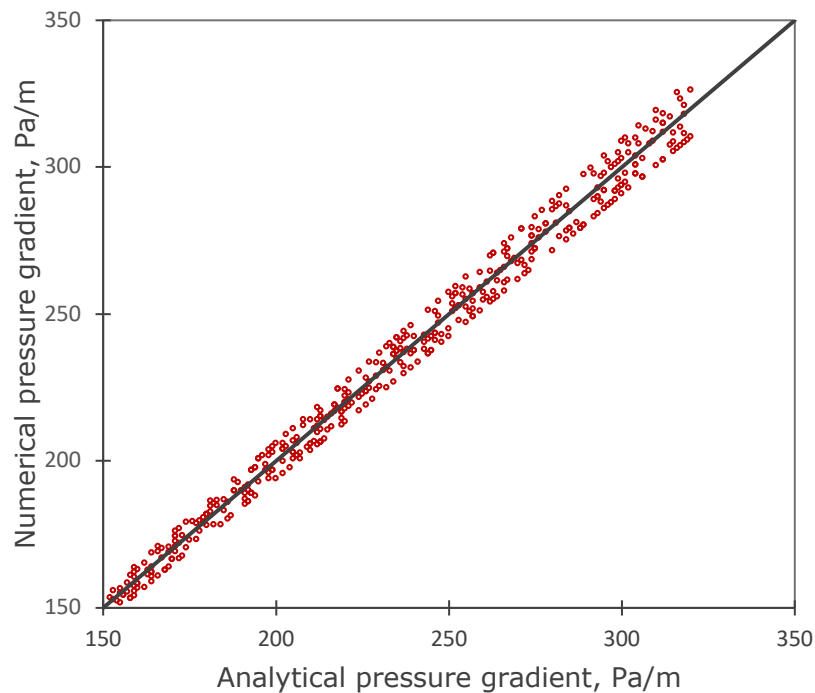


Figure 6.27: Comparison of the numerical and theoretical pressure gradient data (Fluid type B)

The input conditions for this simulation are as provided: Fluid flowrate ranged between  $3\text{m}^3/\text{h}$  to  $10\text{m}^3/\text{h}$ , inner pipe rotary speed varied from 0 to 150rpm and the eccentricity varied from 0 to 0.7. The comparison shows that the results obtained with both methods match closely, validating the theoretical model for determining the friction factor for the concentric and eccentric annuli with or without inner pipe rotation. Considering that the drillpipe rotation does not lead to a transition in the flow pattern under drilling conditions, the theoretical model can be used to determine the friction factor for the annuli when extensive numerical simulations cannot be performed. When the friction factor has been determined, the pressure gradient can be determined based on the flow pattern derived from the input conditions. However, when a detailed knowledge of the flow dynamics is required, the numerical CFD method should be applied.

## 6.6 Chapter summary

CFD simulations were performed for single-phase and two-phase fluid flow in the concentric and eccentric annuli to investigate the effect of the inner pipe rotation on the fluid dynamics and the resulting axial pressure gradient. The governing

equations for fluid flow were discretised using the finite volume method to obtain solutions for mesh grids in the cylindrical and cartesian coordinate systems. Mesh generation equations and algorithms were developed to enable the mapping of the concentric and eccentric annuli and presented in Equation 6.54 to 6.57. Two-phase flow simulations were created using the one-fluid approach, when the governing equations are solved at every cell in the domain and the interface between the fluids is tracked by a marker function. Although the simulation results showed that the velocity, viscosity and pressure field distribution are influenced by the inner pipe rotation in the annuli, for the two-phase flow simulations, the inner pipe rotation of up to 150rpm did not generate enough force to cause a significant distortion that would signal a change in flow pattern. For this reason, the steady-state mathematical flow pattern dependent models can be used without considering the flow pattern transitions. The pressure gradient predicted from the friction factor models in section 4.2 to 4.4 were compared to that which was obtained from the numerical simulation of the flow of different fluid rheological characteristics (Figure 6.26 and 6.27) and maximum errors of about  $\pm 9\%$  were seen. This chapter presented results that were used to validate the analytically developed models, as well as provide a new method in which the CFD simulations can be carried out for flow of Newtonian or non-Newtonian fluid flow through the concentric and eccentric annuli, with and without inner pipe rotation.

## Chapter 7

### Results and discussion

The following sections present the detailed analysis of the results from the experimental study as well as the comparison of measured data to the data obtained from theoretical predictions.

#### **7.1 Effect of inner pipe rotation on flow pattern transitions**

The flow pattern existing in the annulus when operating with a multiphase drilling fluid is a major factor that influences the wellbore hydraulics during drilling. In order to predict the change in pressure through the wellbore annuli, it is important to have a knowledge of the possible gas-liquid flow patterns and be able to track these flow pattern transitions across the entire length of the wellbore. Gas-liquid fluid flow pattern transition boundaries have been established as a function of the fluid properties, flowrate or superficial velocities of the gas and liquid phases by previous researchers (Beggs and Brill, 1973; Taitel and Dukler, 1976; Barnea et al., 1980; Caetano et al., 1992; Petalas and Aziz, 2000; Ibarra et al., 2019 etc.). However, in a concentric or eccentric annulus, the impact of the drillpipe rotation on the flow pattern transitions needs to be investigated and defined, especially if the pressure gradient in a helical wellbore annulus is required. In this study, the effect of the inner pipe rotation on the flow pattern was investigated and details of the results are presented in this section. The flow patterns studied were set by adjusting the gas and liquid flowrate until the required flow pattern was achieved. After the flow was fully developed and the flow pattern was stabilised, the inner pipe speed was varied (0, 60, 90, 120 and 150 rpm) and the resulting impact on the gas-liquid fluid flow pattern behaviour was recorded. The Figures 7.1 to 7.3 presents some of the images that capture the impact of the inner pipe rotation on the flow pattern transitions in both the horizontal and inclined annuli test sections.

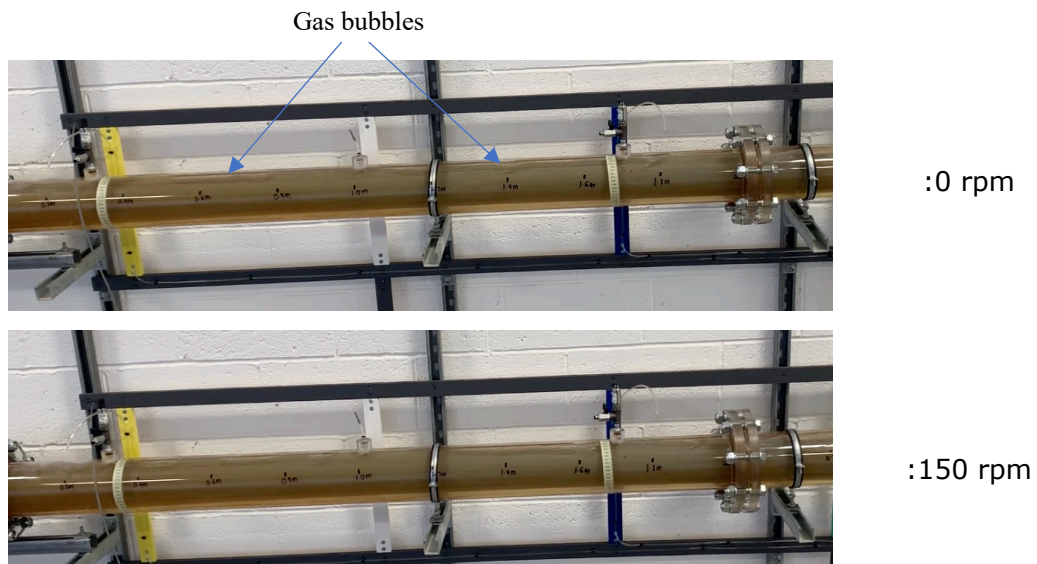


Figure 7.1: Bubble flow pattern in horizontal concentric annulus (Fluid type 2)

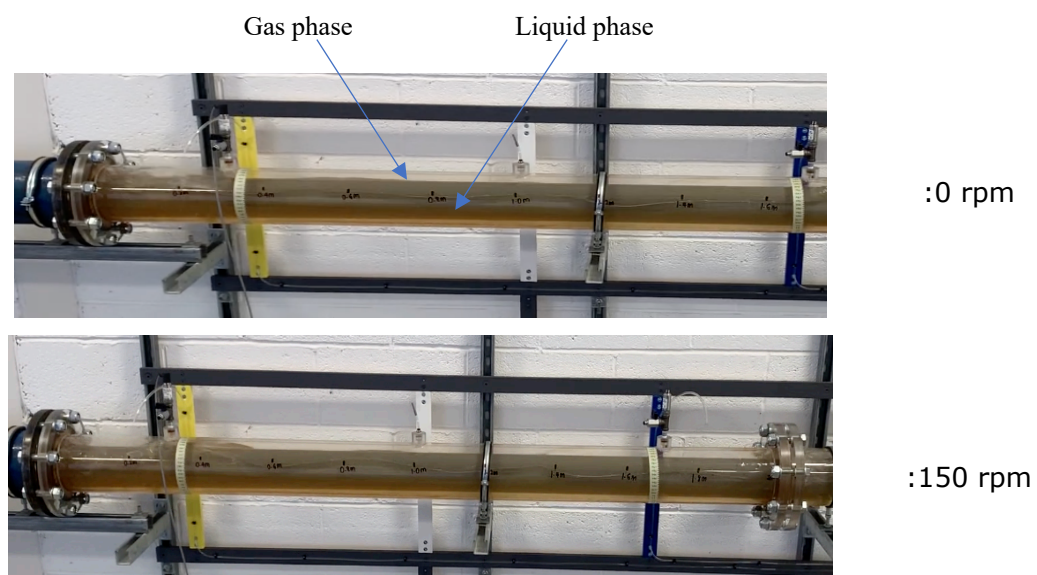


Figure 7.2: Stratified flow pattern in horizontal concentric annulus (Fluid type 2)

The experimental results on the fluid flow pattern for all the fluid types showed that the inner pipe rotation had no significant influence on the flow pattern transitions in both the concentric and eccentric annuli. Once the flow pattern is stabilised, the inner pipe rotation of up to 150 rpm did not cause a transition from one fluid flow pattern to the other. In the stratified flow pattern, the inner pipe rotation transformed the flow from having a smooth interface, to a wavy like interface (Figure 7.2). However, this phenomenon was not independent of the air-

water input flowrates. For the inner pipe rotation to cause a transition in the fluid flow pattern, the forces generated by the rotary motion in the azimuthal direction has to overcome the pressure forces driving the flow in the axial direction. This claim is also backed by the results obtained from the numerical CFD simulation of the effect of drillpipe rotation on two-phase flow pattern, where a transition of flow pattern did not occur despite the disturbance created. Thus, it can be concluded that at standard conditions the prevailing flow pattern in the drilling annuli is mainly a function of the gas and liquid input flowrates and when these flowrates are held constant, the drillpipe rotation speed has to be high enough to overcome the axial forces in order to change the fluid flow pattern.

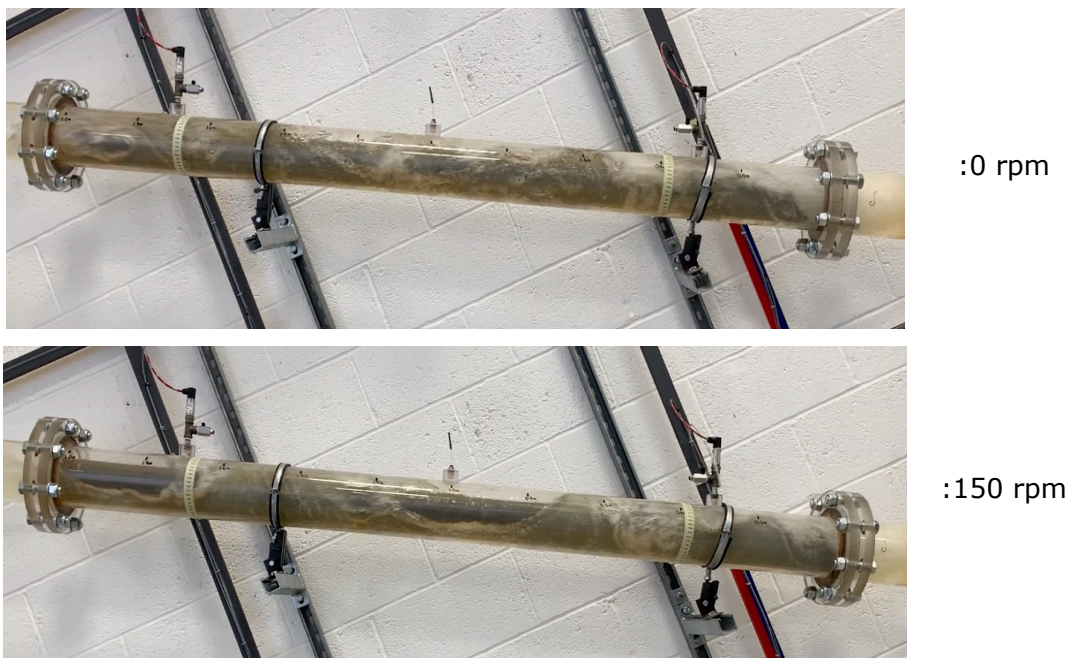


Figure 7.3: Slug flow pattern in inclined eccentric annulus ( $E = 0.7$ , Fluid type 4)

It is important to note that even though the drillpipe rotation has a little or no impact on the flow pattern transitions at standard conditions, it can impact the flow pattern for the drilling hydraulics standpoint. The drillpipe rotation has been reported to have a significant effect on the pressure gradient especially in the eccentric annuli. In a wellbore operating with multiphase drilling fluids or under underbalanced drilling conditions where hydrocarbons (gas and oil) may flow into the wellbore, the liquid phase may contain dissolved gas. As pressures and temperatures change, mass transfer occurs continuously between the gas and the

liquid phases and the in-situ flowrates of the gas and liquid changes. Thus, if the combined effect of drillpipe rotation and eccentricity influences the annuli pressure gradient, the flow pattern downstream the drilling bit can be influenced significantly as this phenomenon is dependent on the in-situ flowrates of the gas and liquid phases. However, when the local pressure and temperature in the wellbore has determined the prevailing fluid properties, fluid flowrates and the corresponding flow pattern, the drillpipe rotation cannot transform the flow pattern. This means that in order to perform wellbore hydraulic calculations it is important to simultaneously apply PVT analysis to determine the fluid properties, in-situ gas and liquid flowrates and the resulting flow pattern in the annuli.

## **7.2 Effect of inner pipe rotation on annuli pressure drop**

The experimental data of the differential pressure in the concentric and eccentric annuli, with and without inner pipe rotation was obtained and compared to the theoretical models developed and detailed in the previous chapters. This section presents the analysis of the effect of inner pipe rotation on the annuli pressure gradient for the single-phase and two-phase gas-liquid Newtonian and non-Newtonian fluids.

### **7.2.1 Annuli pressure gradient**

The results obtained from measuring the pressure difference across the concentric annuli test sections have been analysed based on the fluid type and the existing flow pattern in the annuli. For all the fluid types and flow patterns investigated in the concentric annuli at the different inclination angles, the inner pipe rotation had an insignificant effect on the pressure gradient. Figures 7.4 to 7.7 displays some of the flow pattern dependent results obtained from the experimental investigation.

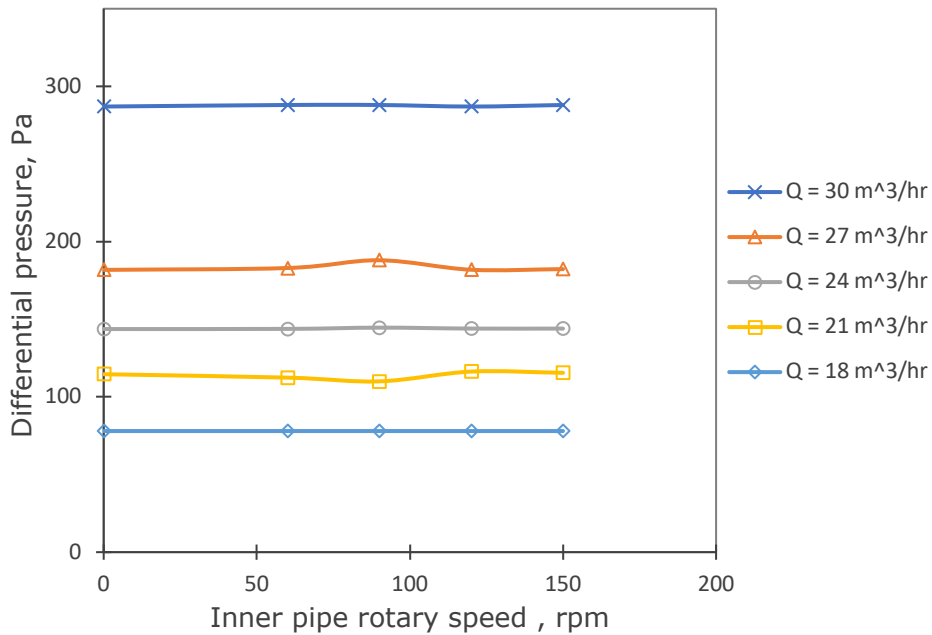


Figure 7.4: Effect of inner pipe rotation on the pressure drop in the horizontal concentric annulus (Water)

The pressure gradient measurement for the slug flow pattern at specific input liquid and gas flowrate was relatively more challenging than the other flow patterns due to its high turbulent and intermittent nature. The slug flow pattern occurs over a wide range of gas to liquid flowrates and is one of the most likely encountered flow patterns for two-phase fluid flows in annuli. The pressure gradient for the slug flow pattern is not constant due to its complex phase distribution and intermittent nature, making it more difficult to measure the effect of the inner pipe rotation on the annuli pressure gradient.

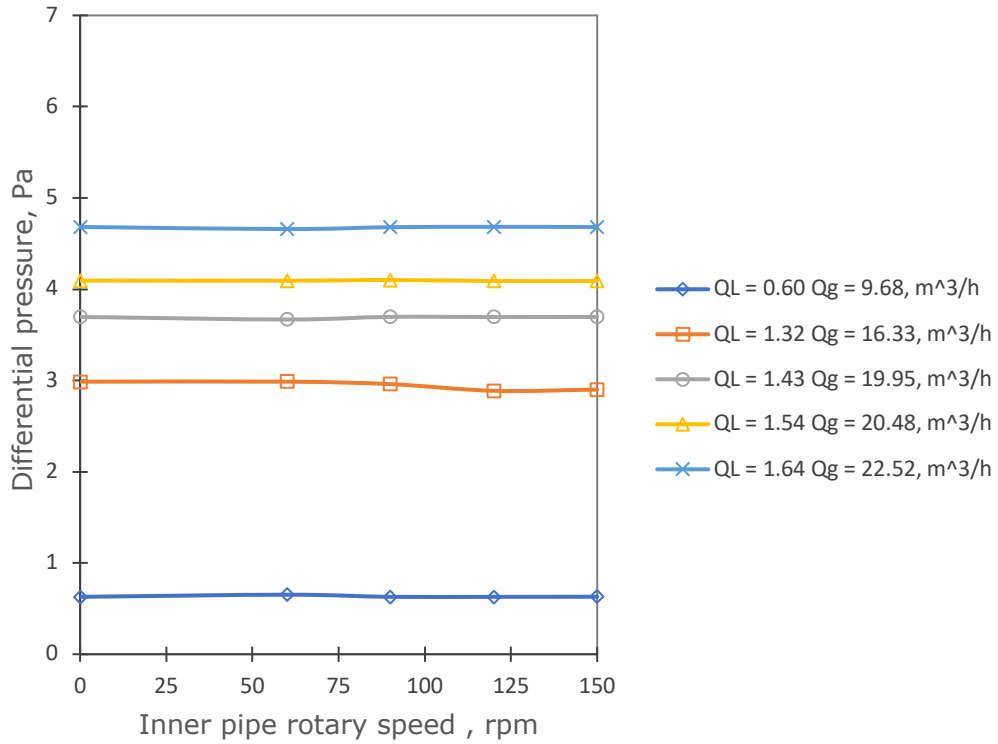


Figure 7.5: Effect of inner pipe rotation on the pressure drop in the horizontal concentric annulus (Water and air, stratified flow pattern)

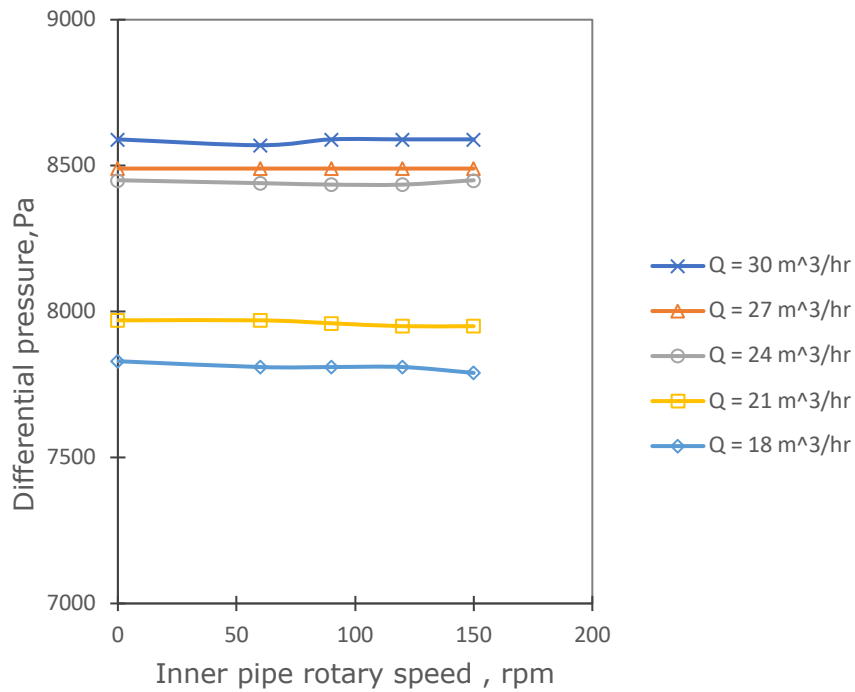


Figure 7.6: Effect of inner pipe rotation on the pressure drop in the 30° inclined concentric annulus (Water)

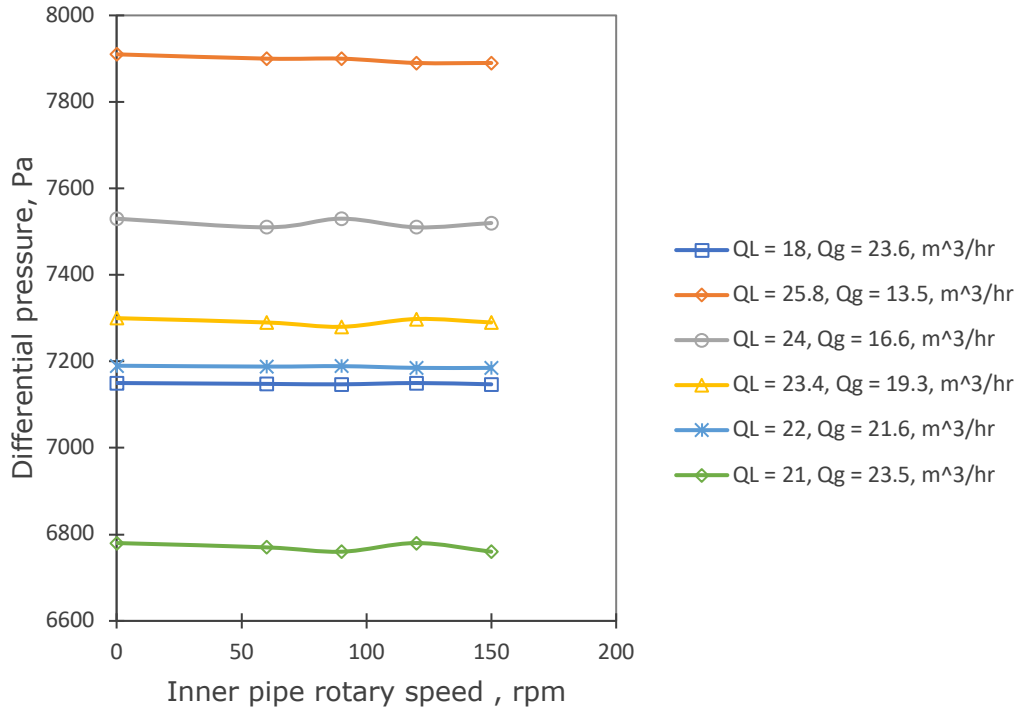


Figure 7.7: Effect of inner pipe rotation on the pressure drop in the 30° inclined concentric annulus (Polymer (0.1% XG) and air, slug flow pattern)

In order to minimise the inaccuracy occasioned by the intermittent nature of the flow, the annuli pressure gradient was obtained by flowing the fluids in the flow loop for a specific period of about 3-5 mins and obtaining the average pressure difference measured within the flowing time. Figure 7.7 shows the effect of the inner pipe rotation on the slug flow pattern in the concentric and inclined annulus test sections. Despite the intermittent nature of the slug flow, there is no conclusive evidence that the inner pipe rotation has a significant effect on the pressure gradient in the horizontal or inclined concentric annulus under the conditions investigated. The pressure gradient predicted using the developed models in this study was tested against the experimental data obtained for the single phase, bubble, stratified and slug flow pattern. Figure 7.8 to Figure 7.10 shows the mathematical model performance for the total pressure gradient prediction in the concentric annulus with or without inner pipe rotation.

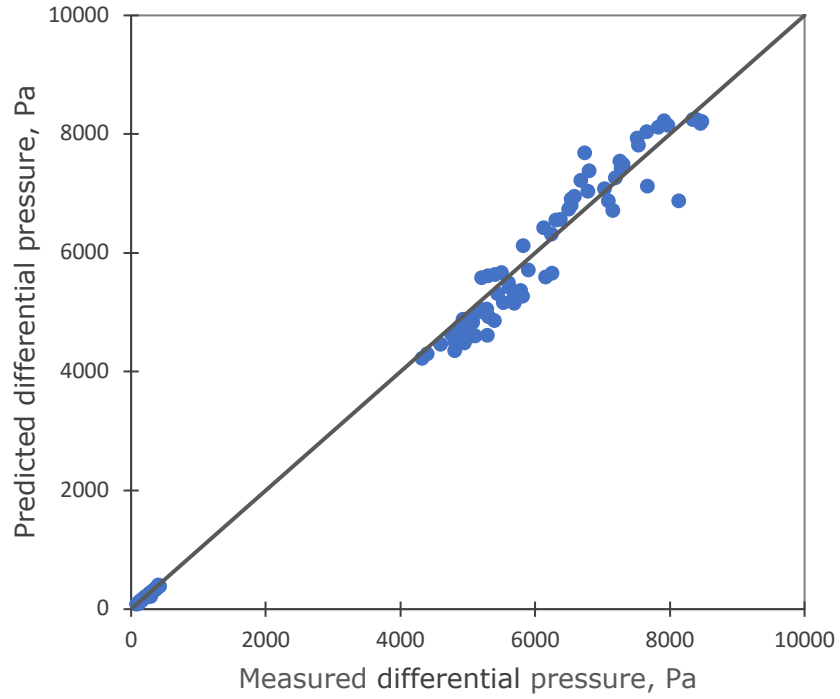


Figure 7.8: Model performance for annuli differential pressure (Water)

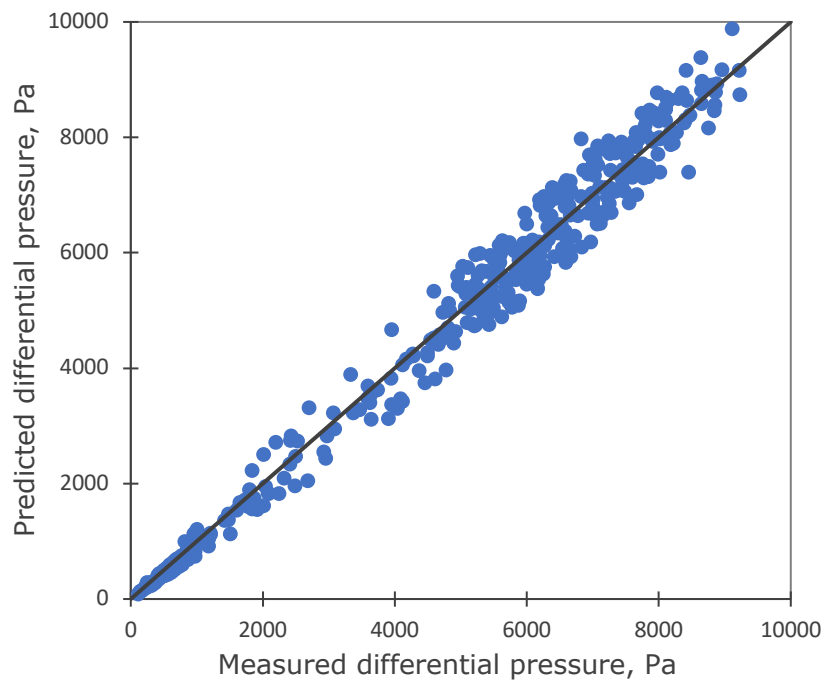


Figure 7.9: Model performance for annuli differential pressure (0.5% XG and air)

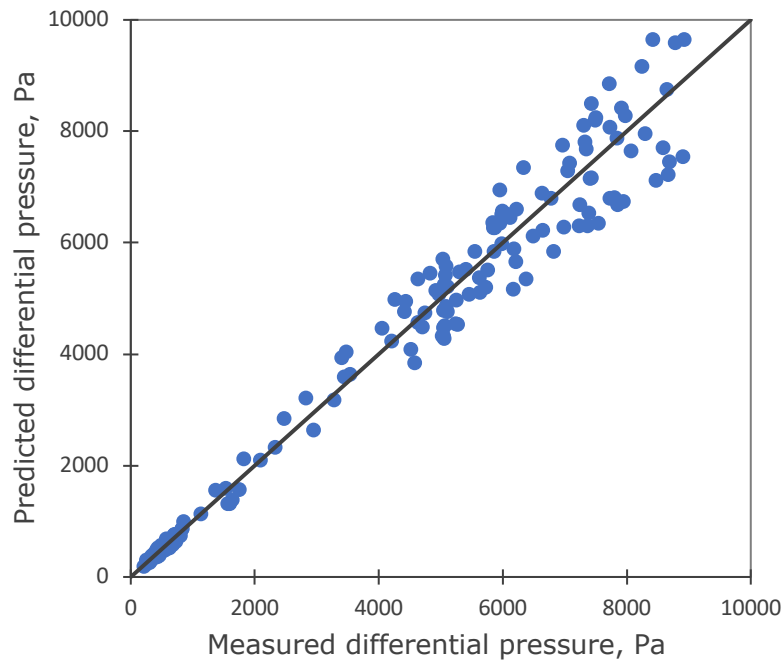


Figure 7.10: Model performance for annuli differential pressure (0.1% XG and air)

Statistical analysis show that the mathematical model has a very good agreement with the experimental results. The average of how large the errors are, is about 3.8% with a low standard deviation value. The mathematical model for the single-phase flow was found to be slightly more accurate than the two-phase flow models when compared to the experimental data. However, the bubble flow and stratified flow models closely matched the experimental results when compared to the slug flow model. This is due to the highly turbulent, intermittent and unsteady nature of the slug flow pattern which increases its degree of unpredictability. However, the errors margin for the prediction of the total pressure gradient in the concentric annulus, with and without the inner pipe rotation for all the flow patterns is about  $\pm 23\%$ .

### 7.2.2 Liquid film length

The annuli pressure gradient for the slug flow pattern is dependent on the length of the liquid film. Under the conditions investigated it was observed that the liquid film length is dependent on the orientation of the annuli sections. In the horizontal flow, the liquid film length is longer than that of the inclined flow for the same input air-liquid flowrates (Figure 7.11 and **Error! Reference source not found.**). This is due to the gravitational force acting on the liquid in the liquid film region of the slug unit. The average liquid film length predicted by the mathematical model for slug flow was compared to that measured in the experiments, showing good agreement.

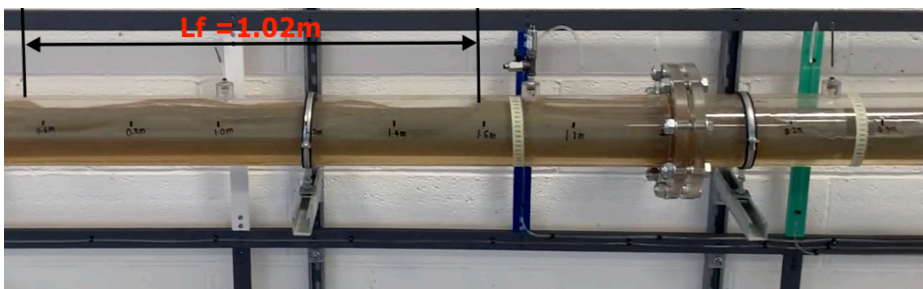


Figure 7.11: Liquid film length in the horizontal concentric annulus (air and water)

The performance of the slug flow model in predicting the liquid film length is presented in Figure 7.13. This was obtained by conducting 20 tests with different air-liquid flowrates for the slug flow pattern, comparing the observed liquid film lengths and the measured pressure gradients to the liquid film length and the corresponding pressure gradients that has been predicted by the mathematical model. The average film length was obtained from the experimental runs and the average pressure difference in the annuli sections was noted. The prediction of the film length and the pressure gradient for the slug flow when compared to the experimental results shows good agreement.

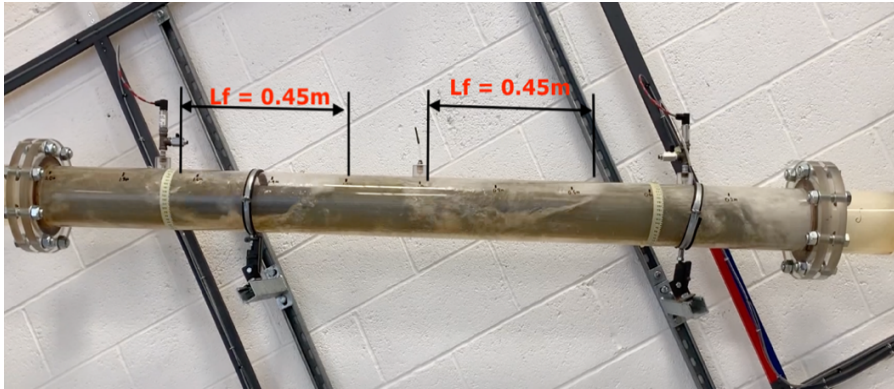


Figure 7.12: Liquid film length in the  $30^\circ$  inclined concentric annulus (air and water)

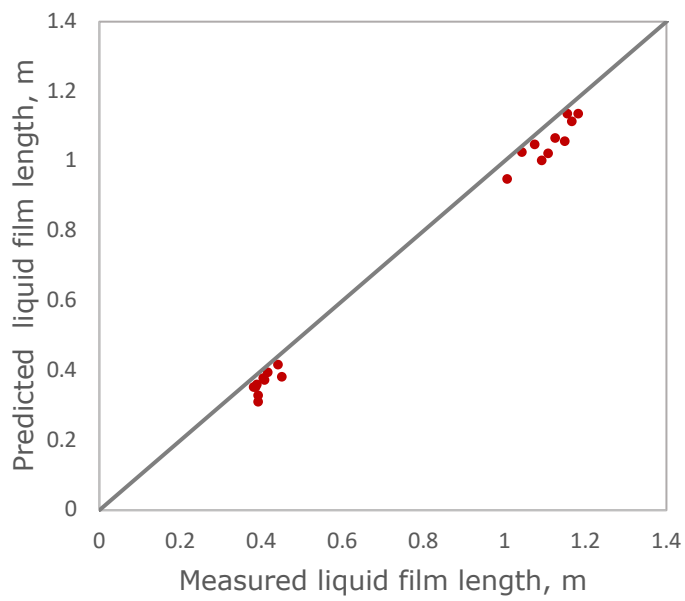


Figure 7.13: Model performance for length of the liquid film in the annuli

### **7.3 Cuttings transport**

One of the major requirements for a cost effective and productive wellbore drilling operation is having an effective cuttings transport system to optimise the hole cleaning operation. In this study a number of drilling parameters that influences the hole cleaning operation have been investigated in order to shed light on the effect of these parameters on both conventional and underbalanced drilling operations and also to validate the theoretically developed cutting transport models. Even though the major concern in hole cleaning is to establish the optimum drilling fluid flowrate that ensures an effective cuttings transport programme as a function of the major drilling parameters, for underbalanced drilling operations, this study shows that the gas-liquid fluid flow pattern is a major factor that influences the cuttings transport mechanism in the annuli and that there is a direct correlation between the flow pattern and cutting transport efficiency. The following sections presents detailed analysis of some of the drilling parameters that impact cuttings transport and how these parameters could be systematically used to optimise the hole cleaning during drilling activities.

#### **7.3.1 Effect of Fluid Flowrate**

The fluid circulation rate must be high enough to ensure that the particles are transported above the minimum transport velocity required to at least slide or drag the particles along the bottom of the annuli. However, for a multiphase fluid flow, this circulation rate is highly dependent on the fluid flow pattern. Several experiments showed that while certain gas-liquid mixture flowrates were favourable for particle transport in a given fluid flow pattern, other fluid flow patterns needed additional flowrate requirements to clean the annuli. In many cases an increase in the gas flowrate through the system led to an increase in the requirement to transport the particles effectively even though the mixture flowrate of the fluid is increased. Unlike single-phase flow the increase in the flowrate for two-phase flow mixtures does not always lead to a corresponding increase in the particle transport rate as this is dependent on the in-situ flowrate of each of the phases in the flow and the prevailing flow pattern. For instance, in the Figure 7.14 the single-phase fluid flowing at a flowrate of about 30m<sup>3</sup>/hr had the cuttings sliding along the bottom of the annuli creating the moving bed transport mechanism, but the two-phase fluids formed a stationary bed at relatively higher

mixture flowrates. The stratified and slug flow patterns formed a stationary bed in the annuli at mixture flowrates of about  $35\text{m}^3/\text{hr}$  and  $42\text{m}^3/\text{hr}$  respectively. Thus, for UBD operations, the flow pattern must be considered along with the gas-liquid flowrates in other to optimise hole cleaning. However, it should be noted that the type of the flow pattern formed in the annuli is also a function of the gas-liquid in-situ flowrates.

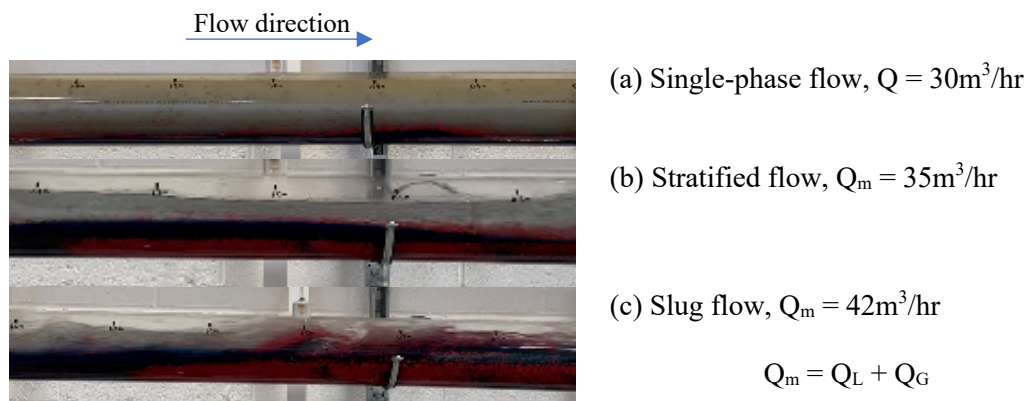


Figure 7.14: Cutting transport mechanism in different fluid flow patterns and gas-liquid flowrates

Generally, the experimental tests showed that unlike the single-phase fluid flow, the minimum transport velocity for the gas-liquid two-phase fluid flows are significantly dependent on the gas-liquid fluid flow pattern along with the other important parameters that influence the particle transport efficiency. If the fluid velocity falls below the critical or minimum transport velocity required to roll, drag or slide the particles at the bottom of the annuli, the particles would settle and form a stationary bed at the bottom of the annuli. The stationary bed height increases, which decreases the area of flow available for the fluids and oncoming particles, thereby leading to an increase in the fluid's average velocity until the point is reached at which the minimum transport velocity required to keep the oncoming particles moving is attained. At this point the oncoming particles are transported above the stationary bed as a moving bed with some particles in suspension depending on the properties of the particles. Thus, the annuli pressure losses experienced by the flow of two-phase fluids with particles are not only dependent on the fluid flow pattern, but also dependent on the particle transport mechanism and different from that experienced by the flow of the fluids without the particles.

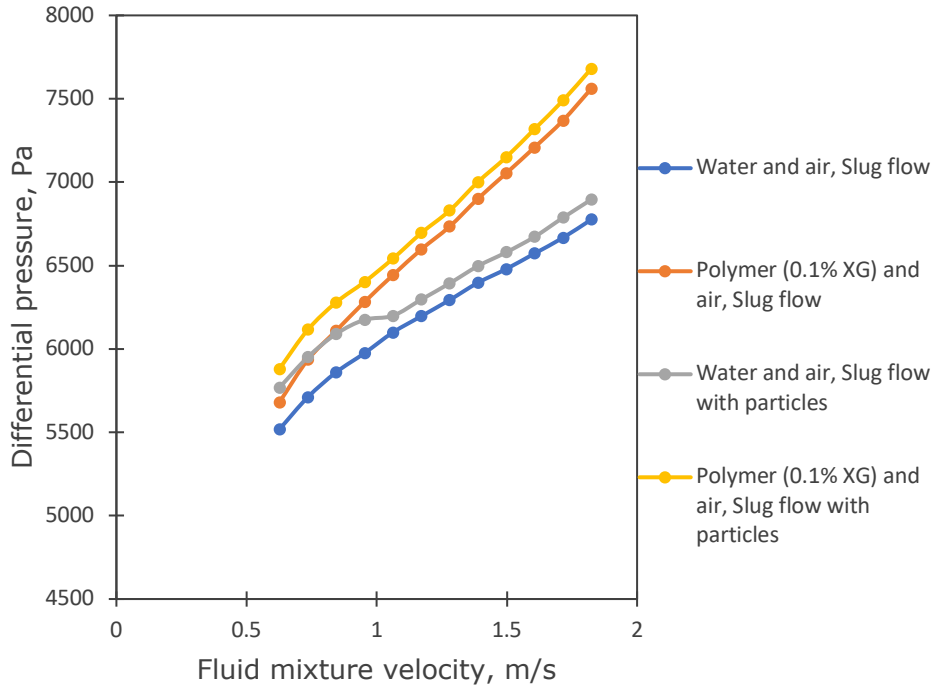


Figure 7.15: Annuli differential pressure at different mixture velocities for two-phase air-liquid flows with and without particles

The pressure loss data obtained from some experimental tests of two-phase air-liquid flow with and without particles in the 30° inclined annuli is presented in the Figure 7.15. The annuli pressure losses for the fluid flow with cuttings was observed to be significantly higher than without cuttings and dependent on the prevailing particle transport mechanism. At low mixture velocities or air-liquid flow rates where the flow is operating below the minimum transport velocity, a stationary bed is formed which significantly increases the pressure losses in the annuli for conditions with both the Newtonian and non-Newtonian liquids (Figure 7.15). Increasing the fluid flow rate reduces the stationary bed height and eventually transforms the stationary bed to a moving bed or suspension mechanism which as a result leads to a decrease in the pressure losses in the annuli. The increase in the fluid flow rate to transport the cuttings influences the fluid flow pattern and produces a corresponding increase in the pressure losses in the annuli. Thus, the necessary analysis of the optimum fluid flow rate required to transport the cuttings and also control or maintain wellbore pressures is required especially for UBD operations.

### 7.3.2 Effect of eccentricity

The average fluid velocity required to transport the particles and prevent the formation of a stationary bed at the bottom of the annuli, increases with an increase in the eccentricity of the inner pipe. Thus, the fluid flow requirement necessary to clean the eccentric annuli is higher than that required for the concentric annuli for flows involving both the single-phase and two-phase fluids with particles. In some experimental tests under fluid flowing conditions were no bed or a moving bed was formed in the concentric annulus, either a moving bed or a stationary bed was formed in the eccentric annulus. However, the effect of the eccentricity on the particle transport was a lot more significant for the two-phase air-liquid fluids than that of the single-phase fluids. The average fluid velocity required to prevent the formation of a stationary bed when the particles are flowing with the single-phase and two-phase fluids were measured from experimental tests and compared in Figure 7.16 for the concentric ( $e=0$ ), and eccentric ( $e=0.7$ ) annuli. The minimum transport velocity MTV required to keep the particles at least rolling at the bottom wall of the annuli, increases with eccentricity.

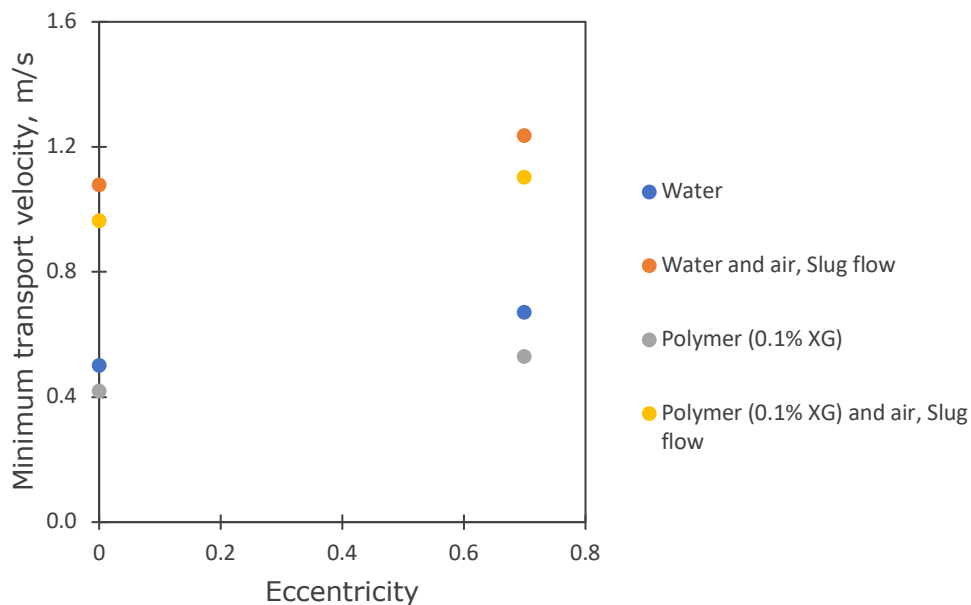


Figure 7.16: Effect of pipe eccentricity on the minimum transport velocity

### 7.3.3 Effect of fluid rheology

The fluid rheology has a significant influence on the transport efficiency of the particles in the concentric and eccentric annuli for fluid flow involving both the single-phase and two-phase fluids. The experimental tests showed that for all the fluid flow patterns investigated, the use of the fluids with the higher viscosity for the single-phase flow or mixture viscosity for the two-phase flow were more effective for the particle transport and the prevention of the formation of a stationary bed in the annuli. However, when a stationary bed is already formed in the annuli, the fluids with the lighter viscosity or the two-phase fluids are more effective in clearing or reducing the stationary bed thickness.

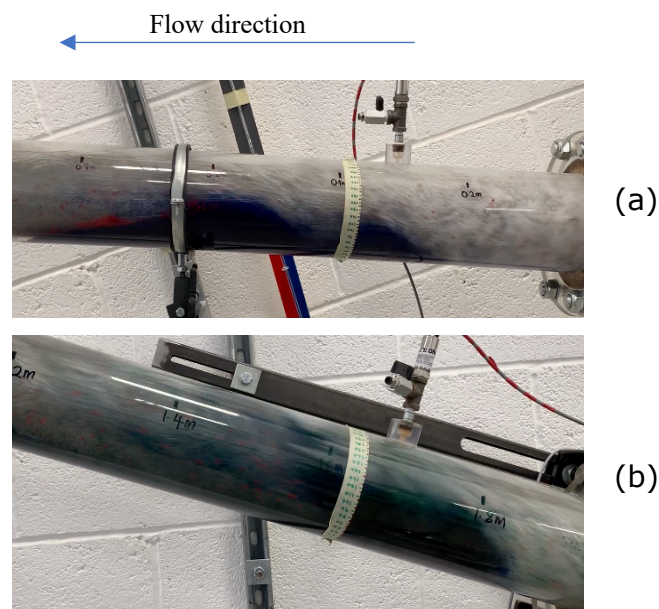


Figure 7.17: Two-phase dispersed bubble flow pattern for the different fluid and particle mixtures at the same air-liquid flowrates. a) moving bed mechanism in air-water mixtures and (b) suspension mechanism in air-polymer mixtures

Generally, the minimum transport velocity required to prevent the settling of the solid particles entrained in the fluid decreases with an increase in the fluid viscosity for both the single-phase and two-phase Newtonian and non-Newtonian fluids, irrespective of the fluid flow pattern. However, several studies have reported that there is a threshold after which a further increase in the fluid viscosity can lead to a corresponding increase in the minimum transport velocity (Penden, et al., 1990). Figure 7.17 displays the comparison of the particle transport mechanism for the two-phase flow of air and water to that of the air and XG polymer mixtures at the

same air-liquid flowrates with the dispersed bubble flow pattern. Due to the higher mixture viscosity of the air and XG polymer mixtures, the particles are transported predominantly in suspension while a moving bed mechanism is formed for the air and water mixtures. The properties of the liquid phase are more important than that of the gas phase for particle transport and in two-phase flow conditions where the stratified and slug flow patterns exist in the annuli, the particles are generally transported in the liquid phase.

#### **7.3.4 Effect of cuttings properties (density and size)**

The density of the particles was more influential than the particle size for all the experimental tests performed using both the single phase and two-phase fluids. The magnitude of the gravitational or resistance force to the movement of the particles are largely dependent on the density and size of the particles and in order to ensure effective transport, the fluid would have to generate a sufficient drag, lift and buoyancy force to overcome the resistance forces acting on the particles in the annuli. The higher the density of the particles, the higher the resistance forces and thus, the higher the minimum requirements to ensure an effective transport. Thus, the single-phase fluids are more likely to present lower transport requirements than the two-phase gas-liquid fluids due to the lower mixture density of the latter. Tests involving the two-phase gas-liquid fluid flow with particles also showed that effect of the properties of the particles are highly dependent on the gas-liquid fluid flow pattern in the annuli. For instance, if the stratified flow exists in the annuli, the liquid properties and velocity would have to be sufficient enough to prevent the formation of a stationary bed. However, for the slug flow pattern, the fluid mixture properties and velocity must be sufficient to generate the required forces to prevent the formation of a stationary bed.

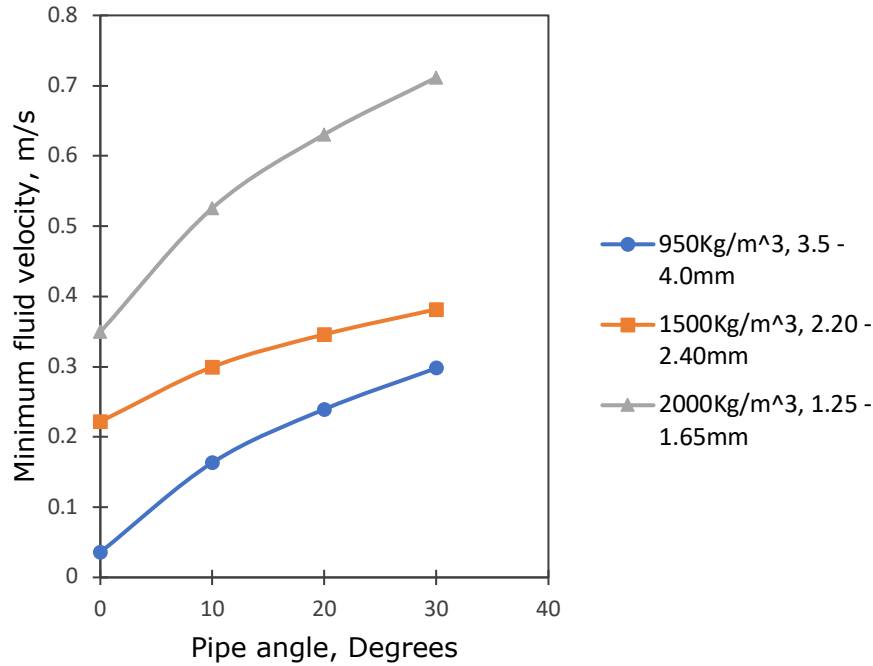


Figure 7.18: Minimum transport velocity versus the annuli inclination angle for different particle properties

Figure 7.18 shows the results of experimental tests performed to measure the minimum transport velocity to ensure the movement of particles with different densities and size ranges. It was observed that the MTV required to transport the heavier particles were significantly higher than that required for the lighter particles even though the size ranges of the heavier particles were much less than the lighter particles. However, if the density of all the particles are the same, the influence of the particle sizes on the MTV becomes a lot more significant. Figure 7.19 shows the phenomenon whereby the lighter red particles with a density of  $950\text{Kg/m}^3$  and a size range of 3.5-4.0mm are being transported in suspension while the heavier blue particles with a density of  $1500\text{Kg/m}^3$  and a size range of 2.20-2.40mm is being transported as a moving or stationary bed. This shows that the effect of the density of the particles on the particle transport mechanism is more dominant than its size and as the heavier particles settle, they in some cases collapse and trap some of the lighter particles in the stationary bed.

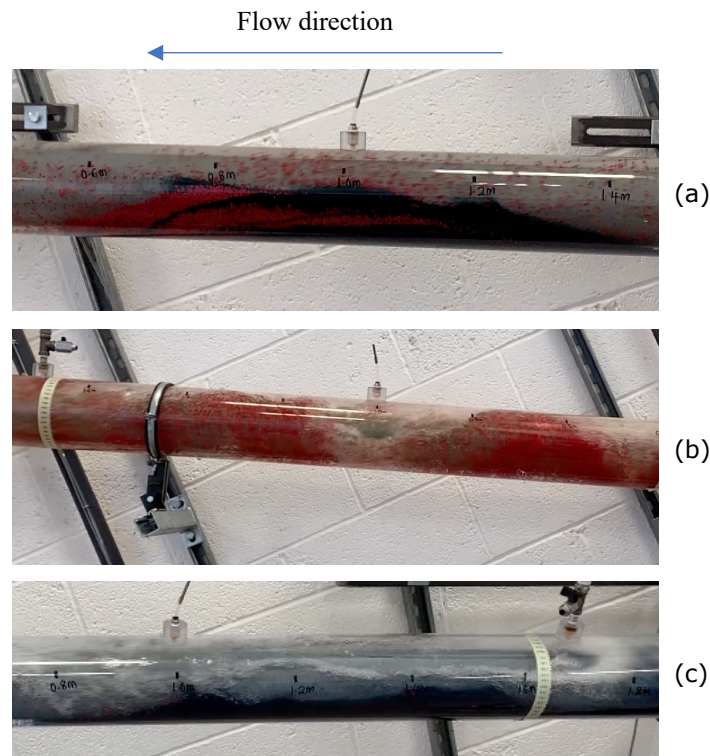


Figure 7.19: Effect of the particle properties on particle transport mechanism. (a) Single-phase water with the red and blue particles, (b) two-phase water and air with the red particles (b) two-phase water and air with the blue particles

### 7.3.5 Effect of wellbore inclination

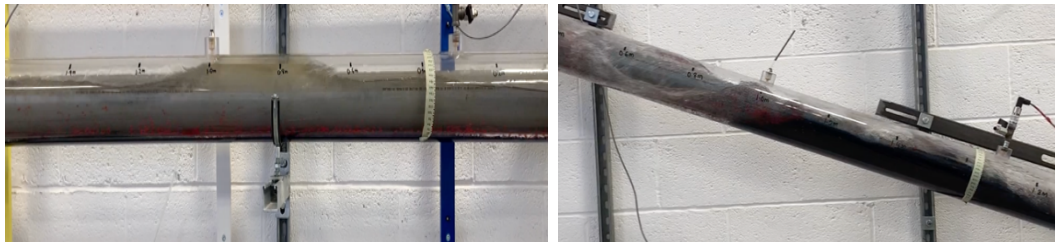
The particle movement in the annuli is highly dependent on the angle of inclination of the wellbore. However, the effect of the wellbore inclination angle on the transport of particles is dependent on the particle transport mechanism and not independent of the drilling fluid flow pattern. Unlike the single-phase flow, the flow configuration or fluid distribution of two-phase flow in the annuli is affected by the angle of inclination of the flow and in some cases if the gas-liquid flowrate is constant, an increase in pipe angle may change the fluid flow pattern from one form to another. This angle effect on the fluid distribution or flow pattern is an additional effect that influences the annuli hydraulics and particle transport efficiency for two-phase flow. Figure 7.20 shows an example of a scenario where gas flowrate of  $24\text{m}^3/\text{hr}$  and a liquid flowrate of  $21\text{m}^3/\text{hr}$  is passed simultaneously into a horizontal and  $20^\circ$  inclined annuli test sections thereby generating the slug flow pattern without the presence of particles. It can be seen that the gas-liquid distribution of the flow in the horizontal annuli differs significantly from that of the inclined annuli even though the slug flow pattern exists in both cases. Experimental tests showed that while the horizontal case had a longer liquid film

length, the liquid film length decreased with an increase in the inclination angle and the local mixture properties of the fluid was also influenced by the inclination angle (Figure 7.20). The effect of gravity on the liquid phase is a lot more than that on the gas phase. Thus, depending on the wellbore inclination angle, this effect tends to influence the fluid distribution in the annuli which will thereby influence the forces that are responsible for the cutting's movement.



Figure 7.20: Comparison of the fluid distribution and mixture properties of slug flow in the horizontal and inclined annuli test sections

Figure 7.23 and Figure 7.24 presents some of the experimental results for the effect of the wellbore angle on the cuttings transport efficiency in the concentric and eccentric annuli. These results were obtained by introducing the particles of a given concentration into the flow and recording the flowrate at which the particles are rolling at the bottom of the annuli and just below which a stationary bed is formed in the annuli. The flowrate required to transport the particles in the rolling mechanism was found to increase with an increase in the inclination angle and the gradient of this increase was greater for the two-phase flow than that of the single-phase flow. An example of the particle transport mechanism for the slug flow pattern in the horizontal and inclined annuli sections is shown in the Figure 7.21. It was observed that at a certain air-liquid flowrate, the particles in the horizontal test sections were being transported predominantly as a moving bed at the bottom of the annuli while a relatively higher stationary bed is formed at the bottom of the inclined annuli test sections and increased over time.



(a)

(b)

Figure 7.21: Comparison of particle transport in the horizontal and inclined annuli for (a) Moving bed with slug flow pattern in the horizontal annulus (Fluid type 2) and (b) Stationary bed for the slug flow pattern in 30° inclined annulus (Fluid type 2)

One of the main reasons for the formation of a stationary bed in the inclined annulus is the change in the local mixture properties of the fluid in the annulus which alters the forces acting on the particles. This makes it harder to transport cuttings in an upward inclined flow when the slug flow pattern is existing in the wellbore annuli. The flow requirement to achieve particle suspension in the annuli increased with an increase in the inclination angle for all the fluid types and flow patterns investigated. This was observed from experimental test where the fluid-particle mixtures at a given particle concentration was introduced to the test sections at a constant fluid flowrate while the angle of inclination was varied.



(a)

(b)

Figure 7.22: Change in cutting transport mechanism from suspension to a moving bed with increase in inclination angle from (a) 20° to (b) 30°

Figure 7.22 shows one of the experimental tests where the suspension mechanism was observed predominantly in the 20° inclined annuli test sections in comparison to the moving bed mechanism that was observed when the inclination angle was increase to 30°. As the inclination angle was increased within the range of 0-30°, most of the particles fell towards the bottom of the annuli showing that it is harder to suspend the particles with increase in inclination angle. It was also noted that the effect of the inclination angle appeared to have more influence on particles in the two-phase flow mixtures than that of the single-phase flow.

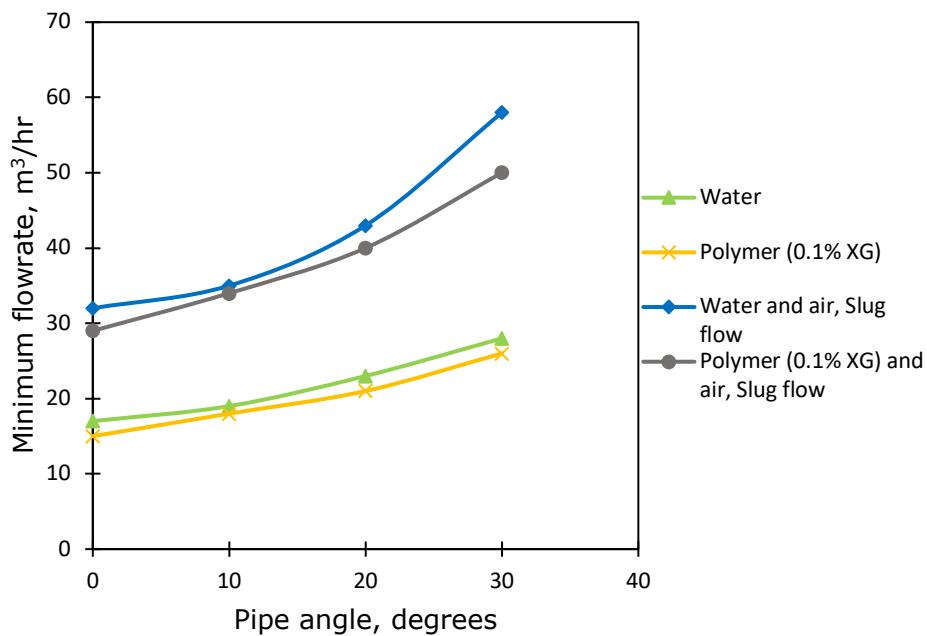


Figure 7.23: Effect of inclination angle on the MTV for rolling in the concentric annuli

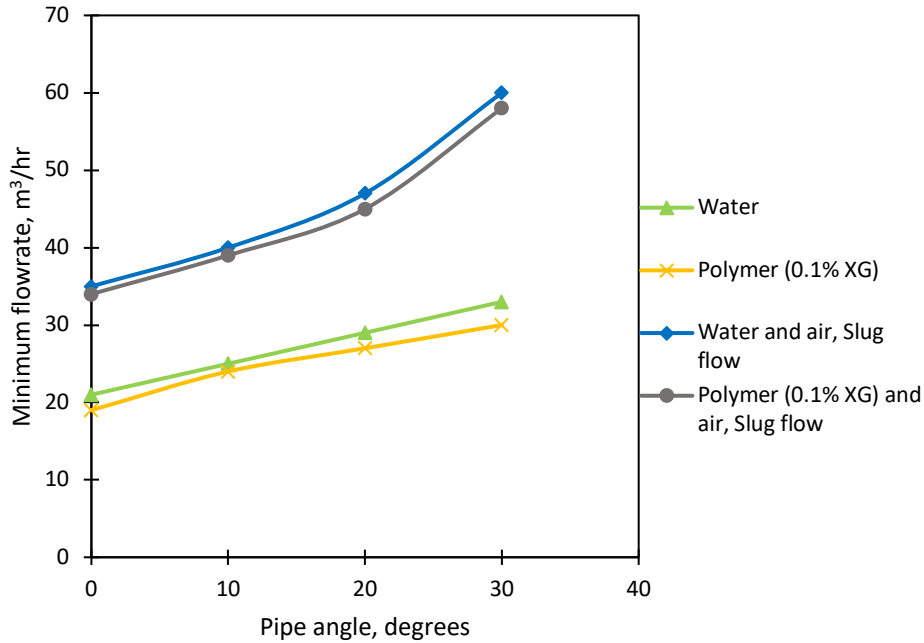


Figure 7.24: Effect of inclination angle on the MTV for rolling in the eccentric annuli

### 7.3.6 Effect of fluid viscosity

The effect of the fluid viscosity on the cutting's movement has been analysed and presented graphically in the Figure 7.25. These tests were carried out using an annular fluid velocity of 0.82m/s. The increase in the viscosity of the fluid corresponds to a decrease in the size or height of the stationary bed formed at the bottom of the horizontal annuli sections. These analyses were only performed for the single-phase fluid types because for the two-phase fluid types, the stationary bed height is not only dependent on the angle of inclination of the pipe but also highly dependent on the fluid flow pattern. For different flow patterns, the local viscosity at the bottom of the annulus, where the particles are likely to settle, varies. However, in general, the higher the mixture viscosity of the two-phase fluid at the low side of the annulus, the higher the tendency for the cuttings to clear from the wellbore. The tests showed that once a stationary bed has been formed, the lighter fluid or two-phase fluid mixtures is of a greater advantage than the heavier fluid towards the clearing of the stationary bed in the horizontal annulus. In the upward inclined annulus, the heavier fluid possesses the cleaning advantage.

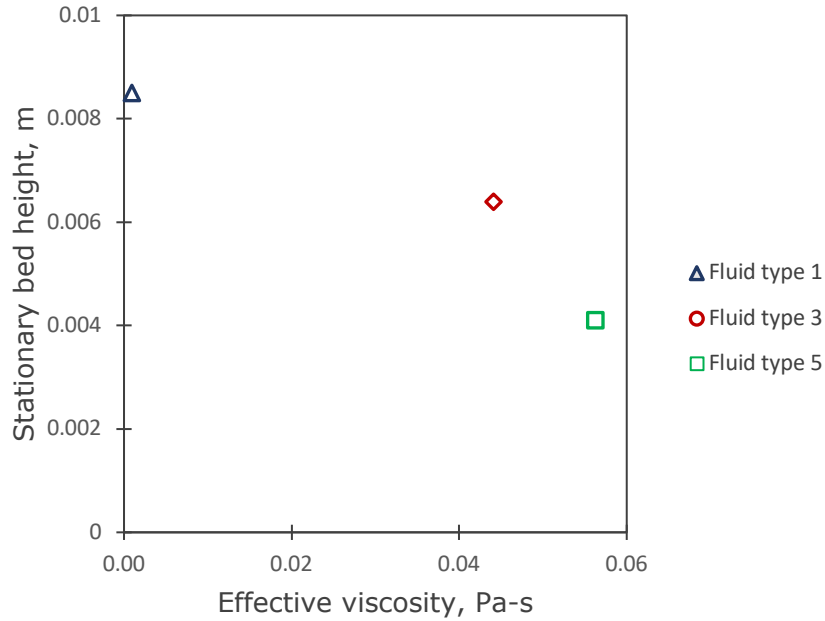


Figure 7.25: Effect of single-phase fluid viscosity on stationary bed thickness

### 7.3.7 Effect of inner pipe rotation

From the experimental study of the effect of inner pipe rotation on the movement of the particles, it was observed that the effect of the inner pipe rotation on the cuttings transport mechanism was dependent on the fluid, the flow pattern and the angle of inclination of the annulus. In the horizontal concentric annuli sections, the increase in the rotary speed of the inner pipe produced a little to no decrease in the height or area of the stationary bed for both the single-phase and two-phase fluids. The height of the bed formed in the annulus was not reduced by the rotation of the inner pipe for all the investigated flow patterns in the horizontal concentric annuli test section (Figure 7.26).

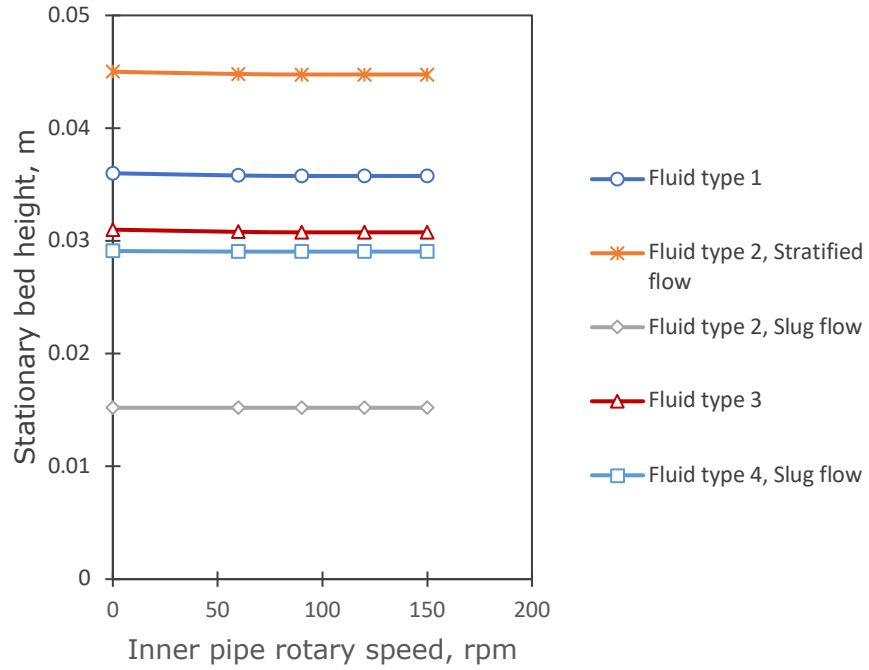


Figure 7.26: Effect of inner pipe rotation on bed thickness in horizontal concentric annuli

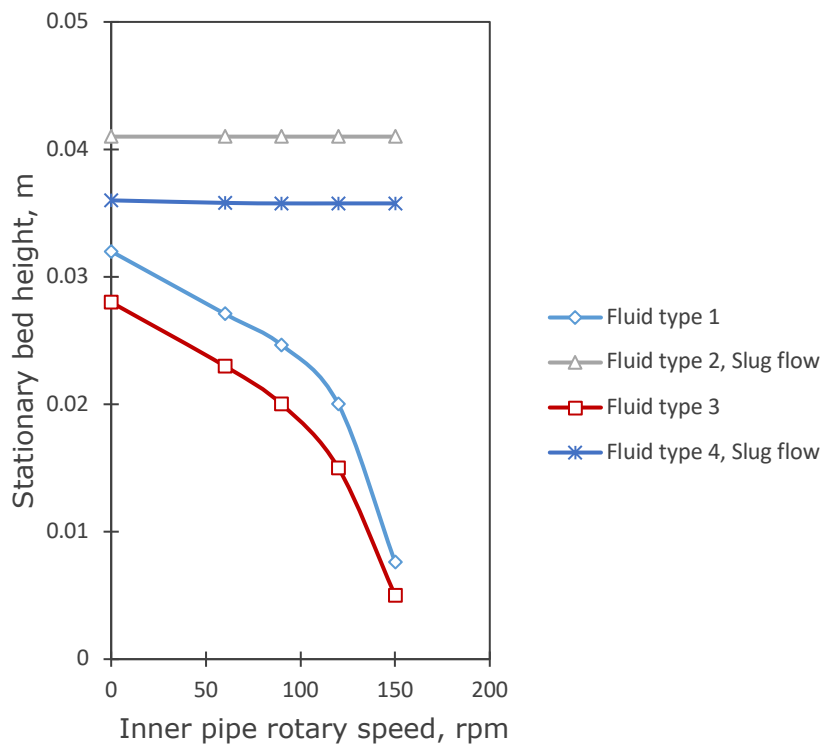


Figure 7.27: Effect of inner pipe rotation on bed thickness in 20° inclined concentric annuli

The effect of the inner pipe rotation on the particle transport for the flow of the different fluid types in the inclined annulus is shown in Figure 7.27. It was observed that while the inner pipe rotation had little or no influence on the area or thickness of the stationary bed formed in the inclined annuli test sections for the two-phase flow fluid types, for the single-phase fluids, the increase in the inner pipe rotary speed leads to a significant decrease in the thickness of the stationary bed. Figure 7.28 shows the effect of inner pipe rotation on the clearing of a stationary bed formed in the 20° inclined annulus test section flowing with a single-phase fluid. It can be seen that with change in time, the transport mechanism of the particles was transformed from the stationary bed regime and the particles were transported in the suspension and moving bed mechanism.

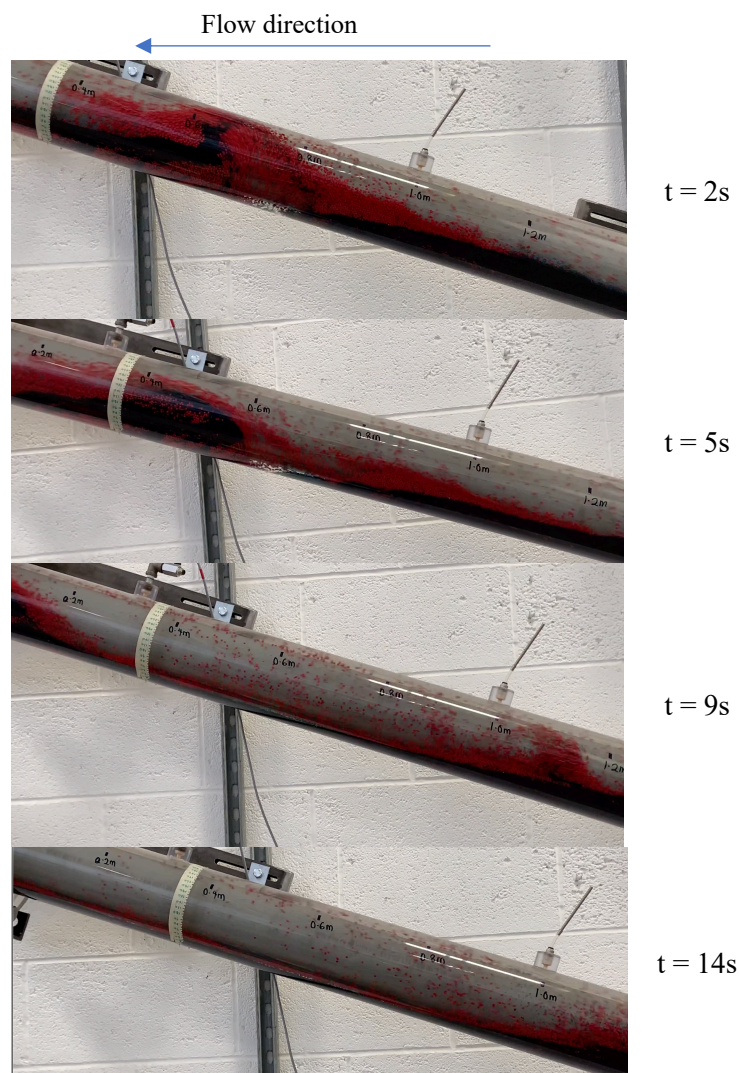


Figure 7.28: The effect of inner pipe rotation (150rpm) on a stationary bed formed in the 20° inclined concentric annulus (water and particles)

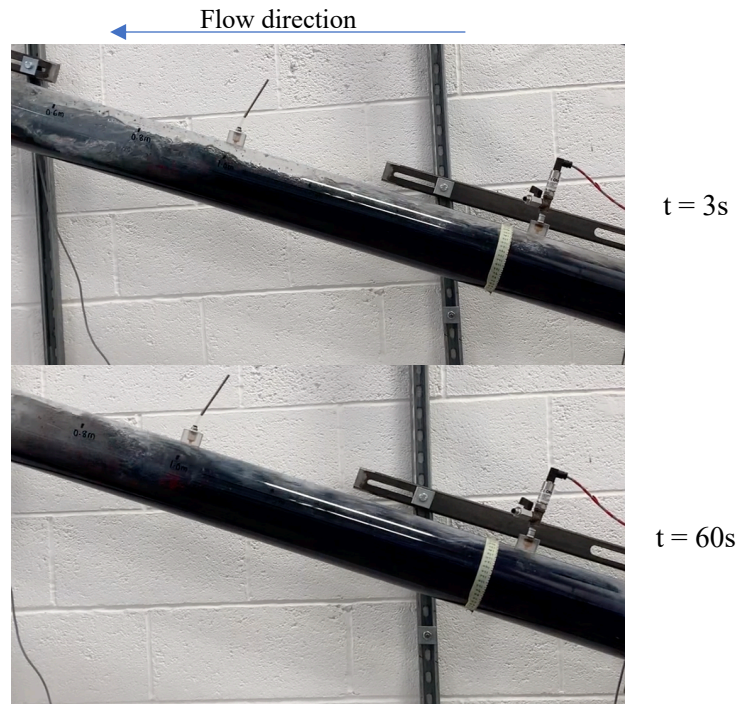


Figure 7.29: The effect of inner pipe rotation (150rpm) on a stationary bed formed in the inclined annulus (Fluid type 2)

Figure 7.29 shows the effect of the inner pipe rotation on the particles in the two-phase flow with the slug flow pattern in the inclined annulus. The increase in the inner pipe rotary speed had little or no significant influence on the size or thickness of the stationary bed formed in the annulus. The effect of the inner pipe rotation on the transport of the particles is a lot more significant in the eccentric annulus. However, the degree of the effect of rotation is highly dependent on the fluid rheology, fluid flow pattern and the angle of inclination of the annuli. For the horizontal eccentric annuli Figure 7.30, the height of the stationary bed reduced significantly with the increase in the rotary speed of the inner pipe. The particles in the single-phase flow responded a lot better to the inner pipe rotation than the particles in the two-phase flow and the fluids with the non-Newtonian rheology generally performed better than the Newtonian fluids especially for the single-phase flows. The Figure 7.31 shows the impact of the inner pipe rotation on the particles in the inclined eccentric annuli. It can be seen that the impact of the inner pipe rotation is a lot more significant in terms of the reduction of the stationary bed for the single-phase fluids. However, for the two-phase fluids the stationary bed is just slightly reduced with the increase in inner pipe rotation.

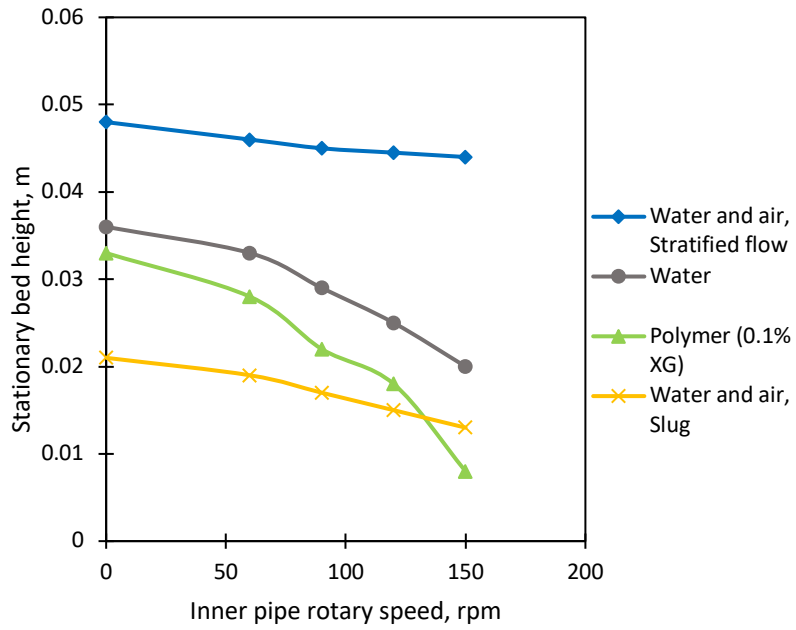


Figure 7.30: Effect of inner pipe rotation on bed thickness in horizontal eccentric annuli

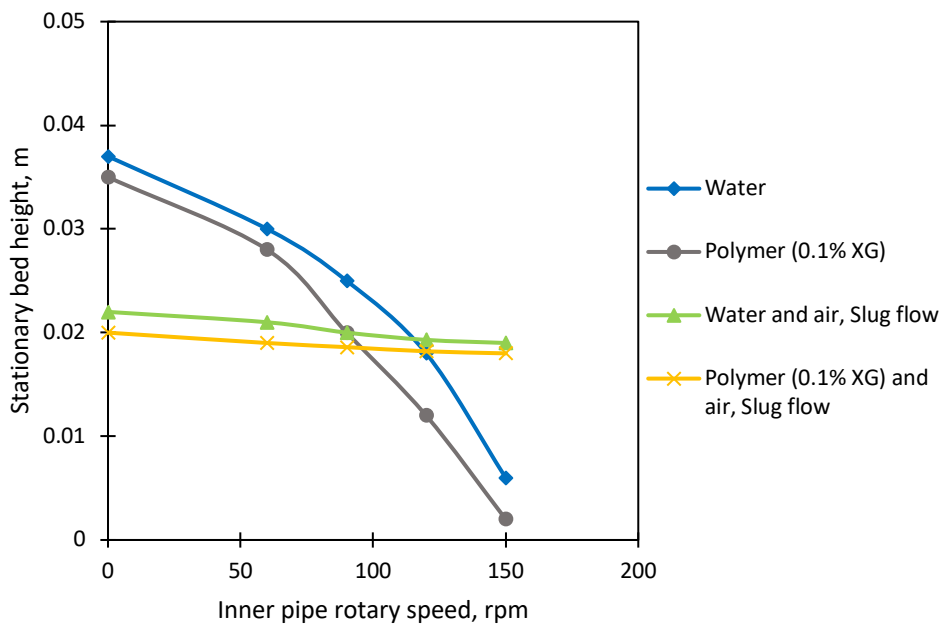


Figure 7.31: Effect of inner pipe rotation on bed thickness in inclined eccentric annuli

## 7.4 Pressure gradient due to particle transport

The annuli pressure gradient of fluid flow with entrained solid particles is significantly higher than the pressure gradient when no solid particles are transported in the flow. The prevailing cuttings transport mechanism and the properties of the particles and the fluid have a significant influence on the pressure gradient in the annuli. If the fluid flowrate generates an annuli average velocity that is below the minimum transport velocity required to keep the particles in suspension, the particle would fall to the bottom of the annuli and be transported as a moving bed. A stationary bed is formed if the average fluid velocity falls below the minimum transport velocity required for the particles to roll or slide at the bottom wall of the annuli.

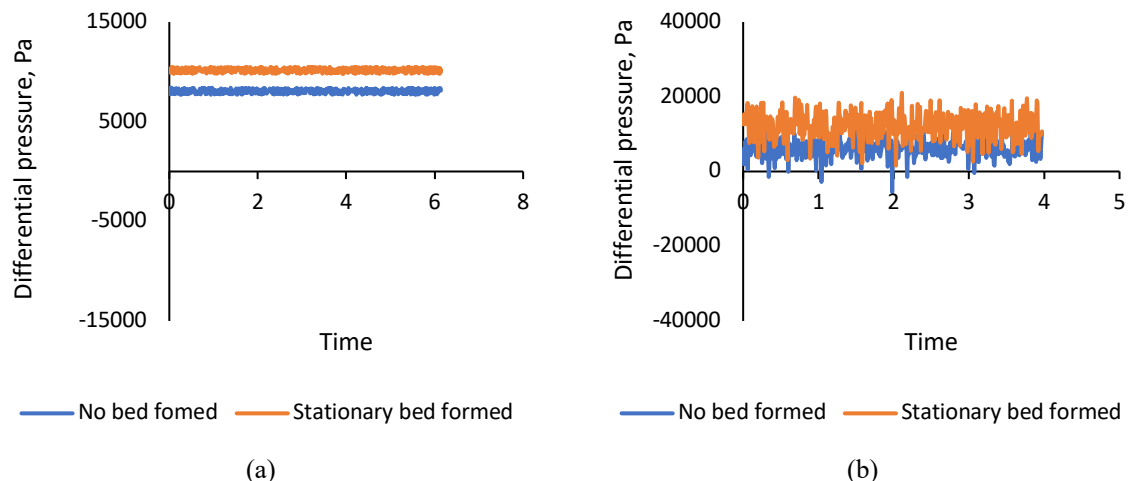


Figure 7.32: Real-time annuli differential pressure for (a) single-phase flow (water) and (b) two-phase slug flow (water and air)

If a stationary bed exists in the annuli, the flow area is reduced, and the fluid is forced to flow in the reduced flow area above the bed. With the flowrate being constant, this leads to an increase in the average velocity of the fluid, increased wall and fluid to bed interfacial shear stresses and a corresponding increase in the annuli pressure gradient. Figure 7.32 shows the difference between the differential pressure measured when a stationary bed is present and when no bed is present in the annulus. It can be seen that the pressure transducer voltage outputs when a stationary bed is present in the annulus is significantly higher than that obtained when no stationary bed is present in the annulus. Even though the stationary bed

increases the annuli pressure gradient, the pressure gradient is still highly dependent on the fluid flow pattern and the existing particle transport mechanism in the annuli.

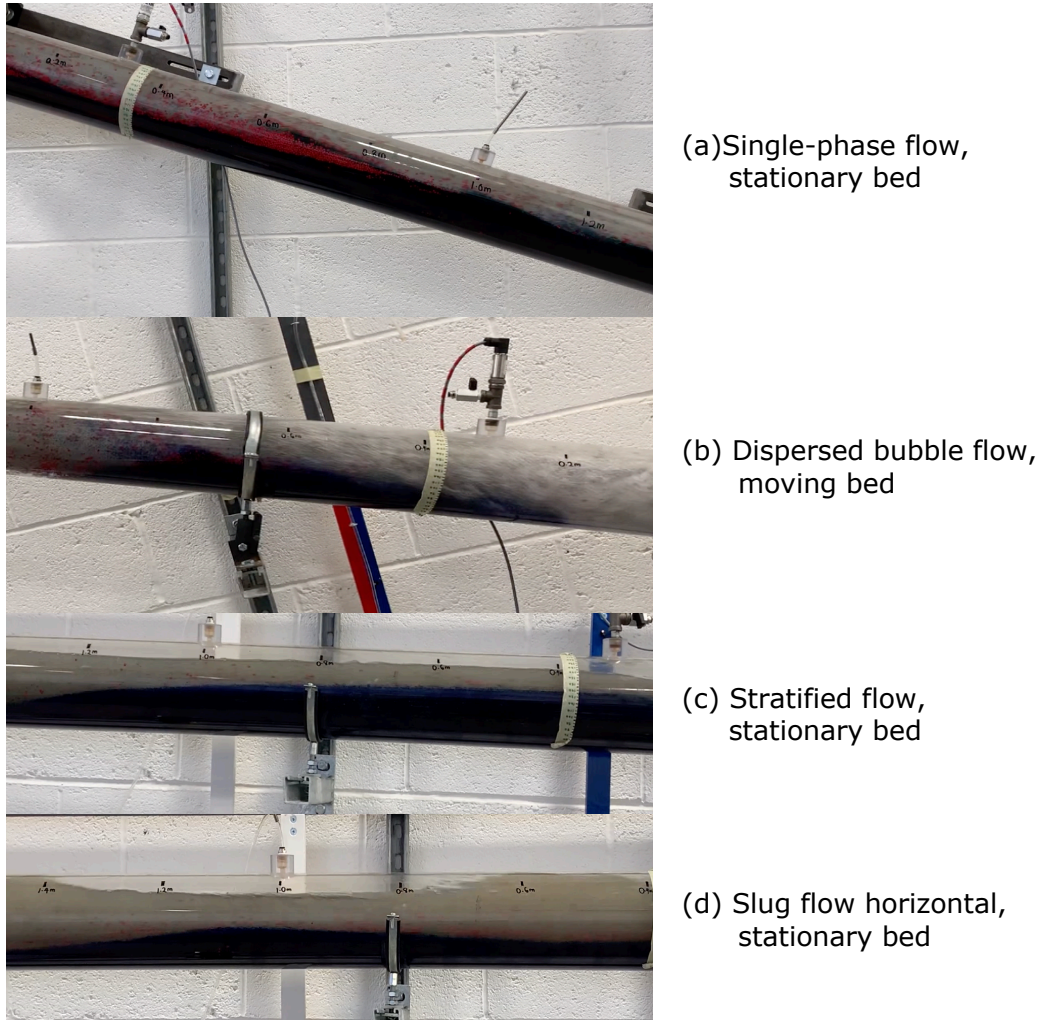


Figure 7.33: Examples of different cutting transport mechanisms and fluid flow patterns

The suspension, moving bed and the stationary bed particle transport mechanism can exist either individually or simultaneously in the annuli irrespective of the fluid flow pattern. However, the particle vertical concentration is highly dependent on the fluid flow pattern. Figure 7.33 shows some of examples of the fluid flow pattern and particle transport configuration experimental investigated in this study. The output of this study is to validate the cuttings transport models developed in chapter 5.

In the development of the multi-layered cutting transport model for the stratified and slug flow pattern, a theory was formulated based on the idea that the cuttings were only entrained in the liquid phase for the stratified flow and for the slug flow, the cuttings were only entrained in the liquid phase of the liquid film/gas pocket region and the slug body region of the entire slug unit. This proposed concept was validated by introducing particles into the two-phase annuli fluid flow under the slug flow pattern conditions and recording the collective movement of the particles in the flowing stream.

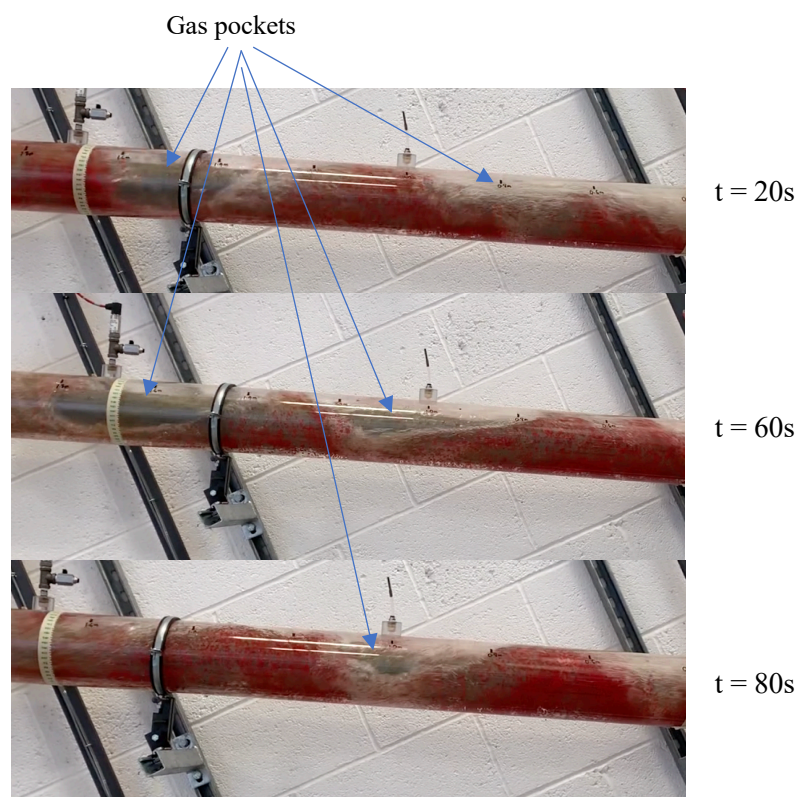


Figure 7.34: Particle transport dynamics with time in the slug flow pattern(Particle1: 3-4mm, 950Kg/m<sup>3</sup>)

Figure 7.34 validates the theory that at all times the particles are only traveling in the liquid phase of the liquid film/gas pocket region and the slug body and as shown in the figure, there is no particle entrained in the gas pocket due to significant density differences and the particles in the liquid film are accelerated with the liquid film to the slug body region. Figure 7.33c and Figure 7.33d also show that for the stratified and slug flow in the horizontal annuli, the particles are

only entrained in the liquid phase and the particle concentration in the gas phase/gas pocket region is zero.

#### 7.4.1 Cutting transport model validation

The model predicted stationary bed height was compared to the measured stationary bed height data from the experimental tests involving the flow of single-phase and two-phase fluids with solid particles in the annuli. and presents the results which show a good agreement between the predicted and measured stationary bed height with a maximum error of about  $\pm 16\%$ .

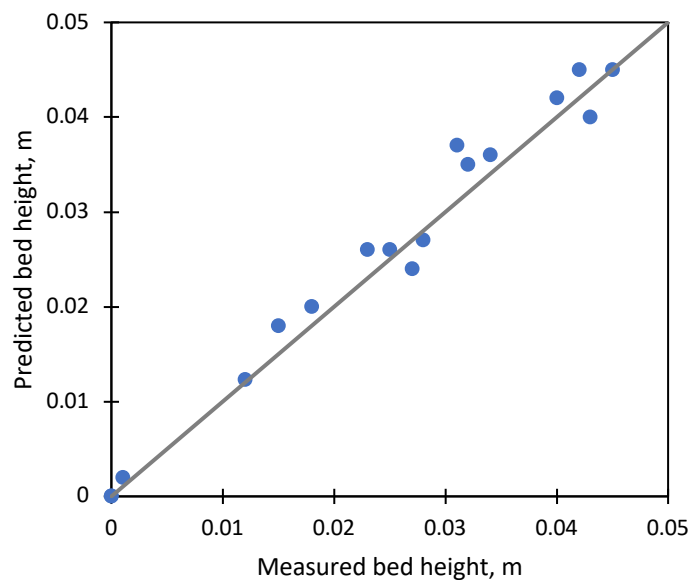


Figure 7.35: Stationary bed height model performance for the annuli flow of water and water and air

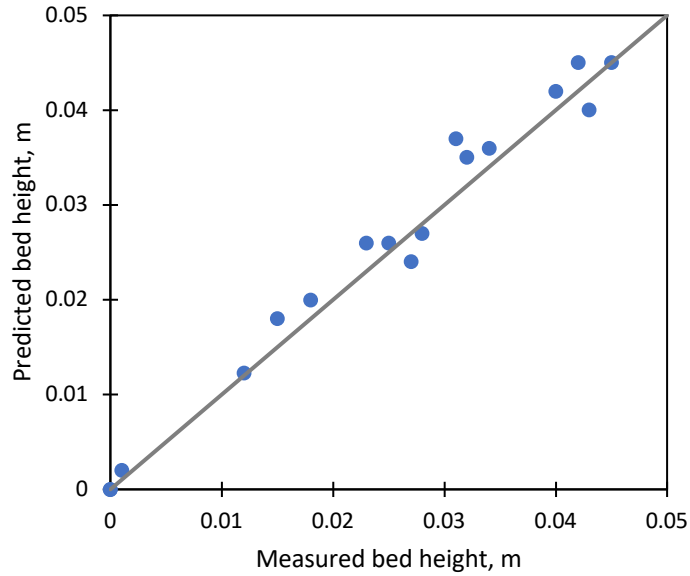


Figure 7.36: Stationary bed height model performance for the annuli flow of polymer(0.5% XG) and polymer and air

The comparison of the pressure gradient obtained from the experimental tests and the pressure gradient calculated from the multi-layered cutting transport model for all the investigated flow patterns and the different particle transport mechanisms in both the concentric and eccentric annuli are presented in Figure 7.37 to Figure 7.39

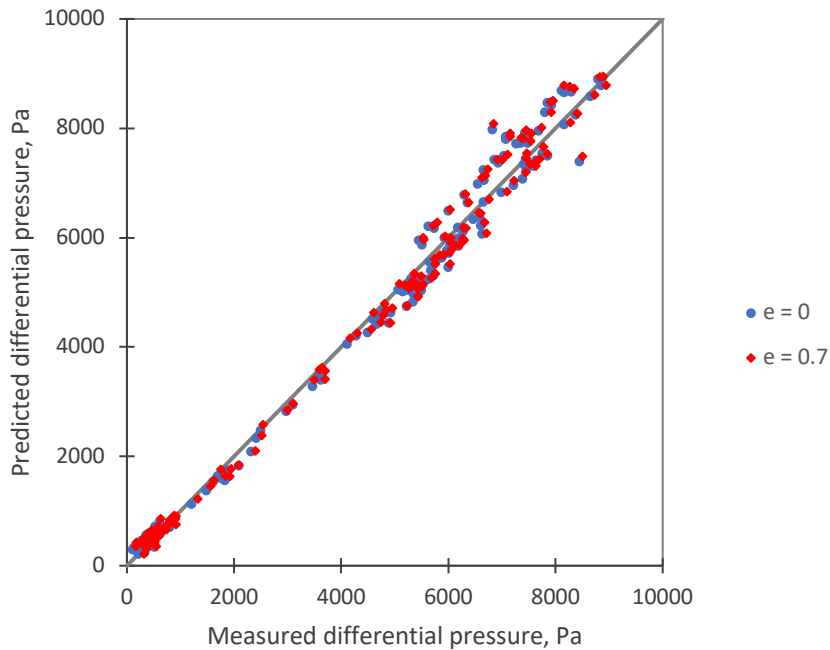


Figure 7.37: Model performance for the annuli differential pressure with the particles in the suspension mechanism (Particle1: 3-4mm, 950Kg/m<sup>3</sup>)

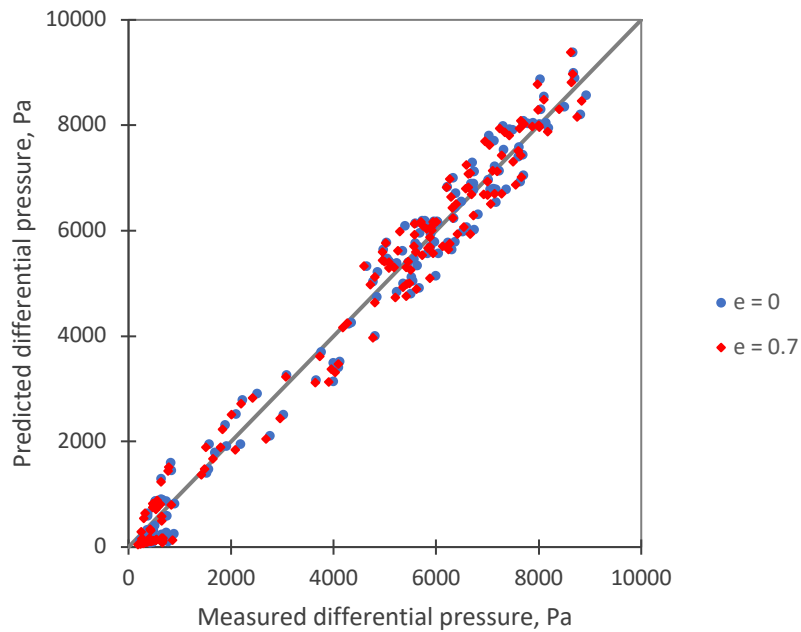


Figure 7.38: Model performance for the annuli differential pressure with the particles in the suspension, moving bed and stationary bed mechanism (Particle3: 2.5-3.7mm, 2100Kg/m<sup>3</sup>)

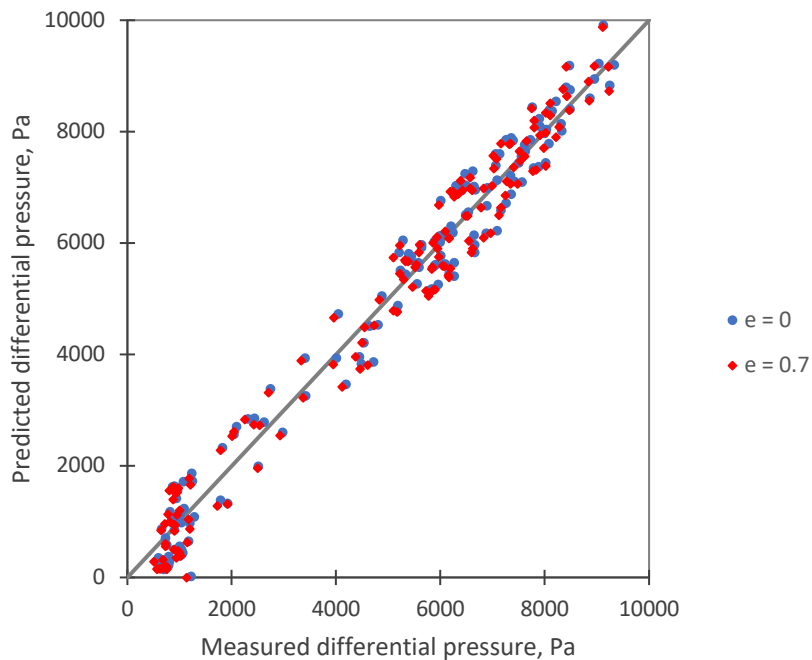


Figure 7.39: Model performance of the total pressure gradient with the particles in the suspension and moving bed mechanism (Particle3: 1.25-1.65mm, 2000Kg/m<sup>3</sup>)

From the plots showing the comparison of the predicted pressure gradient to the measured pressure gradient it can be concluded that the experimental results validate the developed cutting transport multi-layered model. The maximum error margin is about  $\pm 22\%$  with the results for the suspension mechanism showing the least error of about  $\pm 10\%$  and a very low standard deviation.

## Chapter 8

### Conclusions and recommendations

#### 8.1 Conclusions

Effective cuttings transport and accurate drilling hydraulics prediction are issues of concern during drilling operations of horizontal, extended reach and multilateral wells. Unlike the conventional drilling approach, underbalanced drilling operations which allows the flow of multiphase fluids through the wellbore annuli adds more complexity to the system due to the highly transient nature, relatively unpredictable flow dynamics and the need for wellbore fluid control for bottom hole pressure management. The flow of both Newtonian and non-Newtonian, single-phase and two-phase fluids with or without solid particles through the annuli have been studied theoretically, numerically and experimentally. This was done in order to investigate the effect of some of the major or important drilling parameters on the flow hydraulics and cuttings transport mechanism in horizontal and inclined concentric or eccentric wellbore annuli. For this purpose, an experimental unit was designed and constructed at RGU to perform extensive experiments and data acquisition for conditions at various particle concentrations, inner pipe rotary speed, different inclination angles and gas-liquid flowrates. Several mathematical models were developed to enable the accurate determination of the friction factor for both Newtonian and non-Newtonian flow in the concentric and eccentric annulus. Additionally, a numerical CFD technique was applied to discretise the governing equations of motion and obtain numerical data that was favourably compared to the theoretically developed friction factor model. New flow pattern dependent mechanistic models that can be applied to perform predictive wellbore hydraulics calculations were developed and new flow pattern dependent multi-layered cutting transport along with minimum transport velocity models were also developed and validated with experimental data. These models can be applied in the field for a wellbore of any level of eccentricity to determine the pressure gradient during drilling operations, evaluate cuttings transport performance, determine the stationary bed size and establish the required threshold that ensures that the wellbore is maintained at the optimum pressure and the drilled cuttings are transported effectively out of the wellbore. The following are the main conclusions drawn from this study:

1. The friction geometry parameter and consequent friction factor for the flow of non-Newtonian shear thinning fluids through the annuli is significantly dependent on the level of eccentricity, annuli pipe diameter ratio, the rheological properties of the fluid, inner pipe rotary speed and flowrate of the fluid. For this reason, the friction geometry parameter equations developed for Newtonian annuli flow cannot be used to determine the friction factor for drilling fluid flow in wellbores. A friction geometry parameter, equation validated with numerical and experimental data has been proposed in this study (Chapter 4) to determine the friction factor for generalised fluid flows in a concentric and eccentric annulus with and without drillpipe rotation.
2. The use of numerical computational fluid dynamics CFD techniques to map the wellbore annuli and discretise the fundamental governing fluid flow equations was proved to be reliable. This approach was used in this study to obtain velocity fields in the concentric and eccentric annuli, investigate the effect of inner pipe rotation on the distribution of the velocity fields and the pressure gradient. The data obtained from the numerical study was compared to the theoretical study in order to validate the mathematical models, showing good agreement in a range of  $\pm 5\%$ . The CFD approach established in this study can be applied used to obtain detailed information of the flow fields in the concentric and eccentric annuli where experimental work is not feasible.
3. The impact of the drillpipe rotation on the velocity fields in the annuli is dependent on the level of eccentricity of the wellbore. While there is no significant influence of pipe rotation on the velocity fields in the concentric annuli, the rotation of the drillpipe in the eccentric annuli leads to a redistribution of the velocity fields and the improvement of flow in the region of relatively lower or no flow. Thus, the rotation of the drillpipe may be favourable for improving the flow in the bottom region of the wellbore annulus and thereby improving the cuttings transport efficiency while drilling.

4. When the flowrate is kept constant and the flow is fully developed, the increase in the drillpipe rotation has little or no impact on the pressure gradient for the flow of shear thinning non-Newtonian fluids in the concentric annulus. However, for the eccentric annulus, the increase in drillpipe rotation leads to a decrease in the pressure gradient and the rate at which this occurs is dependent on the rheological properties of the fluid. The effect of pipe rotation on the frictional pressure losses diminishes with an increase in the fluid flowrate and after a certain pipe rotation speed, the effect of the pipe rotation on the pressure gradient becomes negligible.
  
5. Although the fluid flowrate is the most important parameter that influences the transport of cuttings in the annuli, unlike the conventional drilling operations, the optimum flowrate to ensure that the cuttings are effectively transported in the wellbore with underbalance drilling conditions is highly dependent on the prevailing flow pattern existing in the wellbore annuli. To ensure effective hole cleaning for UBD operations, the minimum fluid circulation rate or transport velocity must be determined according to the wellbore gas-liquid fluid properties and the flow pattern.
  
6. Under the flow conditions investigated for two-phase horizontal and inclined flow, numerical and experimental study proved that the rotation of the drillpipe within the range of 0-150rpm did not influence the transition of the gas-liquid flow pattern in the flow. The flow pattern formed in the annuli is mainly a function of the gas-liquid properties and the in-situ flowrate of each of the phases. Thus, when performing predictive wellbore hydraulics calculations, the impact of the pipe rotation(0-150rpm) on the gas-liquid flow pattern transition can be neglected.
  
7. The wellbore inclination has a strong influence on the pressure gradient and cutting transport efficiency for annuli flows. Unlike the single-phase flows, the change in the inclination angle can lead to a change in the gas-liquid fluid distribution and the fluid flow pattern for two-phase flows. This means that apart from the gravitational effects, the inclination angle has a huge effect on

the pressure gradient for two-phase flow because the pressure gradient is strongly dependent on the flow pattern and the in-situ mixture properties of the fluids. For instance, for the slug flow pattern at the same gas-liquid input flowrates, the liquid film length for horizontal flow is always larger than that of the upward inclined flow. Although it has been established that the effect of the wellbore inclination angle on cutting transport is dependent on the cutting transport mechanism, the change in the annuli fluid distribution and possible change in the flow pattern influences the cuttings transport efficiency. Under the range of conditions investigated, the optimum flowrate or minimum transport velocity required to transport the cuttings in suspension or as a moving bed increases with an increase in inclination angle for both single-phase and two-phase flows. However, it was also observed that the effect of the inclination angle on cuttings transport for two-phase flow is higher than that of the single-phase flow.

8. The fluid viscosity plays an important role in the effective transportation of cuttings for both conventional and underbalanced drilling operations. The higher the viscosity of the fluid, the lower the tendency for the formation of a stationary bed at the bottom of the wellbore annuli. Once a stationary bed has been formed in the annuli, the lighter fluid or two-phase fluid mixtures has a more advantage in the clearing of the stationary bed than the heavier fluid in the horizontal annulus. However, in the upward inclined annulus, the heavier fluids have more advantage than the lighter fluids.
  
9. Pipe rotation has little or no influence on the cutting transport for both the single-phase and two-phase flows in the horizontal concentric annuli. However, in the inclined concentric annuli, pipe rotation can improve the cuttings transport for single-phase annuli flows. For the eccentric horizontal and inclined annuli, an increase in the pipe rotation speed can significantly improve the cutting transport efficiency for both the single-phase and two-phase flows. However, in terms of improving the cuttings transport efficiency, the influence of the pipe rotation on the single-phase non-Newtonian fluids at relatively

lower flowrates is a lot more significant than that of the single-phase Newtonian and two-phase flows in both the horizontal and inclined orientations.

10. In general, for the single-phase and two-phase fluids, the critical circulation rate or the minimum transport velocity required to transport the cuttings in the eccentric annulus is always higher than that which is required for the facilitation of cutting movement in the concentric annulus.

11. When a stationary bed is formed in the annuli, the pressure gradient is increased due to the reduced area of the flow. For this reason, if an increase in the pipe rotation speed reduces the thickness of the stationary bed, it will correspondingly lead to a decrease in the annuli pressure gradient.

12. Generally, when operating at UBD conditions, unlike the conventional drilling, the influence of the important drilling parameters on the wellbore hydraulics and cutting transport efficiency are largely dependent on the gas-liquid flow pattern. Thus, for UBD operations, it is important to track the flow pattern throughout the length of the wellbore and perform wellbore predictive or real-time calculations as a function of the local fluid flow pattern in the annuli.

13. New flow pattern dependent wellbore hydraulics and cutting transport mechanistic models have been developed with a novel approach and proposed for the carrying out predictive and real-time calculations for underbalanced drilling operations in a wellbore annulus with any level of eccentricity and with or without drillpipe rotation. New flow pattern dependent wellbore hydraulics and multi-layered cutting transport model has been developed with a maximum error of  $\pm 12\%$  when compared to experimental data. These models can be used to determine the wellbore pressure profile and evaluate the cutting transport efficiency during drilling or at the designing phase of a project to help

save costs, mitigate the issues of wellbore instability and prevent non-productive time.

## **8.2 Contribution to knowledge**

The outcome of this study presents the following contributions to existing knowledge:

1. In order to determine the frictional pressure loss in a wellbore annulus, it is important that the method for the calculation of the friction factor takes into account the rheological properties of the drilling fluid. While previous researchers have used methods derived solely for the Newtonian annuli flow of fluids, this study has shown that these methods are largely inaccurate when applied to shear thinning non-Newtonian drilling fluids. Apart from the rheological properties of the fluid, the friction factor for non-Newtonian annuli flows are also dependent on the pipe diameter ratio, level of eccentricity, drillpipe rotary speed and the circulation rate of the drilling fluid. Thus, all these factors must be taken into account when selecting a method to determine the frictional pressure loss in a wellbore annulus. In this study a new method has been proposed and several analytical and mechanistic equations have been developed for the accurate determination of the friction geometry parameter and factor for laminar and turbulent annuli flows. These equations are valid for fluids with Newtonian, Power law, Bingham plastic and Herschel-Bulkley rheological properties.
2. This research presents a novel approach for the determination of the liquid area and liquid height in the annuli with any level of eccentricity, which is important and required for the performing the hydraulics or cutting transport calculations involving the stratified and slug flow pattern. The equation developed for this purpose can also be applied for the determination of the stationary bed thickness/height in the annuli for any level of eccentricity. This

is important because if the area or volume of fluid in the annulus is held constant, a change in eccentricity may lead to a change in the liquid height depending on the initial height of the liquid in the annulus. It is required that this phenomenon is taken into account when determining either the liquid area or the stationary bed height, especially when performing a multi-layered flow modelling.

3. While the methods applied to perform wellbore hydraulics and cutting transport calculations for underbalanced drilling UBD conditions have neglected the effect of the gas-liquid flow pattern, this research showed the importance of the gas-liquid flow pattern by shedding light on the effect of the gas-liquid flow pattern on wellbore hydraulics and how it can influence the important drilling parameters to either the benefit or detriment of the cutting transport efficiency. Taking the gas-liquid flow pattern into consideration goes a long way in preventing wellbore instability issues during UBD operations.
4. New flow pattern dependent models have been developed and presented in this study for the calculation of the pressure gradient for underbalanced drilling UBD operations in wellbores of any level of eccentricity and with or without drillpipe rotation. As the flow pattern is an important factor to be considered when performing UBD calculations, these proposed mathematical hydraulic models have been tested with experimental data obtained from tests with several flow patterns and proved to be reliable for performing flow pattern dependent calculations.
5. When a detailed solution of the annuli fluid flow fields is required, the computational fluid dynamics CFD approach offers a great advantage. This offers the benefit of generating useful numerical results that are not feasible to obtain from physical experiments. For a detailed wellbore hydraulics and cutting transport modelling, the annuli velocity fields, pressure fields and fields

of other material properties of the flow may be required which brings the need for a CFD technique. In this study, a method for the solution for fluid flow through the annuli was developed by discretising the governing equations for fluid flow in both the cylindrical and cartesian co-ordinate system, developing a new method in which the wellbore geometry can be generated and meshed and providing detailed information on how both single-phase and two-phase flow CFD simulations can be accomplished. The method formulated can be applied for both Newtonian and non-Newtonian annuli flow at level of eccentricity and also takes into account the drillpipe rotation speed. This provides CFD method that can be applied to perform numerical simulations in other to investigate the effect of the important drilling parameters on the wellbore hydraulics and cutting transport efficiency.

6. The different cutting transport mechanisms and the fluid flow pattern have not till date been considered simultaneously when performing the two or three-layered cutting transport modelling for annuli flows. Due to the importance of the flow pattern for cutting transport modelling, several mechanistic flow pattern dependent multi-layered models were developed for calculations involving fluid flows in underbalanced drilling operations in wellbores of any level of eccentricity any fluid rheology and with or without inner pipe rotation. This came along with formulation of a systematic technique in which the wellbore annulus is divided into the required number of layers and the formulation of new equations for the calculation of the wetted perimeters of each of the layers as well as the interface between each of the layers or fluids. This is a novel concept which can be applied to evaluate the sensitivity of the major drilling parameters on wellbore hydraulics, thereby saving costs and mitigating wellbore instability issues.
7. A significant deliverable in this research was the design and construction of an experimental rig that replicates the fluid-cuttings flow dynamics of either the conventional or underbalanced drilling process. Data acquisition systems was installed on the rig to enable the systematic collection of real-time information from the experimental test in other to validate the empirical and mechanistic models developed in this study.

### **8.3 Recommendations**

The following are the recommendations for future research:

1. The wellbore inclination angle is one of the key parameters that influence the cutting transport efficiency. Previous researchers that investigated the effect of the wellbore angle on cutting transport using single-phase fluids concluded that while the minimum transport velocity required to transport the cuttings in suspension increased with an increase in the wellbore angle, the minimum transport velocity required to transport the cuttings as moving bed increased with an increase in angle until a certain angle is reached after which the minimum transport velocity for the moving bed decreases. In this study, from experiments conducted using the two-phase fluids, it was observed that the minimum transport velocity for both the suspension and moving bed mechanism increased with an increase in inclination angle. However, the range of the angles considered were between 0 to 30° within the pipe axis and the horizontal. It would be interesting to perform more two-phase flow experiments using a wider range of inclination angles to establish the angle at which the minimum transport velocity for the moving bed climaxes as this is dependent on the fluid flow pattern.
2. In this study, the effect of the drillpipe rotation on the pressure gradient and particle transport was investigated for both single phase and two-phase fluids in both the horizontal and inclined annuli. There are cases where during drilling, the drillpipe rotates in an orbital manner instead of rotating about its axis. It is obvious that the effect of the orbital motion of the drillpipe on the pressure losses and cutting transport would be different to that of the rotational motion. The performance of numerical CFD simulations to imitate this process is highly complex and may in many cases generate unrealistic solutions if not set-up properly. The experimental rig setup developed in this study can be modified in a manner that allows the inner pipe rotate in an orbital manner, to investigate the key differences from the results obtained from the rotational motion of the inner pipe.

## References

- Ahmed, R. & Miska, S., 2008. Experimental study and modeling of yield power-law flow in annuli with drillpipe rotation. *SPE/IADC 112604*.
- Akhshik, S., Behzad, M. & Rajabi, M., 2015. CFD-DEM approach to investigate the effect of drillpipe rotation on cuttings transport behavior. *J. Pet. Sci. Eng*, Volume 127, pp. 229-244.
- Ansari, A., Sylvester, N., Shoham, O. & Brill, J., 1990. A comprehensive mechanistic model for two-phase flow in wellbores. *SPE-20630-MS*.
- Asheim, H., 1986. MONA, An Accurate Two-Phase Well Flow Model Based on Phase Slippage. *SPEPE*, Issue 221.
- Aziz, K., Govier, G. & Fogarasi, M., 1972. Pressure Drop in Wells Producing Oil and Gas. *J. Cdn. Pet. Tech*, Issue 38.
- Baojiang, S., 2016. *Multiphase Flow in Oil and Gas Well Drilling*. s.l.:John Wiley & Sons Singapore.
- Barnea, D., 1987. A unified model for predicting flow-pattern transitions for the whole range of pipe inclinations. *Int. J. Multiphase Flow*, 13(1), pp. 1-12.
- Barnea, D., Shoham, O. & Taitel, Y., 1980. Flow pattern characterisation in two phase flow by electrical conductance probe. *Int. J. Multiphase Flow*, Issue 6, pp. 387-397.
- Barnea, D., Shoham, O., Taitel, Y. & Duckler, A., 1980. Flow pattern transitions for gas-liquid flow in horizontal and inclined pipes, comparison of experimental data with theory. *Int. J. Multiphase Flow*, Volume 6, pp. 217-225.
- Baxendell, P. & Thomas, R., 1961. The Calculation of Pressure Gradients in High-Rate Flowing Wells. *JPT Trans AIME*, Volume 222.
- Beggs, H. D. & Brill, J. P., 1973. A study of two-phase flow in inclined pipes. *JPT(May 1973) 607; Trans., AIM*, 255.
- Bennion, D., Thomas, F., Bietz, R. & Bennion, D., 1996. Underbalanced drilling: Praises and perils. *SPE 35242 presented at the Permian Basin Oil and Gas Recovery Conference held in Midland, Texas*.
- Bernard, D. & Walter, N., 1959. Helical flow of general fluids. *Journal of Applied Physics*, 30(10).
- Bicalho, I., dos Santos, D., Ataide, C. & Duarte, C., 2016. Fluid-dynamic behavior of flow in partially obstructed concentric and eccentric annuli with orbital motion. *J. Pet. Sci. Eng*, Issue 137, pp. 203-213.
- Bilgesu, H., Ali, M., Aminian, K. & Ameri, S., 2002. Computational fluid dynamics (CFD) as a tool to study cutting transport. *SPE 78716*.
- Bird, R., Stewart, W. & Lightfoot, E., 1976. Transport phenomena. *John Wileys and Sons*.
- Bird, R., Stewart, W. & Lightfoot, E., 2002. *Transport phenomena*. 2nd Edition ed. New York: John Wiley & Sons, Inc.
- Brill, P. & Mukherjee, H., 1999. *Multiphase flow in wells*. Texas : SPE.
- Caetano, E., Shoham, O. & Brill, J., 1992. Upward vertical two-phase flow through an annulus- Part I: single-phase friction factor, Taylor bubble rise velocity, and flow pattern prediction. *J. Energy Res. Tech.*, Volume 114, p. 1.
- Caetano, E., Shoham, O. & Brill, J., 1992. Upward vertical two-phase flow through an annulus-part II: Modeling bubble, slug and annular flow. *J. Energy Res. Tech.*, Volume 114, pp. 14-30.
- Cayeux, E. et al., 2014. Real-time evaluation of hole-cleaning conditions with a transient cuttings-transport model. *SPE Drilling & Completion*, pp. 5-21.

Chierici, G., Ciucci, G. & Sclocchi, G., 1974. Two-Phase Vertical Flow in Oil Wells- Prediction of Pressure Drop. *JPT; Trans. AIME.* , Issue 257.

Cho, H., Shah, S. N. & Osisanya, S. O., 2001. Effects of fluid flow in a porous cuttings-bed on cuttings transport efficiency and hydraulics. *SPE Annual Technical Conference and Exhibition. SPE 71374.*

Cho, H., Shah, S. N. & Osisanya, S. O., 2002. A three-segment hydraulic model for cuttings transport in coiled tubing horizontal and deviated drilling. *JCPT*, 41(6), pp. 32-39.

Clark, R. & Bickham, K., 1994. A mechanistic model for cuttings transport. *SPE 28306*, pp. 139-153.

Costa, S., Stuckenbruck, S., Sergio, A. & Martins, A., 2008. Simulation of transient cuttings transportation and ECD in wellbore drilling. *SPE 113893.*

Diaz, H., Miska, S., Takach, N. & Yu, M., 2004. Modeling of ECD in casing drilling operations and comparison with experimental and field data. *IADC/SPE 87149.*

Doan, Q. et al., 2000. Modelling of transient cuttings transport in underbalanced drilling. *IADC/SPE 62742.*

Duan, M. et al., 2008. Experimental study and modeling of cuttings transport using foam with drillpipe rotation. *SPE 116300.*

Duan, M. et al., 2006. Transport of small cuttings in extended reach drilling. *SPE 104192.*

Duckler, A. & Hubbard, M., 1975. A model for gas-liquid slug flow in horizontal and near horizontal tubes. *Ind. Eng. Chem. Fundam*, 14(no.4), pp. 337-347.

Duns, H. J. & Ros, N., 1963. Vertical Flow of Gas and Liquid Mixtures in Wells. *Proc., Sixth World Pet. Cong., Tokyo*, Issue 451.

Erge, O. & Van Oort, E., 2020. Modeling cuttings transport and annular pack-off using local fluid velocities with the effects of drillstring rotation and eccentricity. *IADC/SPE-199587-MS.*

Ettehad, R. & Ozbayoglu, M., 2013. Three phase flow characteristics in inclined eccentric annuli. *SPE/IADC.*

Fancher, G. J. & Brown, K., 1963. Prediction of Pressure Gradients for Multiphase Flow in Tubing. *SPEJ Trans., AIME*, Volume 228.

Ford, J. et al., 1990. Experimental investigation of drilled cuttings transport in inclined boreholes. *SPE Annual Technical Conference and Exhibition. SPE-20421.*

Fredrickson, A. & Bird, R., 1958. Non-Newtonian flow in annuli. *Indus. Eng. Chem*, 50(3), pp. 347-352.

Gao, E. & Young, A., 1995. Hole cleaning in extended reach wells: Field experience and theoretical analysis using a psuedo-oil (acetal) based mud. *SPE/IADC 29425*, pp. 793-808.

Gavignet, A. & Sobey, I., 1989. Model aids cuttings transport prediction. *J. Petrol. Tech*, Issue 41, pp. 916-921.

Gul, S., Kuru, E. & Parlaktuna, M., 2017. Experimental investigation of cuttings transport in horizontal wells using aerated drilling fluids. *International Petroleum Exhibition and Conference. SPE-188901-MS.*

Gunn, D. & Darling, C., 1963. Fluid flow and energy losses in non-circular conduits. *Transactions of the Institution of Chemical Engineers*, Volume 41, pp. 163-173.

Guo, B., Lyons, W. & Ghalmbor A., 2007. *Petroleum production engineering*. s.l.:Elsevier Science and technology books.

Haciislamoglu, M. & Langlinais, J., 1990. Non-Newtonian flow in eccentric annuli. *J. Energy Resour. Technol*, Issue 112, p. 163.

Hagedorn, A. & Brown, K., 1965. Experimental Study of Pressure Gradients Occurring During Continuous Two-Phase Flow in Small-Diameter Vertical Conduits. *JPT Trans., AIME*, Volume 475.

Hajipour, M., 2020. CFD simulation of turbulent flow of drill cuttings and parametric studies in a horizontal annulus. *SN Applied Sciences*, Volume 2.

Hasan, A. & Kabir, C., 1988. A study of multiphase flow behaviour in vertical wells. *SPEPE 263; Trans, AIME, 285*.

Ibarra, R., Nossen, J. & Tutkun, M., 2019. Two-phase flow in concentric and eccentric annuli. Part II: Model development, flow regime transition algorithm and pressure gradient. *Chemical Engineering Science 203*, pp. 501-510.

Ibarra, R., Nossen, J. & Tutkun, M., 2019. Two-phase gas-liquid flow in concentric and fully eccentric annuli. Part I: Flow patterns, holdup, slip ratio and pressure gradient. *Chemical Engineering Science*, pp. 489-500.

Iyoho, A. & Azar, J., 1981. An accurate slot-flow model for non-Newtonian fluid flow through eccentric annuli. *SPEJ*, pp. 565-572.

Kamp, A. & Rivero, M., 1999. Layer modeling for cuttings transport in highly inclined wellbores. *SPE Latin American and Caribbean Petroleum Engineering Conference. SPE-53942*.

Kelessidis, V. & Dukler, A., 1988. Modeling flow pattern transitions for upward gas-liquid flow in vertical concentric and eccentric annuli. *Int. J. Multiphase Flow*, 15(2), pp. 173-191.

Kelessidis, V., Maglione, R., Tsamantaki, C. & Aspirtakis, Y., 2006. Optimal determination of rheological parameters for Herschel-Bulkley drilling fluids and impact on pressure drop, velocity profiles and penetration rates during drilling. *J. Pet. Sci. Eng*, Issue 53, pp. 203-224.

Kelin, W. et al., 2013. Review and analysis of cuttings transport in complex structural wells. *The Open Fuels & Energy Sci. J*, Volume 6, pp. 9-17.

Lage, A., Rommetveit, R. & Time, R., 2000. An experimental and theoretical study of two-phase flow in horizontal or slightly deviated fully eccentric annuli. *IADC/SPE Asia Pacific Drilling Technology. SPE-62793-MS*.

Lage, C. A. & Time, W. R., 2002. An experimental and theoretical investigation of upward two-phase flow in annuli. *SPEJ*, pp. 325-336.

Li, M. et al., 2010. Simulation on the effect of drillstring rotation on hole cleaning for extended reach well. *West-China Explor. Eng.*, Volume 5, pp. 51-54.

Li, Y., Bjorndalen, N. & Kuru, E., 2007. Numerical modelling of cuttings transport in horizontal wells using conventional drilling fluids. *JCPT*, Volume 46, pp. 9-15.

Li, Y. & Kuru, E., 2005. Numerical modelling of cuttings transport with foam in vertical wells. *JCPT*, 44(3), pp. 31-39.

Lockhart, R. W. & Martinelli, R. C., 1949. *Proposed Correlation of Data for Isothermal Two-Phase, Two-Component Flow in Pipes*. s.l.:Chemical Engineering Progress, 45, 38-48..

Luo, Y., 1988. Non-Newtonian annular flow and cuttings transport through drilling annuli at various angles. *PhD thesis, Heriot-Watt University*.

Luo, Y. & Penden, J., 1987. Flow of drilling fluids through eccentric annuli. *Annual Technical Conference and Exhibition. SPE-16692*.

Luo, Y. & Penden, J., 1990. Flow of non-Newtonian fluids through eccentric annuli. *SPE Annual Technical Conference and Exhibition. SPEPE*, pp. 91-96.

Luo, Y. & Penden, J., 1990. Reduction of the annular friction pressure drop caused by drillpipe rotation. *SPE 20305*.

Masuda, Y. et al., 2000. Critical cuttings transport velocity in inclined annulus: Experimental studies and numerical simulation. *SPE/Petroleum Society of CIM 65502*.

Metzner, A. & Reed, J., 1955. Flow of non-Newtonian fluids- correlation of the laminar, transition, and turbulent-flow regions. *AICHE J*, 4(1), pp. 434-440.

Mousavi, H. et al., 2008. Modeling of three-phase flow in the annuli during UBD operations. *SPE* 112679.

Mukherjee, H. & Brill, J., 1985. Pressure drop correlations for inclined two-phase flow. *J. Energy Res. Tech*, pp. 107,549.

Nossen, J. et al., 2017. An Experimental study of two-phase flow in horizontal and inclined annuli. *BHR Group 18 MPT*, pp. 87-102.

Okrajni, S. & Azar, J., 1986. The effects of mud rheology on annular hole cleaning in directional wells. *SPE Dril. Eng.*, Volume 4, pp. 297-308.

Omurlu, C. & Ozbayoglu, M., 2007. Two-phase fluid flow through eccentric horizontal annuli: A mechanistic approach. *SPE/ICoTA Coiled Tubing Conference and Exhibition. SPE-107076-MS*.

Ooms, G., Burgerscentrum, J. & Kampman-Reinhartz, B., 1999. Influence of drillpipe rotation and eccentricity on pressure drop over borehole during drilling. *SPE* 56638.

Orkiszewski, J., 1967. Predicting Two-Phase Pressure Drops in Vertical Pipes. *JPT; Trans., AIME.*, Issue 240.

Oyeneyin, B., 2015. *Integrated sand management for effective hydrocarbon flow assurance*. 1st ed. s.l.:Elsevier.

Ozbayoglu, E. & Miska, S., 2003. Cuttings transport with foam in horizontal and highly-inclined wellbores. *SPE/IADC Drilling Conference. SPE-79856-MS*.

Ozbayoglu, E., Saasen, A. & Sorgun, M., 2007. Estimating critical velocity to prevent bed development for horizontal-inclined wellbores. *SPE/IADC 108005*.

Ozbayoglu, E. & Sorgun, M., 2010. Frictional pressure loss estimation of non-Newtonian fluids in realistic annulus with pipe rotation. *JCPT*, Volume 49, pp. 57-64.

Pandya, S., Ahmed, R. & Shah, S., 2020. Wellbore cleanout in inclined and horizontal wellbores: The effects of flowrate, fluid rheology, and solids density. *SPE Drilling and Completion. SPE-194240-PA*, 35(01), pp. 48-68.

Payne, G., Palmer, C., Brill, J. & Beggs, H., 1979. Evaluation of inclined pipe two-phase liquid holdup and pressure loss correlations using experimental data. *J. Pet. Tech*, pp. 1198-1208.

Penden, J., Ford, J. & Oyeneyin, M., 1990. Comprehensive experimental investigation of drilled cuttings transport in inclined wells including the effects of rotation and eccentricity. *SPE-20925*, pp. 393-404.

Petalas, N. & Aziz, K., 2000. A mechanistic model for multiphase flow in pipes. *JCPT*, pp. 43-55.

Podryabinkin, E., Rudyak, V., May, R. & Gavrilov, A., 2013. Detailed modeling of drilling fluid flow in a wellbore annulus while drilling. *Canadian Eng. Tech. Inno*, Volume 1, pp. 27-36.

Poettmann, F. & Carpenter, P., 1952. The Multiphase Flow of Gas, Oil and Water Through Vertical Flow Strings with Application to the Design and Gas-Lift Installations. *Drill. & Prod. Prac*.

Sadatomi, M., Sato, Y. & Saruwatari, S., 1982. Two-phase flow in vertical noncircular channels. *Int. J. Multiph. Flow*, 8(6), pp. 641-655.

Sanchez, R., Azar, J., Bassal, A. & Martins, A., 1999. Effect of drillpipe rotation on hole cleaning during directional-well drilling. *SPEJ*, 4(2), pp. 101-108.

Sandra, C. D. S., Geraldine, J. & Guy, B., 2008. CFD modeling of all gas-liquid and vapor-liquid flow regimes predicted by the baker chart. *Chem. Eng. J*, Issue 138, pp. 349-357.

Shoham, O., 2005. *Mechanistic modelling of gas-liquid two-phase flow in pipes*. s.l.:SPE.

Sifferman, T. & Becker, T., 1992. Hole cleaning in full-scale inclined wellbores. *SPE Dril. Eng*, Volume 7, pp. 115-120.

Sunthakar, A., Miska, S. & Kuru, E., 2000. New developments in aerated mud hydraulics for horizontal well drilling. *SPE*.

Taitel, Y. & Barnea, D., 1990. Two-Phase Slug Flow. *Adv.Heat Transf.*, Volume 20, pp. 83-132.

Taitel, Y., Barnea, D. & Dukler, A., 1980. Modeling flow pattern transitions for steady upward gas-liquid flow in vertical tubes. *AIChE. J*, Issue 26, p. 345.

Taitel, Y. & Dukler, A., 1976. A model for predicting flow regime transitions in horizontal and near horizontal gas-liquid flow. *AIChE J.*, 22, no. 1, pp. 47-55.

Taitel, Y. & Dukler, A., 1986. Flow pattern transitions in gas-liquid systems. Measurements and modeling. *In Advances in Multiphase Flow*, Volume 2 (Edited by Zuber, N., Hewitt, G. F & Delhaye, J. M.).

Terry, H., 2015. Advances in the calculation of circulating pressure drop with and without drillpipe rotation. *SPE/IADC-173054-MS*.

Terry, H., 2015. Validation of drillpipe rotation hydraulics using drillpipe eccentricity as a key factor. *SPE-176451-MS*.

Uner, D., Ozgen, C. & Tosun, I., 1988. An approximate solution for non-Newtonian flow in eccentric annuli. *Ind. Eng. Chem. Res*, Issue 27, pp. 698-701.

Viera, N., Martins, A., Atiade, C. & Barrozo, M., 2014. The effect of the inner cylinder rotation on the fluid dynamics of non-Newtonian fluids in concentric and eccentric annuli. *B. J. Chem. Eng*, 31(4), pp. 829-838.

Walker, S. & Li, J., 2000. The effects of particle size, fluid rheology and pipe eccentricity on cuttings transport. *SPE 60755*.

Wallis, G., 1969. One-dimensional two-phase flow. pp. Newyork [u.a.]: McGraw-Hill.

Wang, Z. et al., 2010. Numerical simulation on three layer dynamic cutting transport model and its application on extended well drilling. *IADC/SPE 134306*.

Wei, N. et al., 2013. Cutting transport models and experimental visualization of underbalanced horizontal drilling. *Math. Prob. Eng*.

William, R., 1958. Friction factor for axial non-Newtonian annular flow. *IAEC*, 50(10).

Xiaofeng, S. et al., 2014. Effect of drillpipe rotation on cuttings transport using computational fluid dynamics (CFD) in complex structure wells. *J. Petrol. Explor. Prod. Technol*, Issue 4, pp. 255-261.

Xiao, J., Shoham, O. & Brill, J., 1990. A comprehensive mechanistic model for two-phase flow in pipelines. *SPE-20631-MS*.

Yibing, L. & Kuru, E., 2004. Prediction of critical foam velocity for effective cuttings transport in horizontal wells. *SPE/ICoTA 89324*.

Zhang, F. et al., 2020. Modeling of dynamic cuttings transportation during drilling of oil and gas wells by combining 2D CFD and 1D discretization approach. *SPE J*.

Zigrang, D. & Sylvester, N., 1982. Explicit approximations to the solution of Colebrook's friction factor equation. *AIChE*, 3(28), pp. 514-515.

## Appendix A: MATLAB code for the determination of the rheological parameters of fluids

The following function is a subroutine function to be called in main script. This function performs a non-linear regression analysis on the input data

```
function r1 = lin_Reg(a0)

% Performs linear regression on matrix input data and generates a column
vector of the following respectively:
% -Observations
% -Gradient
% -Intercept
% -R
% -R Square

T2 = a0;

[ii, jj] = find(isnan(T2)| isinf(T2));

T2(ii,:)=[];

n = size(T2,1);

%% Determine slope and intercept of the data
=====

no = mean(T2,1); % mean of x and y sample

A1 = T2(:,1) - no(1);

A2 = T2(:,2) - no(2);

A1_A2 = A1 .* A2;    A1x = A1.^2;    A2x = A2.^2;

A1_A2_s = sum(A1_A2);  A1x_s = sum(A1x);  A2x_s = sum(A2x);

rho = A1_A2_s/sqrt(A1x_s * A2x_s) ; % Pearson coefficient

Sy = sqrt(A2x_s/(n-1));

Sx = sqrt(A1x_s/(n-1));

m = rho * Sy/Sx; %Gradient of regression slope

c = no(2) - m*no(1);

%% Determine R and R^2 values =====

B1 = T2(:,1).^2; B2 = T2(:,2).^2;

Bx = T2(:,1) .* T2(:,2);
```

```

Bx1 = sum(T2(:,1)); Bx2 = sum(T2(:,2));

B1_s = sum(B1); B2_s = sum(B2); Bx_s = sum(Bx);

R = (n*Bx_s - Bx1*Bx2)/(sqrt(n*B1_s - Bx1^2) * sqrt(n*B2_s - Bx2^2));

Rs = R^2;

r1 = [n; m; c; R; Rs];

end

```

Prior to the use of this MATLAB program, the shear stress to shear rate data obtained from rheological measurements using a viscometer is saved in Microsoft Excel and ready to be called into the program for processing. The shear rate values are stored in the left column while the shear stress values are stored in the right column in Microsoft Excel. The main MATLAB script to be run to determine the rheological parameters of fluids from the shear stress to shear rate data is given below:

```

clear
clc

T = xlsread('Rheology2.xlsx');

n = size(T,1);

tmin = T(n,2); % minimum shear stress value

GR = (sqrt(5) - 1)/2;

lower_limit = 0.00; upper_limit = tmin; % initial guess of lower and
upper bound yield stress values.

es = 1e-4; % convergence criterion

ea = 1;

count = 0;

while ea>es

count = count + 1;

ty1 = lower_limit + GR*(upper_limit - lower_limit);

```

```

ty2 = upper_limit - GR*(upper_limit - lower_limit);
ty1 = round(ty1,4);    ty2 = round(ty2,4);

T1 = T; T1(:,2) = T1(:,2) - ty1;
T2 = T; T2(:,2) = T2(:,2) - ty2;
T1x = log10(T1); T2x = log10(T2);

a1 = lin_Reg(T1x); a2 = lin_Reg(T2x);
Rc1 = a1(5); Rc2 = a2(5);

%Compare error to tolerance and stop
% ea = 100 * abs(Rc2 - Rc1)/Rc2;
ea = 100 * abs(ty2 - ty1)/ty2;
ea(isnan(ea))=0;
if Rc1<Rc2, upper_limit = ty1;
elseif Rc1>Rc2, lower_limit = ty2;

end

end

ns = a1(1); m = a1(2); int = a1(3); R = a1(4); Rs = a1(5);
K = round(10^(int),3); yield = round(ty1,2);
m = round(m,2);

yx = 0:1:1200;
fx = yield + K.*yx.^m;

plot(yx,fx,'bo-','linewidth',0.01)
xlabel('Shear rate (s^-1)')
ylabel('Shear rate (Pa)')
grid on
hold on
shg

% Rheology characterisation
if m < 1 && m > 0 && yield == 0, Fluid_type = 'Powerlaw fluid';
elseif m<1 && m>0 && yield >0, Fluid_type = 'Herschel Bulkerly fluid';

```

```

elseif m == 1 && yield == 0, Fluid_type = 'Newtonian fluid';

elseif m==1 && yield>0, Fluid_type = 'Bingham plastic fluid';
else

    Fluid_type = 'Not found';

end

% Display of results

Result1 = ['Gradient : ',num2str(m)];
Result2 = ['Intercept : ',num2str(int)];
Result3 = ['R : ',num2str(R)];
Result4 = ['R Square : ',num2str(Rs)];
Result5 = ['Observations : ',num2str(ns)];

Result6 = sprintf ('Fluid rheology - %s',Fluid_type);
Result7 = ['Consistency K : ',num2str(K)];
Result8 = ['Power law index n : ',num2str(m)];
Result9 = ['Yield stress to : ',num2str(yield)];

disp('Regression Result Summary =====')
disp(Result1)
disp(Result2)
disp(Result3)
disp(Result4)
disp(Result5)
disp(' ')
disp('RHEOLOGY PARAMETERS =====')
disp('_____')
disp(Result6)
disp('_____')
disp(Result7)
disp('_____')
disp(Result8)
disp('_____')
disp(Result9)
disp('_____')

```

## Appendix B:



Figure B.1: Druck pressure calibrator

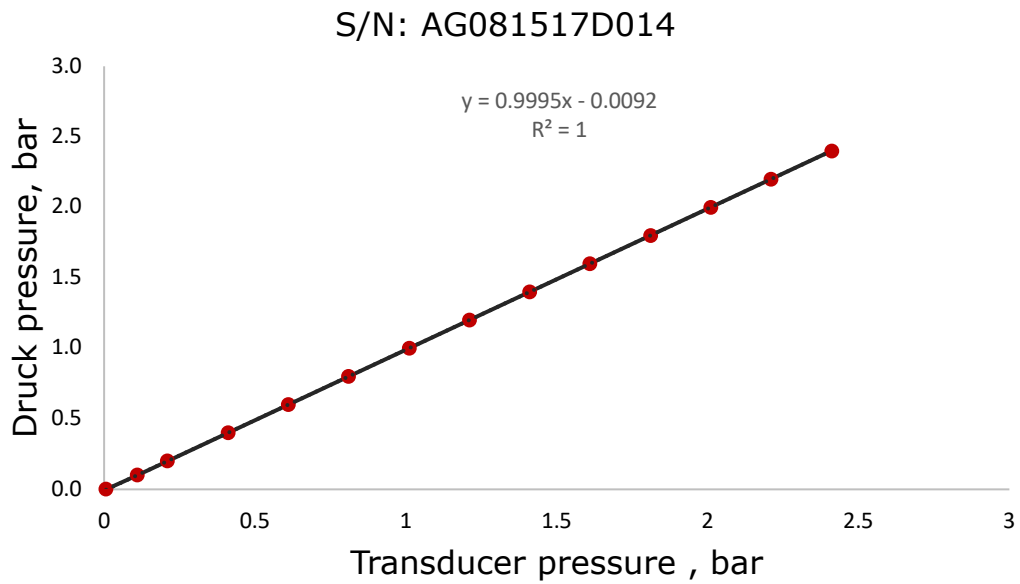


Figure B.2: Calibration of absolute pressure transducer No.1

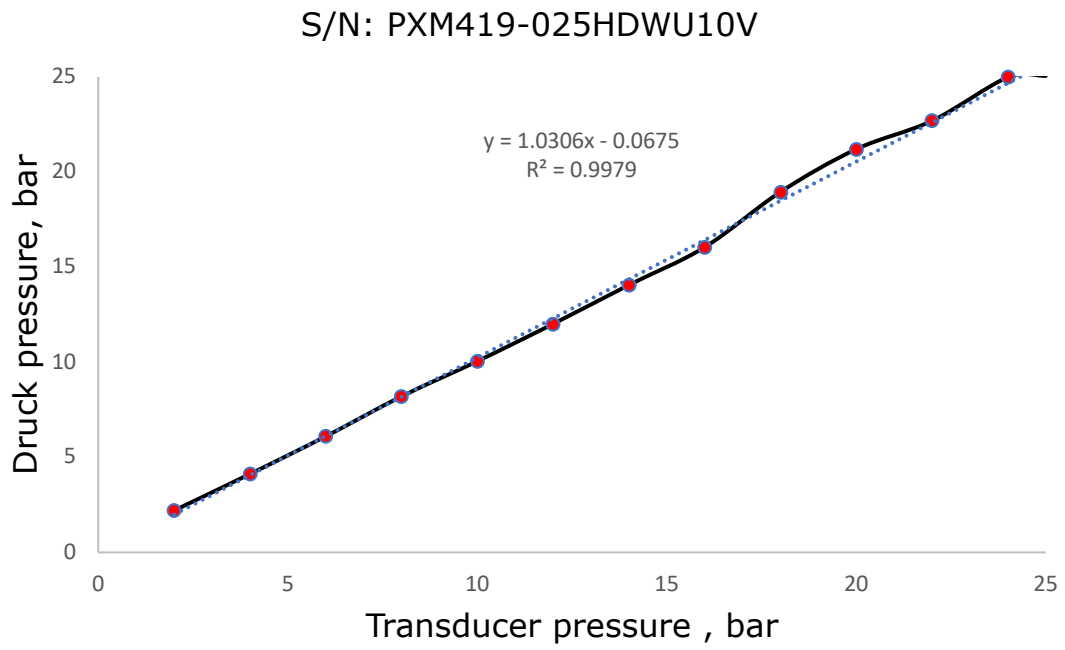


Figure B.3: Calibration of differential pressure transducer No.5

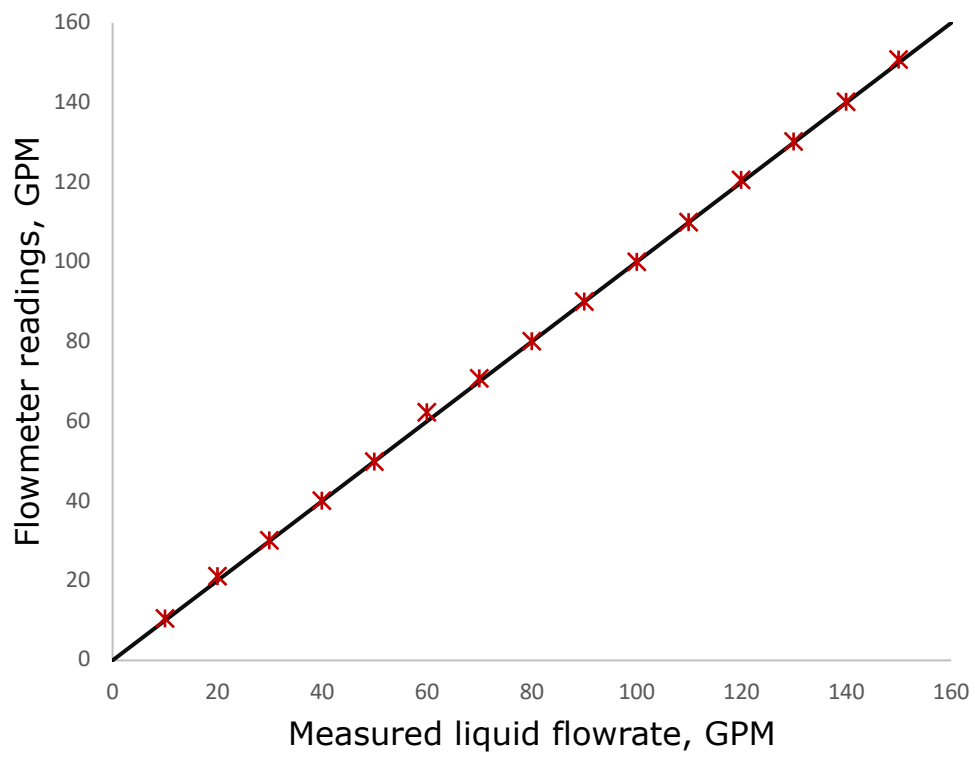


Figure B.4: Comparison of liquid flowmeter readings to manually measured values

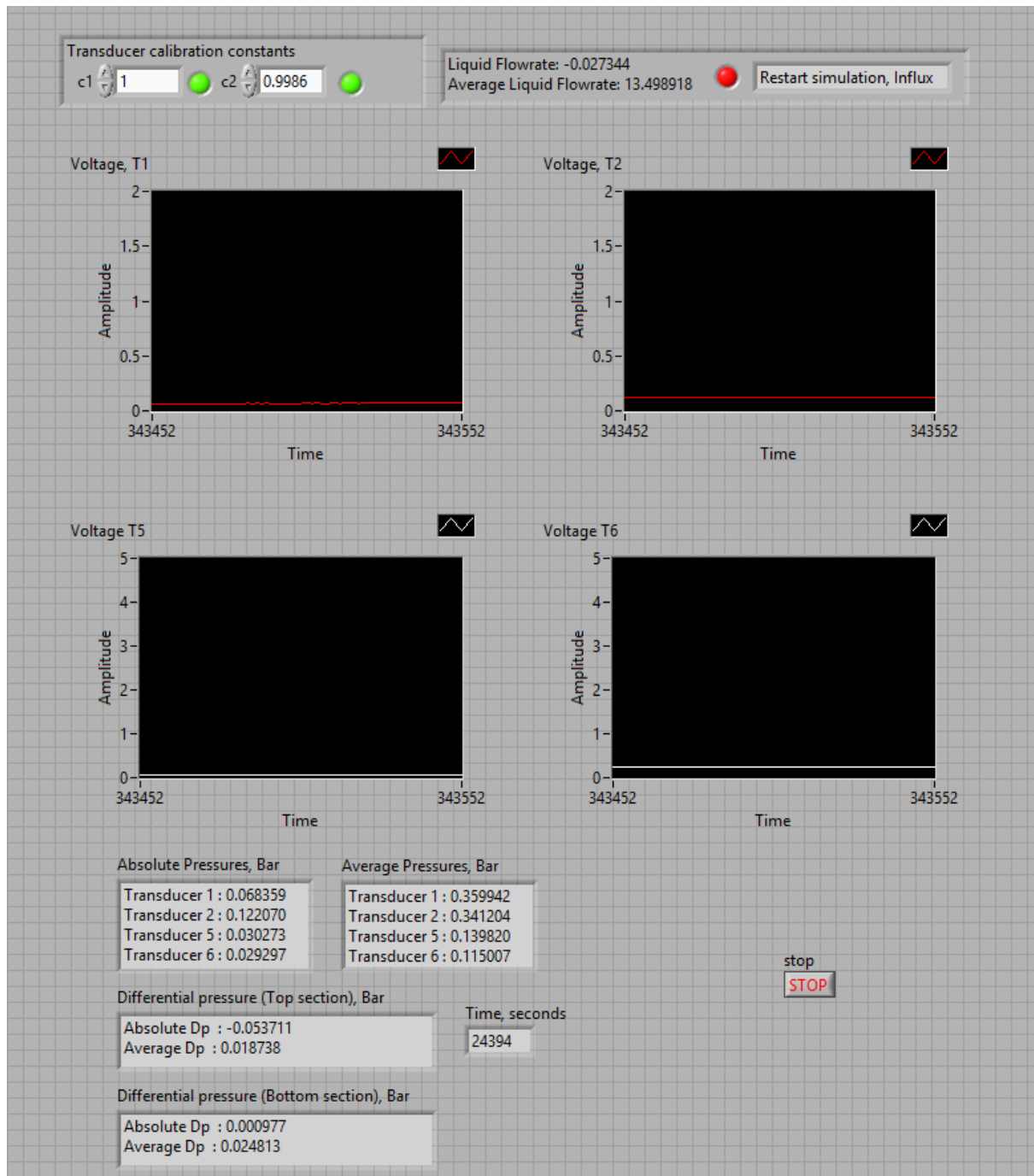


Figure B.5: LabVIEW front panel design for data acquisition